Studies of ω Photoproduction off Proton at the BGO-OD Experiment

Dissertation
zur
Erlangung des Doktorgrades (Dr. rer. nat.)
der
Mathematisch-Naturwissenschaftlichen Fakultät
der
Rheinischen Friedrich-Wilhelms-Universität Bonn

von
Oliver Freyermuth
aus
Bonn-Bad Godesberg

Bonn, April 2017

Dieser Forschungsbericht wurde als Dissertation von der Mathematisch-Naturwissenschaftlichen Fakultät der Universität Bonn angenommen und ist auf dem Hochschulschriftenserver der ULB Bonn http://hss.ulb.uni-bonn.de/diss_online elektronisch publiziert.

1. Gutachter:	Prof. Dr. Friedrich Klein
2. Gutachter:	Prof. Dr. Klaus Desch
Tag der Promotion:	25.07.2017
Erscheinungsjahr:	2017

Abstract

Hadrons are composite particles which experience a mutual, non-fundamental interaction, i.e. the same force responsible for keeping protons and neutrons bound together within the atomic nucleus. This hadronic interaction and the way how hadrons are produced are under experimental investigation since several decades and are not fully understood yet. The newly installed BGO-OD experiment aims to study the mechanisms responsible for the 'photo-production' of hadrons (i.e. production induced via a photon beam). The production of vector mesons, which are hadrons with spin '1', and of hadrons with strangeness are the major processes of interest at BGO-OD. A research programme on the photoproduction of one of the lightest vector mesons, the ω, has been proposed by the BGO-OD collaboration to the physics advisory committee (PAC) of ELSA in 2012.

The BGO-OD experiment has been set up at the ELSA electron accelerator facility in Bonn. It uses a bremsstrahlung-produced photon beam whose polarization can be tuned. The photons impinge on a proton target, which is surrounded by a central, electromagnetic calorimeter covering almost the full solid angle. A magnetic spectrometer is attached in the forward direction to reconstruct the momentum of forward going charged particles. It is complemented by time of flight walls to measure the relativistic speed β and provide particle identification. Furthermore, the experiment is equipped with a very open hardware trigger which allows to acquire events for different physics proposals simultaneously.

This thesis is part of the endeavour to take the BGO-OD setup into operation. Along this project, technical preparation work has been performed focusing on the improvement of the time resolution requested for all detector components. It encompasses the technique for the time alignment of the detector signals to define the trigger conditions and the procedures for the time calibration, which now allow for a full control of the time information for the complete set of almost 6000 channels. Two scintillator walls for time of flight measurement have been installed and commissioned. They are equipped with a new readout electronics which was tested and implemented in the course of this thesis and allowed to improve the identification of forward going charged particles.

In parallel to the improvement of the time resolution performances of the BGO-OD setup, a significant effort has been put into the development of software tools for general use by the full collaboration. These addons are covering common analysis tasks such as the selection or rejection of events and the visualization of physics observables. Furthermore, the processing of

the data in multiple stages has been embedded in the analysis framework such that it is now possible to start from a common, pre-processed and reduced dataset.

Finally, based on data recorded in 2015 with not yet fully completed commissioning of the BGO-OD setup, a first reconstruction of ω photoproduction events is attempted. As a cross-check of the quality of the collected data and of the software procedure, the same dataset is also used for the reconstruction and analysis of π^0 photoproduction events, this reaction being the best known photoproduction process nowadays. While the results for the π^0 channel show good agreement with published data within the statistical uncertainties, the results obtained for the analysis of ω photoproduction indicate that the existing setup is still inappropriate to study the photoproduction of the ω meson. Only if the full setup is brought into operation, and the angular resolution expected within the vector mesons' proposal is achieved, a better discrimination between ω photoproduction events and competing background channels could allow to perform the proposed measurements.

Contents

Chapter 1

Introduction

The discovery of the composed nature of the atomic nucleus consisting of positively charged protons and uncharged neutrons raised the question of the binding force keeping these constituents together. This force had to be stronger than the electromagnetic one to overcome the repulsion among protons. It also had to be attractive in a short range both for protons and for neutrons to keep them bound within the size of the nucleus. In 1935, Yukawa suggested a model of this interaction (c.f. [Yuk35]), describing it as mediated by a massive particle which was later found and called the pion.

In the study of the strong interaction, beams of pions and protons were used as probes scattering off proton targets, taking advantage of the large interaction probability which allowed to collect high statistics in a relatively short time. In these experiments, an unexpectedly large 'zoo' of particles was discovered and the term *hadrons* was developed for all these strongly interacting particles. The newly discovered hadrons were divided into *baryons* with half-integer spin and *mesons* carrying integer spin.

Many of the hadrons' properties have been studied and found since then, and experiments employing refined methods and tools are still ongoing to this day. Advanced studies on the mechanisms for the production of hadrons are performed via electro- or photoproduction experiments, where meson production off a proton target is induced by electromagnetic probes. These probes are point-like, well characterizable and their degrees of freedom (e.g. energy and spin) can be tuned experimentally. However, the use of the electromagnetic probes comes at the disadvantage of interaction probabilities which are orders of magnitude lower than those between hadrons.

Pion production off protons, achievable both with pion beams and in photoproduction experiments, has been the first reaction which was studied extensively. Several states with discrete masses were observed as bumps in the energy spectra. These bumps have been interpreted

as footprint of the resonant excitation of the target proton and its subsequent de-excitation via pion emission. The excited states of protons and neutrons have in the past been denoted by their definite quantum numbers $L_{2I,2J}(M)$ with L being the relative orbital angular momentum of the fictitious proton-pion system, M the mass and I and J the isospin[1] and the total angular momentum, respectively[2]. The observation of the proton's excited states was a further indication that the proton is not point-like, but a composite object featuring a sub-structure instead. The investigation of the full spectrum of excited states and their identification belongs to the field of baryon spectroscopy, which attempts to identify the internal degrees of freedom of protons and neutrons by describing their excitation spectrum.

In the meantime, the research on the hadrons' production mechanism has been extended to other meson-baryon final states. Since the pions are mesons with zero spin while the protons have spin $1/2$, an advanced step in the investigation of the production mechanisms and their dependence on the spin as a degree of freedom is the study of the production of mesons which carry spin themselves. The mesons with spin 1 are called vector mesons, the lightest ones being the $\rho(770)$ and the $\omega(782)$.

The BGO-OD experiment located at the ELSA electron accelerator facility in Bonn is one of the experiments dedicated to studies of the photoproduction of strange and vector mesons off nucleon targets. It comprises a central electromagnetic calorimeter covering almost the full solid angle, and a forward magnetic spectrometer complemented by time of flight walls for particle identification. A linearly polarized photon beam can be employed to study spin-dependencies of the mesons' photoproduction process.

This thesis ventures into the construction and commissioning of the BGO-OD experimental setup both in terms of hardware and analysis software, guiding towards the first reconstruction of ω photoproduction events at BGO-OD with linearly polarized photon beam. A procedure to extract the normalized difference of reconstructed ω photoproduction events for two polarization planes perpendicular to each other, called photon beam asymmetry, is presented. The measurements proposed to the PAC[3] of ELSA in 2012 included the extraction of the photon beam asymmetry of the ω photoproduction both off protons, extending the energy range beyond published results, and off neutrons. The actual knowledge about $\gamma p \to p\omega$ is summarized in section 1.1. The BGO-OD setup is not yet installed completely, namely two tracking detectors for charged particles are still missing, and the foreseen angular resolution for charged particles is not achieved yet. Nevertheless, it was tried to perform an analysis of ω photoproduction events within this thesis to explore the capabilities of the existing setup.

The layout of this thesis has been designed accordingly. Chapter 2 introduces all components of the BGO-OD setup and their characteristic properties. In chapter 3, the technical work on the

(1) The isospin is a discrete quantum number introduced to describe in how many charged states of similar masses and interaction strengths a hadron exists.

(2) Nowadays, the excited states of proton and neutron are called $N(M)$ or $\Delta(M)$ if they have isospin $1/2$ or $3/2$, respectively.

(3) **P**hysics **A**dvisory **C**ommittee

procedures for the trigger time alignment and the time calibration which lay the foundation for the control of the time resolution of the experimental setup is presented. This work is extended by the commissioning of the two time of flight walls complementing the forward spectrometer. This project also included the characterization of a new readout system offering time over threshold information which can be used to improve the resolution of the relativistic speed β for forward going charged particles. Both the necessary hardware studies and software work are discussed in chapter 4. In chapter 5, the developments performed in the context of the analysis framework of BGO-OD are presented. The framework has been largely extended with new building blocks to allow for an easy, yet well performing definition of physics selections cuts and a partitioning of the analysis chain in a common pre-processing and physics analysis part.

Making use of the improved time performances of the BGO-OD setup and of the flexibility of the developed software tools, the final focus is put on the study of the ω photoproduction reaction and the extraction of the beam asymmetry. For this purpose, the software chain and the beam asymmetry extraction have been tested and developed using the π^0 photoproduction process, before the ω reconstruction based on the detection of the three pion final state has been implemented. The developed technique including a dedicated background subtraction method is described in chapter 6. Finally, the results and conclusions of this work are summarized in chapter 7.

As a short introduction into the field, results from recent world-wide experiments on ω photoproduction are recapitulated in the following.

1.1 Status of the Studies on ω Photoproduction

The ω meson has a mass of about 783 MeV and shows two major decay modes: the three-pion decay $\omega \to \pi^+\pi^-\pi^0$ dominating with a branching ratio of about 89 %, and the radiative decay $\omega \to \pi^0\gamma$ with a branching ratio of about 8 % (c.f. [Pat+16]). Its production threshold for photons off protons is 1.1 GeV due to its mass.

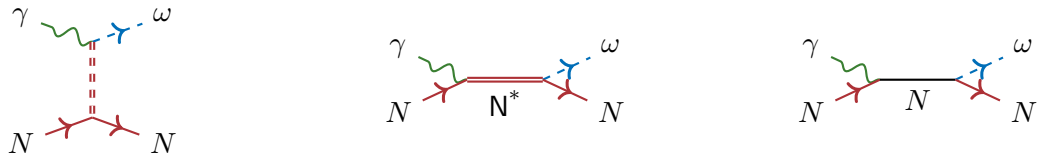

(a) Exchange of virtual particles in the t-channel

(b) Resonant term in the s-channel

(c) Non-resonant term in the s-channel (Born term)

Figure 1.1: Feynman-like diagrams for visualization of the most contributing mechanisms to the ω photoproduction process.

Feynman-like diagrams visualizing the mechanisms considered to be the most contributing ones to the ω photoproduction process are shown in fig. 1.1. In the first diagram (c.f. fig. 1.1a)

the interaction between the photon and the target nucleon is described via the exchange of one or more virtual particles in the t-channel of the reaction. The last two diagrams visualize the interaction as the absorption of the incoming photon in the s-channel of the reaction with (c.f. fig. 1.1b) or without (c.f. fig. 1.1c) lifting the nucleon into an excited state.

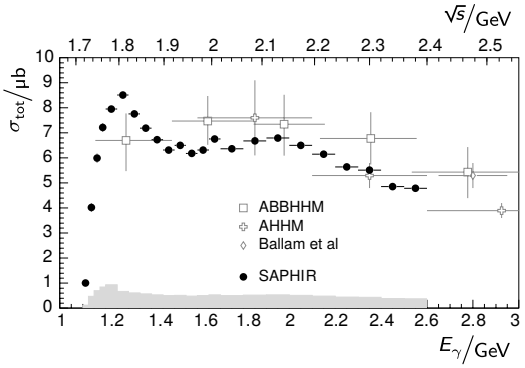

(a) Total cross-section data of the $\gamma p \to p\omega$ reaction.

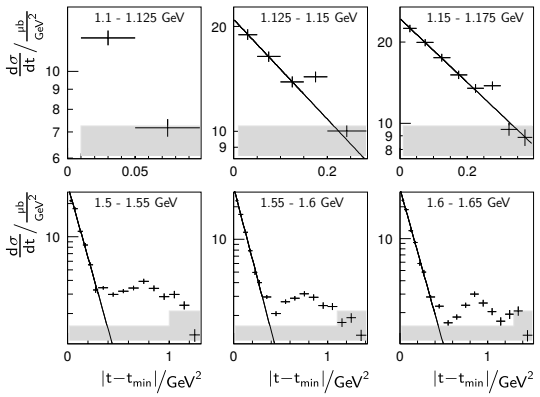

(b) Differential cross-sections of the $\gamma p \to p\omega$ reaction, data points from the SAPHIR collaboration.

Figure 1.2: Total and differential cross-sections of the $\gamma p \to p\omega$ reaction, measured by the SAPHIR collaboration (c.f. [Bar+03]).

Relevant studies of ω photoproduction have already been performed by previous experiments. The SAPHIR(4) experiment at ELSA in Bonn investigated ω photoproduction off the proton with $\omega \to \pi^+\pi^-\pi^0$, using an unpolarized photon beam with energies up to 2.6 GeV. The experiment consisted of a central drift chamber inside a magnetic field and forward tracking (c.f. [Bar+03]). In measurements of the total cross-section, the maximum was found to be approximately 8.5 μb(5) for incoming photon energies of 1.3 GeV (c.f. fig. 1.2a). The extraction of differential cross-sections revealed a dominating diffractive behaviour, with typical exponential fall-off of the cross-section with increasing transfer momentum. This phenomenon suggests that the most contributing term to the production of the ω meson is the exchange of virtual particles in the t-channel of the reaction (c.f. fig. 1.1a). Additionally, energy-dependent bump-structures have been observed in the differential cross-section hinting at contributions from resonant terms to the production of the ω meson (c.f. fig. 1.2b).

The results of SAPHIR have been confirmed by the high precision measurements of differential cross-sections and angular distributions of the ω decay products performed at Jefferson Lab with the CLAS(6) detector setup. Unpolarized photon beam with higher energies up to 3.7 GeV was used to study ω photoproduction identifying the $\omega \to \pi^+\pi^-\pi^0$ decay channel with almost

(4) **S**pectrometer **A**rrangement for **PH**oton **I**nduced **R**eactions
(5) The 'barn' ($1\,\mathrm{b} \mathrel{\hat{=}} 1 \times 10^{-28}\,\mathrm{m}^2$) is an effective area providing a measure of the interaction probability.
(6) **C**EBAF **L**arge **A**cceptance **S**pectrometer, at the **C**ontinuous **E**lectron **B**eam **A**ccelerator **F**acility

full angular coverage, but limited acceptance at very forward angles (c.f. [Wil+09a]). The high precision cross-section results are interpreted close to the reaction threshold as the indication of ω meson production via proton excited states called $F_{15}(1680)$ and $D_{13}(1700)$ in the spectroscopic notation. At higher energy, they are interpreted as the indication of ω production via excitation of the target proton to states with masses of 1.9 GeV and 2.1 GeV and increasingly higher relative angular momentum (c.f. [Wil+09b]).

The A2 experiment at MAMI[(7)] covers a limited energy range with photon energies up to 1.5 GeV and confirmed the previous cross-section results (c.f. [Str+15]).

First measurements using polarized photons have been performed at the ELSA facility in Bonn with the CBELSA/TAPS setup. As a difference to SAPHIR, it is not equipped with forward tracking detectors, but is optimized for detection of final state photons. ω photoproduction studies were performed with two linearly polarized photon beams, whose polarization planes were chosen to be perpendicular to each other. The ω meson was identified through its radiative decay $\omega \to \pi^0\gamma$. The normalized difference of reconstructed ω photoproduction events for the two polarization planes, called photon beam asymmetry, was measured in an energy range from threshold up to 1.7 GeV. The results confirmed the importance of s-channel proton excited state contributions in the ω production process (c.f. [Kle+08]).

The result has been confirmed by the GRAAL[(8)] collaboration at the ESRF[(9)], which collected high statistics data for photon energies up to 1.5 GeV. Both decay modes $\omega \to \pi^+\pi^-\pi^0$ and $\omega \to \pi^0\gamma$ were used and beam asymmetries off a proton target could be extracted. Close to threshold, the data have been found compatible with a model description which foresees an important role of the proton excited state $F_{15}(1680)$ in the production of the ω meson. At photon energies in the range between 1.3 GeV and 1.5 GeV, the data are well described by a phenomenological model which considers the excitation of the proton to the $P_{13}(1720)$ state dominant for ω photoproduction. First studies of data using quasi-free neutron target revealed very different results than the ones obtained off proton target, although the isospin of the ω-nucleon system is the same due to the zero isospin of the ω meson. This astonishing observation requires further investigations (c.f. [Veg+15]).

On the base of already published results, the BGO-OD collaboration presented the intention of a new campaign of measurements on the ω photoproduction to the PAC of ELSA in 2012. The proposal includes the extraction of the beam asymmetry of ω photoproduction off proton target in the energy range between 1.2 GeV and 1.8 GeV, covering the region where published data from the GRAAL experiment is available for an initial cross-check and extending the existing data to higher energies. Furthermore, measurements of ω photoproduction off the neutron are foreseen covering the same energy range to provide further insight into the very different beam asymmetry results indicated by first studies at the GRAAL experiment.

(7) **MA**inz **MI**crotron
(8) **GR**enoble **A**nneau **A**ccelerateur **L**aser
(9) **E**uropean **S**ynchrotron **R**adiation **F**acility, located in Grenoble

Chapter 2

The BGO-OD Experiment

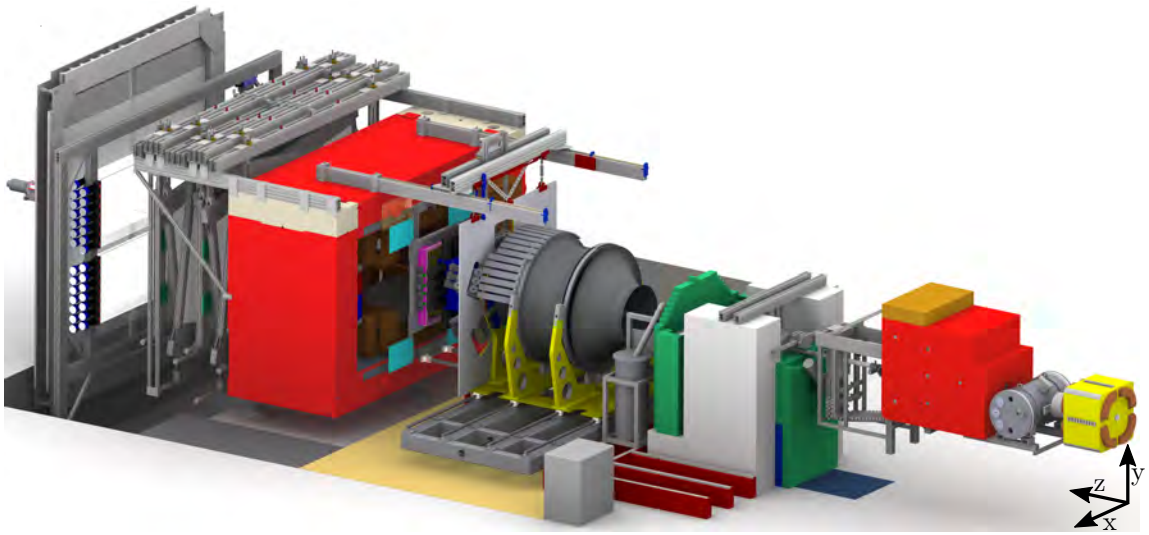

Figure 2.1: Illustration of the BGO-OD experiment setup.

The BGO-OD experiment located at the ELSA electron accelerator facility in Bonn is dedicated to the study of meson photoproduction reactions off nucleon target. It combines a central electromagnetic calorimeter covering almost 4π of solid angle with a forward magnetic spectrometer which is complemented by time of flight walls for particle identification. For the explanation of the BGO-OD set-up, the laboratory frame is defined as the reference frame, with the $\hat{z}$ axis parallel to the photon beam direction, the $\hat{y}$ axis in vertical orientation and the $\hat{x}$ axis satisfying the orthogonality condition $\hat{z} = \hat{x} \times \hat{y}$.

The experimental set-up consists of:

1. a photon beam, produced via bremsstrahlung by the electrons delivered by the ELSA accelerator impinging on a target radiator. The monitoring of the produced photon beam is performed through a tagging system and two flux detectors, which are described in section 2.1.

2. a cryogenic target of liquid hydrogen or deuterium to perform photoproduction off free or quasi-free nucleons, shortly described in section 2.2.

The final state particles are detected in:

3. the central detector region, which covers a polar angle Θ between 25° and 155° with azimuthal symmetry. The trajectory of charged particles will be measured through a system of two **M**ulti-**W**ire **P**roportional **C**hambers (MWPC), whose installation and commissioning are still ongoing. The energy of the photons is determined in the BGO electromagnetic calorimeter and charged particle identification can be performed by combining the information of the deposited energy in the BGO and the energy deposited in an inner barrel of plastic scintillator bars. The central detector region is described in section 2.3.

4. the intermediate detector region, which covers the polar angle range between 10° and 25° with azimuthal symmetry. For this region, the installation of **M**ulti-gap **R**esistive **P**late **C**hambers (MRPC) was foreseen to detect charged particles with an angular resolution of about 2° in azimuthal angle and better than 1° in polar angle. Due to huge delays in the production phase of the detector, a ring of plastic scintillator tiles, the SciRi detector, is installed as a temporary solution. The intermediate detector region is described in section 2.4.

5. the forward detector region, which covers the polar angle between 2° and 10°. Two sets of tracking detectors with an open dipole magnet in between are used to reconstruct the trajectory of charged particles and to measure their momentum. Three layers of time of flight walls complete the spectrometer and allow to perform charged particle identification. The forward detector region is described in section 2.5.

2.1 Photon Beam Production and Monitoring

The BGO-OD experiment uses real photons produced via bremsstrahlung from the electrons provided by the ELSA accelerator impinging on a radiator target.

A short characterization of the accelerator and the inherent macroscopic and microscopic time structures relevant for the analysis will be given in section 2.1.1. The goniometer which contains the radiator targets will be described in section 2.1.2. Afterwards, the detectors necessary to characterize the photon beam will be presented: First off, the photon tagger which provides

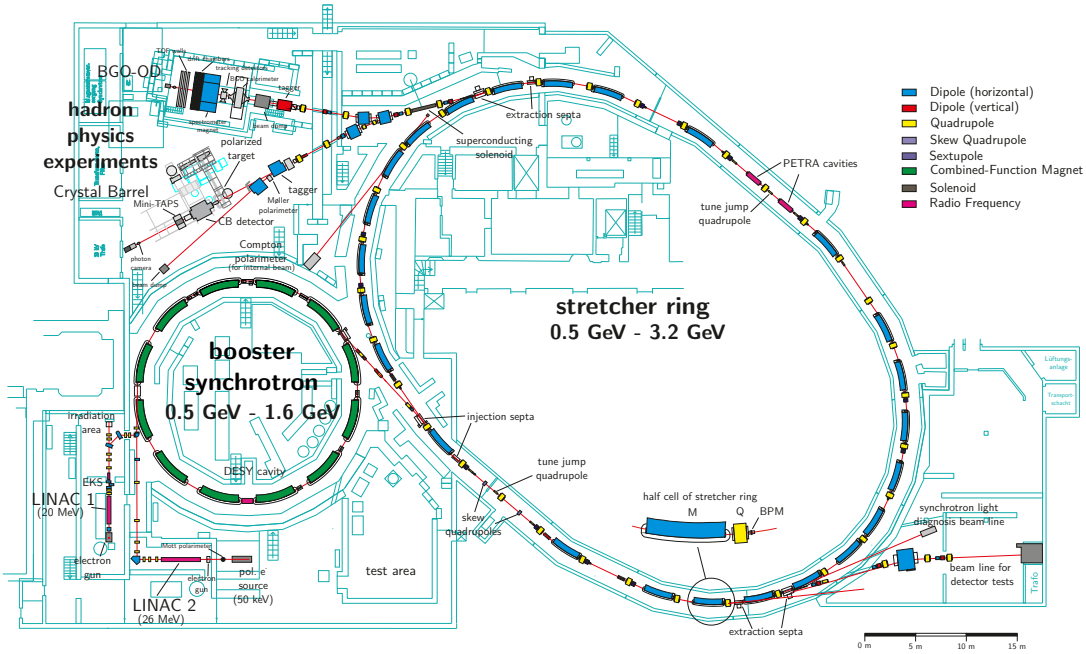

Figure 2.2: Overview of the accelerator facility ELSA in Bonn [Fro+16].

the online time reference and photon energy information for the experiment will be discussed in section 2.1.3. It is complemented by the tagger SciFi detector 'ARGUS' which provides increased energy resolution and will be shortly introduced in the same section. Finally, the flux determination setup consisting of the flux monitoring system 'FluMo' (c.f. section 2.1.4) and a total absorbing counter 'GIM' (c.f. section 2.1.5) is presented.

2.1.1 Accelerator ELSA

The accelerator ELSA (German: **El**ektronen-**S**tretcher-**A**nlage) located in Bonn is a three-staged electron accelerator setup as shown in fig. 2.2. The first stage is the injecting LINAC (**lin**ear **ac**celerator), the second stage is the booster synchrotron ring, and the final stage is the stretcher ring.

For hadron physics experiments, LINAC 2 is used for injection of electrons into the booster synchrotron. These can either be produced using a laser and a Pockels cell which allows for electron beam polarization, or be provided by a thermionic electron gun. Inherent to the synchrotron technique, the electrons are accelerated in bunches. After the electrons have reached the maximum energy in the booster, they are extracted from this first ring and injected into the stretcher ring. This process needs to be repeated multiple times (usually more than 18 times) until the stretcher ring is filled completely. Afterwards, the electrons are accelerated up to an energy of at maximum 3.2 GeV for hadron physics experiments. The accelerated electrons are then extracted to the corresponding beamline of the experiment.

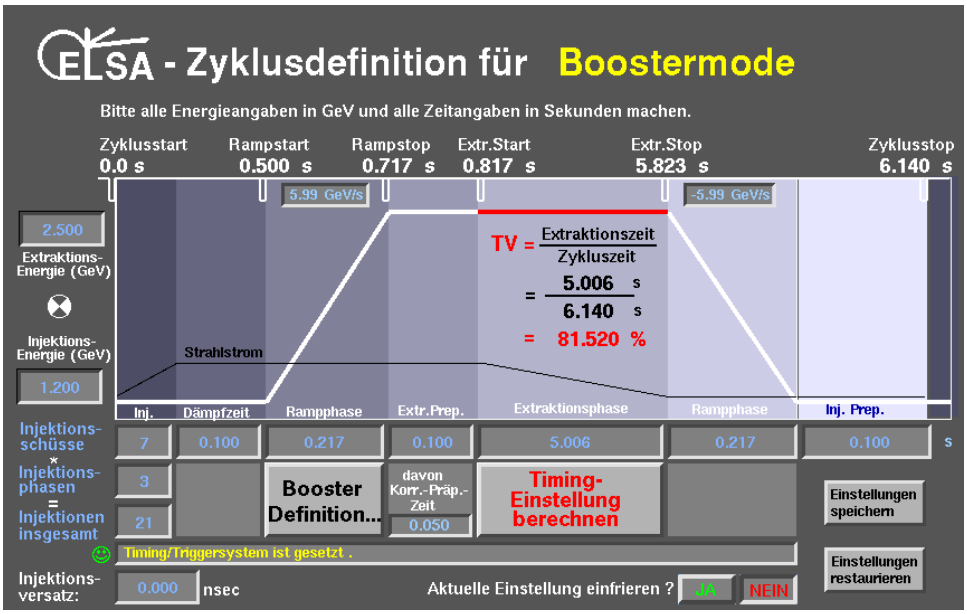

Figure 2.3: Example of a visualization of the macroscopic timing definition of the booster mode operation for the ELSA accelerator. The different phases and number of injections can be seen. The horizontal axis is the time axis. The black line labelled 'Strahlstrom' indicates the change of the beam current during the several phases, while the white line corresponds to the current through the magnets. The figure is extracted from the control system of the accelerator while the system was in standby (c.f. [PFH13]), which is why the settings, for example extraction energy and delay between injections, do not exactly match BGO-OD data-taking conditions.

The accelerator can be operated in different modes (stretcher mode, booster mode and use as a synchrotron light source). For the hadron physics experiments, only the booster mode is used. The different phases of one cycle in this mode of operation of the accelerator are shown in fig. 2.3.

The first phase in the cycle labelled 'Inj.' is the injection phase in which the ELSA ring is filled with electrons extracted from the booster synchrotron, as can be seen in the diagram by the increasing beam current. The second phase, labelled 'Dämpfzeit', is a necessary waiting period to reduce the longitudinal and transversal movement of the beam particles (c.f. [Pic95]). In the third phase labelled 'Rampphase', the ramp-up of the magnet current and the acceleration of the electrons takes place. This is followed by another pause in which the extraction is prepared. Finally, the extraction of the electron beam into the experimental hall can be started. This phase is labelled 'Extraktionsphase' and is usually also named 'in-spill' period from the experiments' point of view. It usually also corresponds to the longest phase of the cycle and is the only phase in which the hadron physics experiments take physics data. It is followed by another ramping phase in which the current through the magnets is reduced again, before the cycle is ended with a phase in which the next injection is prepared.

For the hadron physics experiments, only the 'in-spill' phase is used, the remaining phases are usually not differentiated and just termed 'off-spill'.

Several time structures which are of relevance for the setup and analysis are inherent to the accelerator ELSA:

- The macroscopic duty cycle which is the described spill structure. As visible in fig. 2.3, this is defined by the 'in-spill' extraction time ('Extraktionszeit') of about 5 s and the full cycle time ('Zykluszeit') of about 6 s.
- The revolution time of electrons through the stretcher ring: 548 ns. If the filling of the stretcher ring is not homogeneous, correlated structures may appear in the data (c.f. [Fre12]).
- The bunch length of 80 ps to 100 ps depending on the accelerator configuration.
- The bunch spacing of 2 ns, resulting from the radio frequency of 500 MHz used for acceleration.

2.1.2 Goniometer

After the extraction from the stretcher ring, the electron beam impinges on a target radiator, where the real photon beam is produced via bremsstrahlung. Additionally, a luminous screen for optical beam positioning and a coil used for Møller scattering are also installed in the tank. The radiators are held in position and can be aligned with respect to the impinging electron beam through a goniometer system. This full system is installed in vacuum inside the so-called goniometer tank (c.f. fig. 2.4).

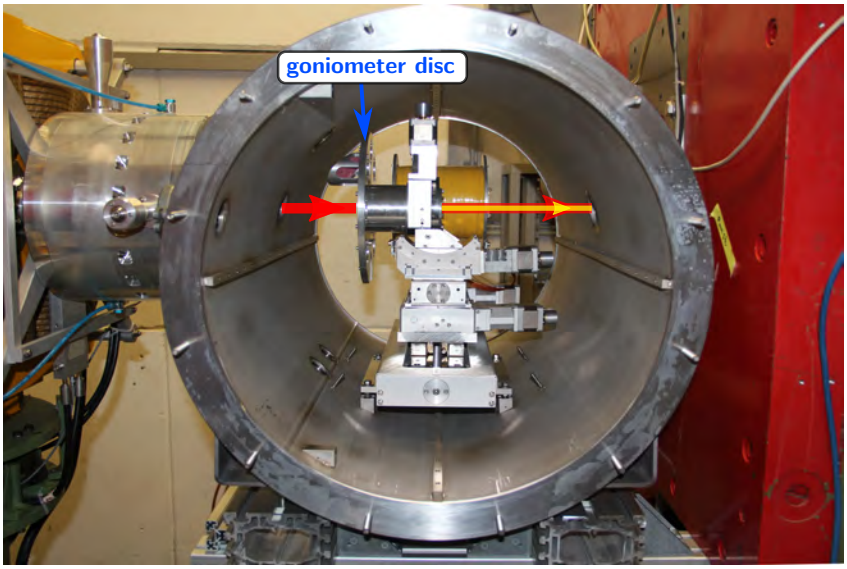

Figure 2.4: Side-view of the goniometer tank before closing and evacuating the full volume. The goniometer inside the tank and the goniometer disc containing the various radiator materials is depicted. In the centre of the goniometer disk, the diamond crystal which is used for linear polarization is mounted. The electron beam enters from the left and is converted to an electron-photon beam after the bremsstrahlung process as indicated by the coloured arrows. On the right hand side, the red tagger dipole magnet deflecting the post-bremsstrahlung electrons can be seen.

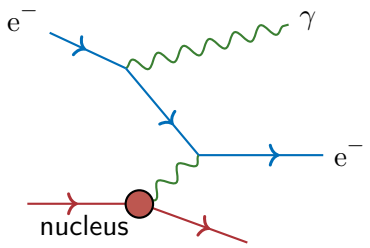

Figure 2.5: Feynman-like illustration of the bremsstrahlung process.

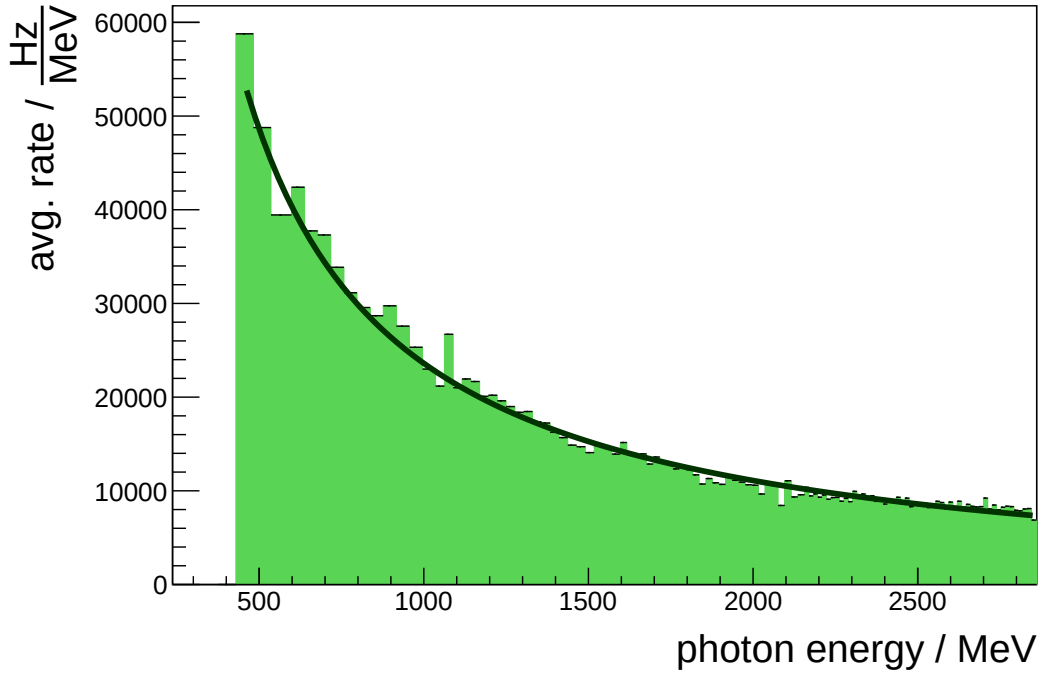

Figure 2.6: Bremsstrahlung intensity spectrum as recorded by the tagger detector, using an amorphous copper radiator. The rate is measured by the hardware double coincidence scalers which will be described in more detail in section 5.4.4 alongside the relative flux normalization for the measurement of the π^0 beam asymmetry. It has been normalized per MeV to overcome the different widths in energy of the coincidence channels, and a $1/E_\gamma$ shape with free scaling factor and constant offset has been fitted to illustrate the expected shape. A short description of the geometric design of the tagger hodoscope will be given in section 2.1.3. This visualization was performed using the normalization runs 29961 to 29969 of the October / November 2015 beamtime which are also used for the extraction of the polarization degree as will be shown in fig. 2.7.

Several radiator targets with varying material and thickness are mounted on the goniometer disc. Using amorphous radiators, for example copper foil with thicknesses on the order of 100 µm, the kinematics of the bremsstrahlung process as illustrated in fig. 2.5 is not restricted. Consequently, an intensity spectrum following a $1/E_\gamma$ shape as shown in fig. 2.6 with azimuthal symmetry is observed.

The usage of an aligned diamond crystal allows to restrict the kinematics of this process. In addition to the incoherent process in which only a single nucleus is involved, coherent bremsstrahlung in which the whole crystal lattice takes over the recoil momentum of the scattering process takes place.

This coherent contributions can be observed as a peak in the energy spectrum, from which the degree of linear polarization of the photon beam can be extracted. An example for this is shown in fig. 2.7 and will be discussed in more detail along the analysis of the π^0p photoproduction in

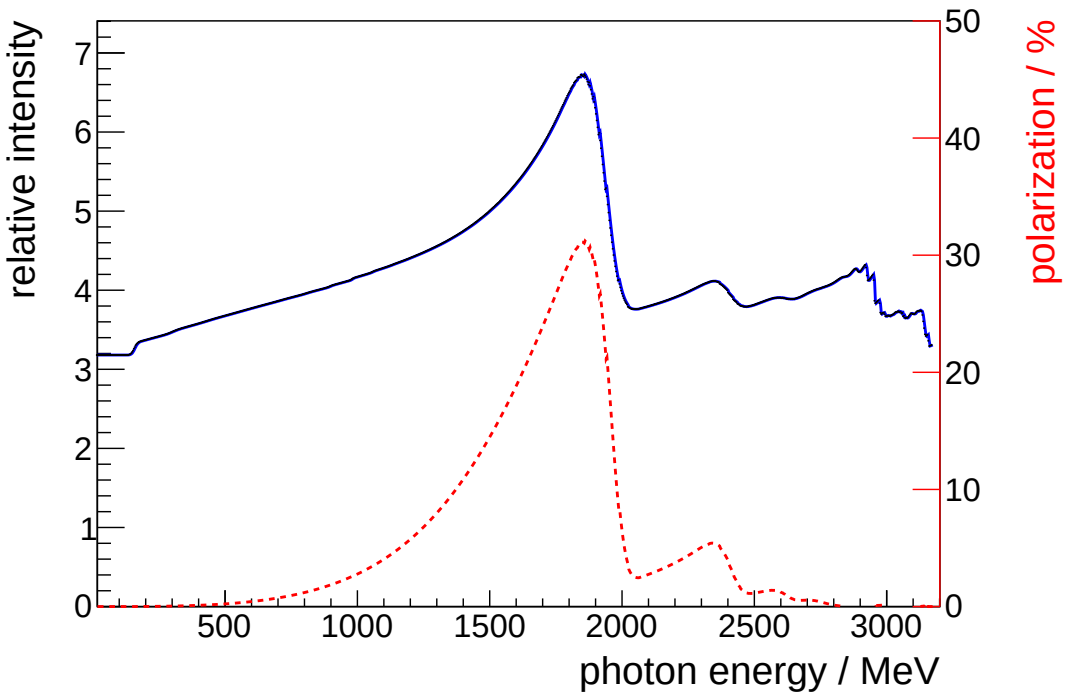

Figure 2.7: Example plot to illustrate the extraction of the degree of polarization from the relative tagger spectrum. The upper, blue, solid line shows the fit to the relative intensity of the spectrum recorded with the diamond radiator for the polarization plane 'plus' divided by the spectrum recorded using the amorphous radiator. The lower, red, dashed line, is the degree of polarization extracted from the result of the fit. This extraction was done for the runs 29900 to 30059 of the October / November 2015 beamtime.

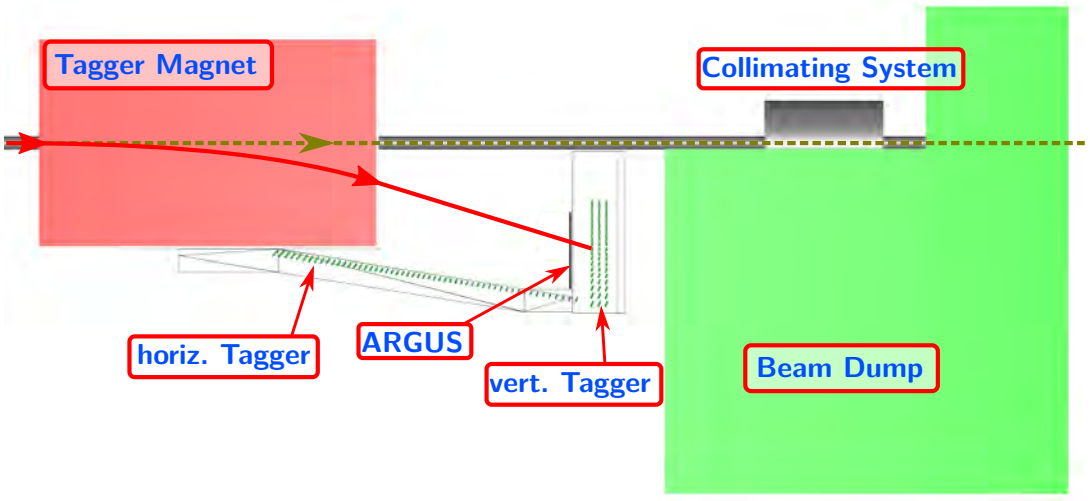

Figure 2.8: Side view of the tagging system including the tagger magnet. The photon beam is shown in dashed yellow, a deflected electron track is indicated in solid red. As can be seen, the photon beam is passing through the evacuated beamline which guides it through the beam dump which contains a collimating system. The electrons are deflected by the magnetic field and detected by the tagging hodoscope and the tagger SciFi detector 'ARGUS'. The ELSA electrons which did not undergo the bremsstrahlung process are deflected the least since they have the highest momentum. They are directed to an absorber inside the beam dump without being tagged.

section 5.4.3. An exhaustive description of the technique used for alignment of the crystal and the extraction of the achieved degree of polarization is described in more detail in [Bel16].

2.1.3 Photon Tagging System

The tagging system is used to 'label' each photon produced via bremsstrahlung (c.f. fig. 2.5) by detecting the corresponding post-bremsstrahlung electron. If the energy of the electronics provided by the accelerator ELSA is known and the energy of the post-bremsstrahlung electron is measured, the energy of the bremsstrahlung photon can be calculated by energy conservation.

The first element of the tagging system is a magnet which deflects the post-bremsstrahlung electrons on different trajectories depending on the energy lost via the bremsstrahlung process. The deflected electron is then detected in the tagging hodoscope, often also termed 'Tagger'. Through a calibration procedure, the position of the deflected electron detected in the tagger can be converted to its energy. The ELSA electrons which did not undergo bremsstrahlung and thus conserved their initial energy are deflected by the smallest angle and are absorbed in the beam dump without being tagged.

The tagging hodoscope is constructed from 120 scintillators and covers an energy region ranging between 10 % and 90 % of the incoming ELSA electron energy. For suppression of uncorrelated background, the scintillators always overlap by approximately 55 % with their geometrically adjacent partner. A time coincidence between signals measured by two adjacent

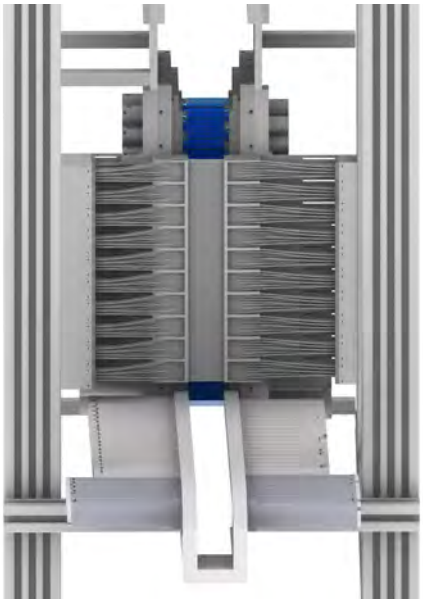

Figure 2.9: CAD rendering of the tagging system and the tagger SciFi 'ARGUS', view in beam direction.

scintillators is required as a signature of the passage of an electron both in the online trigger logic and also in the offline analysis.

The tagging hodoscope has been split into two parts due to spatial constraints: the 'horizontal' part covers the energies between 10 % and 32 % of the incoming electron energy with 54 scintillators and is placed directly in the focal plane of the deflection magnet, while the vertical part covers 32 % to 90 % and consists of 66 scintillators. For technical considerations, different widths of scintillators have to be used, hence the energy resolution varies between 1.7 % of the incoming electron energy at high post-bremsstrahlung energies (corresponding to low photon energies) up to 0.4 % for low post-bremsstrahlung energies (corresponding to high photon energies). The energy calibration and the measurement of the energy resolution have been performed using a dedicated procedure with low intensity electron beam not undergoing bremsstrahlung (c.f. [Bel16]). The efficiency of the system has been shown to be close to 100 %, and the design time resolution of about 250 ps which determines the quality of the start time of the experiment is achieved starting with the October / November 2015 beam time.

The measurements intended at BGO-OD foresee the use of a photon beam polarized in an energy range between 1.5 GeV and 2.0 GeV. For these photon energies, the corresponding post-bremsstrahlung electrons are deflected in the direction of the vertical part of the tagger. To monitor the stability of the position of the peak of the coherent bremsstrahlung (c.f. fig. 2.7) during data-taking, a higher energy resolution in this vertical part is desired. This is achieved by a scintillating fibre detector called 'ARGUS' which is placed in front of the vertical part of the tagger with respect to the flight direction of the post-bremsstrahlung electrons.

The detector is depicted in section 2.1.3. It covers an energy range from 30 % to 66 % of the incoming ELSA electron energy and consists of 480 double-clad BCF-10 scintillating fibres from

Saint Gobain which are arranged in three layers. The readout is performed with 30 Hamamatsu H6568 multi-anode photomultipliers with 16 channels each. An energy resolution of 0.08 % to 0.45 % of the incoming electron energy is achieved. Details about the construction of this detector and the in-beam characterization are provided in [Ale15] and [Rei15].

2.1.4 Flux Monitor 'FluMo'

The FluMo setup consists of three plastic scintillators with only 5 mm thickness with a size of 7 cm × 7 cm. They are made for detection of electron-positron pairs produced further upstream of this detector configuration. For this reason, the expected rate is by far lower than that of the fully absorbing GIM detector located behind, thus reducing rate limits due do dead time. Since the measured quantity is still linearly correlated to the photon flux, a scaling factor extracted in a dedicated calibration procedure with the GIM detector allows to determine the absolute flux.

The thin scintillators are made of BC404 material from Saint Gobain (originally Bicron) as is also used for the tagger hodoscope. They are adapted to ET Enterprises 9111B photomultipliers via fish-tail shaped light guides. The photomultipliers have been equipped with active bases designed in-house to improve the rate stability of the detector (c.f. [Zim12]).

The combination of the 3 scintillators lessens the dependency on the stability of the efficiency of each single detector, since in the analysis, a looser requirement of e.g. '2 out of 3' can be used.

Additionally, this detector setup provides a high time resolution almost sufficient to separate the bunches of the accelerator and can thus be used for time calibration of the other beam-related detectors, most notably the photon tagger. More details on the calibrations will be provided in chapter 3.

2.1.5 Gamma Intensity Monitor 'GIM'

At the very end of the beamline, the gamma intensity monitor 'GIM' has been placed. It is a lead glass detector with a PMT directly pressed against the glass. The detection process is based on the Cherenkov effect, which is why a wide distribution of pulse heights can be observed. The counter is fully absorbing and meant to be used for absolute normalization of the photon flux.

However, this statement is only valid for low beam currents and does not extend to usual data-taking intensities. Due to dead time effects, the GIM detector saturates already at rates of about 4 MHz. For this reason, the FluMo detectors described in the previous section are used for the actual monitoring of the photon flux. The GIM is only used for the absolute calibration of this flux monitoring system. For this purpose, data at lower beam intensity are recorded with trigger on the GIM detector. Otherwise, the lead glass device is removed from the beamline during normal data-taking to reduce radiation damage of the material.

The detector is read out with a Hamamatsu R2083 photo multiplier which is connected directly to the lead glass block with dimensions 6.5 cm × 6.5 cm × 30 cm via a silicone pad. The tube has been equipped with an in-house developed booster base to increase the rate stability (c.f. [Zim12]).

2.2 Cryogenic Target System

The target of the BGO-OD experiment contains a cylindrical cryo-cell which can be filled with liquid hydrogen or deuterium. The target cell itself is 6 cm long with a diameter of 3 cm and is connected to the end of the evacuated photon beamline, as shown in fig. 2.10a. To minimize the in-beam material, the target cell consists of an aluminium tube with Mylar windows at the front and the back. More details about the target construction can be found in [Rom12].

2.3 Central Detector Region

The central detector system directly surrounding the target covers the polar angle range between 25° and 155° with azimuthally symmetric detectors. It consists of three sub-detectors, the **M**ulti-**W**ire **P**roportional **C**hambers, short MWPCs, the BGO electromagnetic calorimeter and the scintillator barrel.

The MWPC detector system is still under commissioning. It consists of an inner and an outer chamber and could thus provide two points such that an absolute trajectory can be reconstructed. It will allow to increase the angular resolution in the central region and in case of multiple charged tracks facilitate vertex resolution which is crucial for the detached vertices common to the decay of particles with strangeness content.

The BGO electromagnetic calorimeter consists of inorganic crystals with each block being 21 radiation length deep which allows for full longitudinal absorption of electromagnetic showers. Additionally, the partial energy deposition of hadrons can be measured. In combination with the scintillator barrel which also measures the energy loss of charged particles through the thin plastic scintillator, charged particle identification can be performed.

In the following sections, the three sub-detectors are described in more detail.

2.3.1 Multi-Wire Proportional Chambers

The MWPCs are already fully installed, but still under commissioning and hence not yet used in the physics analysis of this thesis. The two chambers are designed to cover a polar angle range between 10° and 155° with an angular resolution of approximately 2° both for the polar and azimuthal angle.

2.3.2 BGO Rugby Ball

The main part of the central detector system is the electromagnetic calorimeter, the BGO rugby ball. It consists of 480 inorganic crystals from $Bi_4Ge_3O_{12}$ material.

The rugby ball is constructed from 15 'crowns'. Each such 'crown' covers the full azimuthal angle with 32 crystals. In the polar angle Θ, the range of 25° to 155° is covered. Consequently, each crystal covers 11.25° in azimuthal angle, while the crystal size in Θ varies such that the covered angle varies from 6° to 10°. It should be noted that the effective resolution of the

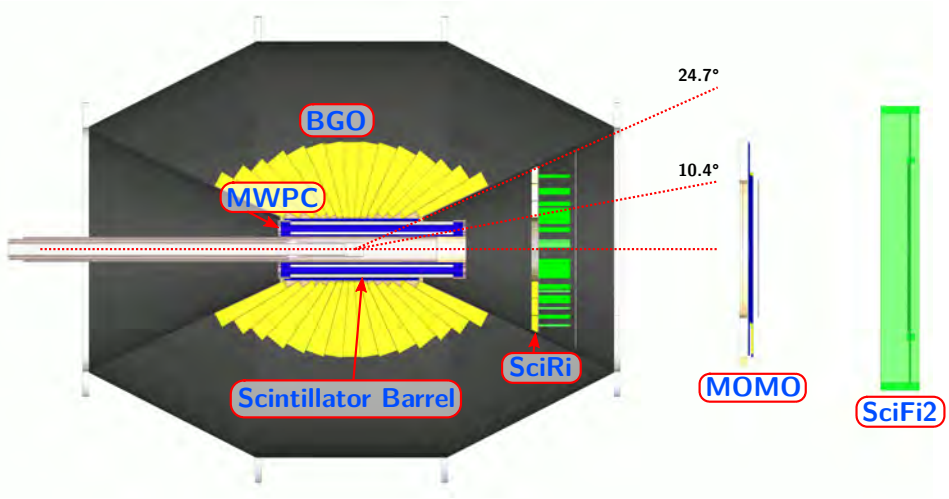

(a) Cut drawing made using the geometry description used in the software for analysis and reconstruction.

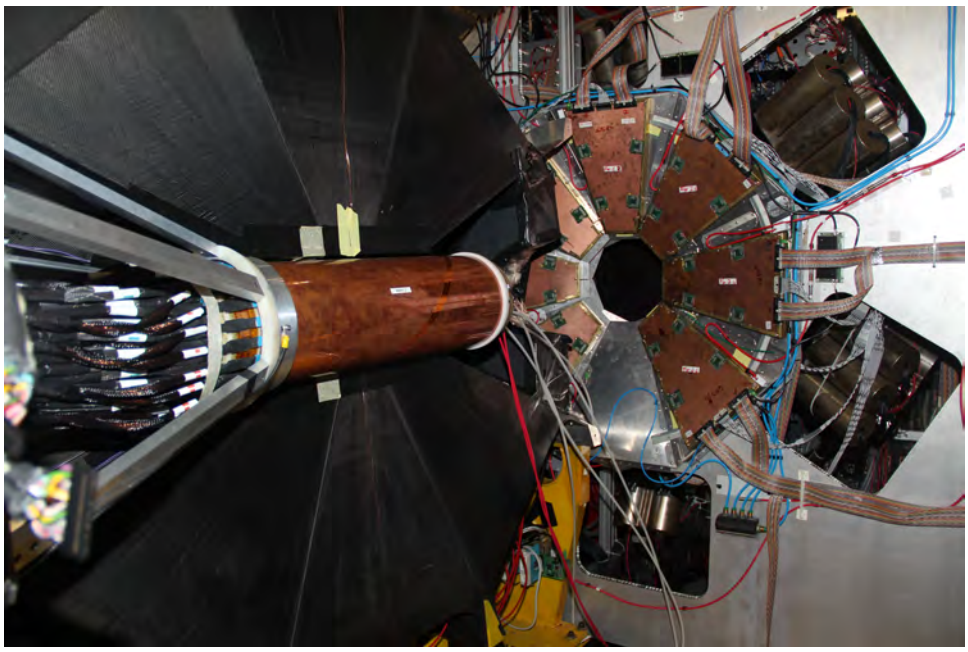

(b) Photograph of the central detector systems with BGO half opened.

Figure 2.10: Side views of the central and intermediate detectors. In the cut view in fig. 2.10a, the BGO, scintillator barrel and MWPC surrounding the target in the central region can be seen. Additionally, the SciRi detector covering the intermediate angular region is shown, and the two fibre tracking detectors of the forward spectrometer, MOMO and SciFi2, are also indicated. For higher time and spatial resolution, an MRPC detector between SciRi and MOMO is currently under commissioning. In the photograph in fig. 2.10b, MWPC, BGO, SciRi and the phototubes of the MOMO detector are found back. Additionally, the first petals of the flower-like design of the MRPC are visible.

detector is enhanced by the possible clustering especially for photons, and distorted by the length or misalignment of the target cell. All crystals are tapered and shaped like pyramids with 24 cm depth, which corresponds to approximately 21 radiation lengths (c.f. [Lev+96]). This geometric design is indicated in the cut view shown in fig. 2.10a. As visible in fig. 2.10b, the rugby ball is built from two halves which can be moved on a rail system separately to allow for insertion of the target and the MWPC detectors.

In inorganic crystals, the scintillation process is due to the electronic band structure of the material, in case of $Bi_4Ge_3O_{12}$, the scintillation is caused by an optical transition of the Bi^{3+} ion. In comparison to organic scintillators, the resulting signals are much longer in time, extending up to the order of several 100 ns. This allows for a more refined integration of the charge and thus an improved resolution of the deposited energy can be achieved, allowing for calorimetric applications. The achieved energy resolutions depend on the particle type. For photons with a measured energy of E, the Gaussian sigma of the fitted error was determined to be about $0.722 \cdot \sqrt{E}$. For other charged particles with measured energy E, a Gaussian sigma of $2.09 \cdot E^{0.16}$ was fitted.

On the other hand, the long signals spoil the time resolution, which can be mostly compensated by sampling the signal. For the physics analysis, the energy and time resolution of the system is crucial. All crystals are read out with W-Ie-Ne-R AVM16 sampling ADCs(1) which extract the signal start time and the pulse integral (c.f. [WIE11]). The achieved time resolution remains dependent on the energy mainly for single-crystal energy deposits below 20 MeV, while above this value the time resolution is better than 2 ns approaching 1 ns (c.f. [Jud16]).

During data-taking, it is possible to define trigger conditions based on the energy sum deposited in the BGO. This is facilitated by the attenuation electronics: the 15 attenuator modules treat 32 channels each, corresponding to one crown of the detector. Each of the attenuator modules provides an analogue sum output, which is then further summed together by linear fan-in fan-outs. The energy sums on the single crowns and the final analogue sum of all crowns is then discriminated at several thresholds depending on the trigger condition. More details on these and their use in combination with other detectors will be provided in the overview of all local triggers given in section 3.1.2.

For the definition of this analogue trigger threshold, a gain matching of the detector is crucial. This procedure and also a first level calibration is performed using radioactive ^{22}Na sources which are placed inside the detector. Two characteristic energies can be observed: The 511 keV of the positrons from the β^+ decay, which annihilate and produce a photon that is observed, and 1.275 MeV photons from the subsequent electromagnetic decay. Using both these characteristic lines, a gain matching of all crystals can be done by adjusting the high voltage such that the higher-energetic peak is observed at the same position in the ADC spectra for all channels and calibration constants for a first level calibration can be extracted. Due to the temperature dependency of the effective gain, dedicated calibration data are recorded at regular intervals, usually twice a day.

(1) **A**nalogue to **D**igital **C**onverters

This calibration procedure, however, assumes a high linearity of the readout electronics: the calibration is performed using energy deposits of approximately 1 MeV while during data-taking, energy deposits on the order of 100 MeV are common. This is in part accommodated by the already mentioned attenuators, which are set to 12 dB during regular data-taking and turned off for calibration runs. To overcome remaining scaling effects and temperature variations, a high level calibration using an iterative correction procedure after reconstruction of π^0 and η mesons is employed.

2.3.3 Scintillator Barrel

Inside the BGO calorimeter, a set of 32 longitudinally oriented plastic scintillator bars with trapezoidal shape are installed covering the full azimuthal angle. The bars are made from NE102 plastic scintillator material with a thickness of 0.5 cm and 43 cm length, and read out with Hamamatsu H3164–10 photo-multipliers on the upstream side.

They are used to disentangle charged and neutral particles and also allow for triggering on charged particles and studies with cosmic muons. Furthermore, a $^{dE}/_{dx}$ energy loss information is recorded which allows to differentiate between protons and pions if combined with the energy information deposited in the BGO. Examples for this reconstruction will be shown in section 4.6.2 in a comparison study of different readout electronics.

2.4 Intermediate Detector Region

For coverage of the polar angle between 10° and 25°, a **M**ulti-gap **R**esistive **P**late **C**hamber (MRPC) in blossom-like shape has been installed and is currently under commissioning. It consists of two layers of which each is equipped with 8 petals. A partial overlap between both layers allows for full coverage of the azimuthal angle. The 16 readout pads per petal define the granularity of the polar angle information. In lab tests, the time resolution of the detector was determined to be 60 ps (c.f. [Mes16]) which should allow for time-of-flight measurements. An azimuthal angular resolution of at least 2° can be expected.

In the meantime, the SciRi (**Sci**ntillator **Ri**ng) detector which covers the same polar region with 96 plastic scintillators has been installed 58 cm behind the target centre and is used mainly as a charged particle veto. The plastic scintillators are 2 cm thick and read out by avalanche photo diodes, short APDs. Using a time walk compensation technique similar to the one which will be described for the time of flight walls (c.f. section 4.8), a time resolution of approximately 3 ns can be achieved which is sufficient for correlation with other detectors. Additionally, the detector is used in two trigger conditions during data-taking in combination with the central calorimeter and the forward detectors as will be discussed in more detail in the discussion of the physics trigger logic in section 3.1.2.

The detector has been constructed in two half elements matching the two halves of the BGO calorimeter. Furthermore, the scintillator elements are designed such that the angular coverage

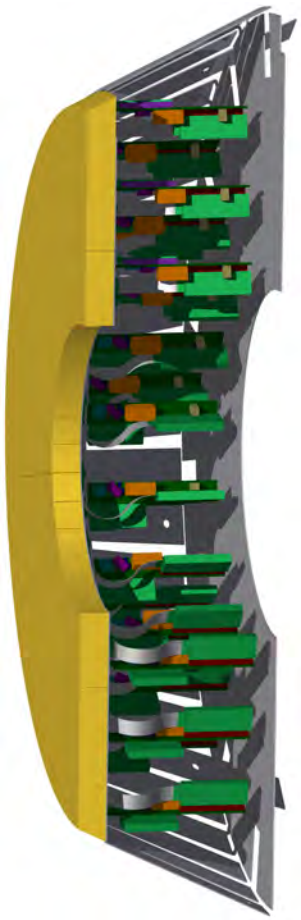

Figure 2.11: CAD drawing of one half of the SciRi detector. The plastic scintillator material is shown in yellow, additionally, the aluminium holding and shielding structure containing the readout electronics can be seen. As shown in fig. 2.10a and fig. 2.10b, each half of the detector is fixed to the corresponding half of the BGO calorimeter.

by one scintillator is close to that of one BGO crystal, i.e. 5° in polar angle for each 'crown' and 11.25° in azimuthal angle.

2.5 Forward Spectrometer

The forward part of the BGO-OD experiment covers the polar angles below 8° in the vertical direction and below 12° in the horizontal plane. It consists of a spectrometer to measure momentum and trajectory of charged particles emitted at very forward angles in the laboratory frame and of a time of flight system for charged particle identification. The magnetic spectrometer is equipped with two scintillating fibre detectors upstream and eight drift chambers downstream of a large open dipole magnet.

2.5.1 MOMO

The first of the two scintillating fibre tracking detectors is located 127.4 cm behind the target origin. It consists of 6 trapezoidal modules with 112 fibres each. The modules are rotated by 60°, such that the full, hexagonal detector area is covered by three layers of scintillating fibres and ambiguities caused by multiple particle hits can be resolved as illustrated in fig. 2.12. The scintillating fibres are cylindrical with a diameter of 2.5 mm. The radius of the sensitive area covered by the hexagon is 44 cm, while a central hole of 5 cm corresponding to a polar angle of about 2° is left for the main photon beam to pass through.

2.5.2 SciFi2

The second scintillating fibre detector 'SciFi2' is located closely behind the MOMO detector, 177.975 cm behind the target centre. It consists of 288 horizontal and 352 vertical fibres as indicated in fig. 2.13. The cylindrical fibres have a diameter of 3 mm. Both the horizontal and vertical fibres are arranged in two layers such that each particle arriving with an angle of −10° to 10° traverses at least 2.1 mm through fibre material of one orientation for the full detector plane (c.f. [Bös16]). This is achieved by staggering the fibres such that the distance between adjacent fibres is 2 mm.

The active material covers an area which is 66.4 cm wide and 53.6 cm high, with a central, square hole of 4 cm to allow for the main photon beam to pass through.

2.5.3 Open Dipole Magnet

Between the two fibre tracking detectors MOMO and SciFi and the system of 8 drift chambers, the horizontally deflecting open dipole magnet is placed. The magnet has an opening of 84 cm in the vertical direction and a wide horizontal opening of 150 cm width, allowing for an acceptance of 8.2° in the vertical direction and 12.1° in the horizontal deflection plane, respectively.

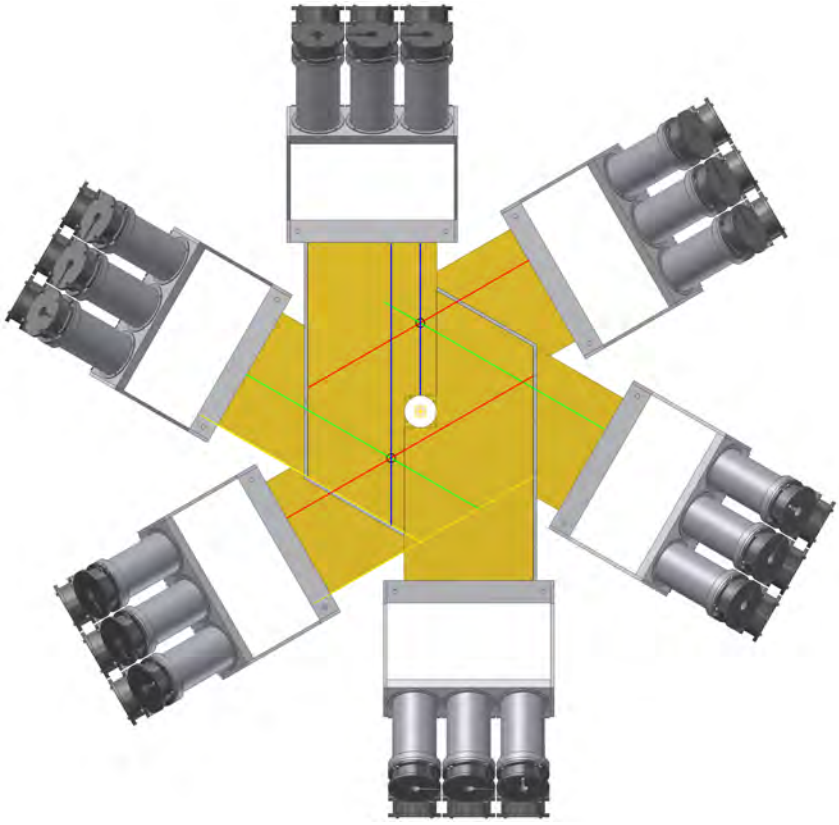

Figure 2.12: CAD drawing of the MOMO detector, without the holding structure. The housing of the photomultipliers of the 6 modules can be identified clearly. The coloured lines indicate how the different layers can be combined in the reconstruction to unambiguously identify particle impact points in case of multiple hits.

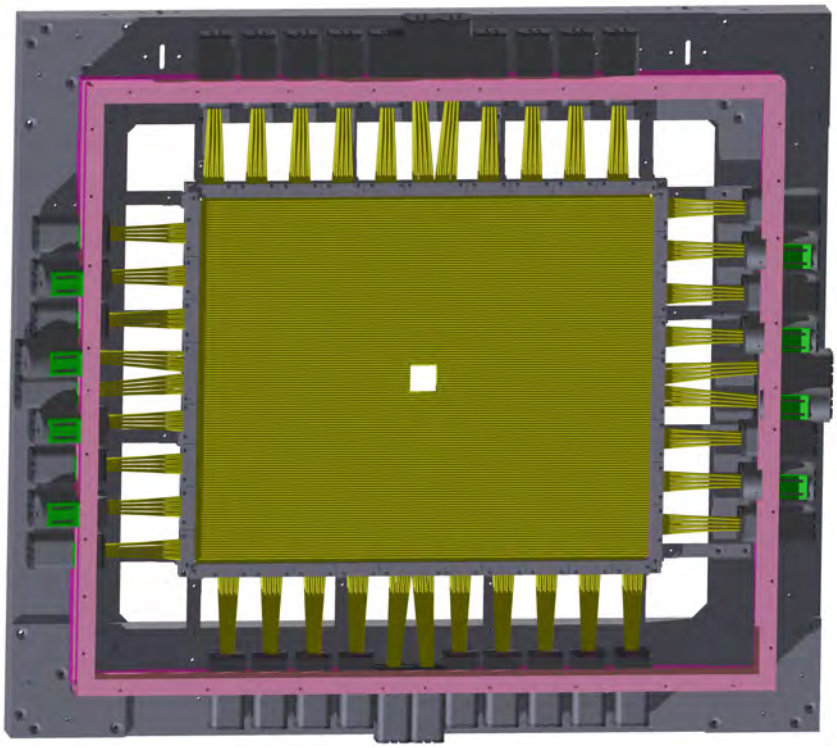

Figure 2.13: CAD rendering of the SciFi2 detector, view from upstream. The fibres and how they are connected to the photomultipliers can be seen. Additionally, the holding structure is depicted. In the setup, the detector is mounted directly to the open dipole magnet.

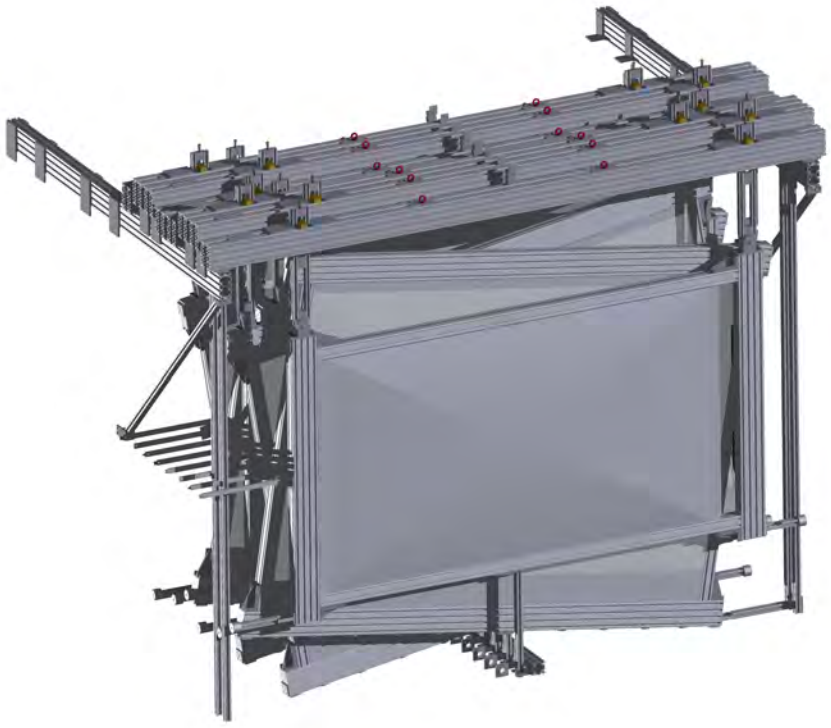

Figure 2.14: CAD drawing of the system of 8 drift chambers which are mounted behind the spectrometer magnet. The view is from downstream, i.e. the magnet is located behind the depicted chambers, as also indicated by the aluminium bars. The chambers are tilted against each other such that the full system consists of two chambers measuring in the horizontal plane, two chambers measuring in the vertical plane, and two chambers measuring in the 'U' and 'V' planes, respectively. The 'U' and 'V' planes are rotated by $\pm 9°$ to provide additional stereo information.

This magnet, which is on permanent loan from DESY[(2)], allows to reach fields larger than 0.5 T in the central region at full current. For experimental data-taking, a reduced 'half field' setting corresponding to 0.216 T in the central region is commonly used to increase the acceptance of the forward spectrometer for low momentum protons, which would otherwise be bent outside of the acceptance of the drift chambers and time of flight walls.

2.5.4 Drift Chambers

The tracking system behind the open dipole magnet consists of 8 drift chambers which are mounted with 4 different wire orientations as illustrated in fig. 2.14. Each of the chambers features two layers of drift cells as illustrated in fig. 2.15 thus allowing to resolve ambiguities. Combining the information from the different chambers, a full 3D reconstruction is possible.

The central part of the chambers which is exposed to the highest intensity is made insensitive

(2) **D**eutsches **E**lektronen-**Sy**nchrotron, a national research centre located in Hamburg, Germany

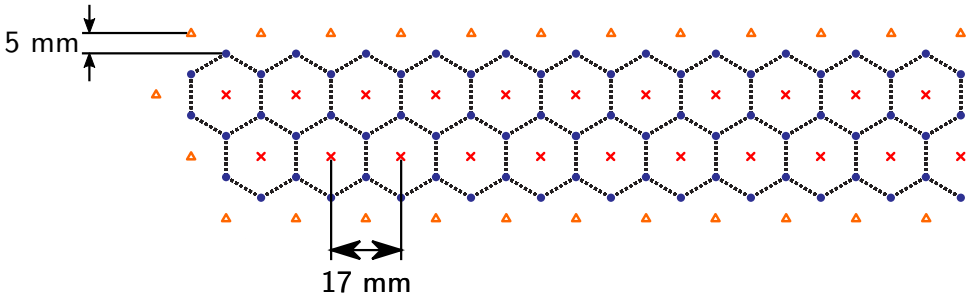

Figure 2.15: Arrangement of the signal (red crosses), field forming (orange triangles) and potential (blue circles) wires inside each of the drift chambers. The signal and field forming wires are both on ground potential, while the potential wires are connected to a negative high voltage. The resulting hexagonal drift cell geometry is indicated by dashed, blue lines (c.f. [Ham08]).

by adding a gold plating around the sensitive wires, thus reducing the electric field density.

The drift chambers are read out by custom electronics designed at the PNPI[3] which allows to record multi-hit time information from all 2176 sensitive wires with a time binning of 2.5 ns. Additionally, the thresholds can be adjusted for each group of 16 channels. The time resolution is sufficient to extract the drift time which can be used to improve the spatial resolution beyond the size of the drift cells. Further details about the readout electronics and the construction can be found in [Ham08].

2.5.5 Time of Flight Walls

The time of flight walls located at the end of the forward spectrometer complement the momentum information from the tracking detectors with the time of flight, allowing for particle identification. The time of flight setup and the readout electronics is one of the substantial parts of this thesis and will be presented in great detail in chapter 4. In preparation of this work, the measured variables and resolutions of all detector components are listed in the following section, and chapter 3 will thoroughly discuss the necessary procedures for the time calibration and alignment.

(3) **P**etersburg **N**uclear **P**hysics **I**nstitute

2.6 Overview of Detector Resolutions

Table 2.1 summarizes the main features of the previously described detectors. The implemented triggers will be discussed in more detail within the following chapter.

detector	detected particles	measured variables	resolution
Tagger	post-bremsstrahlung e^-	energy	1.7 % to 0.4 % $\cdot E_0$ [4]
		time	about 250 ps
ARGUS	post-bremsstrahlung e^-	energy	0.08 % to 0.45 % $\cdot E_0$ [4]
		time	better than 1.0 ns
Barrel	charged particles	time	better than 1.5 ns
		Δ energy	*to be determined*
		azimuthal angle	about 11.25°
BGO	photons	total energy	$\approx 0.722 \cdot \sqrt{E}$
		time	usually better than 1.7 ns
		azimuthal angle	better than 7°, E dep.
		polar angle	better than 5°, E dep.
	hadrons	dep. energy	$\approx 2.09 \cdot E^{0.16}$
		time	usually better than 1.7 ns
		azimuthal angle	about 11.25° [5]
		polar angle	about 6° to 10° [5]
SciRi	charged particles	time	better than 20 ns [6]
		azimuthal angle	about 11.25°
		polar angle	about 5°
Forward Spectrometer	charged particles	time of flight	better than 250 ps
		azimuthal angle	better than 1°
		polar angle	better than 1°
		momentum mag.	at best 7 % @ 1.5 GeV [7]

Table 2.1: Overview of the variables measured by the various detectors and the effective resolutions.

(4) E_0 is the energy of the initial, incoming electron beam.
(5) Granularity of the detector, since hadronic showers are often contained within one crystal.
(6) No time walk correction. With software correction, a resolution better than 5 ns is achieved (c.f. [Sch15]).
(7) It must be noted that this value was extracted from simulation, i.e. the magnetic field map used for the generation of the information and for the reconstruction was the same by definition. Due to known, but not characterized deficiencies in the description of the real magnetic field, it should be expected that the real momentum resolution is worse. On the other hand, the tracking algorithm is not yet optimized for momentum resolution: for example, the drift time information is not taken into account at all.

CHAPTER 3

Time Calibration and Alignment

In the course of this thesis, a strong focus has been put on the optimization of the time performances of the full BGO-OD setup. The first part of this work consists in the automation of the procedure to calibrate and align all the signals which can be logically combined to a complex trigger condition. In parallel to the automated procedure, a visualization tool to graphically present all the results to the user is developed, such that the calibration results can easily and quickly be assessed and eventually tuned one-by-one. The procedures and the graphical utility are described in sections 3.2 to 3.4.

As last step, the technique which proved to be fast and reliable has been extended to the offline time calibration of the almost 6000 channels of the BGO-OD setup as described in section 3.5.

3.1 General Concept

The general idea of time calibrations and alignments is the simplification of triggering and analysis tasks by aligning the time information of all detector channels such that correlated signals appear simultaneously.

The first part preceding any time calibration is the conversion of hardware information to physics quantities, for example, raw information recorded with the granularity of the TDCs[1] (commonly called 'TDC bins') to time information in seconds. The other part is a time offset correction on both hardware and software level, both on a global and an event-by-event basis. This translates to modifying hardware delays to let correlated signals arrive simultaneously at the trigger logic and relating all time information to a common time reference, termed the t_0.

(1) **T**ime to **D**igital **C**onverters

In the following, the general steps will be outlined. The next chapters will then describe all the details of the various procedures.

The first step in software is the conversion of the raw data to a physics information, which for time information means that a TDC bin is converted to a value in nanoseconds. This usually means that the read out raw data values have to be multiplied with a fixed calibration constant. Additionally, in the conversion process analogue electronics such as delay elements and capacitors are used which give rise to non-linearities due to inevitable manufacturing spread of the electrical properties of these elements. For these, an additional non-linearity correction should be performed, termed INL[(2)] in the following. The necessary techniques to determine and apply these calibrations are explained in section 3.3. After this technical conversion is done, all data have a common time unit and the next steps can be applied in a common way.

The second step is the time alignment of the detector signals which are to be used to build a trigger signal for the corresponding detector or sub-detector. The alignment procedure is necessary to let all signals related to one physics event enter the logic simultaneously, such that subsequently the logic condition and gates can be applied. For this, the delays for each detector signal entering into the trigger logic are adjusted. This is first done locally per detector-specific or sub-detector-specific trigger module.

Classically, the lengths of signal cables would be modified to align the signals in time. At the BGO-OD experiment, these delays are usually done inside the very same FPGA[(3)] modules which also contain the trigger logic and the TDCs. This does not only ensure that the TDCs and the logic are supplied with exactly the same signals, but also allows to implement scalers to count the hits on all single channels and also the trigger logic outputs. A prominent example in the setup is the tagger hodoscope for which both the single channels and the logic coincidences feature their own scaler channels. A short overview of the various detectors and local triggers will be given in section 3.1.1, while the technique to align these signals in hardware will be described in more detail in section 3.4.1.

The third step comprises the alignment of all these local trigger channels as they enter into a global trigger module. The global trigger is a flexible hardware trigger system which allows to define dynamic trigger conditions, relying again on all physically correlated signals to arrive simultaneously. More details on the flexible trigger definition possible with this module and the way the hardware time alignment is done will be given in section 3.1.2 and section 3.4.2, respectively.

Finally, the already mentioned t_0 calibration is performed. For this calibration, distributions of time differences between all single detector channels against the trigger time used as the common start are plotted. Then, time offsets for all channels of all detectors are determined and later applied in software to pull the 'prompt distributions'[(4)] to one common absolute time. To

(2) **I**ntegral **N**on-**L**inearity
(3) **F**ield **P**rogrammable **G**ate **A**rray
(4) 'Prompt' relates to the enrichment of signals observed at one distinguished time in a detector channel correlated to the hadronic event. This is at BGO-OD predominantly caused by the relativistic decay products of the hadronic reaction.

realize this t_0 calibration, several trigger reconstruction steps have to be performed in software to determine the correct common start time with maximum time resolution for each single event. These procedures are detailed in section 3.5.

Chronologically, the trigger time alignment is necessarily done at the beginning of each data-taking period. The t_0 calibration and tuning of the trigger reconstruction steps are performed once shortly after the start of every data-taking to simplify online data analysis and after each data-taking re-performed using the full available statistics. The non-linearity correction described in the first step may be performed even after data-taking since the granularity of the trigger logic and delay elements and thus the precision with which the time alignment can be performed is more coarse than any effect from a non-linearity correction.

3.1.1 Detector and Local Trigger Overview

All the procedures shortly outlined before need to be applied to the time information recorded within each detector channel of the experiment. In this section, a short overview of all these detector channels and the necessary procedures for trigger time alignment and time calibration is given.

As can be seen in table 3.1, in total 5987 readout channels recording time information are used throughout the BGO-OD experiment. The custom TDCs based on the jTDC require an integral non-linearity correction, while a t_0 offset calibration is required for all channels as already presented in section 3.1.

Apart from these modules which are predominantly used, the table lists the 'V1190' and 'V1290' TDCs which are commercially produced by CAEN and already contain a non-linearity correction as part of the firmware. Additionally, the 'Wiener AVM16' SADCs[(5)], which already perform feature extraction in hardware[(6)] and thus provide a time and energy information directly are in use. Their time information does not require special additional treatment, and the calibration of the energy information is not detailed here. Finally, the 'AD16' modules, which have been developed at the PNPI[(7)] within the collaboration, provide a readout system optimized for high channel density with a time resolution of 2.5 ns for the drift chamber wires. This TDC uses only clocked logic, so the size of the TDC bins is defined by the clock frequency and a dedicated non-linearity correction is not needed.

Furthermore, the table indicates the local triggers for all the listed detectors and whether a dedicated hardware time alignment of the single channels is necessary for definition of the local trigger logic.

(5) **S**ampling **A**nalogue to **D**igital **C**onverters
(6) The software feature extraction implemented for the CAEN V1742 SADC which uses similar techniques is described in appendix A.3.
(7) Petersburg National Physics Institute

detector	channels		readout	time calib.	trigger	trigger align.?
tagger	120		jTDC	INL, t_0	coincidence trigger logic on adjacent scintillators	✓
ARGUS	480	+ToT	jDisc	INL, t_0	OR trigger per board, OR of full detector	✓
Møller	4	+ToT	jDisc	INL, t_0	cross-coincidence trigger logic	✓
barrel	32	+ToT	jDisc	INL, t_0	OR trigger & cosmic triggers	✓
BGO	480	(SADC)	AVM16	t_0	triggers on sum at different thresholds, OR of crowns	(✓)
SciRi	96	+ToT	jDisc	INL, t_0	OR trigger & cosmic triggers	✓
MOMO	672		V1190	t_0	no trigger	
SciFi2	640		jTDC	t_0	ORs for horiz. and vert. fibres	
Drift Ch.	2176		AD16	t_0	no trigger	
ToF walls	72	+ToT	jDisc	INL, t_0	mean timing, OR of meantimes	✓
FluMo	5	+ToT	jDisc	INL, t_0	single channel	
GIM	1	+ToT	jDisc	INL, t_0	single channel	
MRPC	512	+ToT	V1290	t_0	AND of hardware-ORs (simple meantime trigger)	✓
MWPC wires	416		jTDC	INL, t_0	no trigger yet	
MWPC strips	272	(SADC)	AVM16	t_0	no trigger yet	

Table 3.1: List of the detectors, necessary time calibrations and triggers at the BGO-OD experiment. As can be seen, 5978 total readout channels need to be taken into account. A detailed explanation of the readout modules is provided in the text. The two per-detector calibrations are the INL (which needs to be performed for any of the custom TDCs) and finally the t_0 calibration. The last column indicates whether a time alignment of the single channel signals for definition of the local trigger logic is required. The BGO is marked in brackets, since the OR trigger which allows to set individual thresholds per crown needs a dedicated alignment, while all triggers on the full analogue sum are constructed by fixed hardware delays. This is also true for the SciFi2 trigger.

3.1.2 The Global Trigger

The Global Trigger module has been developed in-house by J. Bieling and is described further in [Bie11]. In this section, a short overview of the provided functionality and the application will be presented.

The global trigger module accepts all digital local trigger outputs. It implements a very flexible mechanism to allow for almost arbitrary selection of coincidences, logical ORs and vetoes. This is facilitated by an input stage which allows to set individual gates and delays for each single logic trigger input, followed by a sequence of two logic stages: a *primary logic* stage and a *secondary logic* one. The *primary logic* allows to select up to 32 logic trigger inputs and to combine them either with an AND condition or an OR. Furthermore, single channels can be inverted to function as a veto. The global trigger firmware features 16 of these primary logic elements also called *primary logic blocks*, whose outputs then enter into the second stage, the 6 secondary logic blocks. These allow, in turn, to combine the primary logic results via an AND or an OR. Again, usage of a condition as a veto is possible. Furthermore, a prescaling factor can be set.

Finally, the outputs from all secondary logic blocks define the overall trigger condition: each of them will activate the global trigger output, since they are put in an OR condition. For each of these secondary logic conditions, a separate scaler and TDC channel exists to allow for later studies of the trigger reconstruction and efficiencies. Additionally, the bitmask of the secondary logic triggers which were involved in causing this event are stored in an FPGA register and read out by the DAQ so it becomes accessible for trigger studies and event selection.

To give a better overview of the possibilities and the actual use, in following, the most important trigger conditions used during physics data-taking are described. All conditions contain the tagger detector which is required for all analysis to tag the energy of the bremsstrahlung photon and furthermore provides the time reference.

The numbers given in the following example and used for fig. 3.1 are from a regular data-taking in the October / November 2015 beam time, using a beam current of approximately 1200 pA at an electron beam energy of 3.2 GeV. The upper three tagger channels corresponding to the highest intensities have been turned off.

1. **tagger & BGO (high threshold)** The most open trigger condition only requiring the BGO and tagger local triggers achieves a trigger attempt rate of approximately 720 Hz. This condition uses the local trigger with the high threshold on the energy sum of the BGO calorimeter of approximately 135 MeV just below the π^0 mass, yielding a local trigger rate of about 1680 Hz.

2. **tagger & SciRi & BGO (low threshold)** This trigger condition was chosen to enhance hadronic events with low energy deposition in the central detectors and charged particles, e.g. protons, in the intermediate angular region covered by the SciRi detector. The SciRi detector alone shows a trigger rate of approximately 14.5 kHz. Again, the combination with the tagger trigger and the BGO trigger with low threshold reduces the rate of the combined

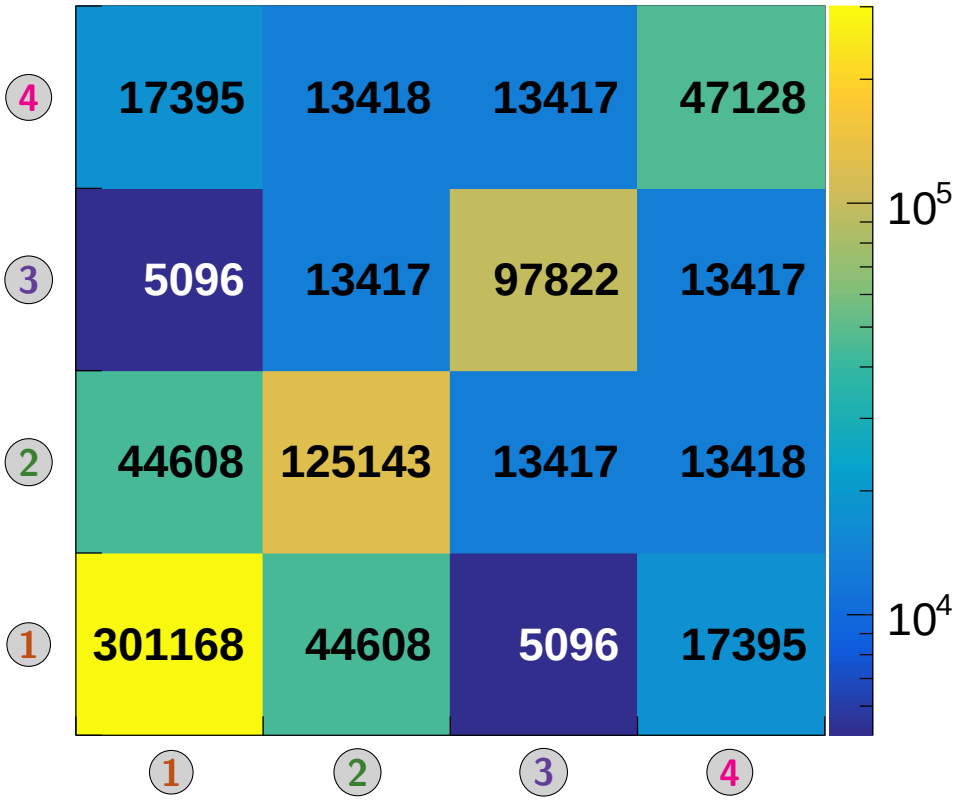

Figure 3.1: Visualization of the correlations of the trigger conditions used during physics data-taking. The conditions depicted here are

1. tagger & BGO (high threshold)
2. tagger & SciRi & BGO (low threshold)
3. tagger & SciRi & SciFi2 & ToF
4. tagger & SciFi2 & ToF & BGO (low threshold)

The several conditions are described in more detail in section 3.1.2.
For each triggered data event, the Global Trigger module records which of the four trigger conditions was fulfilled. The histogram is filled for each event for every fulfilled trigger condition versus all other fulfilled trigger conditions.
Considering the example of the trigger conditions 1 and 2 causing one single event, the histogram would be filled four times in total, once in each of the four bins in the lower left corner.
This means the diagonal entries correspond to the number of events in which the corresponding trigger condition was part of the global trigger decision, while all off-diagonal elements show the correlation between the different trigger conditions. For this reason, this visualization allows both to extract information about the contribution of each trigger condition and also their correlation. Data are from a single run (31341) recorded in the October / November 2015 data-taking period.

trigger to about 360 Hz which is feasible for the data acquisition without imposing a high dead time.

3 **tagger & SciRi & SciFi2 & ToF** This is the only standard data-taking trigger condition not requiring the BGO, thus also enhancing the contribution of hadronic reactions for which little to no energy is deposited in the central calorimeter. Even though the trigger rates of the local triggers combined in this condition are all in the order of several kilohertz on their own, especially the requirement on correlated hits in the different angular regions covered by SciRi and the forward detectors reduces the overall trigger attempt rate for this condition to approximately 240 Hz.

4 **tagger & SciFi2 & ToF & BGO (low threshold)** This trigger condition enhances hadronic events with low energy deposition in the central detectors and extremely forward going protons reaching the **T**ime **o**f **F**light (from now on, ToF) walls. The rate of the tagger trigger is found to be larger than 25 MHz and the rate of the mean timer trigger[(8)] for example from the ToF1 wall which features the scintillator bars closest to the beam is typically about 100 kHz for regular data-taking conditions. A similar rate of approximately 200 kHz is seen for the SciFi2 triggers. A combined trigger even for accidental coincidences from these detectors alone exceeds the maximum DAQ rate, thus imposing a huge DAQ dead time (c.f. [Ham16]). In combination with the BGO low threshold trigger which requires approximately 120 MeV of deposited energy in the BGO, the combinatorics trigger is reduced to a trigger rate of about 115 Hz.

scaler trigger With a fixed rate of 20 Hz, a scaler trigger is produced by the global trigger module. Scaler triggers are thus 'random' since they are not correlated to a physics trigger. The readout for events triggered like this is different: in addition to all TDC and ADC modules, the scaler information (c.f. appendix A.2 for a technical description) is read out. Apart from this scaler information, these events are excluded from all physics analysis, but can be used for random trigger studies.

spill trigger Additionally, when the 'spill start' or 'spill stop' provided by the control system of the accelerator ELSA is received, the same readout of all scaler information and all other modules is triggered by the global trigger module.

The mentioned rates are for the individual discussed trigger conditions, the global trigger puts all these conditions in a global OR, such that they are active 'simultaneously'. For this reason, the total rate of this *physics trigger* condition is not the sum of the several rates, but much less: indeed the total trigger attempt rate is about 1215 Hz, while the accepted trigger rate is about 1002 Hz. The difference can be explained in part with not accepted triggers due to DAQ dead time. The major part of the reduction in rate, however, is given by the combinatoric overlap

(8) A general explanation of the mean-timing is provided in the discussion of the ToF detectors in chapter 4, while a technical description of the mean timer trigger system itself is attached in appendix A.2.

between the conditions. Their interplay is visualized in fig. 3.1 which indicates the correlations between the trigger conditions in the off-diagonal bins.

Additionally, several calibration triggers are regularly used during data-taking. These rely on single local triggers which the global trigger module then accepts as global trigger signal:

GIM trigger For the calibration of the FluMo detector system, the trigger on the GIM detector is used at low beam intensities. Furthermore, the global trigger module then applies a prescaling on this local trigger. The prescaling only accepts a defined fraction of the trigger events to reduce the dead time of the DAQ. This is necessary since the scaler information is required, and the scalers are gated to count the signals during live time only. For this reason, the prescaling of the trigger signal increases the counting time of the scalers, thus actually increasing the effective measurement time for the FluMo calibration runs.

fixed live time trigger If the next trigger is generated with a defined interval after the DAQ dead time for one event is over, the live time of the DAQ between each event is fixed to this time interval. Choosing a minimum setting for the live time, the data-taking rate can be maximized if the event timing is completely irrelevant. This special trigger is used for example to record the BGO calibration data.

FluMo trigger The FluMo detector is built to detect events related to the photon beam and not to hadronic reactions. As will be presented in section 4.11 in the discussion of the corresponding readout electronics, it furthermore provides a good time resolution and sufficiently energy-independent time walk. For this reason, this detector is used as time reference for the time alignment of the tagger channels and also the tagger local triggers as will be discussed in more detail in section 3.4.

For the time alignment of the various local triggers, the global trigger and also the t_0 time alignment of the 5987 readout channels for every hardware modification and data-taking period, a convenient utility taking care of performing the fits and calculating the necessary delays or offsets has been developed. It will be presented in the following section.

3.2 Calibration Fitter Utility

In the course of this thesis, a flexible software tool has been developed which allows to perform the various calibration and alignment procedures mostly automatically. The tool accepts time or energy distributions for all single channels of each detector and then performs fits using predefined distributions and background descriptions. The start parameters for fits and background estimates are guessed automatically. The quality of the result of the minimization procedure is assessed and displayed visually. Finally, the user can access all results and still modify the fits, change the start parameters or even fix values.

This tool is used both for the trigger time alignment procedures and for most calibration procedures, including also the BGO energy calibration. The graphical user interface and the calibration file output differs according to the use case.

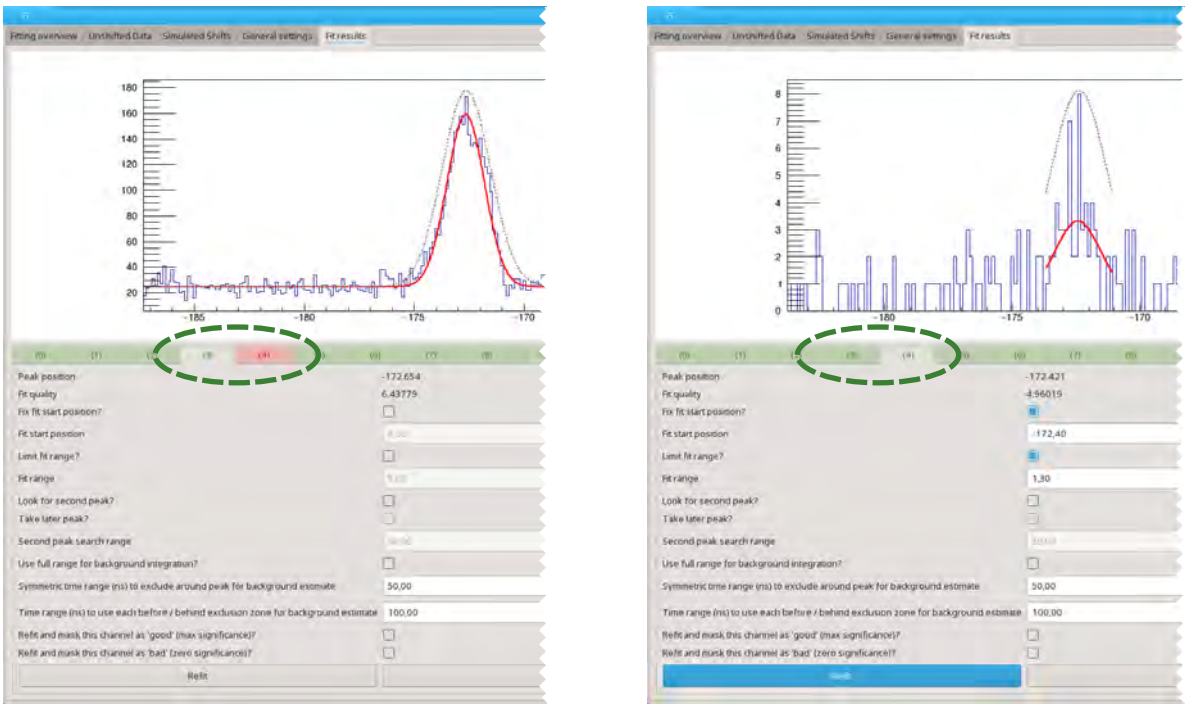

(a) Data from channel 3 of the tagger detector. The Gaussian fit was performed completely automatically.

(b) Data from channel 4 of the tagger detector. The Gaussian fit was possible after tuning the fit parameters.

Figure 3.2: Screenshots of the trigger-timing utility with data for alignment of the single channels for one of the tagger local triggers. The plots display the time distribution of the time differences between all hits recorded in a single detector channel and all hits measured using the FluMo reference channel. Details on this choice and the alignment procedure will be presented in section 3.4.1. The tool visualizes the start values by the dashed, grey line, while the fit result is shown in red. The bar of tabs below the plot, highlighted with the green circle, allows to select the channel which is investigated. The colour coding indicates whether the fit worked well or likely failed. As shown in fig. 3.2a, the automatic fit procedure worked well for all channels apart from channel 4, which showed a reduced efficiency in this dataset. In fig. 3.2b, channel 4 is displayed after choosing different start parameters and reducing the fit range with the control elements below the plot. The minimization was now successful as indicated by the change in colour of the tab labelled '(4)'.

As an example, screenshots of the trigger-timing tool are shown in fig. 3.2. In this case, the application fits each channel with a simple Gaussian distribution after guessing start parameters for mean, sigma and amplitude offering several techniques for background subtraction. The background can be estimated either by integration of the full spectrum excluding the peak, or by sideband subtraction. Furthermore, the fit range can be limited.

Some of these settings are limited to known-good values per detector, such that for sufficient statistics, all fits work well without any user interaction. Defining such limits beforehand is especially helpful for detectors with very wide time distributions with non-Gaussian shapes underneath the correlated peak. In this case, fitting a Gaussian to determine the mean works best if a smaller fit range is enforced from the start.

As shown, the fit status is assessed with a colour coding and made available as a guideline to the user to highlight which results should be checked most carefully. The fit quality used for this assessment is not only derived from the result of the minimization procedure, but additionally includes checks of the results against various dynamic limits. This includes, for example, a check of the fitted amplitude versus the initial guess. If this is exceeded by a large factor, the fit is marked as 'bad' to guide the user to check the result most carefully. In the provided example, the fits for all channels apart from a single one (channel 4) worked fine without any user interaction.

This problematic channel is shown in fig. 3.2b. As can be seen, a strongly reduced efficiency for this channel was observed which caused the initial Gaussian fit to fail. After manually tuning the fit range and start parameters using the provided features of the user interface, the minimization worked and a result could be extracted as is indicated by the change of the colour of the channel number.

After the user has checked all fits and applied corrections if necessary, the tool calculates the new delays to be used for the FPGA configuration and can also visualize the expected result after alignment by using the known size of the available delay steps. Furthermore, it is possible to specify the minimum delay setting to be used. This is necessary for the alignment of the local trigger signals inside the global trigger to allow for complex, dynamic trigger configurations. Applying a minimum delay for all channels allows to later apply a *negative* delay in the trigger condition setup. More details will be given in section 3.4.2. Additionally, the tool allows to keep the central value of all delays at the previous setting to minimize the overall timing change, which is crucial if delays which can only be adjusted by a manual hardware modification, e.g. by changing the cable lengths.

In the final step, the tool presents the calculated new delays and the previously used delays in a colour-coded way to the user for a final cross-check, also writing out a new file with the determined FPGA configuration alongside the previous one. To apply these settings, the user only has to explicitly overwrite the old configuration file with the new one. The DAQ of the experiment will then automatically pick up this configuration as soon as the next run is started.

This technique reduces the necessary knowledge about the details of all local triggers for the experimentalist, since it is applicable in almost the same way to all local triggers.

For the ToF detectors, the very same method is used even though they feature a very different

trigger based on the meantime of adjacent channels as described in appendix A.2. This does not change the time alignment procedure at all: for each detector, the delays of the single channels are chosen such that all 'prompt times' end up at the same value within the precision of the 5 ns binning. The 'prompt times' for the ToF detectors correspond to relativistic particles with $\beta \approx 1$ which can be distinguished as a prominent structure in the time distribution. This means that the two channels which belong to the same ToF bar will be aligned to be in time, and thus also their resulting meantimes will be aligned, since no further channel-dependent delays larger than 5 ns are introduced by the FPGA trigger logic.

The very same technique is used for the offline time calibration procedure. The graphical user interface has been modified for this purpose to additionally show the values of the old calibration constants and highlight the channels for which the newly determined calibration has changed significantly. Different kinds of distributions or even fitting techniques are implemented, including the integral non-linearity correction technique for the jTDC modules and also the energy-calibration of the BGO calorimeter.

Furthermore, this calibration-specific tool directly integrates with the calibration-database and produces an output file which can be applied either to a local copy of the experiment's calibration database or also be inserted into the official database for the collaboration. An example for the usage of this utility will be given in section 3.5.

3.3 TDC Calibration and Integral Non-Linearity

As a first step along the time calibration procedures, the TDC calibration factor and any non-linearity correction have to be applied to the raw data to convert all information to a common time base. This is schematically visualized in fig. 3.3.

These calibrations are independent of any absolute timing, but depend on the hardware module in use. This usually means that the read out raw data values have to be multiplied with a fixed calibration factor. This is the case for the 'CAEN V1190A' and 'CAEN V1290A' TDCs which are in use in the BGO-OD experiment[9]. Both these modules use a similar hardware internally, the only difference is in possible operation modes, which changes the maximum possible number of channels per module and also the achievable time resolution and thus the multiplicative calibration factor. In reconstruction, this known factor is applied and will not be further detailed here.

Indeed there is an additional component apart from this multiplicative factor: all such measurement devices are usually subject to non-linearities by design, for example by usage of analogue elements the digitization which are subject to a spread in their properties by the manufacturing process. These are for example the delay elements typically used inside a modern TDC, but also capacitors used in an ADC module.

In a commercial module, such non-linearities are usually documented and correction tables

(9) These hardware modules will be discussed in more detail in section 4.4.3, since they have also been in use for the ToF detector system.

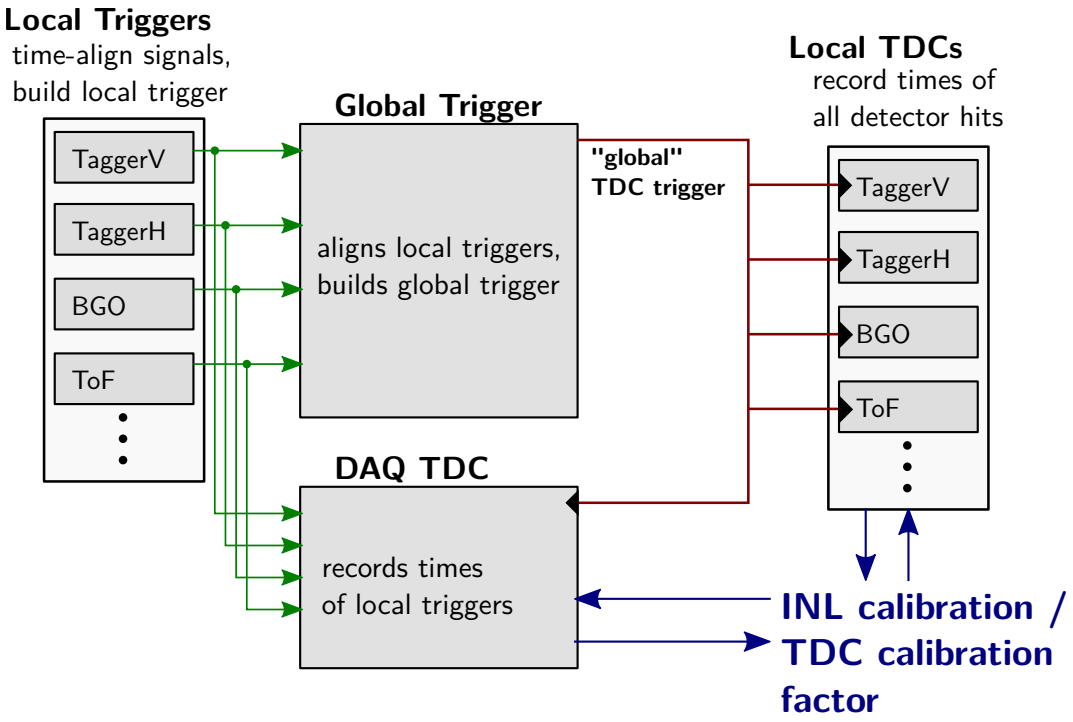

Figure 3.3: Schematic drawing of the effects of the integral non-linearity (INL) and TDC calibration constant (c.f. fig. 3.6). Only the time information itself is affected (conversion to a common unit), but no absolute offsets are introduced.

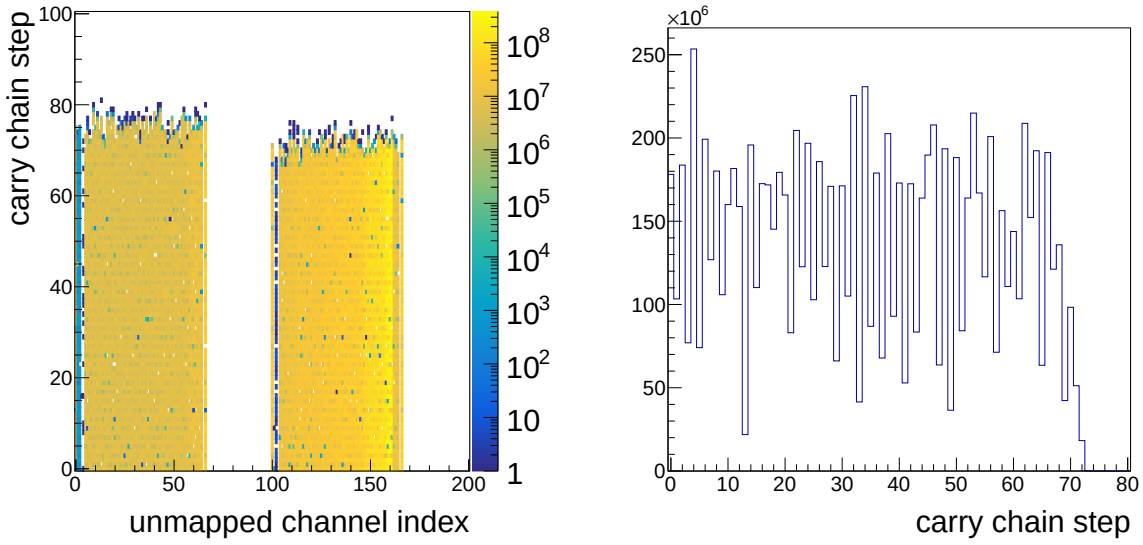

(a) (b)

Figure 3.4: Visualization of the raw information recorded by a jTDC, in this case the two jTDC modules of the tagger detector. Figure 3.4a displays, in colour-coding, how often a leading edge has been identified at a specific step of the carry chain of the FPGA for a given unmapped channel index. Figure 3.4b displays a projection of an arbitrarily chosen channel (150) and illustrates the strong variations in bin content for each of these steps. Assuming an uncorrelated 'white noise' distribution as input, the bin content can directly be related to the effective bin width. The data shown are from the October / November 2015 beamtime, spanning 3421 runs from run numbers 28395 to 32098 with 1 878 181 499 total events.

provided or the correction is even done in the hardware module itself. This is also the case for the mentioned CAEN TDCs. However, for the in-house developed jTDC, this calibration still needs to be determined. The technique is already hinted upon in appendix A.1, and is a standard statistical integral non-linearity correction which will be described in the following paragraphs.

As input, all data taken under the same condition can be used under the assumption that there is no correlation between the TDC clock and the recorded time information. This can indeed be assumed, since the 200 MHz clock of the jTDCs is uncorrelated to the independently produced physics signals (which are however, in turn, strongly correlated to the radio frequency of the accelerator ELSA which determines the distance between the electron bunches).

For this reason, the data should be statistically equally distributed per time unit (a 'white noise' distribution). Relying on this, the effective widths of the TDC bins can be determined directly from their relative content. The procedure can be best explained by looking at the example in fig. 3.4. The first plot is filled for each detected leading edge in a channel of the tagger detector.

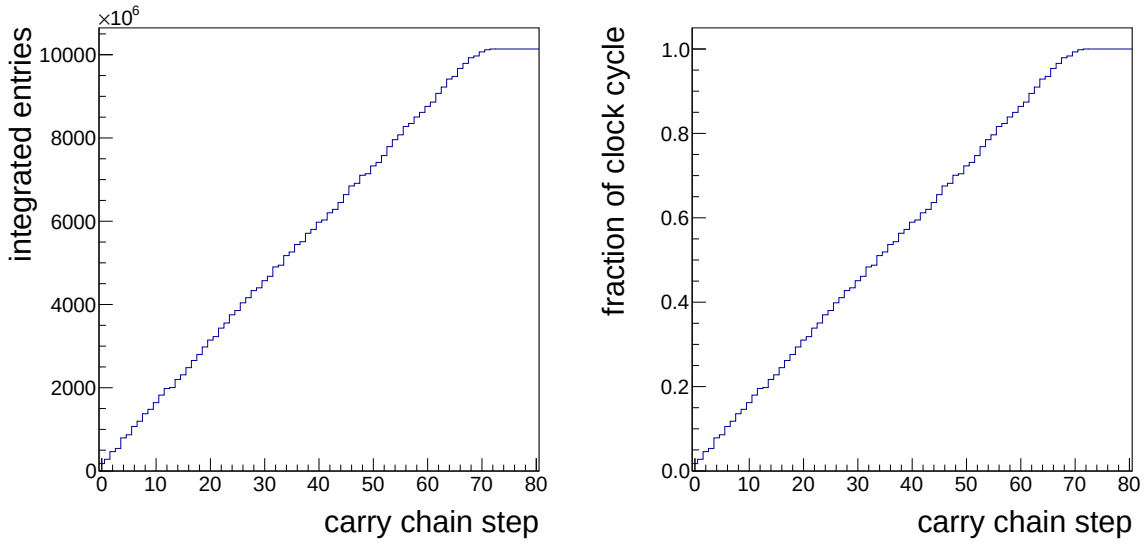

(a) (b)

Figure 3.5: Integration of the example plot shown in fig. 3.4. Figure 3.5a shows the direct result of the integration, while fig. 3.5b is re-scaled such that the percentage of clock cycle corresponding to each carry chain step can directly be read off. These values are stored in the calibration database and used for the INL calibration.

The horizontal axis in fig. 3.4a corresponds to the unmapped channel indices of both tagger FPGA boards. The position in the carry chain at which the leading edge of the signal was found is shown on the vertical axis (for further details, c.f. appendix A.1). In fig. 3.4b, a projection along this axis for a single channel (unmapped index 150) is shown. In the assumption that a flat random distribution is the input, the relative content of the bins corresponds directly to their effective widths. To normalize this, the data per channel is first integrated by accumulating all entries up to each carry chain step.

This procedure is illustrated in fig. 3.5. Figure 3.5a shows the accumulated sum up to each carry chain step, while fig. 3.5b is based on the same data, but has been normalized to the final result for the sum. In this way, it directly maps the percentage of the active carry chain length to a bin. The full length of the used part of the carry chain is known since it is sampled each half clock cycle, so the bins in which leading edges are detected correspond to a time range of 2.5 ns. Using this information, the percentage can be converted to a value in nanoseconds.

This statistical technique is in common use and can be applied for any non-linearity correction, provided the input data are normally distributed in terms of the measured quantity. Other examples may be a space to drift time relationship for drift chambers[10] or the non-linearity of ADCs.

(10) In this case, there are usually additional dependencies on angle and particle type or velocity.

Of course, there are some corner cases. First of all, as usual for any calibration, a 'good' dataset has to be selected. For this kind of calibration, it has to be made sure that no datasets are included which either violate the basic requirement of being uncorrelated or in which there was a setup issue. A setup issue can happen due to misconfiguration in a test-run, or real bit flips in the FPGA configuration or memory caused by incident radiation. In such cases, bits in the carry chains can become 'stuck', i.e. 'on' continuously, or false triggers can be generated which may then indeed cause unwanted correlations. To reduce any such effect, the experiment features an online, automatic data integrity check detecting some of these issues and alerting the shift crew to reprogram the FPGA.

By design, all sampling carry chains have been allocated with a fixed number of steps making sure that this is longer than one clock cycle so no signals should go undetected. For the shown example, the actual length of the chain in which leading edges can be detected corresponds to 84 steps, while effectively, the last used bin is 79.

This in turn means that it is possible that a leading edge is detected twice: once at the start of the chain, and then again in the next clock cycle at the end. The firmware suppresses this effect by imposing a veto on the edge detection at the end of the chain in the clock cycle following a hit detected early in the chain. This vetoing logic will naturally fail if a hit is *only* detected at the end of the chain and not at the beginning. This issue is indeed found to occur rarely. It is thoroughly investigated along the discussion of the first results obtained with the read out electronics for the ToF system in section 4.6.1.

The software integration procedure has been adapted to take these effects into account: the last bin is capped by first calculating the full integral, dividing that by the full number of carry chain steps available (84) and choosing the latest bin which contains more than 15 % of this value as 'real' last step. Furthermore, in case the bin after that one still contains entries, it is chosen as the last step instead. The final integration and normalization used for the calibration is then re-performed up to this last step only.

This empirical method has proven as a stable technique to remove the contribution from the rare cases of short signals which are only detected as leading edge late in the carry chain from the calibration procedure. In addition, when decoding the data, any entry found after this determined, effective end of the carry chain is associated to the previous clock cycle since this is the cycle during which it should have been detected instead. For these few hits, the effective length of the carry chain is subtracted from their carry chain step number, i.e. the lookup is done as if they had been detected in a corresponding bin at the beginning of this chain. The calibration is of course not valid in this region, which results in a small loss of resolution for this small number of hits only.

After employing this calibration, all values from the TDCs will be in a common time base. The next steps are then a fine software time alignment of all channels and the reconstruction of the trigger time.

It must be noted that the non-linearity correction is usually performed with a high statistics dataset, which means that it must be done after the trigger timing procedures and subsequent collection of data. This is not an issue, since the trigger time alignment is more coarse than

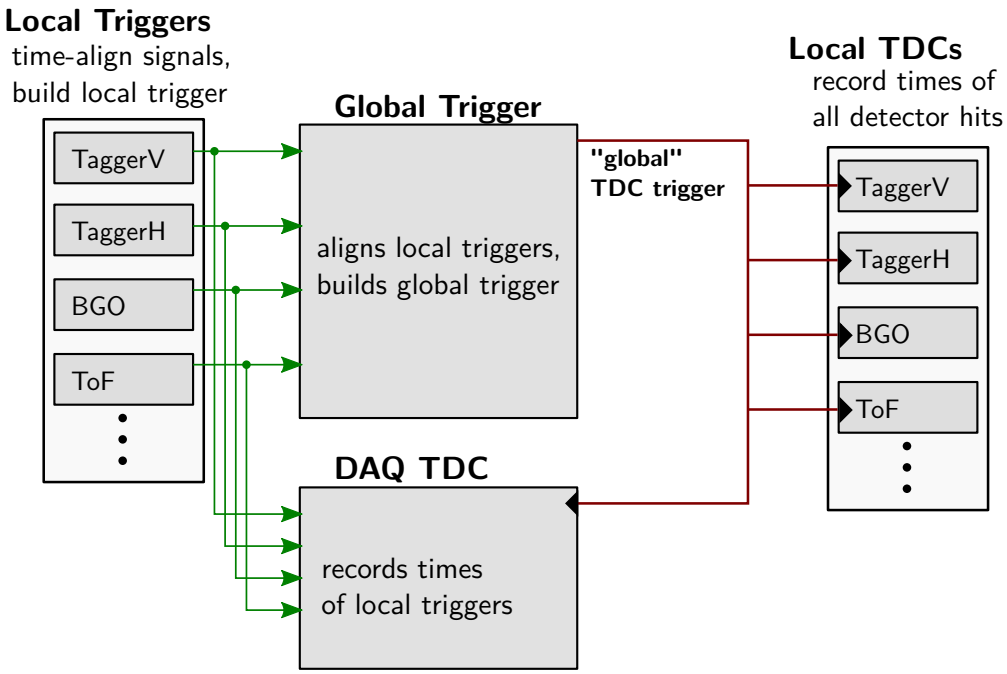

Figure 3.6: Schematic overview of the trigger system of the BGO-OD experiment: each detector subsystem is equipped with local TDCs and in most cases also with a local trigger system. The 'start' signal for all TDCs is produced by the global trigger and distributed via the DAQ synchronization system as described in [Ham16]. A separate TDC (labelled 'DAQ TDC' here) is used to reconstruct the trigger time offline with improved resolution.

the variation of the bin sizes by the non-linearity effects, which is why the usage of an older calibration or even just an averaged bin size is completely sufficient for the time alignment procedures.

3.4 Trigger Timing

The BGO-OD experiment uses a very flexible hardware trigger system implemented in FPGA technology (c.f. [Bie11]) as already outlined in section 3.1. It requires an alignment of all signals in time before the data-taking can be started.

The general scheme is shown schematically in fig. 3.6. A list of available local triggers and a short description of the global trigger module have already been given in section 3.1. In this section, the two necessary steps of time alignment procedures will be described: first, the alignment of all single detector channels entering a local trigger module in section 3.4.1, and secondly, the time alignment of the various local trigger signals themselves as they enter the global trigger module in section 3.4.2.

For all these trigger timing procedures, the choice of the trigger to record the necessary data is essential. In most cases, a clean hadronic trigger is the most useful choice, since signals

correlated with one another must be seen in all involved channels to allow for the delay tuning. Additionally, this trigger should not involve combinatorics of different local triggers which might not be aligned in time yet.

The most obvious candidate for this trigger is the BGO energy sum trigger. It is fully built in analogue hardware elements with fixed cable lengths, so this trigger does not need any additional time alignment (c.f. section 2.3.2). Furthermore, the chosen energy sum threshold is usually set above 100 MeV which means that a hadronic reaction is required to take place in the central part of the experiment. Another choice would be the scintillator barrel detector, which is however not as suitable since it is located closer to the beam and more susceptible to halo particles. Additionally, the logic is made with an FPGA which needs a time alignment by itself.

Detectors of the forward part of the experiment are not a good choice, since they are all, at least in parts, located close to the beam and thus may also see electron positron pairs produced along the experimental setup. The tagging detector would not select hadronic events, and additionally features a complicated trigger logic by itself (c.f. section 3.4.1).

For this reason, the BGO energy sum is used in the time alignment procedure for both the local triggers and also the global trigger module.

There is one major exception related to the tagging detector. The tagger is made for tagging the photons produced at the bremsstrahl radiator and would not profit from the selection of hadronic events at all. Furthermore, a high time resolution of the reference signal for the time alignment is required already on the hardware level. Two detectors could fulfil this role: the gamma intensity monitor 'GIM' and the FluMo detectors at the very end of the beamline. The GIM detector is a lead glass device using Cherenkov radiation as detection mechanism as described in section 2.1.5. This leads to a wide distribution of signal amplitudes and thus time walk effects reducing the time resolution. Furthermore, this detector is not designed for use at high rates and will exhibit large dead time effects.

The FluMo detectors, however, are made from thin plastic scintillator material featuring a time resolution sufficient to identify the bunch structure of the accelerator, as will be presented in section 4.11 alongside the discussion of the readout electronics. For this reason, they are the ideal choice for the trigger time alignment of the tagger local trigger. One channel of the FluMo setup will be used as reference. Additionally, this FluMo detector is also used to align the two separate tagger local triggers for the global trigger time alignment, as will be explained in section 3.4.2.

3.4.1 Local Trigger Timing

The 'local trigger timing' corresponds to the time alignment of all single detector channels which take part in a local trigger, such that the electronics signals produced by a physics particle arrive simultaneously at the corresponding local trigger logic.

For this reason, for the calibration of all local triggers, any 'hardware configuration' which may affect the timings of the signals such as tuning of high voltages and thresholds should be optimized first. As outlined previously in section 3.4, a trigger on the hardware energy

sum of the BGO calorimeter is commonly used in the alignment procedure. All measured time distributions should then contain a trigger-correlated peak which in the following be called the 'prompt' peak.

The dataset taken in this condition is analysed without applying any corrections on the 'absolute' time, i.e. just using the TDC raw values, applying the correction for the integral non-linearity, and converting them to nanoseconds. More details on these calibrations and corrections will be given in section 3.5. The analysis of the raw data produces histograms with these raw time distributions for all channels involved in any local trigger.

All FPGA-based triggers feature input delays. Depending on the implementation, two different delay steps (or combinations of them) are available:

- 5 ns for clocked delays (signals delayed via a shift register), in the following termed 'coarse shifts'. These delays are always in units of '1 clock cycle'.
- $^5/_6$ ns using delays applied to the 6-bit-pattern from the common pattern detection implemented in some of the trigger modules, in the following termed 'fine shifts'. These delays are 'finer' than one clock cycle, since they are applied after the carry chain sampling has been performed inside the FPGA (c.f. appendix A.1).

These delays are configured dynamically: a delay-setting is written into a firmware-specific register, and the delay becomes active immediately.

The trigger timing procedure for any local trigger is always performed keeping the last used delay setting active, since the necessary changes are usually minimal. The general procedure per local trigger is as follows:

1. Read in the active delay settings and convert them to nanoseconds.
2. Create histograms filled with this time information, for each channel.
3. Fit all time spectra for each single channel with a simple Gaussian.
4. Take the mean of the fit (in nanoseconds).
5. Find the minimal necessary delay value to move the 'prompt' peak positions to a common 'absolute' time within the recorded time window using the available precision for the delays.
6. Store the new delays settings to be written via VME into FPGA registers.

The procedure is fully automated with the utility described in section 3.2, allowing the user to still check all calculated delays and fitted distributions before they are finally applied. These calculated delay settings themselves are stored by the utility in appropriated DAQ configuration files which are automatically used to configure the FPGAs when a new run is started.

As an example for such an alignment procedure for a local trigger, the tagger is used in the following. The tagger detectors is the online time reference for the experiment and necessary for

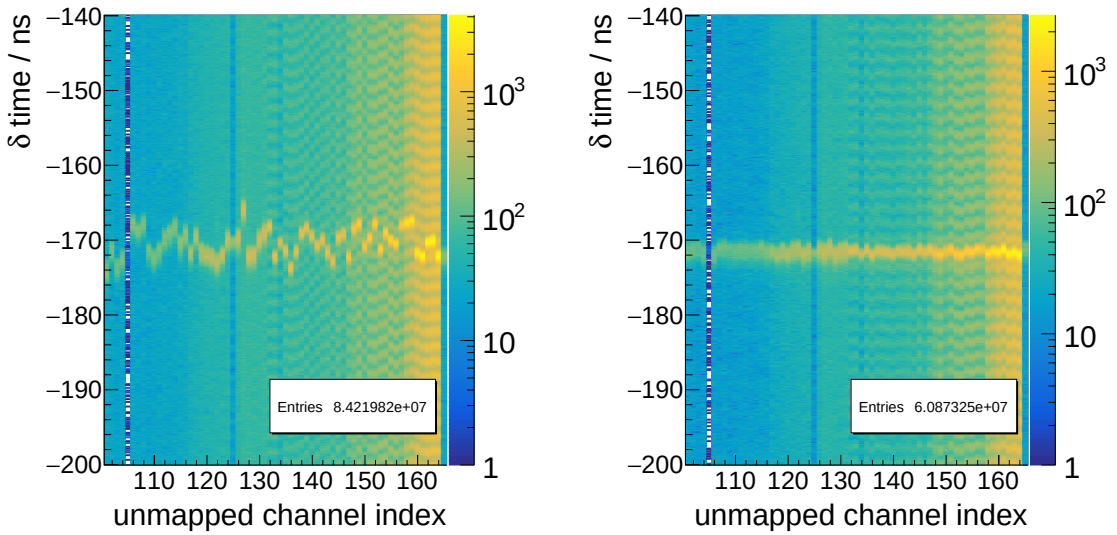

(a) Time distributions before alignment.

(b) Time distributions after alignment.

Figure 3.7: Example of the input data used in the alignment procedure of the local trigger for the vertical part of the tagger detector extracted from BGO-OD runs 26035 and 26036 recorded during the July 2015 beamtime. Figure 3.7a shows the time-difference distributions (tagger channel minus FluMo reference channel) before, fig. 3.7b shows the situation after time alignment. The additional 'fine shift' delays used only in the trigger logic are already applied to the time distributions. The indices are unmapped, i.e. they correspond directly to the order in which the hodoscope channels are connected to the board with an arbitrary offset of 100. This also matches the geometric order, i.e. adjacent channel numbers have geometric overlap. One channel (105) with strongly reduced efficiency can be seen. It required dedicated tuning of the fit parameters, but could still be included in the alignment procedure. The very last channel corresponds to the highest channel index of the horizontal tagger and needs to be included in the alignment for the coincidence pair between the TaggerV and TaggerH boards.

the characterization of the initial state. For this reason, it is part of all trigger conditions used in regular data-taking. Additionally, it is also the best resolved local trigger in the BGO-OD experiment.

The tagger detector is equipped with FPGA logic to form coincidences of adjacent channels. As shown in section 2.1.3, the geometric design of the detector enforces a hit in adjacent channels for each real physics particle. For the time alignment of these coincidences in the trigger logic, the tagger trigger features the higher-resolving $^5/_6$ ns delay steps.

An additional complication has to be taken into account in the alignment procedure. Technically, the tagger local trigger is split in two parts since two FPGA boards are necessary to handle the 120 total channels with the added complicated logic. These parts are called 'TaggerH' and 'TaggerV' since they roughly match the horizontal and vertical part of the tagger hodoscope, respectively (c.f. section 2.1.3). The 'TaggerV' trigger always dominates the statistics, since it corresponds to the higher intensity part of the bremsstrahl spectrum.

The plots displayed in fig. 3.7 show the distribution of all time differences between the TDC hits in each tagger channel and the hits in FluMo, which are all measured by the very same TDC. As can be seen, the prompt peaks of the single channels are initially not well aligned. Any absolute offset on the reference signal is not of interest for the alignment procedure — it is arbitrary since it involves cable length and delays introduced by discriminators for the FluMo signal.

However, it must be noted that these time differences have already been modified by the applied 'fine shifts': since the 'fine shifts' are only used for the trigger logic to apply a numeric 'offset' for the coincidence check and are not applied to the TDC data, they would not show up in the time spectra. Still, they must be taken into account in the alignment procedure. For this reason, the 'fine shift' values which were loaded into the FPGA are added back as offsets in software. The 'coarse shifts' are already part of the TDC data, so no special treatment is needed.

The alignment procedure itself can be performed without keeping all these technical details in mind, since the fitting tool described in section 3.2 takes care of calculating the possible delays for both coarse and fine shifts, if available for the local trigger in question, and generating the configuration files for the FPGA modules.

After this procedure is performed for all local triggers of all detectors, the time alignment of the local trigger signals themselves as they enter the global trigger can be performed. This is necessary since all local triggers can be combined for the overall trigger condition as already shown in section 3.1.2.

3.4.2 Global Trigger Timing

The 'global trigger timing' corresponds to the time alignment of all local trigger signals which may take part in a global trigger decision, such that the electronics signals produced by one physics particle or a hadronic reaction arrive simultaneously at the global trigger logic.

The time alignment procedure itself is very similar to that outlined for the local triggers. The global trigger features the 'fine shift' delay binning of $^5/_6$ ns.

However, the technical details of the alignment are quite different. For the global trigger, a calibration TDC explicitly developed for this alignment is part of the firmware. It is not used for physics reconstruction. It's binning matches exactly the resolution of $^5/_6$ ns and it includes the applied 'fine shifts' in the data stream, so they do not need to be added back in software as was done in the example of the tagger local trigger (c.f. section 3.4.1). This TDC is also read out during data-taking for monitoring purposes, albeit not for every event to reduce the data rate.

As mentioned in section 3.1, the BGO energy sum trigger which selects mostly hadronic reactions is also used to collect the data for the global trigger time alignment procedure. As time reference for the alignment, the 'TaggerV' local trigger is used. This choice is made since the tagger local triggers feature the highest resolution and in any case also take part in all production triggers during later data-taking. The 'TaggerV' local trigger is selected since the vertical part of the tagger detector is exposed to higher intensity, so higher statistics is expected.

Similar to the alignment procedure for the local triggers, 'time reference' means all time differences between all hits in a channel and all hits in the 'TaggerV' local trigger as measured by the global trigger module's calibration TDC are calculated and filled. This reveals a strong prompt peak from physics correlations, and a combinatoric, triangular shaped background from random correlations.

For the 'TaggerH' local trigger, this technique fails: there are no real correlations expected between the two parts of the tagger detector, however, the two tagger local triggers may not be in time with one another as measured by the global trigger. For this alignment, an additional detector related to the photon beam is needed.

As a consequence, for the 'TaggerH' local trigger signal, the FluMo local trigger which is directly derived from a discriminated FluMo signal is used as reference. The time difference distributions of 'TaggerH-FluMo' and 'TaggerV-FluMo' are plotted and the offset is extracted for the alignment of 'TaggerV' to 'TaggerH'. This alignment calculation is performed within the analysis part and the determined offsets are applied to the produced time distributions. For the 'TaggerV', the histogram is even filled with dummy entries exactly at 0 ns. The advantage of this technique is that the experimentalist can again make use of the very same time alignment utility described in section 3.4.1 without keeping the details of these offsets in mind.

An example of the time distribution used for alignment is shown in fig. 3.8. Two cosmics triggers from the ToF walls are also included in this spectrum. Any cosmics triggers must be ignored in the alignment, since they are optimized for self-triggering operation of the detector with cosmic muons, i.e. in case of ToF for the muons passing through the walls from top to bottom. These triggers are never used in time correlation with other detectors of the experiment. Furthermore, since the expected rate is by far lower than that of operation in-beam, no dedicated time alignment procedure of the single channels entering the trigger logic is needed to provide a useful cosmics trigger: the gates for the logic trigger can be widened without issues, since a highly resolved time correlation is not required. Since the cosmics triggers usually still show correlations with other local triggers in regular data-taking conditions [11], they must be explicitly excluded from the alignment procedure to prevent the introduction of unnecessary trigger delays.

An example for the ToF1 local trigger is shown in fig. 3.9. The prompt peak is clearly visible. The dip before the prompt peak is caused by the two dead times of the involved trigger signals. The triangularly shaped distribution below the peak results from the convolution of two uncorrelated, random time distributions within the limited TDC time window. The time-difference calculation convolves these two flat, rectangular distributions, which leads to the observed triangular shape. The strong falloff at about −120 ns is the result of the prompt peak structure being convoluted with that rectangular distribution.

The long tail after the correlated peak which is caused by particles with β smaller than 1 can already be observed at this first level of analysis. It can be concluded that for the global trigger time alignment procedure, the calculated delays should not be fully minimized: the same delays

(11) This is also true for the ToF cosmic triggers, albeit the correlated structure is outside the displayed time range.

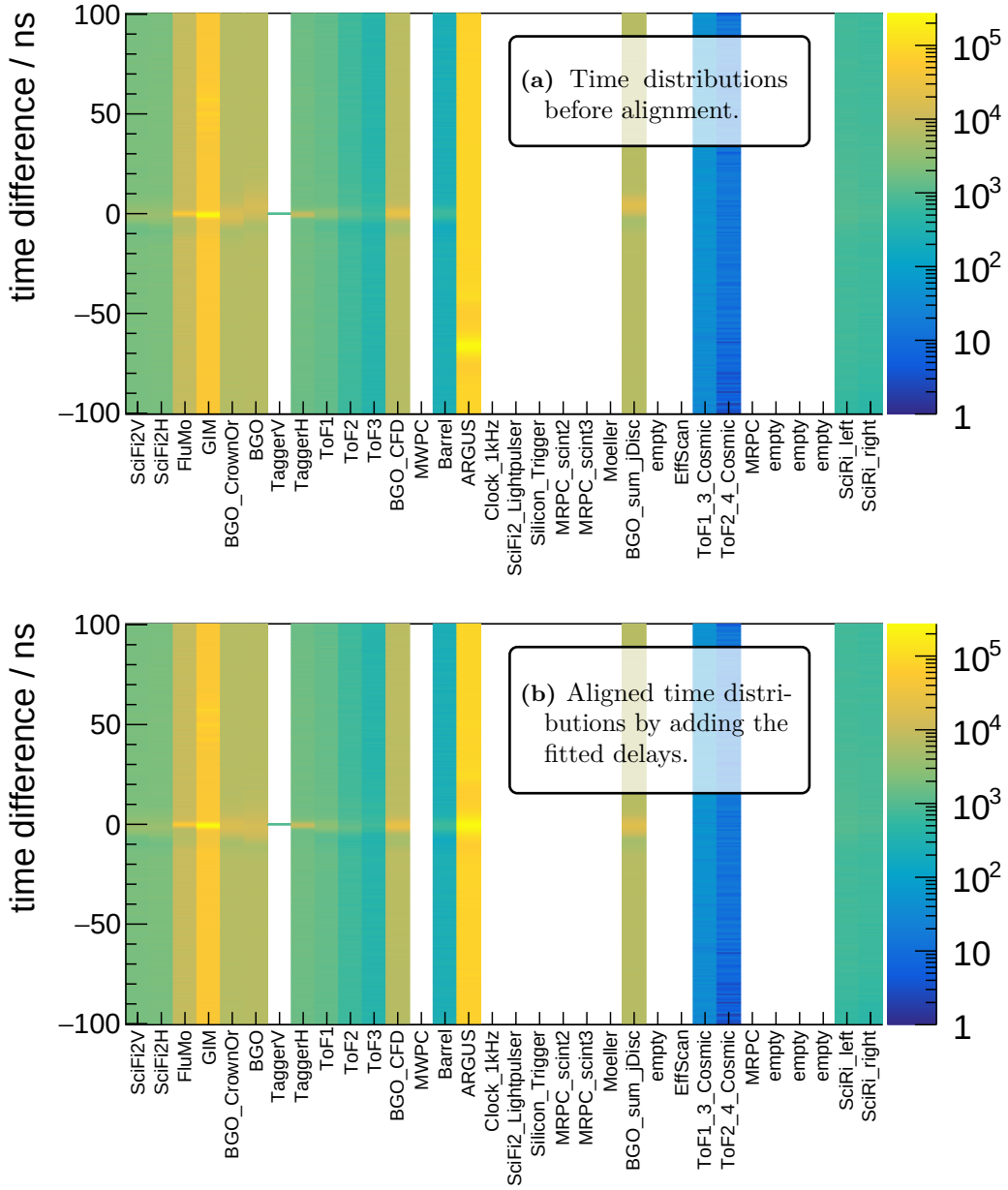

Figure 3.8: Visualization of the data used in the global trigger time alignment procedure, extracted from BGO-OD run 25163 recorded during the June/July 2015 beamtime. Figure 3.8a shows the time difference distributions between TaggerV and all other local triggers before alignment, while fig. 3.8b shows the same dataset after adding the newly fitted delays to the data. This 'simulated' result matches perfectly with data taken afterwards. In this example, mainly the ARGUS local trigger is affected since it was included in the alignment procedure for the first time in the June / July 2015 beamtime.

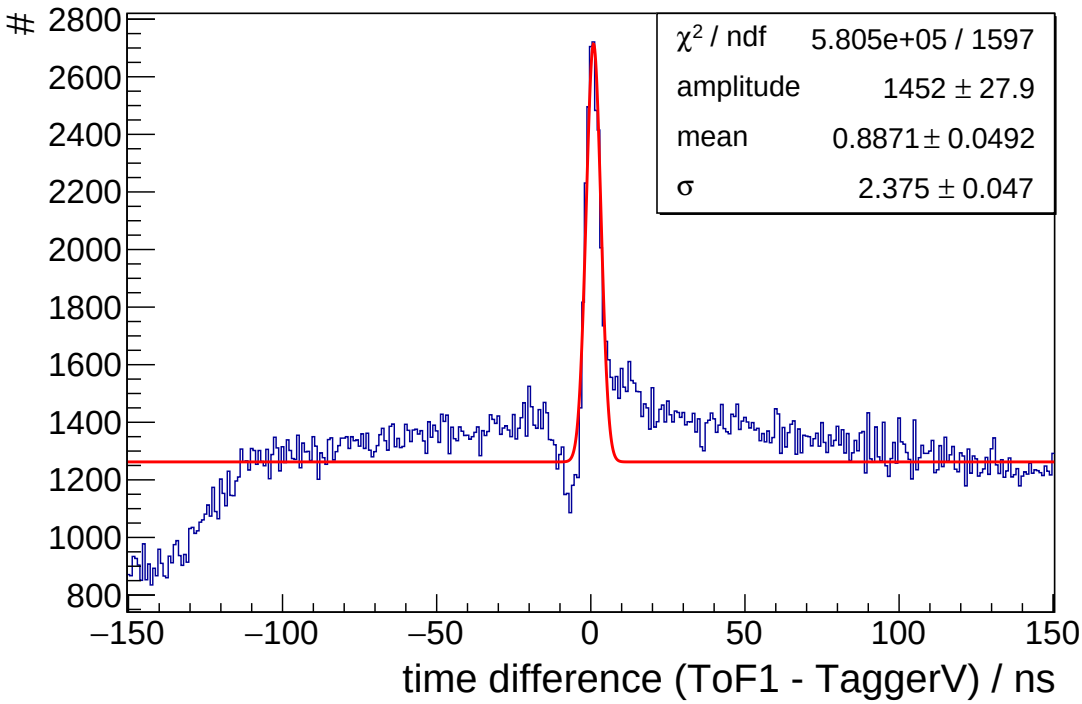

Figure 3.9: Example for the global trigger time alignment histogram, extracted from BGO-OD run 25163 recorded during the June / July 2015 beamtime. It shows the time distribution of the ToF1 local trigger as recorded by the Global Trigger Calibration TDC. The red line illustrates the finally accepted fit result. The distribution peaks at about 0 ns since this trigger remained aligned from the previous trigger timing procedure.

are again needed for the dynamic setup of the trigger logic. In case ToF is going to be used in the trigger, a reduced delay is necessary to allow for coincidences with the late (i.e., slow) particles.

The trigger logic configuration tool developed by J. Bieling indeed allows for negative 'logic' delays to accommodate exactly this functionality. To allow for these delays, a minimum delay needs to be enforced during the alignment procedure. Since the first two ToF walls are located about 560 cm behind the target centre, in the simplification of using straight tracks, the β and the minimum accepted momentum p can be estimated. Assuming protons and a maximum accepted time of flight of 40 ns:

$$\beta = \frac{v}{c} = \frac{\frac{560\,\mathrm{cm}}{40\,\mathrm{ns}}}{c} \approx 0.623$$

$$p = \sqrt{\frac{m_\mathrm{p}^2}{\left(\frac{1}{\beta}\right)^2 - 1}} \approx 495\,\mathrm{MeV}/{c_0}^2$$

This number matches approximately the minimum momentum of protons which reach the ToF walls and are still detected by them at half of the maximum magnetic field strength, which is also the configuration used for the data analyses in chapter 5 and chapter 6. This is why for any 'forward' trigger condition used during data-taking, a delay of 40 ns on the ToF local triggers with a gate of 50 ns was used. For this reason, the alignment procedure needs to 'reserve' a minimum delay of 40 ns for all channels, which can actually be enforced by the developed utility.

Apart from the reason of including a time of flight information in the trigger, the delays should usually be minimized as far as possible to reduce the time between the signal detection in the electronics module and the global trigger signal which causes the readout, since the time difference between these needs to be kept in buffers on the readout modules. Furthermore, especially for the global trigger, the functionality to keep the central value of all delays fixed is not only a convenience feature to minimize the necessary change to the t_0 calibration, but also crucial for the hardware setup: some modules (classic ADCs, but also SADCs with limited recording time windows) depend on the relative time offset between the signal recording and the arrival of the global trigger.

3.5 Offline Time Calibration

After data-taking, the times stored on disk are just the times measured by the individual TDCs relative to the global 'TDC start' which is the global trigger signal. This signal is distributed to all readout modules by the synchronization system which uses a common 40 MHz clock for synchronization (c.f. [Ham16]). The global trigger signal from the global trigger module is generated synchronously to a 200 MHz clock which is derived from that slower clock signal.

For this reason, the global trigger signal at each detector is not the sufficient time base for high resolution: by design, it jitters up to 5 ns as compared to the hits which originally caused

the trigger signal. These are for all physics data-takings originating from the start detector of the experiment, the photon tagger. This is ensured by all data-taking trigger conditions containing the tagger local triggers with the minimum gate, such that this local trigger always defines the overall timing.

The time calibration in software is performed in various steps. As a very first step, the individual TDC calibration constants and corrections for the integral non-linearity need to be applied to the raw data to convert all decoded information to a common unit as already described in section 3.3.

Afterwards, a correction for the trigger time needs to be done to remove the inherent jitter. This again has to be performed in several steps for full precision, as will be outlined in the sections of this chapter.

3.5.1 Reconstruction of the Local Trigger Time

The next step is the reconstruction of the local trigger which caused the global trigger to activate. For all regular data-taking runs, this will be the tagger detector which is the start detector of the experiment and always part of a data trigger condition. For the following calibration procedure, only such standard data-taking runs will be used.

Additionally, a software plugin has been developed which decodes the configuration of the global trigger module and extracts all trigger conditions. From these, it determines the channel with the smallest gate setting and can check whether this matches with the local triggers of the tagger detector before applying any of the corrections described here.

The goal of this correction is to reduce the 5 ns jitter of the global trigger signal which in turn propagates to all TDCs, since it is the global TDC start, by correcting every time information with the offset between this global trigger signal and the local trigger which caused the global trigger. This will reduce the time jitter to the jitter of the corresponding local trigger, which for the tagger local trigger is again defined by the resolution of the coincidence trigger logic and thus corresponds to $^5/_6$ ns. This offset is measured event by event with the 'DAQ TDC' as can be seen in fig. 3.10.

To simplify all corrections, an offset calibration needs to be performed first. This is achieved using the same calibration utility that was already in use for the integral non-linearity calibration (c.f. section 3.3). Two different fit functions are necessary:

- *Gaussian*: a Gaussian is used to fit the prompt peaks in all time distributions.
- *Trapezoidal*: for those channels which take part in the creation of the global trigger signal itself, a trapezoidal distribution is expected (a smeared out rectangle).

Figure 3.11 shows an example for such a trapezoidal fit. The time distribution for the 'TaggerV' local trigger as measured by the DAQ TDC is displayed. This time distribution effectively visualizes the time difference between the global trigger signal and this single local trigger. For this reason, the 5 ns width and the rectangular shape of the main peak is fully expected. The

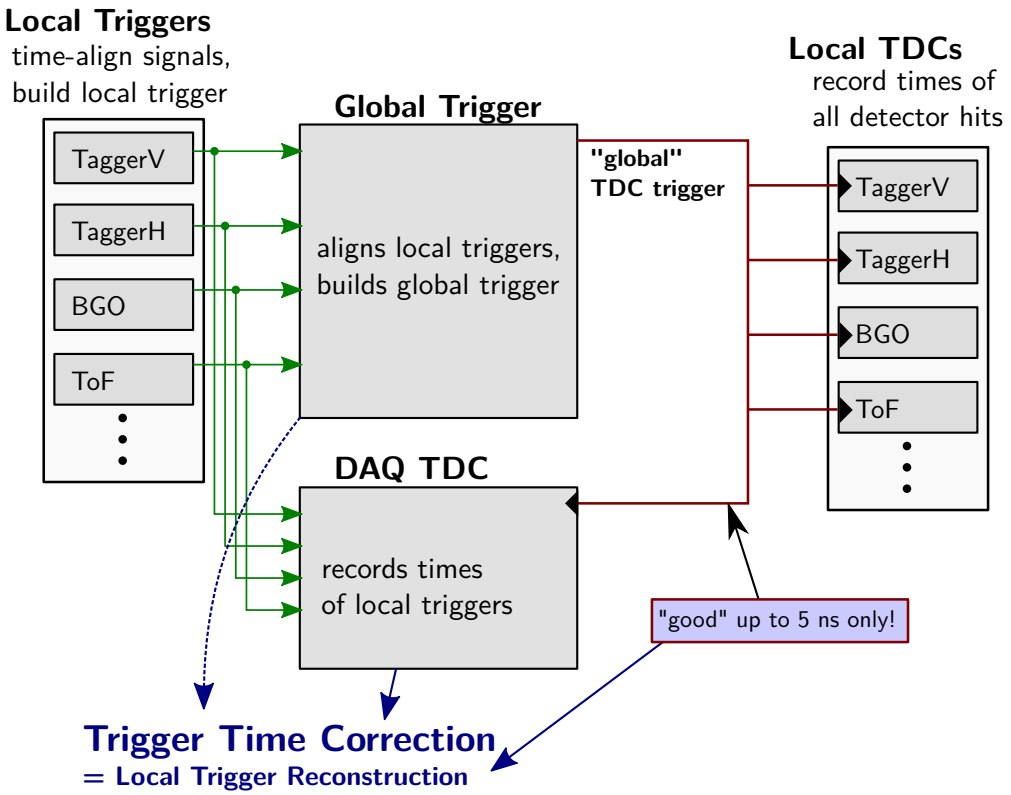

Figure 3.10: Schematic drawing illustrating at which point the trigger time correction (local trigger reconstruction) gathers information and applies offsets to the data: the trigger information from the global trigger configuration and the TDC data from the DAQ TDC are used to reconstruct the time of the local trigger which most likely caused the event. This information can be used to correct the time of the global TDC start which is clocked each 5 ns to de-jitter all time information to that of the corresponding local trigger.

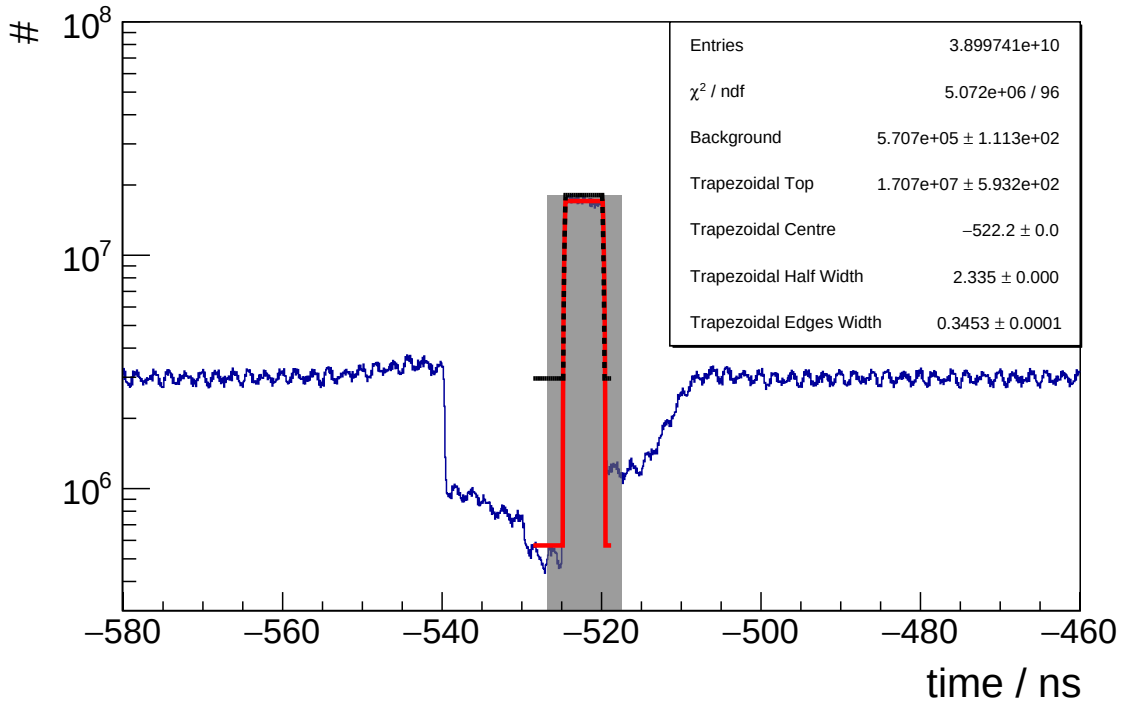

Figure 3.11: t_0 calibration histogram for the TaggerV local trigger. Data are from the October / November 2015 beamtime, spanning 2747 runs from run numbers 28454 to 32092. The black, dashed line is made from the (automatically) guessed values for the start parameters of the trapezoidal fit function. This *guess* involves an estimate for the background content made by averaging over the content of bins far from the prompt region. The red, solid line is the final result from the fitting procedure (only plotted within the actual fit range). In addition, the *mean* of the grey box indicates the result of the previous calibration (as extracted from the database) to help the calibrator in determining potential systematic issues.

distribution also contains a 5 ns gap directly before and also after the prompt peak which shows an exponential suppression. This dead time gap is also expected, since any local trigger signal which would have occured in the 5 ns before or after the trigger signal would have caused another global trigger, which is not possible since all trigger signals (also those from local triggers created by FPGAs) are at minimum 5 ns long (ensured by the FPGA firmware).

As can be seen from the figure, this 5 ns dead time window is located inside a larger dead time window. This is caused by the BGO trigger which is most commonly used in data trigger conditions. Since the time resolution on trigger level is by far poorer than that of the tagger, a larger gate has to be used (more details in [Ham16]). Directly outside of this time window, a small enhancement of the rate can be observed which is the expected statistical behaviour for high trigger rates.

The positions of the fitted means of the trapezoidal or Gaussian fits are extracted and inserted into the calibration database. In the next step, they will be applied to the raw data so that all local trigger channels measured by the DAQ TDC are shifted to an artificial time of '0 ns' to simplify all further time adjustments. This technique is often termed 't_0 calibration' and notably removes any setup dependent differences in time offsets, thus simplifying analysis.

A few important points should be noted:

- Any time differences are completely unaffected by a 't_0 calibration'.
- The calibration necessary changes with each hardware change.
- This calibration may be dependent on the trigger setting.

For the BGO-OD experiment, the 't_0 calibration' of the DAQ TDC is dependent on the trigger setting by design: if a different local trigger would define the timing, the 't_0' point might be shifted. This is not really a huge issue as long as the tagger detector always defines the timing, so the calibration is done choosing only data trigger runs.

The next step after the offset calibration is to really correct the event-wise offset between the tagger local trigger and the global trigger. This offset now directly corresponds to the calibrated time for the corresponding local trigger since that already encodes the time difference between global and local trigger, and the mean of these offsets will be 0 ns. These offsets have to be looked for within the full 5 ns window, i.e. ± 2.5 ns.

However, there may be multiple TDC hits in this window, and especially there might be hits in both the separate tagger local triggers. The software chooses the hit closest to the calibrated 't_0' time in the assumption that this hit most likely caused the real trigger. This offset is then applied to all time data by the analysis step termed 'trigger time correction', reducing the underlying jitter from the 5 ns of the global trigger to the $5/6$ ns binning of the tagger local trigger signal.

One issue remains: the 'Tagger trigger' actually consists of two local triggers ('TaggerV' and 'TaggerH') as mentioned previously during the time alignment of all local triggers (c.f. section 3.4.2). Since the local trigger alignment in hardware can only be performed using the

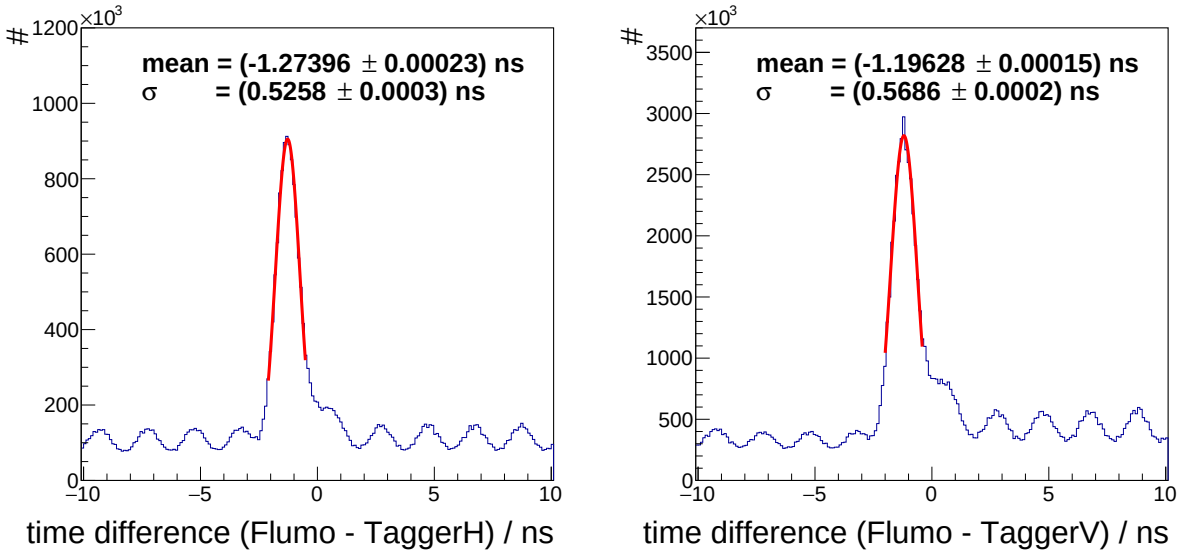

Figure 3.12: Time difference distribution of the local trigger signals for FluMo and the respective tagger local triggers. These data are extracted from the October / November 2015 beamtime, spanning 76 runs from run numbers 28447 to 30729 taken in the special condition of triggering on FluMo only. For this reason, the time difference distribution is suitable to also extract the offset between the two tagger local triggers which is otherwise hidden in the overall time distributions (by triggering on these).

5/6 ns delays, it must be expected that a smaller offset between these two local trigger signals remains, which now must be corrected for in the offline analysis. This offset is again not visible in standard data-taking, since the tagger local trigger which caused the global trigger decision will determine the time reference. For this reason, the necessary offset depends on which of the two tagger local triggers has caused the global trigger decision for each event.

For the extraction of this offset, the cleanest technique is to record special data runs with trigger on a single local trigger channel, such as the FluMo detector alone. These runs are usually also needed for normalization purposes when taking polarized data. In case these runs are not available, a software cut on the FluMo local trigger can be made to achieve similar results.

The offsets can then be read off directly from the time difference distribution between each tagger local trigger and the FluMo local trigger (c.f. fig. 3.12). The offsets are stored in the calibration database and then automatically applied event by event by the 'trigger time correction' after the tagger local trigger which most likely caused the global trigger has been determined. An example of the effect of this correction on the time distribution of the TaggerV local trigger is shown in fig. 3.13.

The t_0 calibration of the tagger detector can now be performed. As input for this, the very same datasets with the FluMo local trigger should be used. This is necessary for the same reason: if the tagger would be included in the trigger, the event by event-offset between the

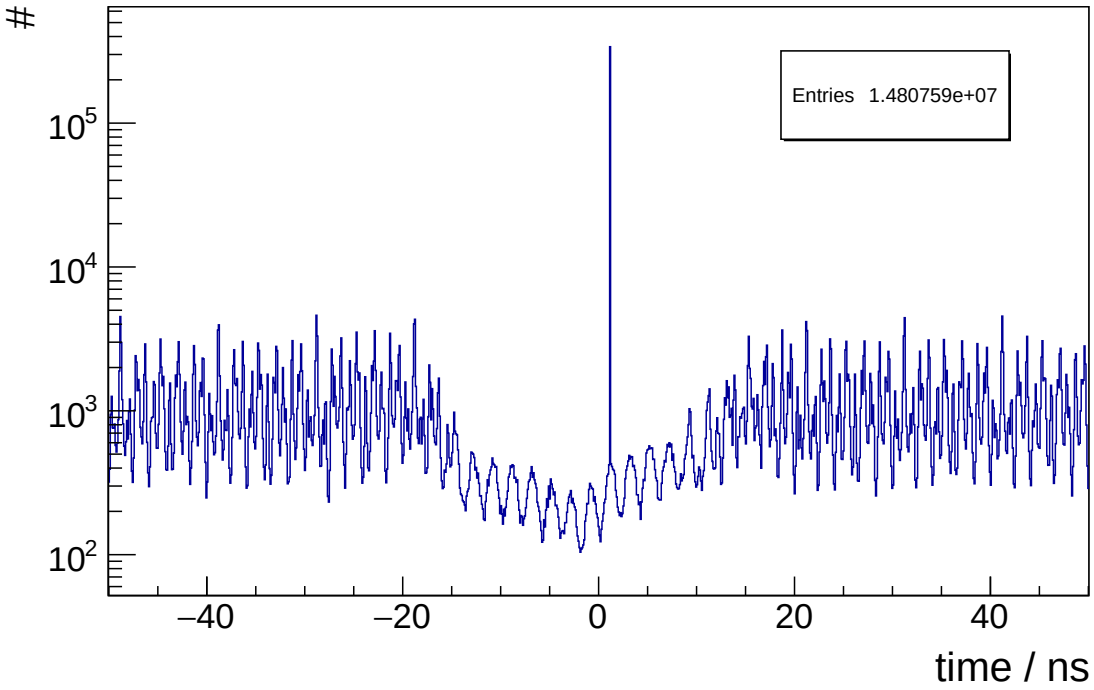

Figure 3.13: Time distribution of the TaggerV local trigger after application of the trigger time correction (data from the October / November beamtime, run 31213). The sharp peak made by the local trigger begin pulled to 0 ns with an additional small offset (c.f. fig. 3.12 can be clearly seen, note that the offset shifts towards the opposite sign of what is shown there). Hits within the dead time region are still seen: they occur if the global trigger was actually caused by the other tagger local trigger. Furthermore, the bunch structure of the accelerator becomes visible.

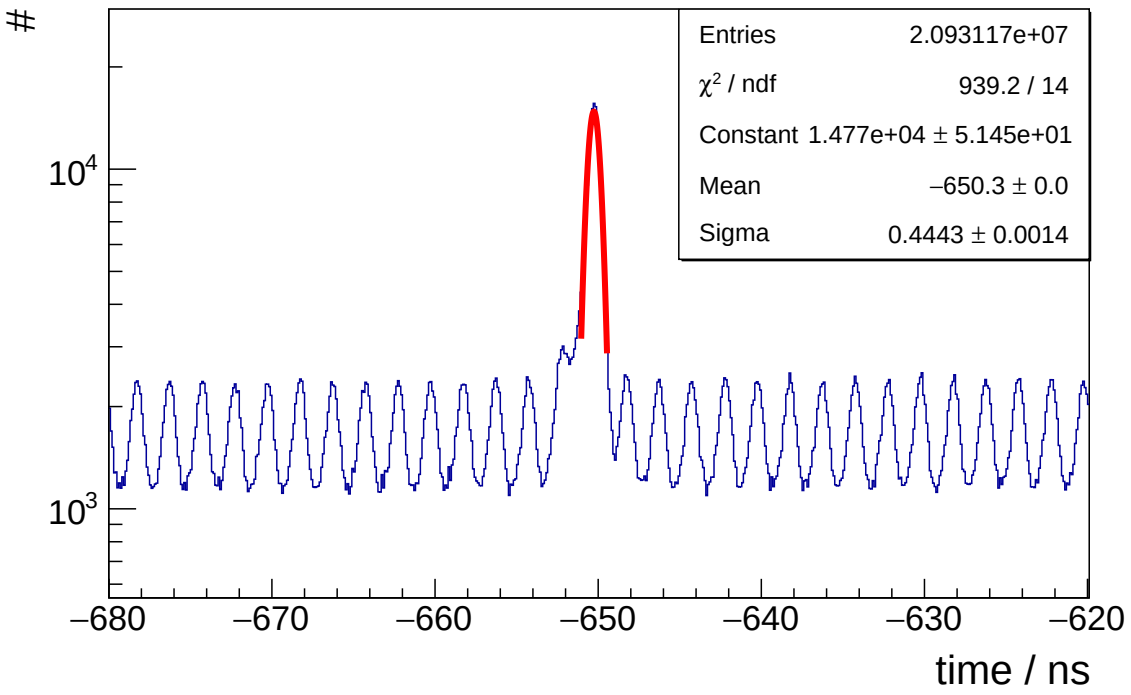

Figure 3.14: t_0 calibration histogram for the Tagger detector. The histogram shows the time distribution for a single channel (hardware channel 7) of the detector. Since the (single) FluMo trigger was used, this is effectively a time difference distribution between this channel and the FluMo detector. The fitted offset can directly be used to determine the t_0 offset for all tagger channels if in addition the offsets determined with fig. 3.12 are taken into account. Data are from the October / November 2015 beamtime, spanning 2747 runs from run numbers 28454 to 32092.

tagger local trigger and the tagger coincidence which caused the trigger would be hidden in the data. An example for this calibration for one channel is shown in fig. 3.14.

After these corrections, the inherent time jitter is now reduced to the $^5/_6$ ns width of the tagger local trigger.

3.5.2 Reconstruction of the Tagger Local Trigger

To resolve the remaining $^5/_6$ ns jitter on the time reference, the next step is to reconstruct the coincidence which caused the tagger local trigger. For this, the FPGA logic to construct the coincidences in hardware needs to be rebuilt in software.

Inside the FPGA, the sampled carry chain information is converted to a 6 bit pattern (c.f. appendix A.1). This pattern is delayed by as many clock cycles as is configured via the 'coarse shifts' (c.f. section 3.4). The 'fine shifts' determined in the trigger timing section 3.4.1 are added to the 6 bit patterns. Afterwards, a gate (≈ maximum time difference) on these

numbers is applied for each pair of hardware-adjacent channels. This gate is made by prolonging the patterns to a configurable length and then checking for overlaps. More details on the implementation can be found in [Bie11] and [SB14].

In the data, only the 'coarse shifts' are already included, thus, the event-by-event correction needs to add the corresponding 'fine shifts' to the data first, channel by channel. In case the tagger trigger time alignment outlined in section 3.4.1 was done correctly, this will lead to aligned prompt peak positions across all channels (within the precision of the $^5/_6$ ns delays).

The major difference now is that this time difference can not be build from all tagger hits and a FluMo reference time as was done in the trigger time alignment previously, since the FluMo detector is not very efficient (by design) and naturally not fully correlated to data triggers. For this reason, the 'corrected' time is used, i.e. the time difference between the measured times and the local trigger, corrected event-by-event by the 'trigger time correction' outlined before.

Within these time distributions which are investigated using the same hardware mapping as the FPGA, the next step is to check, event by event, for coincidences between adjacent channels around the prompt peak. Special cases like usage of spare channels (remapping due to broken hardware) or the daisy channel connecting the two boards to allow for a coincidence between the last and first channel, respectively, have to be taken care of.

In this case, the additional t_0 calibration step does not require a channel-by-channel fit, since the only information to be extracted is the number of the coincidence channel which created the trigger. Improving the alignment to be better than the alignment used by the FPGA would destroy the result. For this reason, the t_0 step is replaced by a more simplistic method: a Gaussian is fitted to the common prompt peak per tagger FPGA board. The mean of this Gaussian is used to search for the correct coincidence within a window of two times the gate-setting used during data-taking[12].

The coincidence is reconstructed as follows:

1. All hits within the time window of twice the gate around the fitted prompt peak are collected and sorted in time.
2. A list with all existing indices is created.
3. In time order, all TDC hits are checked. Their indices and the corresponding subsequent index are marked in the list.
4. As soon as a second TDC hit is found for an index which is already marked like this, this is the earliest coincidence pair.

As soon as the coincidence pair which most likely caused the tagger local trigger is identified, the time offset to be applied can be determined from this. At this point, we can now choose to use the best defined time information available for this channel. This means that the mean of the t_0 calibrated times for the identified indices can be used. This correction step is called

(12) A gate setting of about 7.2 ns is used during data-taking.

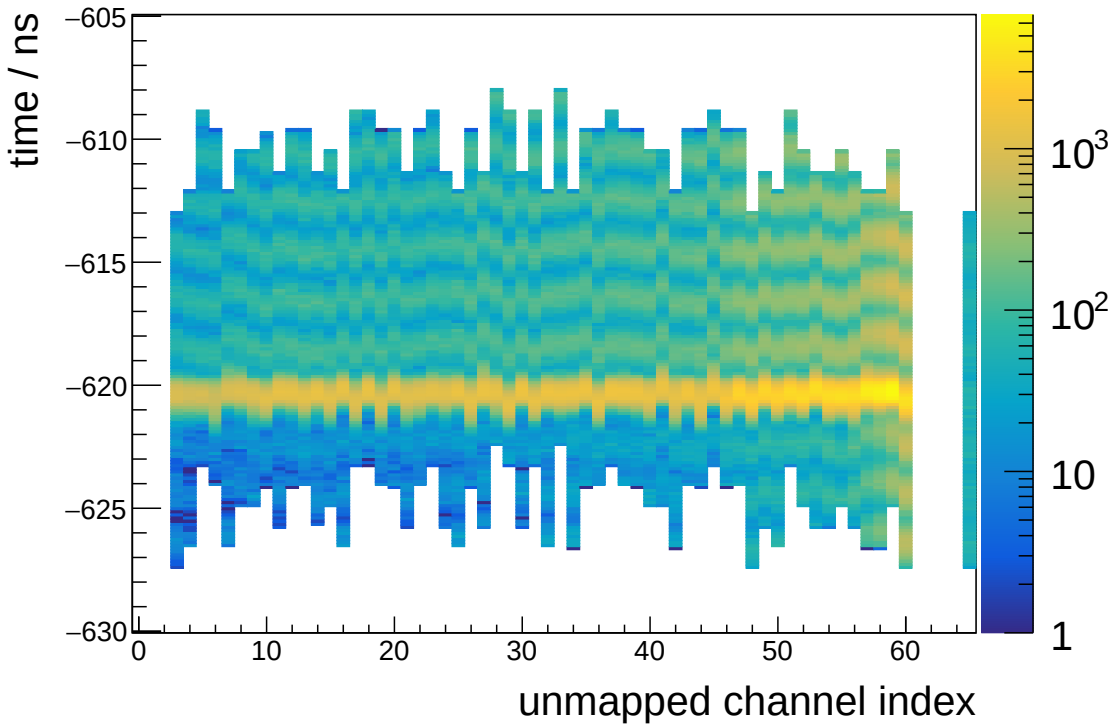

Figure 3.15: Histogram visualizing the near-prompt hits in the tagger channels. This histogram is filled with the non-t_0 calibrated time information (but adding the known 'fine shifts' from the trigger-timing) for all hits found within a window of two times the gate width around the prompt peak region. This histogram gives a direct handle on the quality of the trigger timing for the tagger coincidences (c.f. section 3.4.1) and contains the data in which the tagger coincidences are reconstructed. The data shown are from a single run (number 31213) of the October / November 2015 beamtime.

'event time correction' in the software for historical reasons. The effect of this correction can be seen in fig. 3.15 and fig. 3.16.

Applying all these corrections, the effective reference time for all time information in the experiment is now the reconstructed time of the coincidence in the tagger detector, which, assuming all corrections are working correct, means that the time resolution of the reference time has been improved to be that of two channels of the tagging detector. A study of the time resolution of the tagging detector was part of the PhD work of F. Messi (c.f. [Mes15]) and is not further detailed here. After all these corrections are applied, the tagger cluster time distribution illustrates that the separation of the bunches from the accelerator ELSA is now clearly possible as is visualized in fig. 3.17.

After these corrections, the start time resolution of the tagger detector is fully recovered. Two more techniques can be applied to further improve the quality of the start time on a higher level of analysis:

- It is possible that the correction was done to the wrong bunch due to the wide time

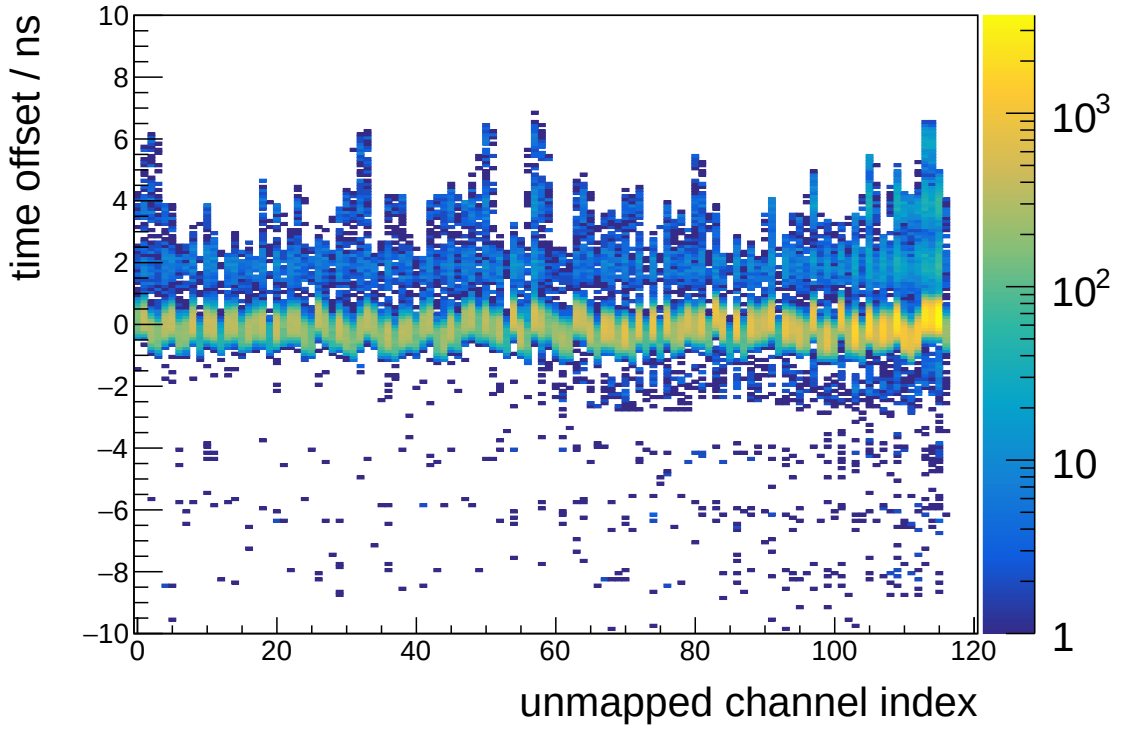

Figure 3.16: Histogram filled with the offsets determined and applied by the 'event time correction'. It can be seen clearly that the offset is usually within the expected range (i.e. within the achievable quality of the trigger timing). In rare cases, the correction does not find a matching coincidence within that window. In this case, a matching pair is usually found within the neighbouring bunch. If even that is impossible, the correction will not be applied (and the histogram not filled). The data shown are from a single run (number 31213) of the October / November 2015 beamtime.

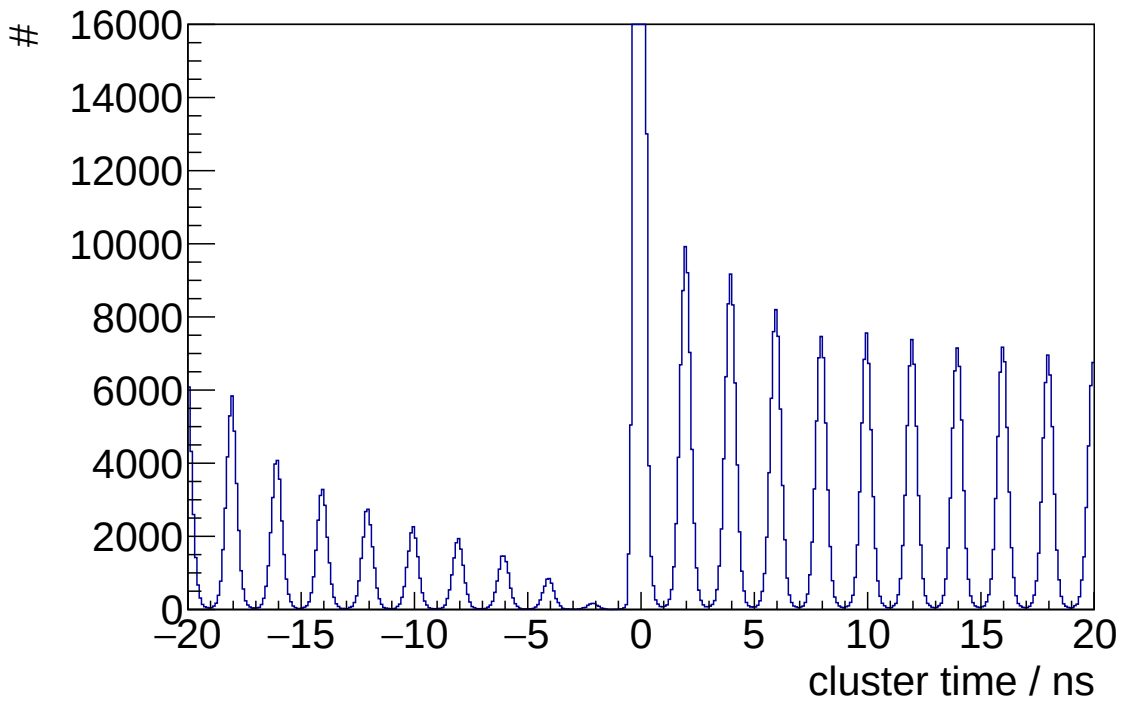

Figure 3.17: Time distribution of all tagger clusters in one run after application of all time corrections (including the 'event time correction' and also the correction described in appendix B.1). The main prompt peak is explicitly cut off to show that also the off-prompt clusters perfectly allow to identify the bunches of the accelerator. The data shown are from a single run (number 31213) of the October / November 2015 beamtime.

gates used for the hadronic trigger components, e.g. the BGO energy sum. Taking basic reconstruction in the central detectors into account, the correct bunch can be recovered and the reference time can be shifted accordingly. This procedure is outlined in more detail in the appendix (c.f. appendix B.1) since basic reconstruction is required.

- Due to the bunch structure of the accelerator, the start time information can be improved even further. Since the tagger detector is capable to clearly separate the bunches, it is sufficient to determine the phase offset to the bunch frequency which is given by the 500 MHz radio frequency of the accelerator. The start time resolution is then only limited by the TDC time resolution and the electron bunch length, which was measured to be between 80 ps to 100 ps depending on the accelerator configuration. The technique has been investigated in a bachelor thesis (c.f. [Kna15]) using a TDC which is using a clock signal derived directly from this radio frequency signal for measurement of the global trigger time. First successful tests were done in the October / November 2015 beamtime and use in future data-taking is foreseen.

Chapter 4

The Time of Flight Walls

During the time period of this PhD thesis, the BGO-OD collaboration had to find a new and fast solution to replace the already installed time of flight wall, which was damaged due to an accident in the ELSA hall. Several detectors already used in other photoproduction experiments (ELAN[1] and SAPHIR in Bonn, GRAAL in Grenoble) have been characterized and the one from the former GRAAL experiment was found to be the one showing the best performance nowadays.

Within this thesis, the idea of using a ToT[2] information to recover time walk effects is tested and motivates the characterization of several readout electronics chains. The developed correction proves to be successful and the recorded ToT is also shown to allow for an online gain matching of the detector channels.

The time resolution achieved with the ToT information convoluted with the start time of the trigger event (as explained in section 3.5) permits to fulfil the technical requirements for the time of flight walls at BGO-OD, which are presented in section 4.1. In section 4.2, an introductory overview of the characteristic properties of a time of flight system is given. The available time of flight setups are presented in section 4.3. Possible readout chains and their electronic components are described and compared in sections 4.4 and 4.5. As is found, the new electronics chain requires a more elaborate reconstruction procedure to make full use of the additionally available ToT information. For this reason, the extraction of the ToT and its use as a pulse integral information are discussed in detail in section 4.6. In section 4.7, it is shown that the ToT information is sufficient for the in-beam gain matching of the detector. Section 4.8 explains the time walk compensation technique which is again based on the ToT. Finally, the reconstruction of the related physics information, the mean time and subsequently

(1) '**EL**ektronstreuung **A**n **N**ukleonen' (german), i.e. electron scattering on nucleons
(2) **T**ime **o**ver **T**hreshold

the β, is presented in sections 4.9 and 4.10. As an addendum, additional monitoring functionality which can be exploited combining the time and time over threshold information is discussed in section 4.11.

4.1 Requirements for the Time of Flight Walls at BGO-OD

The BGO-OD experiment is equipped with a momentum-resolving magnetic spectrometer for charged particles in the forward direction. This is provided by the combination of two fibre tracking detectors in front and 8 drift chambers behind the open dipole magnet (c.f. section 2.5). For particle identification, however, an additional information is needed. This could be provided by a Cherenkov detector or by measuring the time of flight of the particles.

Setting up a Cherenkov device in front of the open dipole magnet was indeed part of the original layout of the experiment, but proved difficult both due to space constraints and technical issues of operating the photomultipliers very close to the magnetic field of the open dipole. These problems do not apply to the time of flight walls which are installed at the most downstream position of the experimental hall to maximize the flight path and thus the time of flight for the detected particles.

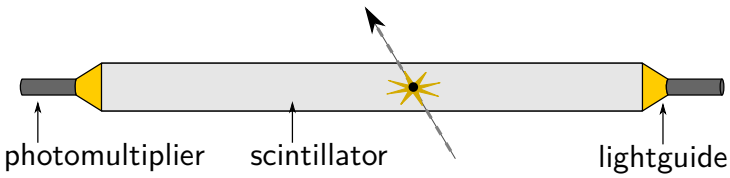

Figure 4.1: Schematic drawing of a single ToF bar.

The **T**ime **o**f **F**light (ToF in the following) setup is constructed from bars of plastic scintillator material which are arranged to a ToF 'wall'. Each bar is wrapped in reflective foil to improve the light collection and enclosed by black foil for light tightness. They are equipped with light guides and photomultipliers at each end to facilitate a two-sided readout as illustrated in fig. 4.1.

Recording the time information of the scintillation light at the two sides of the bars allows to reconstruct the impact point along the bar from the time difference:

$$x_{\text{pos}} = \frac{t_1 - t_2}{c_{\text{eff}}}$$

with c_{eff} being the effective speed of light inside the material. The two sided readout is also a requirement to determine the time of flight information. It can be extracted by calculating the *mean time* of the times measured at the two ends:

$$t_{\text{mean}} = \frac{t_1 + t_2}{2}$$

To subsequently extract the β of the measured particle, the time and incident point information

provided by the ToF detectors needs to be combined with the tracking detectors such that the length of the curved track can be taken into account. Combining the β information with the momentum reconstruction of the magnetic spectrometer, the particle type can be discriminated. For the BGO-OD setup, the discrimination is required between charged kaons, protons and pions.

The quality of the particle ID is dominated by both the momentum resolution of the spectrometer and the time resolution of ToF detectors. This time resolution is determined by several contributions from the scintillator material and geometry, the **p**hoto**m**ultiplier **t**ubes (PMT) and their bases, the high voltage setting, the readout electronics and also the details of the software reconstruction.

A rough estimate of the necessary time resolution neglecting any effects from momentum reconstruction can be performed with a simple calculation: one of the goals of the ToF system is the identification of charged kaons versus protons by their time of flight or, subsequently, their β, for a given reconstructed momentum. The time resolution necessary to distinguish these two particles can be estimated by:

$$\beta = \frac{p}{E_{\text{total}}} = \frac{p}{\sqrt{p^2 + m_0^2}}$$

$$\delta t_{\text{ToF}} = \left(\beta_{\text{K}^+} - \beta_{\text{p}}\right) \cdot \frac{d}{c}$$

with d =564.5 cm being the time of flight distance assuming a straight track in this simple approximation. For a momentum of 2 GeV, a time difference δt_{ToF} of 1.23 ns needs to be resolved[(3)].

In 2011, an accident in the accelerator hall damaged the already installed ToF detector permanently and a new and fast solution had to be found. In the course of bachelor and diploma theses (c.f. [Sch12], [Mei13] and [Bau14]), three kinds of available scintillator bars (formerly used at the ELAN, SAPHIR and GRAAL experiments, respectively) were re-characterized in a dedicated setup using cosmic muons. The procedure and setup which was used is based on the technique described in [GPW86]. This technique notably allows to determine the achievable time resolution with the material and electronics without a dedicated time reference or a defined particle beam.

The bars from the former ELAN experiment were discarded due to their large attenuation length leading to a strongly reduced efficiency (c.f. [Sch12]). The time resolution of the SAPHIR bars was found to be about 750 ps in the clean test environment (c.f. [Mei13]), which would have been barely sufficient for a proper charged particle discrimination. For the GRAAL bars, a time resolution of about 250 ps has been measured within the cosmics test (c.f. [Bau14]). When

(3) This time resolution is the convolution of the time resolutions of the ToF system and the start time of the experiment. A detailed treatment of the start time determination is provided in section 3.5, while this chapter focuses on the characterization of the ToF system.

installed in the experimental area and connected to the readout chain, the time resolution got so spoiled that the detector did not deliver the required performance anymore.

For this reason, the focus of this work is put on the replacement of the readout electronics chain and the optimization of the time resolution using a refined software reconstruction to compensate time walk effects. As will be shown in section 4.8, a resolution better than 350 ps is finally achieved in normal data-taking conditions within the experimental environment.

4.2 Characteristic Properties of a Time of Flight Setup

The characteristic material properties of a plastic scintillator are directly related to the detection mechanisms and the geometry of the bulk material. The properties of the full detector setup include further effects by the wrapping and light-guiding, the photomultipliers and the readout electronics.

In this section, a non-exhaustive definition of the most important characteristics will be given.

4.2.1 Plastic Scintillator

The ToF walls are made from plastic scintillator material and thus belong to the category of *organic scintillator*. The scintillation process itself is very different from that found in inorganic scintillators: while for inorganic scintillators the crystal structure is crucial for the scintillation, for organic scintillators the mechanism is determined by the benzene ring structure of the employed aromatic molecules. Commercial scintillator material usually is a cocktail of such aromatic molecules, a polymer base component, a scintillating fluor component which is also a first wavelength shifter, and potentially secondary wavelength shifter molecules to increase the light yield and decrease the decay time. For these reasons, a huge offering of plastic scintillator materials exist which are optimized for various use cases.

In this work, the decision on available material was already taken since all scintillator bars had been used in previous experiments. Accordingly, the focus will be on the characterization of the existing plastic scintillators and especially on optimization of the readout electronics chain and reconstruction algorithms to optimize the time resolution of the setup.

4.2.2 Time Resolution

The time resolution of the detector system is determined by several ingredients:

- the speed of the scintillation process itself which is material dependent,
- the shape and discrimination of the signal, especially after attenuation effects,
- the TDC time resolution.

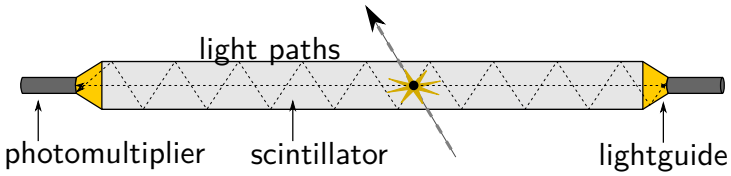

Figure 4.2: Schematic light paths in a scintillator bar.

Furthermore, to achieve a mostly uniform efficiency and the maximum time resolution, a gain-matching of the photomultipliers is necessary to optimize the high voltage setting for high efficiency and minimum time walk.

In this thesis, a strong focus is put on the signal shape and its discrimination, since the time resolution of modern TDCs is usually better than 100 ps and thus not determining the resolution limit of the system.

4.2.3 Effective Speed of Light

The speed of light in a medium can be related to the speed of light in vacuum by the refractive index of the material:

$$c_{\text{med}} = \frac{c_0}{r}$$

Furthermore, the effective speed of light in a scintillator bar is modified by the combination of direct and indirect light paths as illustrated in fig. 4.2. This introduces the refractive index as a factor again:

$$c_{\text{med,eff}} = \frac{c_0}{r^2}$$

For a typical refractive index of approximately 1.47 for plastic scintillator, one can thus use about $16\,\text{cm}\,\text{ns}^{-1}$ as a rough estimate for the effective speed of light in the plastic scintillator bar.

4.2.4 Effective Attenuation

Light travelling through a medium is attenuated depending on the traversed distance. This attenuation basically follows a simple exponential behaviour, but for a scintillator bar is further complicated by the different possible paths the light can travel. Indeed, the light yield is strongly determined by the total reflection on the surfaces of the scintillator.

This is indicated in a simple scheme in fig. 4.2. Furthermore, there is an additional, non-exponential contribution when the signal is created close to the photomultiplier from the direct, non-reflected light. For modelling of this contribution, the following relation is used (based

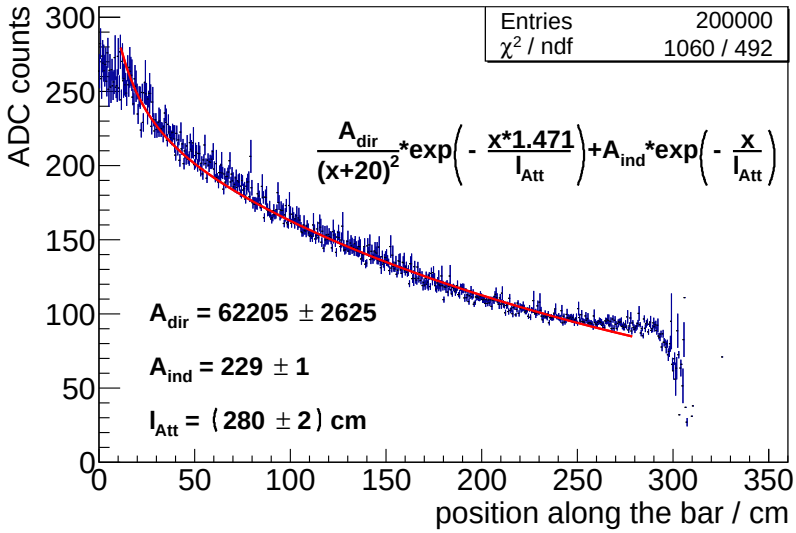

Figure 4.3: Example plot showing the fit used to extract attenuation length and direct to indirect light ratio. The data shown were collected for one GRAAL bar using cosmic muons (c.f. section 4.3). The horizontal axis describes the distance from one photomultiplier calculated from the time difference between the signal measured at the two ends, while the vertical axis displays pedestal subtracted ADC values.

on [Sch12] and [Mei13]):

$$L_{\text{measured}} = Q(d) \cdot \exp\left(-\frac{d \cdot r}{l_{\text{att}}}\right) + \exp\left(-\frac{d}{l_{\text{att}}}\right)$$

with d being the distance from the impact point where the light is generated to the photomultiplier tube, l_{att} being the attenuation length and r being the refractive index of the material. The factor $Q(d)$ empirically describes the ratio between the direct and indirect light which depends on the point of impact:

$$Q(d) = \frac{A}{\left(d + l_{\text{lightguide}}\right)^2}$$

As can be seen, this empirical factor 'scales up' the direct light contribution close to the photomultiplier.

The constant factor $A = {}^{A_{\text{dir}}}/_{A_{\text{ind}}}$ models the ratio between direct and indirect light contributions, depends on the geometry and can be extracted from a fit to the data. An example for such a fit is shown in fig. 4.3. These fits show a variation per bar and photomultiplier tube. During reconstruction, a more conservative value for the direct to indirect light ratio A and the attenuation length will be used which is then commonly applied for the full setup.

	SAPHIR bars (ToF3 & ToF4)		GRAAL bars (ToF1 & ToF2)	
bar orientation	horizontal	vertical	horizontal	horizontal
# bars	8	14	14	14
# readout channels	16	28	28	28
central gap	22 cm	13.1 cm	10 cm	21.5 cm
thickness of bars	5 cm	5 cm	3 cm	3 cm
width of bars	21.5 cm	20 cm	11.5 cm	11.5 cm
lengths of bars	340 cm	270 cm	300 cm	300 cm
min. attenuation length	100 cm	100 cm	250 cm	250 cm
distance from target	596.5 cm	622.5 cm	558 cm	571 cm

Table 4.1: Characteristic data of the ToF setups.

4.3 Time of Flight Setup

Before the start of this work, the BGO-OD experiment was already equipped with a ToF setup consisting of two walls termed 'ToF 3' and 'ToF 4' which were constructed from scintillator bars formerly used at the SAPHIR experiment. Both these walls were constructed with commercial NE-110 (*Nuclear Enterprises*) plastic scintillator material and have already been in use at the former SAPHIR experiment. A characterization of the setup is given in table 4.1.

During this thesis, two additional ToF walls have been set up. They were constructed with 28 bars already used at the former GRAAL experiment, including photomultiplier tubes, light guides and cables which were made available on loan for the BGO-OD experiment.

Before the transportation from the IPN Orsay in France to Germany, all light guides had been removed from the scintillator bars. Thus, after arrival of the components, all bars were unwrapped, cleaned and the light guides were re-glued to the scintillator material. For optimal light yield, a glue with a refractive index close to that of the scintillating material is ideal. The original glue used for the GRAAL experiment was 'Vitralit 9502' with a refractive index of 1.476 manufactured by Panacol which is not available anymore. In contact with the company, two alternative glues with similar refractive indexes were identified and tested. 'Vitralit 4731' with a refractive index of 1.471 was chosen since it was easier to handle and the achieved mechanical connection was found to be more stable. All these transparent glues are well suited for plastics and glass. They are hardened under ultraviolet light as is shown in fig. 4.4, so no classical evaporation of a solvent takes place which would spoil the optical connection.

Figure 4.4: Hardening of the UV glue connecting light guide and scintillator.

The photomultipliers (Philips 'XP2282/B' tubes) are then pushed with springs against the

light guide material, a silicone pad ensures the optical connection. The pads and the housing for the photomultiplier tubes and bases were also provided together with the scintillator material.

Finally, all scintillator bars have been re-wrapped in two layers of aluminium foil and two layers of black foil before they were re-characterized during a bachelor thesis (c.f. [Bau14]) using the same cosmics technique mentioned previously. The characteristic information of this new setup based on the scintillator bars formerly used at the GRAAL experiment is also included in table 4.1.

Furthermore, a holding structure was needed to install the bars in the experimental area. This structure was designed by P. Meiß using standard, commercially available aluminium profiles to best match the existing structures of the experiment.

The design of the frame is shown in the technical drawing in fig. 4.5 and fig. 4.6. As can be seen, the frame holds both the new ToF1 and ToF2 walls in place. The structure allows to exchange single bars and photomultipliers, furthermore, the central gap for the beam can be adjusted. The holding profile for the bars is mounted on two slides on one side to allow for temperature dependent stretching of the plastic material.

A photograph of the final installation of all four walls is shown in fig. 4.7. On the left side, the open dipole magnet with the tracking detectors MOMO and SciFi2 in front and 8 drift chambers on the downstream side can be seen. At the very downstream end, all four ToF walls can be made out. The ToF1 and ToF2 wall share a common frame as described previously.

A schematic side-view indicating the central gaps left for the main beam and the distance of the walls from the target is shown in fig. 4.8. The drawing is to scale, but only contains the sensitive material and ROHACELL®, while all holding structures are removed. This is also the material budget which is used in simulation.

4.4 Readout Electronics

For optimization of efficiency and especially time resolution, a detailed study of the full readout chain is crucial. Since the available ToF bars had already been used in the former GRAAL experiment and were re-characterized in cosmics studies with a simplified setup using a dedicated readout, a characterization of the electronics in use for data-taking concerning the requirements of a high time resolution and the possibility to monitor the gain of all single channels is the next logical step.

The existing electronics setup at the beginning of this thesis work comprised of:

- Leading edge discriminators with adjustable threshold and dual output (section 4.4.1),
- Analogue splitters (active and passive) used to split the signal for gain matching purposes (section 4.4.2),
- 'CAEN V1190A' TDC for digitization (section 4.4.3),
- A sampling ADC module 'CAEN V1742' (section 4.4.4),

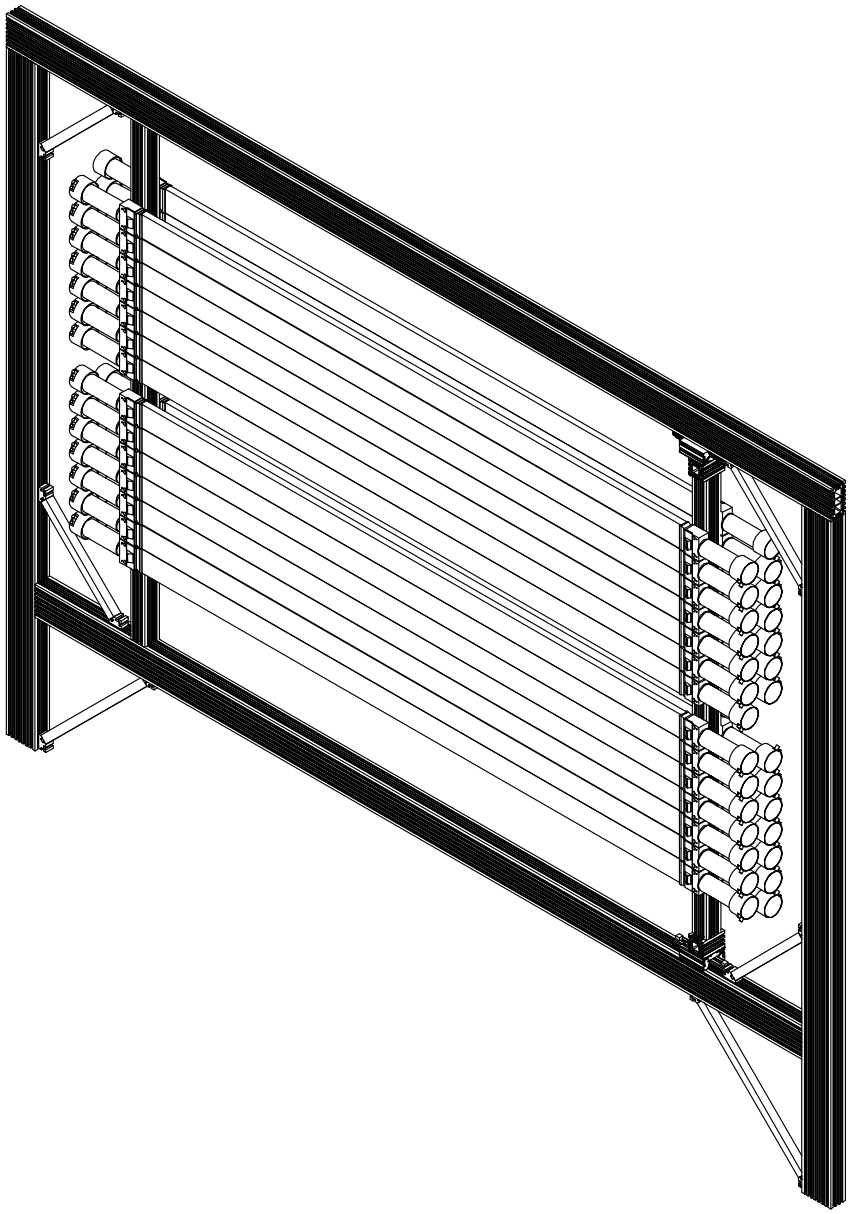

Figure 4.5: Technical drawing of the holding frame for the ToF1 and ToF2 walls. The drawing includes the photomultiplier tubes with their cylindrical housings, bases and connectors.

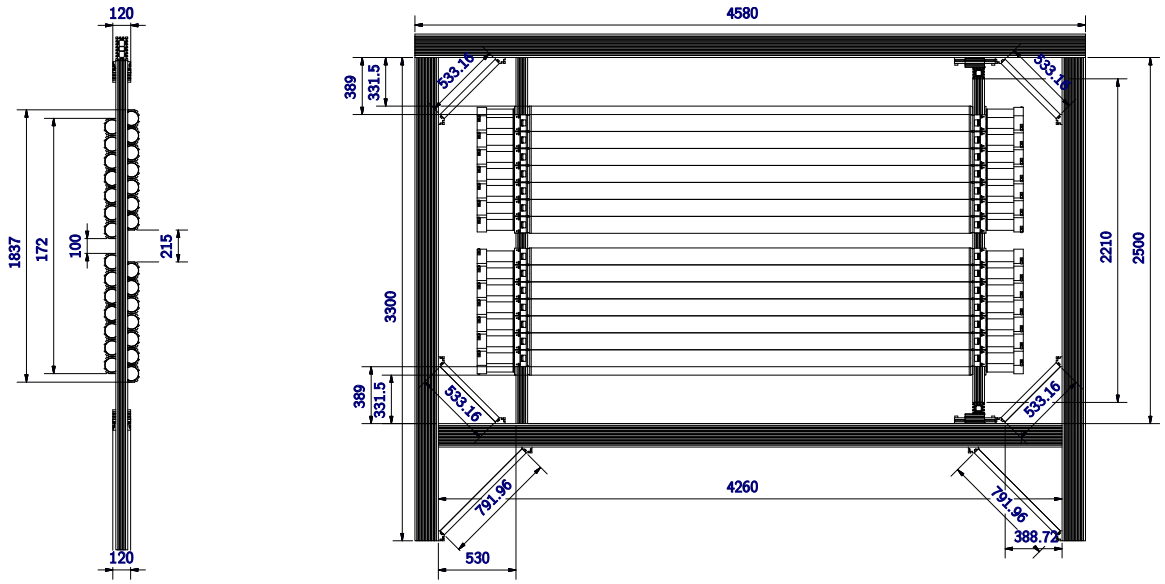

(a) Side view. The beam enters from the left side.

(b) Front view, i.e. view in beam direction.

Figure 4.6: Technical drawings of the holding frame for the ToF1 and ToF2 walls. All units are in millimetres.

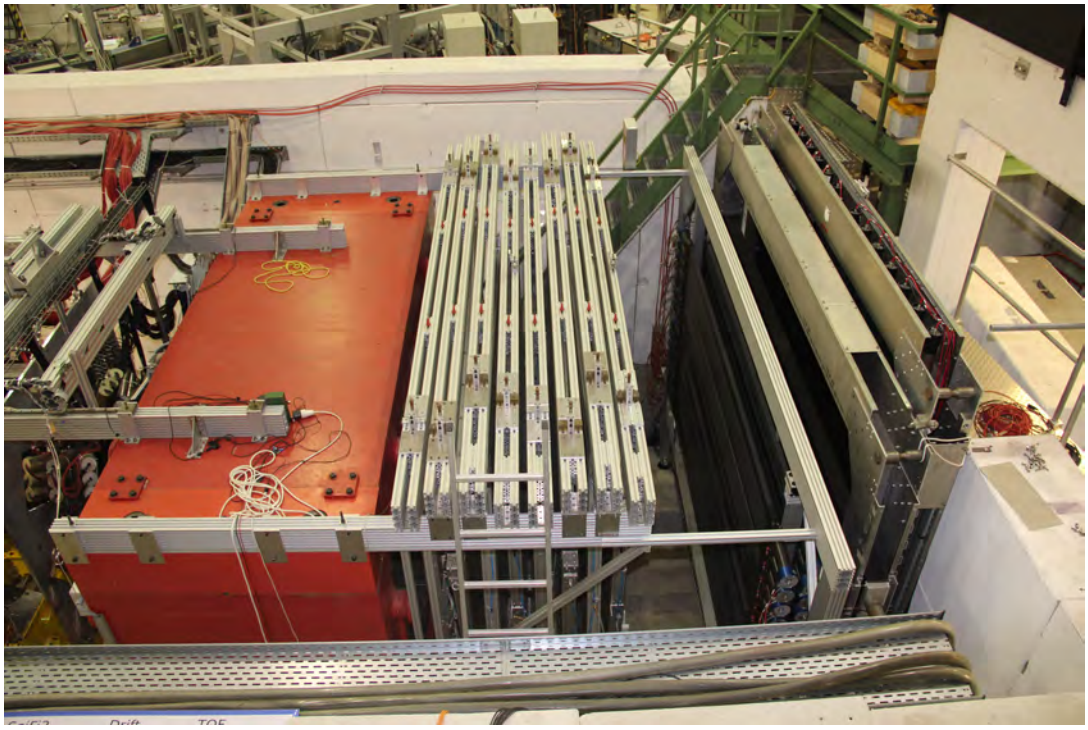

Figure 4.7: Photograph of the final installation of all four ToF walls. The ToF1 and ToF2 frame is fixed to the open dipole magnet, while the ToF3 and ToF4 walls are fixed to the concrete blocks behind.

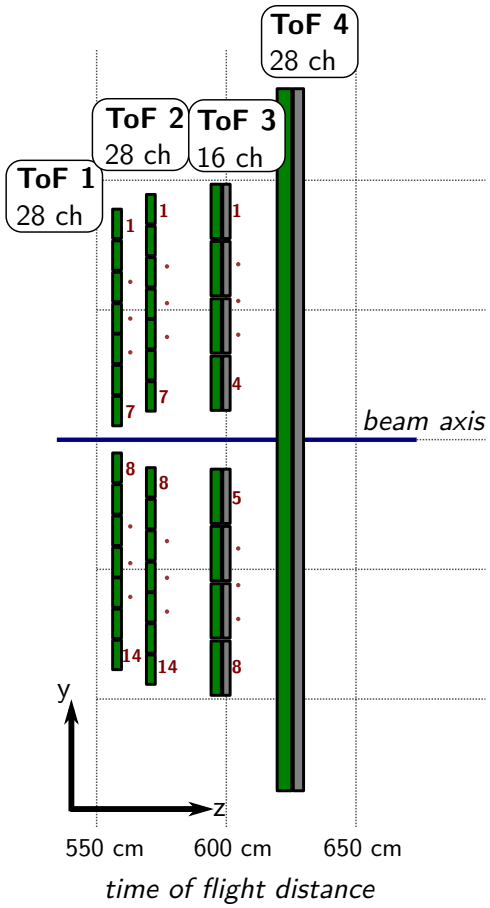

Figure 4.8: Schematic side-view of the geometry of all four ToF walls. The picture includes the sensitive scintillator material in green and the additional ROHACELL® structure for the bars formerly used at SAPHIR (c.f. [Mei13]) in grey. The drawing is to scale, the beam axis and the straight distance of the wall from the target is indicated. The numbers indicate the naming scheme for the ToF *bars*.

Figure 4.9: Labelled photograph of the **A**nalogue **f**an-out **A**mplifier board (short: 'AfA') which features one input and two outputs, one of them with a gain of 1 and one with a gain of 2. Picture courtesy by F. Messi.

- an FPGA board with mean timer trigger logic (appendix A.2).

A more detailed schematic of this setup will be given in section 4.5.

In addition, in the course of this thesis, a new discriminator mezzanine(4) for the FPGA boards used throughout the experiment became available which can be used in conjunction with an in-house developed TDC firmware (c.f. section 4.4.5). The following subsections will shortly describe the hardware components and list their properties, while the later sections will go into more detail about the studies which were done in comparing the different electronic chains.

4.4.1 Leading Edge Discriminator (PNPI)

The discriminators already installed for the existing setup are common between the ToF walls and the SciFi2 detector at BGO-OD. The same modules are also in use at the neighbouring CB experiment.

These leading edge discriminators are NIM modules with 16 channel analogue LEMO inputs on the front and two LVDS outputs per discriminated signal on top. The length of the output signals is fixed to 50 ns while the thresholds can be adjusted electronically in a range between 5 mV and 80 mV.

It has been found previously (c.f. [Bös16]) that the threshold does actually not change anymore for lower set-values than about 10 mV to 15 mV, which is why a stable value of about 20 mV is in use for the SciFi2 detector system and was also applied for the ToF setup.

4.4.2 Analogue Fan-Out Amplifier

An **A**nalogue **f**an-out **A**mplifier board (short: 'AfA') which was developed for use at the tagger hodoscope of the experiment has also been used for the ToF detectors to split the signals for the gain matching procedure.

This AfA board is shown in fig. 4.9 and is described in detail in an internal note of the experiment [Mes11] and also in the PhD thesis of F. Messi [Mes15]. It is an active splitter board with a high analogue bandwidth and low jitter. The equipped amplifier chip features a slew rate of $3100\,\mathrm{V\,\mu s^{-1}}$. Two outputs provide amplifications of 1 and 2 over the original signal. The

(4) The term mezzanine is used to describe a piggyback daughter board, more details in section 4.4.6

system is completed by a dedicated power supply board (termed PeBBLeS) built for minimizing noise on the low voltage power supply.

In the ToF setup, the AfA boards have been used for an active splitting of the signals to allow for parallel measurement with the sampling ADC and the digital components behind the discriminator, i.e. the TDC and trigger logic.

4.4.3 CAEN TDC

For readout of the TDC information, a commercial 'CAEN V1190A' module is used initially [CAE16]. It is a multi-hit TDC providing 128 input channels with up to 100 ps of time resolution and was in successful use throughout the experimental setup before the jTDC was available (c.f. appendix A.1).

The CAEN TDC is based on the 'High Performance TDC' chip developed by the 'CERN/EP-MIC' group. It combines a DLL[(5)] and a coarse counter running with the clock frequency. If a hit is detected, both the DLL state and the clock counter are stored so the achieved time resolution well exceeds the clock frequency, which can be chosen in various steps up to 320 MHz. The integral non-linearity inherent to the DLL technique[(6)] is already calibrated by the manufacturer and corrected for by the firmware of the module.

All such multi-hit TDCs used in an event-based readout environment need to offer internal buffers to store the multiple hits collected in one event. Commonly, a ring buffering technique is used to store all hits continuously and discard them unless a trigger signal, which arrives later in time than the other input signals, is seen, which triggers the readout or persistification of the buffer. This is also the case for the CAEN TDC, which also allows to tune the recorded time window.

However, one known issue with this module is that if the rate per channel becomes too high (several MHz) hits may be dropped without sufficient error information being available (c.f. [Chr04]). For the ToF system, such rates are not expected, but for usage at the tagging detector such critical, silent loss of hits was indeed observed.

4.4.4 CAEN SADC

To extract an information about the integral of the signals which is necessary for gain matching (c.f. section 4.7), a commercial sampling ADC ('CAEN V1742') was used. This module is based on four 'DRS4' chips developed at the Paul Scherrer Institut[(7)]. These chips embed a switched capacitor array with 1024 cells and can be configured for digitizing rates of $1\,\mathrm{GS\,s^{-1}}$, $2.5\,\mathrm{GS\,s^{-1}}$ or $5\,\mathrm{GS\,s^{-1}}$ for 9 channels each. The complete VME board can thus handle 32 channels and additional trigger channels, such that a full ToF wall can be covered.

(5) **D**elay–**l**ocked **l**oop
(6) These non-linearities are caused by inevitable manufacturing spread of the electrical properties of the delay elements, causing the bins of the TDC to be of slightly varying size.
(7) DRS4 stands for *'Domino Ring Sampler'*, c.f. [Rit].

This SADC module does not provide any feature extraction by itself, but only digitizes the samples and provides these as a raw data stream. Due to the sheer amount of raw data, it can not be kept in constant readout during normal data-taking conditions, but it provides a high resolution and full debugging information for electronics development.

A software feature extraction was developed in the course of a diploma thesis (c.f. [Mei13]) and was extended and improved in the course of this thesis (c.f. appendix A.3).

4.4.5 jTDC

At the BGO-OD experiment, the FPGA-based 'jTDC' is actively used since it provides high rate stability and can be equipped with different electronics inputs. Since the firmware was developed in-house by J. Bieling, it is readily available for extension with customized trigger logic and scalers as necessary for each detector, removing any complications of combining separate electronic modules with different properties for these tasks. The jTDC is implemented as a firmware for commercially available Spartan®3- and Spartan®6-based FPGA boards.

Details about the basic principle of the implementation and the achieved characteristics are provided in appendix A.1. For the usage in the readout chain of the ToF detectors, the following key features are of importance:

- High time resolution.
  The TDC bin size is 40 ps on average, 30 ps RMS are achieved.
- Short minimum signal length of 400 ps.
  The limit is imposed by the in-firmware pattern detection mechanism, usually the determining factor is the limit of the electronics input stage.
- Flexible electronics inputs.
  In this case, a discriminator input board will be used.
- Flexible trigger logic.
  In this case, a dedicated mean timer trigger logic is implemented. It is described in more detail in appendix A.2.

The achieved time resolution and the minimum signal length of the jTDC are by far sufficient for this application, so the main focus will be on the properties of the discriminator module and its configuration.

4.4.6 jDisc Discriminator Mezzanine

As an alternative to the use of external discriminators, a discriminator input board for direct connection to the FPGA boards was investigated. The original idea for these discriminators was suggested by J. Hannappel to the manufacturing company 'ELB-Elektroniklaboratorien Bonn UG'. The main beauty of this approach is that the full input electronics is contained on a

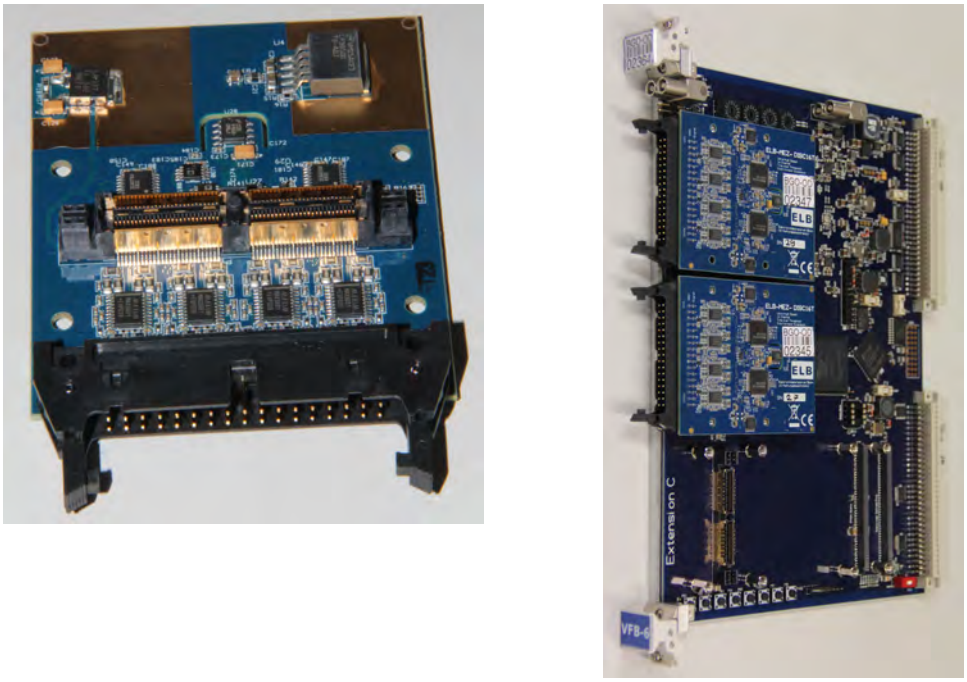

Figure 4.10: Photographs of an ELB-MEZ-DISC16T mezzanine and a Spartan®6-based FPGA board equipped with two of these modules.

daughter board (so-called *mezzanine*) and the digitized signal is directly entering the FPGA which can handle all roles at the same time provided the necessary firmware is developed: TDC, time over threshold extraction, rate monitoring and trigger logic. One such FPGA board can be equipped with up to three mezzanines.

This discriminator provides the following features and key specifications (c.f. [Ele], a datasheet is also available non-publicly):

- 16 inputs per mezzanine, offered with various connectors
- Time over Threshold information
- input bandwidth larger than 500 MHz
- 14-bit DAC for threshold setting between −4 V and 4 V
- 8-bit DAC for hysteresis setting between 0 mV and 80 mV
- 16-bit ADC for readback of thresholds and hysteresis
- pass-through time: 500 ps
- pass-through time jitter: 30 ps

Most of these features are defined by the input comparator 'MAX9601' by *maxim integrated* (c.f. [Max02]). The key features for our application are the wide input range, finely adjustable thresholds and the ToT information which will be found to be extremely useful to not only provide a crude signal integral information for gain matching, but also improve the achieved time resolution.

To make best use of this modular system, a new FPGA firmware was developed in-house, combining the existing jTDC (c.f. appendix A.1) and mean-timer trigger (c.f. appendix A.2) firmwares.

4.5 Comparison of Readout Techniques

For a well-founded decision on the final readout system, a comparison of the available configurations was necessary. The existing setup using the leading edge discriminators described in section 4.4.1 had several known drawbacks:

- the lowest possible threshold is rather high and may differ from channel to channel
- no time walk compensation possible (simple leading edge discriminators)
- additional signal splitting is needed to measure the ADC information in parallel, not all channels can be connected to the ADC in parallel
- the TDC module and the trigger module were separate electronics, relying on the discriminators to feature two functional outputs for each channel
- the ADC information can not be read out during normal data-taking, special runs (and hence beamtime) are needed, which in turn means gain monitoring is not easily possible

The newly available jTDC-based readout with the time over threshold discriminator mezzanines was not yet in wide use at the experiment and the quality of the time over threshold information was still unclear at this point. However, due to the known issues with the existing setup and the availability of the new hardware which may fulfil the requirements for the ToF walls [(8)], the new electronics was used in several test setups. In the following paragraphs, the various electronics setups which were examined during a test beam time in June 2014 to determine the best configuration will be presented. An in-depth analysis of the data which were taken will be given in section 4.6. The comparison is performed through the sampling ADC, which provides the most complete digitized information about the analogue signals.

The existing setup and the tentative new configuration are shown in fig. 4.11. It must be noted that already for the gain matching procedure, the old setup had to be extended with the additional SADC in any case. Based on this, the *complete* testing setup as shown in fig. 4.12 was used for some of the comparison studies. Since a direct connection between the photomultiplier

(8) The necessary energy resolution for gain matching is by far lower than for a calorimetric application, and the thresholds which are crucial for the time resolution could be expected to be under better control.

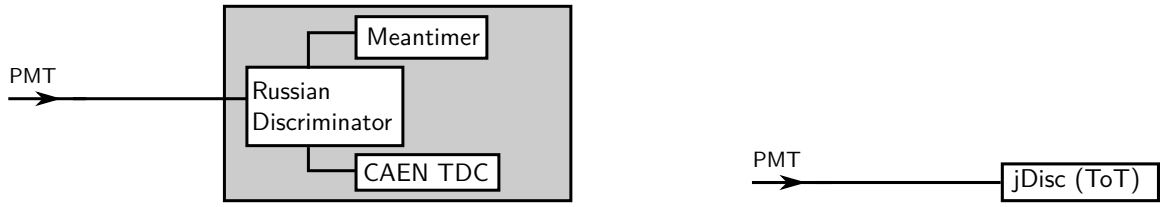

(a) Existing setup with leading edge discriminator and separate trigger logic / TDC

(b) Goal: Direct connection of photomultiplier to jDisc discriminator

Figure 4.11: Schematics of the previously existing setup, which had to be recabled for SADC measurements, and the tentative new setup.

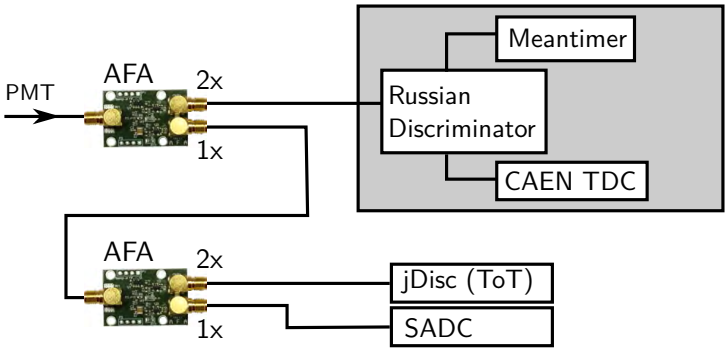

Figure 4.12: Combined testing setup. In this case, the output from the active splitter with double amplification is led into the 'classic' electronics chain of TDC and mean-timer logic behind the old discriminator modules. In parallel, the non-amplified output is led to another active splitter feeding the 'new' electronics and the sampling ADC. Again, the amplified output of the splitter was used for the discriminated path (since the sampling ADC has a large dynamic input range, it can cope well with smaller signals).

and the SADC module (as explained in fig. 4.13) is not usable, one of the two active splitter stages was necessary in any case.

It is important to exclude potentially significant effects from the active splitter, the AfA, since these would spoil any comparison based on such a setup. For this reason, the additional configurations shown in fig. 4.14 were used to disentangle such effects. Indeed, it was found that a DC offset added by the AfA may distort the jDisc module since the baseline is shifted. This can be accommodated by measuring the baseline and modifying the threshold channel by channel. The SADC is unaffected by this issue due to the high dynamic range and the baseline fitting procedure applied during the feature extraction process.

It was already known previously that the achievable time resolution with the classic setup shown in fig. 4.11a did not fulfil the requirements on time resolution, likely due to the limit on the lowest possible threshold possible with the leading edge discriminators (c.f. section 4.4.1) and the remaining time walk which could not be corrected. This was confirmed in a test setup comparing the resolutions determined using cosmics data (c.f. [Bau14]) with the resolutions

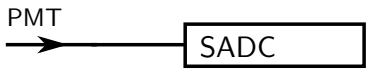

Figure 4.13: Direct connection to SADC input. This setup is not really usable, since the CAEN V1742 sampling ADC (based on the DRS4 chip, c.f. section 4.4.4) introduces a DC offset at the inputs which distorts its own measurement. Using an active splitter with a terminating resistor as done in fig. 4.11 circumvents this issue.

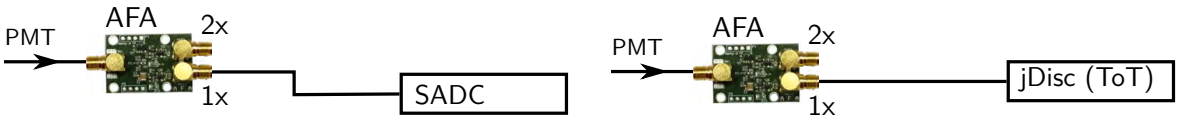

(a) Direct connection to the SADC input with AfA in front (necessary since the SADC introduces a DC offset on the input).

(b) Direct connection to the jDisc module with AfA in front to be able to disentangle AfA effects.

Figure 4.14: Direct connection setups to the SADC and the jDisc module. With these configurations, effects introduced by the AfA module can be studied.

determined from the in beam setup.

The time resolution with the jDisc setup was found to be of similar order using the straightforward approach of taking the leading edge time. However, due to the availability of the time over threshold information, a correction of the time walk is possible. This will be discussed and results will be shown in section 4.8, making use of the parallel setup with jDisc and SADC as shown in fig. 4.22 to study the behaviour of the ToT information as compared to the pulse integral.

Finally, the jDisc module was found to provide a full replacement for the old setup. In the meantime, also the mean timer trigger logic was integrated on the same FPGA (c.f. appendix A.2). It can even be used to facilitate the gain matching procedure instead of using the SADC as will be shown in section 4.7.2. For this reason, the electronics setup could be largely simplified since now the PMTs are directly connected to the jDisc boards as shown in fig. 4.11b. The final electronics configuration is shown in fig. 4.15. The SADC is still available for debugging studies, but not in active use anymore.

4.6 Study of the Time over Threshold Information

As illustrated in fig. 4.16, the time over threshold is determined by the difference between an initial start time (at which the threshold was exceeded) and a stop time at which the signal fell below threshold again.

In reality, an electronics threshold is never exact: as already visualized in the picture, the pulse shape is usually distorted and especially the trailing edge of the signal may exhibit fluctuations at threshold level which can cause a ‘re-triggering’ of the system. This is not masked by the

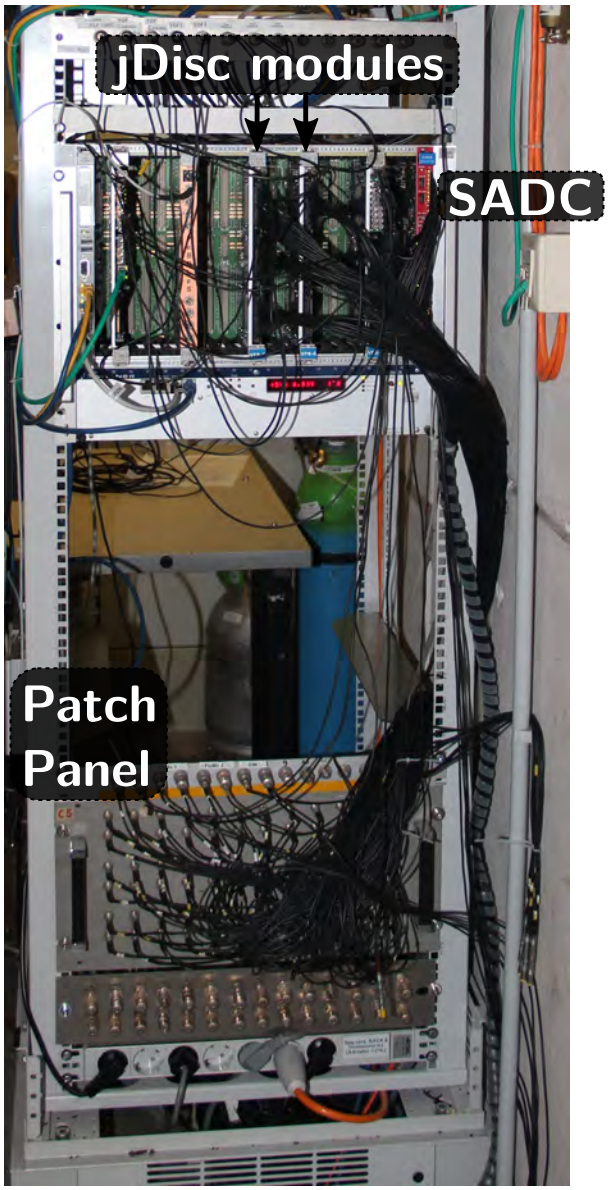

Figure 4.15: Photograph of the electronics rack for all ToF walls. At the bottom, a patch panel adapting from BNC to LEMO can be seen. It allows to investigate the signals of single channels in case of problems. In the top VME crate, the two jDisc modules and the SADC module at the very right are installed.

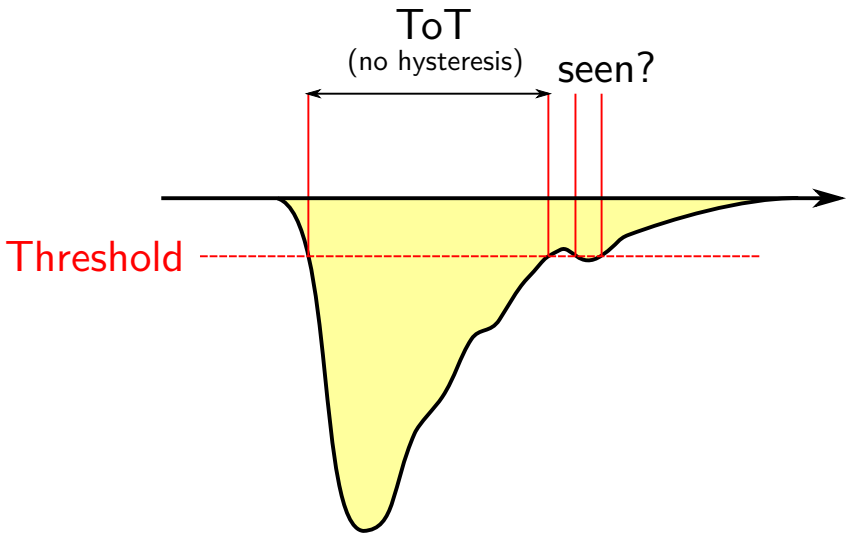

Figure 4.16: Illustration of the time over threshold information without hysteresis for a fixed, single threshold setting.

TDC, since the time needed for the jTDC to be able to accept a second signal is short[(9)] and the minimum signal length required to detect a leading / trailing edge is even shorter (c.f. appendix A.1). The high speed comparator used on the mezzanine does also not suppress such short signals due to the high analogue bandwidth of 500 MHz. In addition, this means that also electronics noise (for example pickup of high frequent noise on signal or ground lines) may create accidental threshold crossings which survive throughout the digitization. These effects will be studied in more detail in the subsequent chapters dealing with first raw data analysis.

The offline software technique for reconstruction of the time over threshold described in section 4.6.1 is designed to counteract these effects as far as possible. Additionally and more important especially for a clean trigger signal, the discriminator module already features a hysteresis setting which can reduce these effects in hardware. The hysteresis shifts the two thresholds (the 'start' threshold and the 'stop' threshold) away from each other. This reduces the noise pickup and especially the 're-triggering' of the system on the trailing edge, since after the signal has fallen below the lower 'stop' threshold, a much larger fluctuation is needed to cross the higher 'start' threshold again. This is visualized in fig. 4.17: in this case, the previously unstable situation of potential 're-triggering' of the system is suppressed by the two thresholds.

There are also two downsides to the application of a hysteresis on the threshold:

1. The 'start' threshold usually needs to be higher, since the 'stop' threshold can not be chosen arbitrarily low. This hinders the optimization for minimum threshold, which is required to reduce the time walk effect and consequently improve the time resolution (c.f. section 4.8).

(9) At maximum 2.5 ns, i.e. shorter than a usual PMT signal.

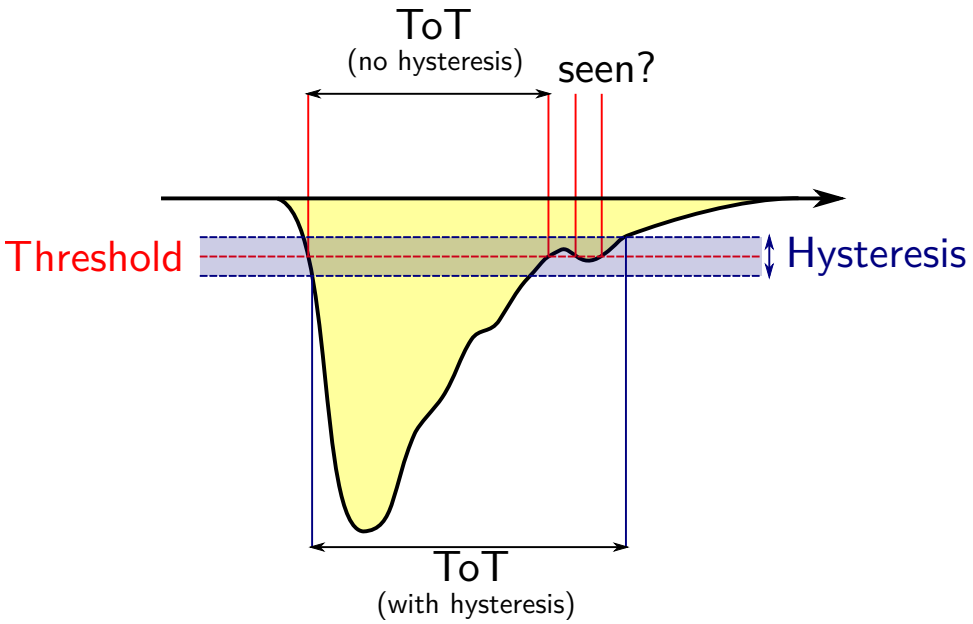

Figure 4.17: Illustration of the time over threshold information when adding an additional hysteresis to effectively use two different thresholds for 'start' and 'stop'.

2. The time over threshold information information is modified by the hysteresis. Depending on the pulse shape, this may lead to additional non-linearities which might need characterization.

From this point of view, a crucial ingredient for an optimized time over threshold-based digitization especially in view of time resolution is the optimization of both threshold and hysteresis settings. The hysteresis and its effects especially on the time over threshold information will be studied in more detail in section 4.6.4.

Additionally, if an ideal, fixed pulse shape is assumed, the time over threshold information can be used as a measure for the pulse integral. As first approach, the assumption visualized in fig. 4.18 is made: approximating the pulse shape with a simple triangle with equally scaling 'lengths' for the 'time' axis and the 'amplitude' axis, the area of the signal is proportional to the ToT^2. The tests in section 4.6.2 will check for the validity of this assumption by comparing the measured time over threshold with the pulse integral extracted using either the SADC or a classic ADC. In addition, a simulation of the time over threshold information was implemented in the SADC reconstruction (c.f. appendix A.3) to allow for a characterization of the time over threshold behaviour for realistically shaped signals with high statistics.

4.6.1 Time over Threshold Reconstruction

The data provided by the jTDC after decoding and application of time calibrations (c.f. section 3.3) consists of time information for leading and trailing edges separately. These are

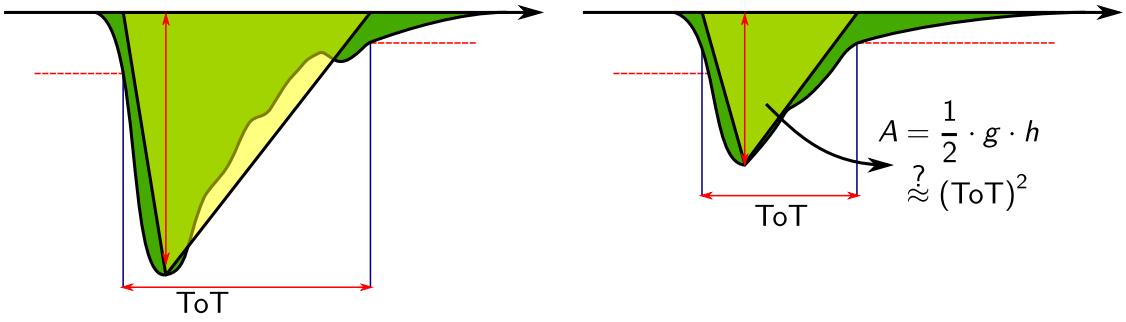

Figure 4.18: Basic extraction of a charge information from the time over threshold information. Assuming the ideal case of a fixed pulse shape independent from the signal amplitude, a triangular approximation can be made to extract the area / pulse integral from the ToT^2.

effectively handled as different TDC channels, one sampling for the leading edge, and the second in parallel sampling for the leading edge in the inverted signal.

For this reason, the leading and trailing edges are still stored separately and are not yet matched up to form a pair for one signal, so the time over threshold information is not readily available. Thus, the first step in software is to link together matching pairs of leading and trailing edge. Performing this pairing in software leads to two main advantages:

1. The interpretation of the signal polarity can easily be changed a posteriori by just exchanging the interpretation of leading and trailing edges.
2. Artefacts such as the pickup of noise or single missed edges may be understood better and removed.

The algorithm to match up the pairs of corresponding leading and trailing edges may be outlined as follows:

1 Separately sort all leading and trailing edges in time, per channel.

2 Take the first unused leading edge.

3 All trailing edges earlier than this, if any, are marked as invalid, but not discarded immediately so they could be looked at in further analysis.

4 The first trailing edge after the selected leading edge is combined with it and the ToT is calculated.
Exception: If this trailing edge is later in time than the next leading edge, the leading edge is marked invalid and the algorithm restarts at step **2** with the next leading edge.

5 If this is not the last leading edge, return to step **2** and handle the next one. Otherwise, mark all remaining trailing edges as invalid.

This basic algorithm can of course be tuned to discard identified noise or unrealistic artefacts which may remain in the data even with a moderate hysteresis setting (c.f. section 4.6.4). Several features have been implemented and tested in the course of this thesis:

minimum pulse length Discard any constructed leading / trailing edge pair for which the ToT is *smaller* than a given value (after step 4). Can be used to suppress high frequent noise.

maximum pulse length Discard any constructed leading / trailing edge pair for which the ToT is *larger* than a given value (after step 4). Can be used to suppress overly long signals.

artificial dead time Impose an artificial dead time after each valid leading / trailing edge pair. This dead time is imposed after the trailing edge time. In this dead time, further leading edges and any corresponding trailing edge are marked as invalid. New leading edges are only accepted after this pause.

An example to show the effect of these cuts is presented in fig. 4.19. We neglect the structures at higher time difference and ToT for now, they will be discussed in more detail in section 4.11. The artificial dead time cut removes the diagonal band which can be identified as 're-triggering' due to high frequent noise on the falling slope of the signal leading to an additional threshold crossing (c.f. section 4.6.4). Additionally, signals with too short ToT (shorter than the photomultiplier may produce) are neglected by the minimum pulse length requirement. These can for example be caused by electronics noise on the line due to the low discriminator threshold.

Finally, all valid leading / trailing edge pairs enter the time walk compensation which will be described in section 4.8.

This algorithm has another important advantage. As described in appendix A.1, the carry chains of the jTDC are chosen to be longer than one clock cycle so signals may be seen twice, once at the beginning and once at the end of the chain. An example plot visualizing the raw data (at which 'step' of the carry chain the leading edge was found) is shown in fig. 4.20. A significant number of entries behind the effective end of the carry chain can be seen clearly. These should not occur if the in-firmware protection against detecting a hit twice would be working as expected.

This issue was investigated together with J. Bieling. It turned out that the *propagation time* of 'high' and 'low' signals inside the carry chain is not equal, which is likely caused by different high-to-low and low-to-high transition times of electronics elements on the FPGA fabric. For this reason, the effectively achievable resolution for '1–0' transitions turns out to be higher than that of '0–1' transitions — and there is a possibility for 'holes' to occur in signals only at the end of the chain. These might then be identified as leading / trailing edges and are not seen at the beginning of the chain but only at the end, such that the in-firmware double-detection protection fails to work.

Such short interruptions in a discriminated signal can occur easily due to high frequent noise on the signal. They are strongly reduced by the application of a hysteresis in hardware

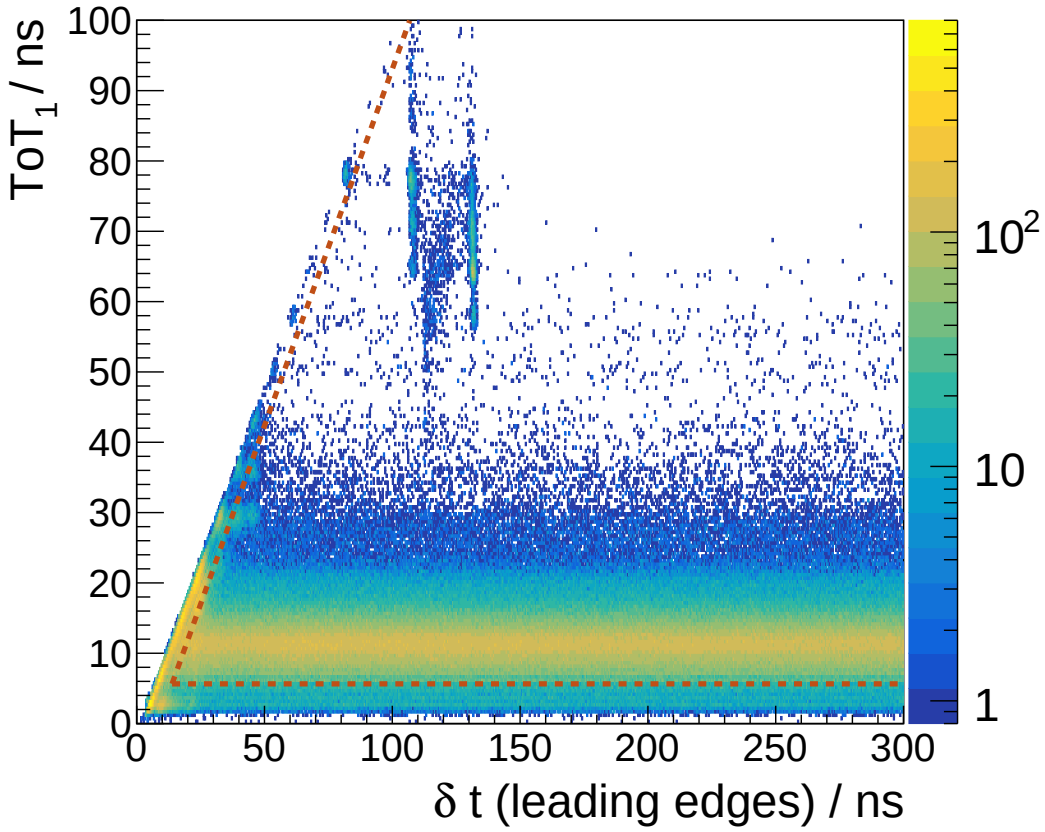

Figure 4.19: Example for electronics artefacts recorded by the time over threshold system. The data shown were recorded for one channel of the ToF 1 detector. On the horizontal axis, the time difference between the leading edges of all pairs of consecutive signals is plotted. Correlated to this information, on the vertical axis the corresponding time over threshold of the earlier signal of the pair is shown. The histogram is filled for all recorded digitizations without applying any time or ToT cut before. The red, dashed lines indicate the applied cuts during ToT reconstruction. The obvious structures will be discussed in more detail in section 4.11.

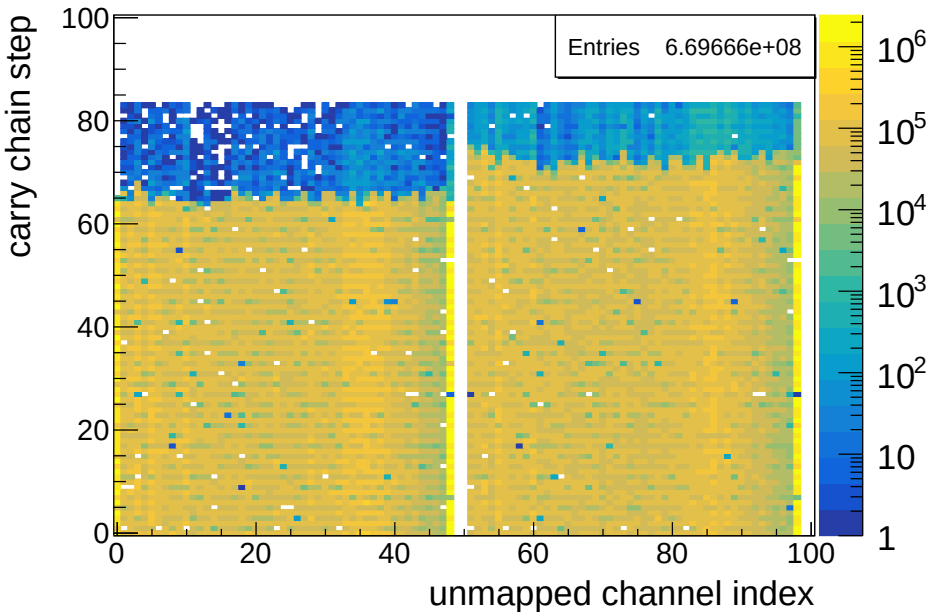

Figure 4.20: Raw data visualization of the carry chain step in which the leading edge was detected by the jTDC versus the channel number. The data shown are from the November 2014 test beam time. The first block of 48 channels shows the leading edges, the second block of 48 channels corresponds to the trailing edges for the signals, i.e. the jTDC logic was searching for a leading edge in the inverted pattern. The first 32 of each channel block are from the Barrel detector, the remaining 16 are from the outputs of the BGO attenuators. Zero hardware hysteresis was used.

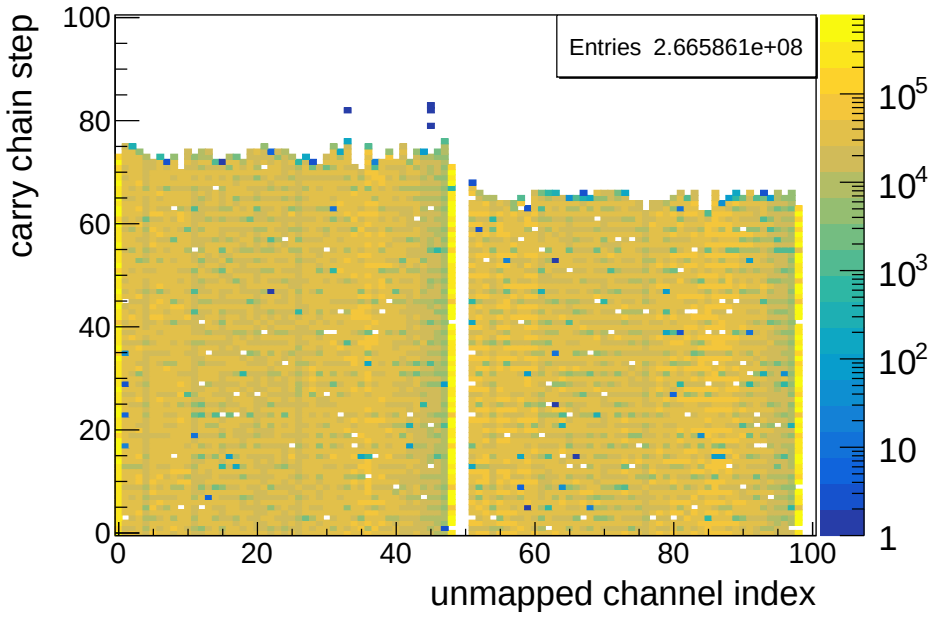

Figure 4.21: Raw data visualization of the carry chain step in which the leading edge was detected by the jTDC versus the channel number, similar to fig. 4.20. The data shown were again taken during the November 2014 test beam time, but after change of firmware and application of a hardware hysteresis of 5 mV to 10 mV for all the Barrel channels.

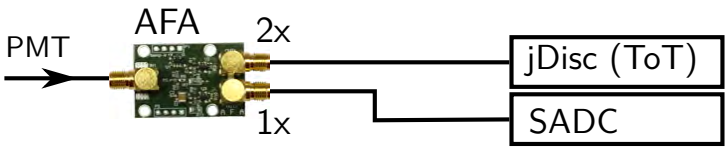

Figure 4.22: Comparison setup between jDisc and SADC. This setup is mainly useful to study non-linearities of the ToT information. It also allows to disentangle effects of additional noise and DC offsets which might be added by the AFA board.

(c.f. section 4.6.4). Additionally, the firmware was modified such that all signals are inverted before entering the carry chain. Using this technique, the role of '1' and '0' is exchanged, which allows to make use of the slightly higher resolution for the leading edges[10]. The dramatic result of this modification and the application of a small hysteresis can be seen in fig. 4.21.

However, this effect cannot be fully overcome, even though the problem is strongly reduced. The calibration procedure (as was described in section 3.3) takes this issue into account already, and such 'overshoots' which are found in the data are wrapped back into the previous clock cycle. Due to this approach, they become accessible to the time over threshold algorithm as if they had been detected normally, accepting a small loss in resolution for this small subset of hits.

Still, in rare cases it might occur that only one edge of the leading / trailing edge pair is found by the pattern detection logic in the FPGA due to the very same issue, since the firmware reconstructs leading edges from the carry chain pattern and finds the trailing edges by applying the same technique to the inverted pattern separately. The outlined algorithm also detects such 'extra edges' and allows for further cleaning of non-physical data using the described special cut on the minimum pulse length and by imposing an artificial dead time.

4.6.2 Time over Threshold as Measure of the Pulse Integral

The square of the time over threshold is in first approximation directly correlated to a pulse integral information as already outlined in section 4.6. The quality of this approximation still has to be determined, which can be done easiest by checking the correlated data recorded with the SADC, since this should provide the best pulse integral resolution of the available electronics.

The setup used for this study is shown in fig. 4.22. It allows to directly compare the measured pulse integral and ToT information from SADC and jDisc module, correlating the quantities for each single hit. An example plot for such a linearity study is shown in fig. 4.23.

As can be seen, the hits can be well correlated. The ToT extracted from the sampling ADC data matches the ToT measured by the jDisc very well. In rare cases, the ToT extracted from the SADC is slightly higher than that measured by the jDisc — this is likely since the ToT reconstruction, as described in section 4.6.1, is more sensitive to short threshold-crossings on

(10) The resolution is higher since for faster propagation time, more carry chain steps are used leading to a finer sampling granularity.

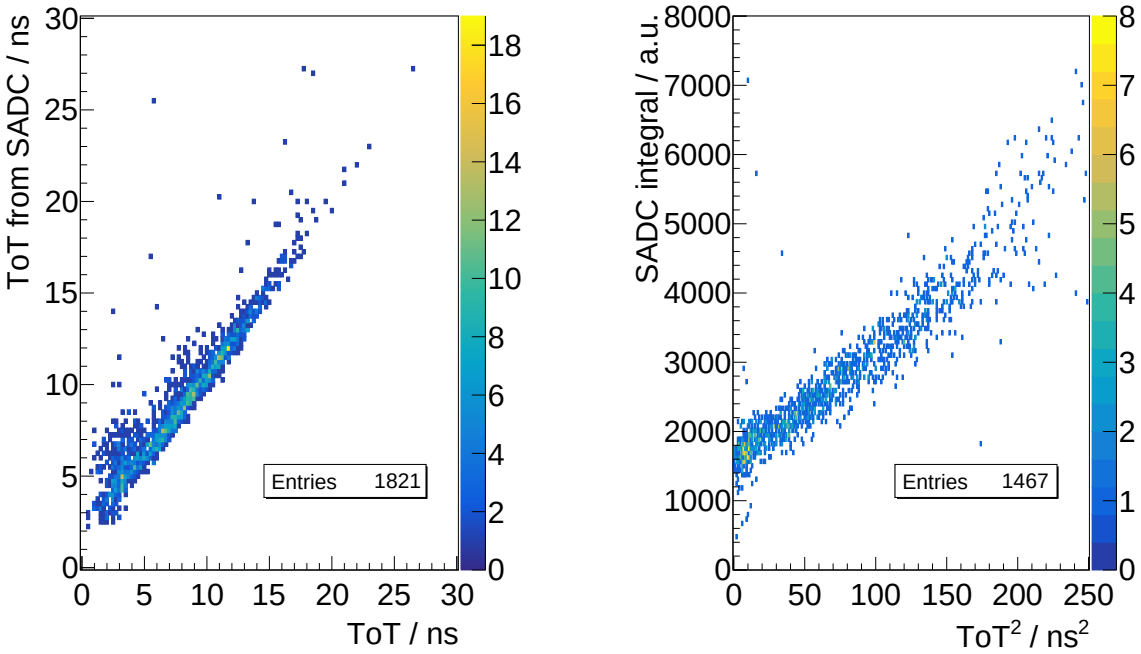

(a) Time over threshold extracted from the SADC reconstruction versus correlated time over threshold from the jDisc module.

(b) SADC integral versus correlated time over threshold squared from the jDisc module.

Figure 4.23: Comparison of the SADC 'ToT' and pulse integral information with the time over threshold measured by the jDisc module. The data between these two modules are correlated event by event. Figure 4.23a shows the time over threshold as measured with the SADC (c.f. appendix A.3) using a similar threshold as was set for the jDisc hardware. A nice agreement of the two measurements can be seen. A broad distribution is to be expected since the time resolutions, electronics terminations and especially the noise on the line are different (the active splitter has to be used to allow for parallel measurement).

the falling slope of the signal, which tends to produce smaller time over thresholds in cases of high frequent noise.

The relation between pulse integral and ToT^2 is also found to be astonishingly linear, albeit a difference in resolution between SADC and time over threshold can be made out. As will be described in section 4.8, the ToT is resolved sufficiently well to facilitate a time walk correction.

By now, the BGO-OD experiment is also using a ToT based readout for the central scintillator barrel. For this detector, the quality of the ToT information versus the usage of a conventional ADC has been tested, since the extracted $\mathrm{d}E/\mathrm{d}x$ information is crucial for this detector.

It was originally read out with a 'classical' QDC (CAEN V792) providing a high resolution on the analogue integral, but needing long cable input delays to delay all analogue signals until the trigger signal arrives, which in turn starts the integration time window. Furthermore, the classic QDC modules are not multi-hit capable. These long cables necessarily distort the signals and decrease the flexibility of the trigger configuration, which, apart from these modules, is fully configurable via dynamic delays in FPGAs.

The results from a test beam time in December 2014 for which both readouts were used in parallel are shown in fig. 4.24 and fig. 4.25.

The resolution of the energy spectrum seems to be very similar between the ToT^2 based readout and the classical ADC. This can be accounted to the long cable lengths which distort the signals and increase the accumulated noise which enters the charge integration done by the ADC. Since the resolution of the ToT^2 was even at a slight disadvantage due to the necessary signal splitting and overlong cabling which affects the time over threshold even more than the charge integral, it was decided to move to the jDisc based readout for the scintillator barrel.

Additionally, this study shows that the hysteresis helped to remove very short signals from the ToT^2 spectrum which could either be caused by the issues which will be outlined in section 4.6.4 or be caused by the sodium sources used for calibration which are placed in the BGO also during data-taking. Furthermore, the resolution of the $\mathrm{d}E/\mathrm{d}x$ information is mostly unaffected by the chosen moderate hysteresis setting.

4.6.3 Thresholds

The key property of the ToF system is the time resolution. For this reason, a minimization of the thresholds was attempted by scanning various threshold settings for all channels. To not superpose the two main tuning variables for the effective threshold, the high voltage setting and the electronics threshold, the employed procedure was to fix all discriminator thresholds to a common, low value first and then perform the gain matching (c.f. section 4.7.2). Only afterwards, the scanning of the electronics thresholds is performed. Due to the rate stability of the jTDC, the lowest possible setting with a small safety margin can be used to minimize time walk and maximize efficiency.

During data-taking, at each start of a run a baseline scan is performed by the DAQ by turning off any hysteresis and varying the threshold. This allows for a long-term baseline stability monitoring. It is found that the baseline is stable within a few millivolts for the ToF detectors

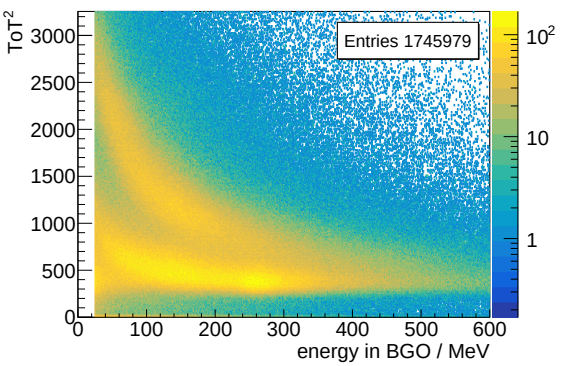

(a) ToT^2 measured in the Barrel vs. cluster energy in the BGO, no hysteresis

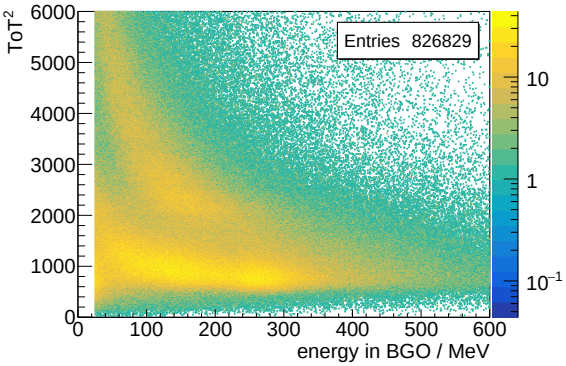

(b) ToT^2 measured in the Barrel vs. cluster energy in the BGO, hysteresis of 5 mV to 10 mV

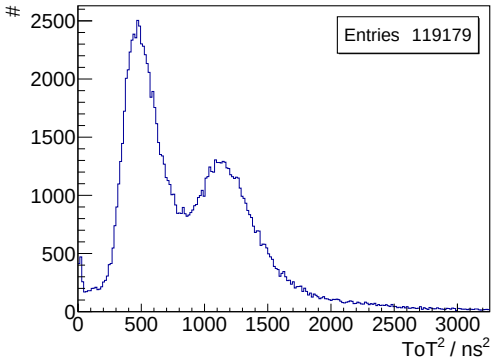

(c) Projection of fig. 4.24a for BGO cluster energies of 140 MeV to 160 MeV

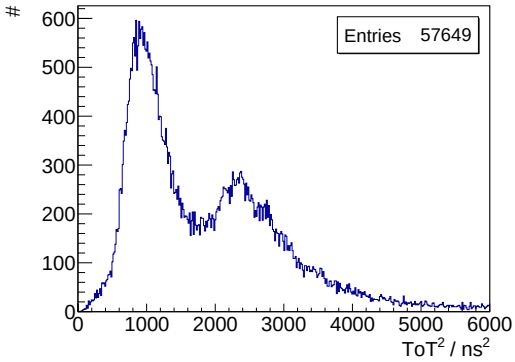

(d) Projection of fig. 4.24b for BGO cluster energies of 140 MeV to 160 MeV

Figure 4.24: The coloured 2D plots show the ToT^2 for signals recorded from the Barrel detector for one example channel (31) on the vertical axis, describing the $\mathrm{d}E/\mathrm{d}x$ in the scintillator bar, after time correlation with a corresponding BGO cluster whose energy is plotted on the horizontal axis. The loci of pions and protons can be easily separated. The effect of the hysteresis setting can be seen (very low ToT^2 are suppressed). Additionally, projections for a fixed BGO cluster energy range are provided to illustrate the achievable $\mathrm{d}E/\mathrm{d}x$ resolution. Data recorded with the jDisc module in the December 2014 test beam time.

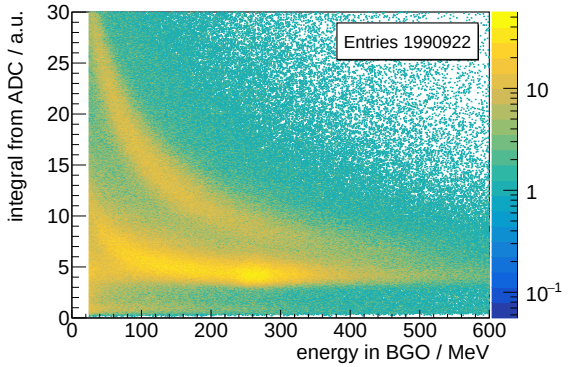

(a) ADC integral measured in the Barrel vs. cluster energy in the BGO, same dataset as shown in fig. 4.24a

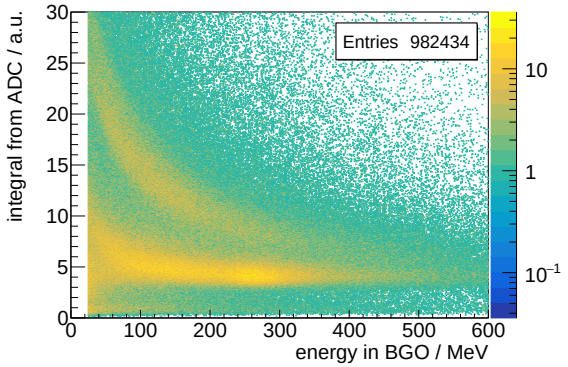

(b) ADC integral measured in the Barrel vs. cluster energy in the BGO, same dataset as shown in fig. 4.24b

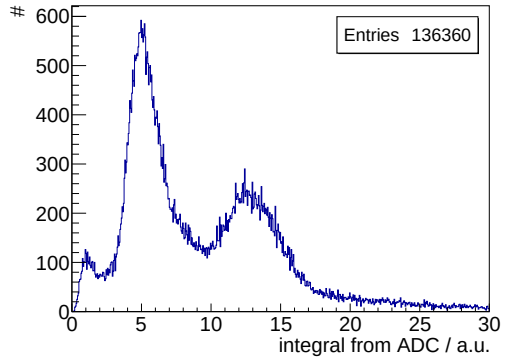

(c) Projection of fig. 4.25a for BGO cluster energies of 140 MeV to 160 MeV

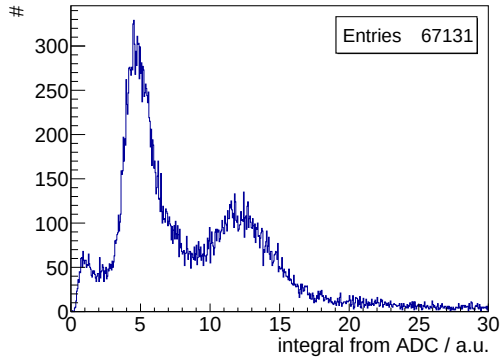

(d) Projection of fig. 4.25b for BGO cluster energies of 140 MeV to 160 MeV

Figure 4.25: The coloured 2D plots show the ADC integral for signals recorded for the Barrel detector for one example channel (31) on the vertical axis, describing the $^{dE}/_{dx}$ in the scintillator bar, after time correlation with a corresponding BGO cluster whose energy is plotted on the horizontal axis. The loci of pions and protons can be easily separated. Two datasets are shown matching those presented in fig. 4.24. Additionally, projections for a fixed BGO cluster energy range are provided to illustrate the achievable $^{dE}/_{dx}$ resolution. Data recorded with a CAEN V792 QDC module in the December 2014 test beam time.

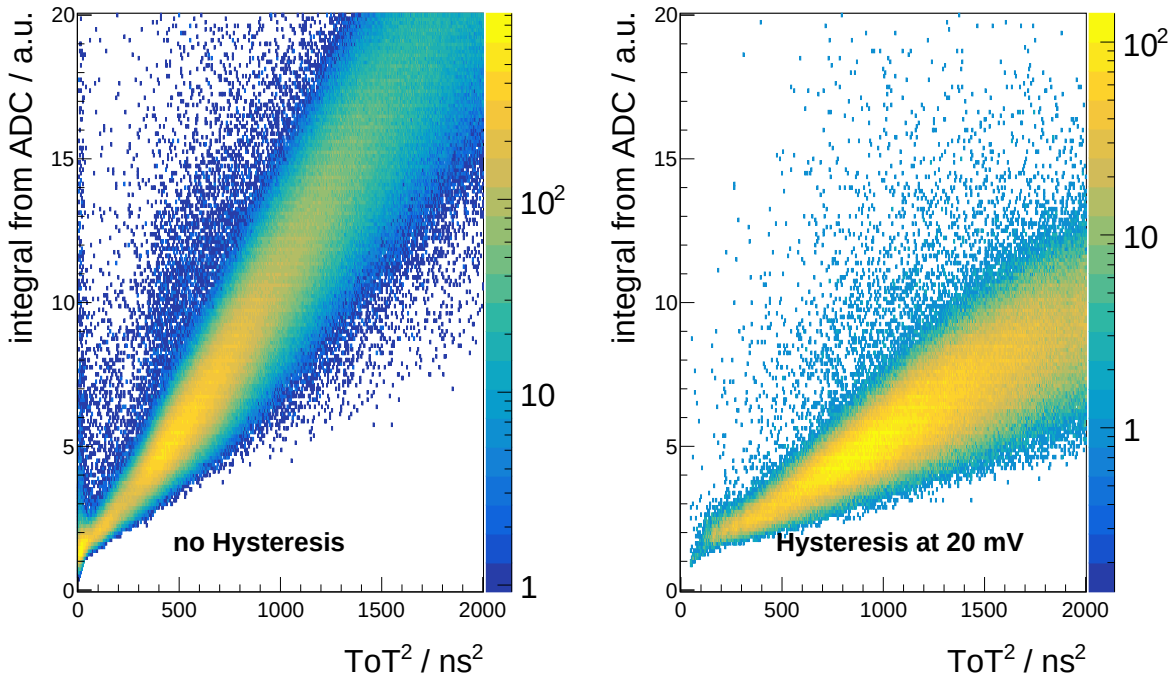

Figure 4.26: Visualization of the effects of hysteresis on the time over threshold information, correlating this information event by event with the pulse integral measured by a classical ADC. This data were taken during the November / December 2014 beamtime and is from the Barrel detector.

on this macroscopic timescale, so a low threshold setting of about 20 mV to 25 mV from the baseline is chosen. For even lower values a significant contribution from electronics noise and also high sensitivity to distortions on the trailing slope of the signals are seen. This is confirmed for example by the SADC data-taking as shown in fig. A.4: a threshold of 25 mV corresponds to approximately 200 ADC counts since the setup shown in fig. 4.22 was used for that data-taking. Additionally, the noise situation was also studied using the techniques described in section 4.11. Combined with a small hysteresis of 5 mV, most such distortions are suppressed without affecting the ToT to pulse integral relation significantly. This is studied in greater detail in the following section.

4.6.4 Hysteresis

As already outlined in section 4.6, the hysteresis shifts the two thresholds (the 'start' threshold and the 'stop' threshold) away from each other, which is helpful for suppression of noise, but may complicate the ToT to pulse integral relation and spoil the time resolution. In this section, a study of the effects of the hysteresis on the time over threshold behaviour is performed.

As already discussed in section 4.6.3, during the October / November 2014 beamtime, the barrel detector was cabled to both the QDC and a jDisc time over threshold discriminator board

to allow for parallel readout and direct comparison of the electronics. For this reason, it is also the ideal setup to study the effects of the hysteresis on the recorded data and especially on the linearity of the ToT information.

The pulse integral information recorded by the two electronics has been correlated event by event. Assuming the relation between ToT and pulse integral described in section 4.6, the square of the ToT has been plotted against the ADC value. The results for different hysteresis settings for the jDisc module are shown in fig. 4.26.

The different slopes which can be explained by the changed effective threshold can be clearly seen: if the hysteresis is increased and the threshold setting unchanged, the 'start threshold' is increased while the 'stop threshold' is decreased. For any real signal which follows the approximate shape shown in fig. 4.17 still crossing the increased 'start threshold', this means that the ToT will be increased and even more so the square of the ToT, since the rising slope is always steeper than the falling one.

Furthermore, the additional structure at small ToT squared has vanished. As can be seen in the 'no hysteresis' case, signals with an almost zero value for the ToT are found in time correlation with various high pulse integrals of the ADC. These should not occur, since the shortest real signals from the PMTs are at least several nanoseconds above threshold. Possible explanations for these signals might be:

- High-frequent noise caught with the long cables (approximately 14 m) from the PMTs to the readout electronics.
- Sensitivity to 'ripple' noise on top of the signals as shown in fig. 4.17. If the signal fluctuates close to the threshold, re-triggering may occur and an additional, unrealistically short signal is seen.

All these mostly vanish with the higher hysteresis setting, which effectively suppresses high-frequent noise. This issue has also been observed and studied independently in [GKR15] which also includes simulations confirming this effect.

Since for maximization of the time resolution, a low threshold and thus also low hysteresis setting is wanted, a small remaining contribution from this effect is still accepted. As already outlined in section 4.6.1, the time over threshold reconstruction algorithm can be tuned to further reduce this effect.

4.7 Gain Matching

A crucial ingredient for the operation of detectors with PMT readout is the gain-matching procedure.

Gain-matching in this context means the equalization of all detector channels to produce a signal of similar height or with a similar integral for the same physical interaction. In addition, care should be taken to both minimize the high voltage to increase the live time of the tubes and to choose a sufficient voltage setting to achieve a high efficiency.

The equalization of all channels is an important requirement also to optimize the time resolution of the full setup even more so if leading edge discriminators are used, since the signal height determines the steepness of the rising slope which defines the strength of time walk effects.

Detectors using scintillator bars feature a wide pulse height distribution caused by attenuation of the light along the bar (c.f. section 4.2.4) in addition to any effects from different energy deposits by the various incident particle types which may have very different speeds and masses.

This automatically means that time walk effects will be more pronounced and can only be taken care of later in software when an additional information on the pulse shape is available. For that reason, it is very desirable to reduce any gain-mismatch between the different detector channels to a minimum.

The gain matching procedure itself requires an information on the pulse height or integral for each identified analogue pulse. To simplify the procedure, it is often common practice, especially for calorimeters, to use radioactive sources with a known spectrum or to use a light pulsing system to inject a known, characterized light pulse mimicking the light created by a scintillation process. Such a system was also foreseen and used in the original setup of the GRAAL detectors, which is why all PMT mounts are equipped with both an LED and a fibre inlet for each single channel. Since the setup of a light pulsing system including a technique to create well characterized pulses would have been a time consuming process and absolute precision of the energy information is usually not necessary for a ToF detector, the gain matching at BGO-OD was performed in-situ using beam particles.

To extract the pulse integral information, classically, an ADC would be used. In this case, a sampling ADC (c.f. appendix A.3) is available, albeit it's not used for regular data-taking due to the sheer amount of produced raw data since no hardware feature-extraction is available. However, it features a high sampling rate (c.f. section 4.4.4) which allows to study even the shape of the signal. In addition, the time over threshold information from the jDisc module (c.f. section 4.4.6) can be interpreted as an information related to the integral of the signal (c.f. section 4.6). The expected resolution of this information is naturally worse, but it might be sufficient for the gain matching procedure. The main advantage is that this information will be available during regular data-taking which increases the available statistics and allows for a continuous, online gain monitoring.

Furthermore, the mean-timer trigger logic (c.f. appendix A.2) features single-channel scalers which allow to measure the rate of detected signals. In the assumption that this rate reaches a plateau when raising the high voltage setting as soon as all incident particles which produce light are above the effective threshold of the setup, this information could be used in the gain matching procedure.

In this thesis, all these possible approaches, the usage of the SADC integral distribution, the usage of the ToT distribution and the scaler rate plateauing were studied and tested to determine the most suitable technique for data-taking. The primarily used method based on the distributions of the pulse integrals is detailed in section 4.7.1. Further details on the SADC based method, which was also used previously for the existing ToF setup, are given in [Mei13].

In this work, the same technique will be applied successfully using the time over threshold information available with the jDisc module (c.f. section 4.4.6). The procedure will be described in detail in section 4.7.2. Finally, it will be found that the ToT information alone without corrections is sufficient for the gain matching procedure, which also allows for a continuous gain monitoring during data-taking.

As an addendum, the scaler-rate based technique is described in section 4.7.3.

4.7.1 Tuning via Landau Distribution

The energy loss of ionizing radiation in thin material is a statistical process which can be approximated by the Bethe-Bloch formula very well in the regime of $\beta\gamma$ between 0.1 and 100. Assuming that the scattering process occurs on quasi-free electrons and there are no other effects, the statistical distribution of the energy loss can be approximated by a Landau, or, more refined, a Vavilov distribution (c.f. [Wil96]).

These probability distributions for the energy loss follow a Gaussian-like shape peaking at the most probable value (MPV) for the energy loss, but are supplemented by a very long tail towards higher energies which takes the production of δ-electrons into account. The Landau distribution can thus be characterized by an 'MPV' parameter and a σ-like parameter characterizing the width of the distribution. The Vavilov-distribution is extended by an additional parameter and converges to the Landau distribution when the energy transferred in the single collisions is small, i.e. up to 1 % of the maximum transferable energy.

For the gain matching procedure, one can make use of this statistical distribution: it can qualitatively also be found back for the distribution of the pulse integrals of the signals which are produced by the PMTs, since they measure a fraction of the energy loss of incident particles via the produced light in the scintillator bar. One can thus use the 'MPV' of the measured distribution to equalize the response of all channels.

This light output is however already subject to several other effects which may distort the shape of the probability distribution:

1. Modification for response to incident particle type as compared to electrons, e.g. for protons impinging on commercial 'NE102A' plastic scintillator (c.f. [CAM79]):

$$E_{\text{electron equivalent}} = 0.95 * E_{\text{proton}} - 8.0 * \left(1 - \mathrm{e}^{\left(-0.1 \cdot \left(E_{\text{proton}}\right)^{0.9}\right)}\right)$$

2. Attenuation along the bar. The behaviour in general follows an exponential falloff with the length, more details will be given in section 4.2.4.

3. Light collection / light-guiding effects and quantum efficiency of the PMT (assumed to be constant factors independent of the energy).

4. Attenuation and non-linearities introduced by the measurement electronics.

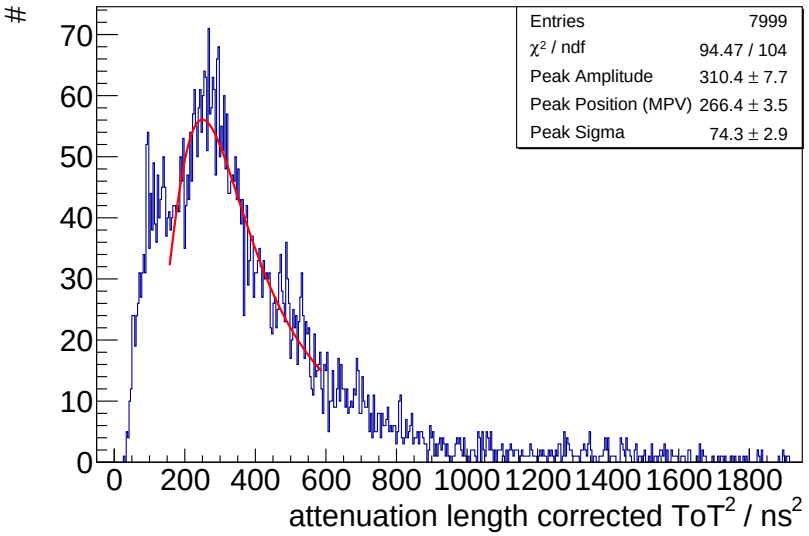

Figure 4.27: Example for an attenuation length corrected ToT^2 spectrum for a single ToF channel. Due to the attenuation length correction technique, this histogram is only filled if a cluster has been found (c.f. Section 4.9). A Landau distribution has been fitted. The data are from the June 2014 test beam time, run number 17568.

5. Mixture of different incident beam particles which even have a preferred direction due to the spectrometer magnet.

If only the 'MPV' is looked at for the gain-matching procedure, all effects which do not determine or depend on the intensity of the originally produced light are negligible. For this reason, we can neglect any 'damping' factors from the PMTs and the inefficiencies in light collection on first order. The attenuation effect along the bar and non-linearities introduced by the electronics may not be a negligible, however, since they impose an additional distribution which is folded with the Landau.

An example for such a distribution is shown in fig. 4.27. It has been made using the attenuation length corrected ToT^2. More details on this technique and the method finally used for the gain matching will be given in the following section.

4.7.2 Gain Matching via Time over Threshold Information

As shown in section 4.6, the linearity of the square of the time over threshold information versus the pulse integral appears to be good enough to extract a pulse integral information for gain matching. For that reason, the gain matching was attempted making use of this information in several possible ways which will be outlined as follows. Several possible techniques are investigated. All rely on the usage of the square of the time over threshold as 'pulse integral' information, following the idea of the triangular approximation described in section 4.6.

The first idea which comes to mind is to emulate the gain matching procedure which was previously done with the SADC. The approach is described as follows (more details in [Mei13]):

1. One run is taken for each high voltage setting, always changing the high voltage of all channels of one wall.
2. The distributions per channel are plotted for each run.
3. The Landau distributions are fitted and the 'MPV' is extracted for each channel and high voltage setting.
4. The fitted 'MPV' values versus the high voltage settings are plotted per channel.
5. Fitting an exponential to each 'MPV' vs. high voltage diagram and choosing a target 'MPV', the high voltage setting for each channel for a uniform gain can be extracted.

In the course of this thesis, the process has been partially automated: a tool based on the same implementation used for the calibration procedures outlined in in section 3.2 is used to fit the Landau distributions and still allow for manual tuning of each fit. As input data from the new electronics, a first approach would be to use the ToT^2 (interpreted as pulse integral) after attenuation length correction (c.f. section 4.2.4).

An example for recorded ToT^2 distributions for different high voltage settings is shown in fig. 4.28. After analysing the data with attenuation length correction applied, the Landau distributions were fitted for each single channel and high voltage value. An example result for one channel is shown in fig. 4.29. The expected exponential behaviour is observed and can be fitted. A common 'MPV' can be chosen for all channels to equalize their response. Care should be taken that no channel would be assigned a high voltage value higher than the tubes can stand.

Using the attenuation length corrected information, however, comes with a fundamental problem: this correction necessarily relies on knowledge about the impact point of the incident particle to determine the distance to the PMT. This can only be extracted by using the time of the signal created by the PMT, which is only useful if one has a reference time to compare it to. Since the time calibration is usually not yet performed and applied when the high voltage tuning is in progress, and additionally the time offsets change during the high voltage tuning since the pulse height distribution is strongly affected by it, the attenuation length correction is necessarily incorrect — it is even systematically wrong in a correlated manner to the observable which is tuned.

For this reason, the effect on the ToT distribution of the single channels should be investigated after this calibration. If these single channel ToT distributions would be used for gain matching directly, a biasing might be expected, since especially if the spectrometer magnet is on, the positively charged particles which are predominantly produced for hadronic events (due to the use of a proton target), may distort the pulse integral distribution towards one side of the bars.

The resulting distributions after the calibration done using the attenuation length corrected values are shown in fig. 4.30. As can be seen, also these distributions appear to be very well

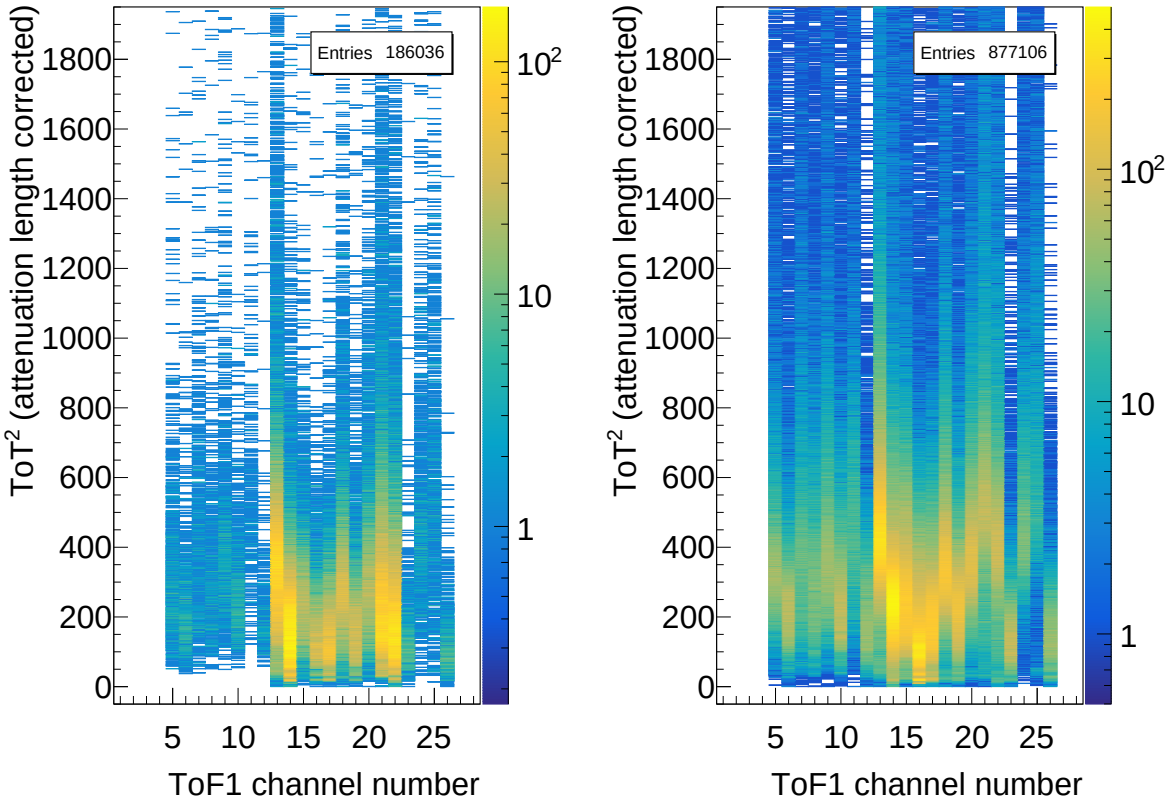

Figure 4.28: Example for the measured, attenuation length corrected ToT^2 distributions for the channels of ToF 1 from the first test beam time with the jDisc electronics. Not all channels were equipped yet. The high voltage was set to 1250 V for all channels for the left dataset while 1450 V were used during the data-taking whose results are displayed on the right. One can directly see that with the lower high voltage setting the gains are very different, also affecting the efficiency already on first glance. The position of the 'MPV' has moved to higher ToT^2 with the increase in high voltage setting. As explained in section 4.7.2, this information may be strongly affected by mismatches in the time calibration.

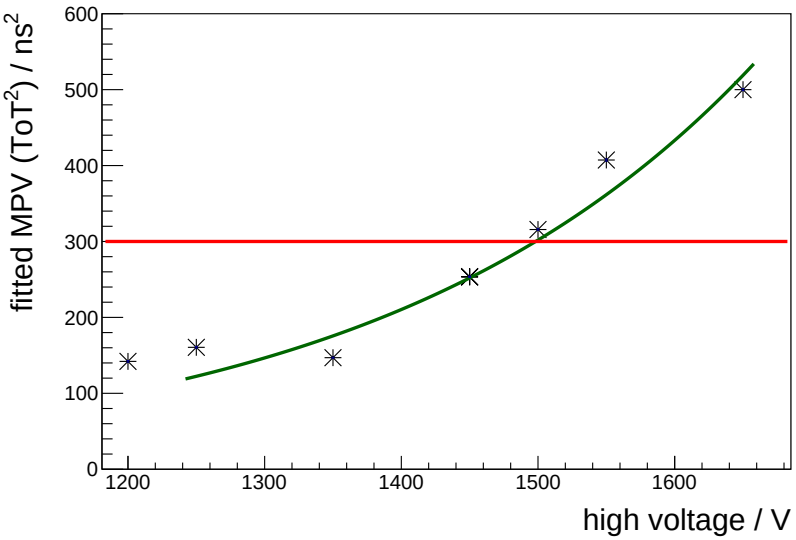

Figure 4.29: Behaviour of the fitted 'MPV' versus high voltage setting for one of the ToF1 channels during commissioning data-taking.
The expected exponential behaviour is observed and can be fitted if the attenuation length corrected ToT^2 is used. The fit is indicated by the green, solid line. Choosing a common 'MPV' for all channels as indicated by the red, solid line in this example, the high voltage setting can be extracted from this exponential fit.

aligned, so it seems that the described biasing can be neglected. This was also confirmed by first performing the alignment procedure with magnetic field off, and then re-checking it after the field was turned on. The fact that the bias is not really observed is likely caused by the predominance of e^+-e^--pairs and charged pions reaching the ToF walls.

For this reason, the alignment of the ToT distributions for the single channels is already considered sufficient for the gain matching procedure. These have the huge advantage that tuning is possible online during the setup phase of the experiment without the requirement of special conditions, also not yet needing any sophisticated calibration. As such, it can be performed in parallel to the tuning and gain matching procedures of other detectors and does not require a previous software time calibration beforehand.

An additional crosscheck can also be done by using the following relation for the pulse integrals (based on [Bla+92]):

$$x = \ln\left(\frac{(\mathrm{ToT}_1)^2}{(\mathrm{ToT}_2)^2}\right) \cdot l_{\mathrm{att}} \tag{4.1}$$

with x being the position of the incident particle hit along the bar, l_{att} being the attenuation length and ToT_1 and ToT_2 being the time over thresholds recorded by the two photomultipliers at the ends of the bars, respectively. This simple relation removes the exponential attenuation

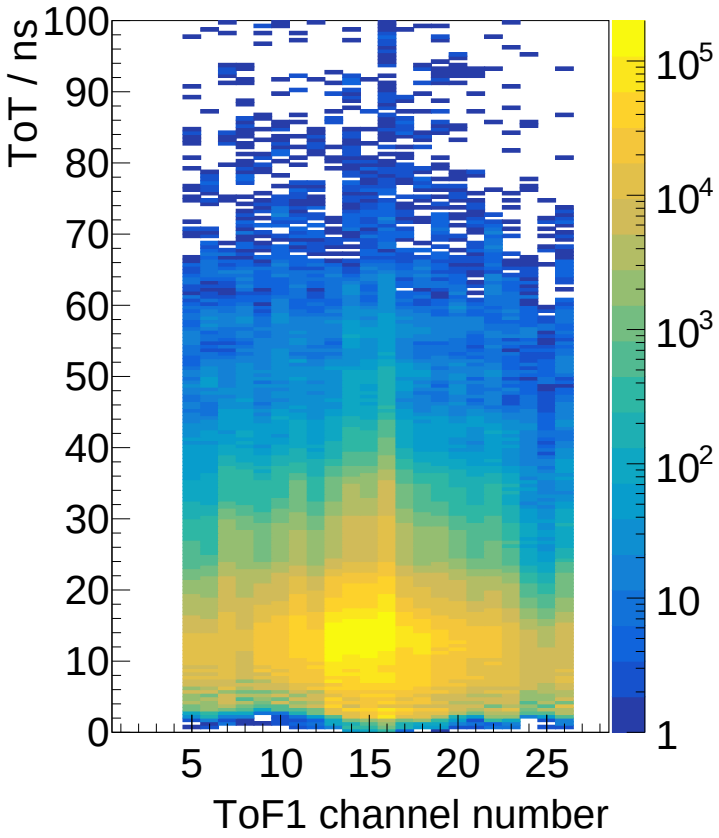

Figure 4.30: Distributions of the time over thresholds for the single channels of ToF 1 after gain matching without further corrections. This initial gain matching was done as described in section 4.7.2 using the attenuation length corrected ToT^2.

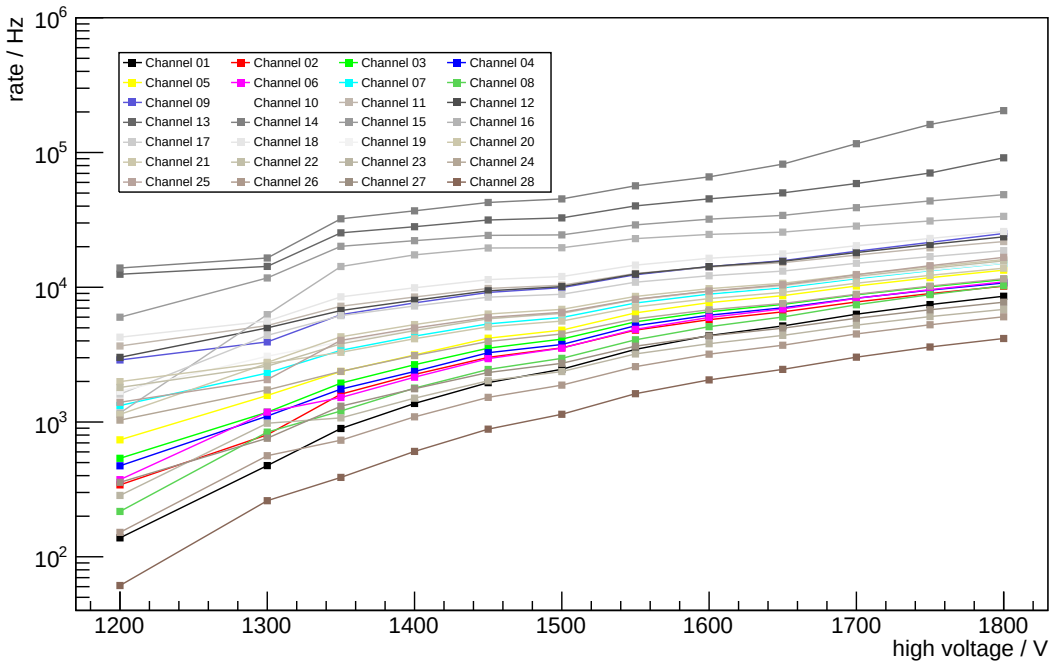

Figure 4.31: Behaviour of measured rate versus high voltage setting for mostly constant electronics threshold and beam intensity.

factor assuming it is a simple exponential component alone[11] and neglecting any remaining non-linearities on the ToT to pulse integral relation.

Additional, more sensitive checks of the gain stability are also available online after an initial time calibration on higher levels of analysis, as will be shown for example in fig. 4.39.

4.7.3 Scaler Rate Plateauing

The plateauing technique employs the idea that the scaler rate should saturate when lowering the effective threshold if the rate of incident particles is kept constant, since at some point a maximum rate of real signals should be detected, i.e. the maximum efficiency should be achieved.

As a first attempt, the electronics threshold was kept at the lowest value achievable for all channels with the old electronics (c.f. section 4.4.1) which corresponds to about 20 mV. The high voltage for all photomultiplier tubes for the ToF 1 wall was modified in steps of 50 V and after each change, a dataset was recorded. The incoming beam current and other experimental conditions were kept stable, as far as possible.

The results are visualized in fig. 4.31. As can be easily seen, no plateau is reached. As found during the cosmics test with the Philips 'XP2282/B' tubes, this is already not too far from the

(11) This is not fully true, as explained in section 4.2.4.

maximum high voltage the tubes can stand[12]. For this reason, it can be deduced that this technique is not really applicable. It seems that either the lowest electronics threshold is still too high, or a source of noise which can not be distinguished by the scalers is also enhanced with higher high voltage. This could even be correlated to the real signal (e.g. it could be a reflection or a second threshold crossing which is more probable with larger signals). The scalers can by design not provide further insight into this analogue part of the information.

4.8 Time Resolution and Timewalk Compensation

The crucial property of the ToF detector is the time resolution. To remove any external effects on the determination of this characteristic quantity with the installed detector, one can make use of the fact that the plastic scintillator bars of the first and the second wall of the combined GRAAL ToF wall system have a geometric overlap. However, care has to be taken if beam particles are used, since then the full length of the bars may be hit. This will create a wide time distribution since the incident points of the particles vary and the light has to travel along the bar.

To remove the effect of the speed of light in the material, the mean times of the two PMTs attached to each bar are used[13]:

$$t_{\mathrm{mean,A}} = \frac{(t_{\mathrm{A1}} - t_0) + (t_{\mathrm{A2}} - t_0)}{2}$$
$$t_{\mathrm{mean,B}} = \frac{(t_{\mathrm{B1}} - t_0) + (t_{\mathrm{B2}} - t_0)}{2}$$

The reference time component t_0 can be removed by taking the time difference between the mean times of the overlapping bars:

$$\begin{aligned}\delta t_{\mathrm{mean}} &= t_{\mathrm{mean,A}} - t_{\mathrm{mean,B}} \\ &= \frac{t_{\mathrm{A1}} + t_{\mathrm{A2}}}{2} - \frac{t_{\mathrm{B1}} + t_{\mathrm{B2}}}{2}\end{aligned}$$

In the assumption that the time resolutions of all single channels and thus the two mean times are equal, the error on this mean time difference distribution can be determined as:

$$\begin{aligned}\Delta\left(\delta t_{\mathrm{mean}}\right) &= \sqrt{\left(\Delta t_{\mathrm{mean,A}}\right)^2 + \left(\Delta t_{\mathrm{mean,B}}\right)^2} \\ &\approx \sqrt{2} \cdot \left(\Delta t_{\mathrm{mean\ time}}\right)\end{aligned}$$

(12) The manufacturer states 2500 V are possible [Pho07], but a custom base and voltage divider developed at the IPN Orsay has been used. Further details on the properties of the tubes are also available in [BBS00].

(13) In the following formulae, δ is used to indicate a time *difference* while capital Δ indicates a *Gaussian error*.

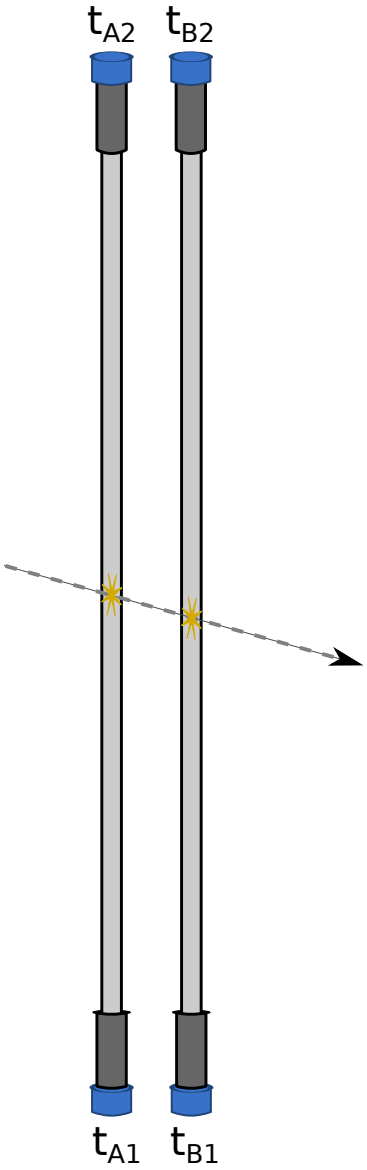

Figure 4.32: Illustration of the method used to extract the inherent time resolution of the ToF detector without involving external time references (e.g. the trigger time / start time). Assuming similar time resolutions for all four involved channels, the width of the mean time difference distribution which is free of any reference times can be used.

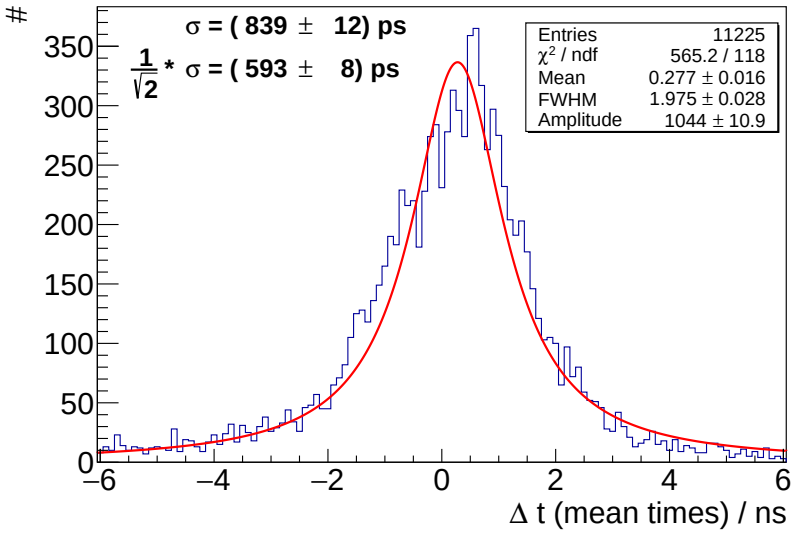

Figure 4.33: Mean time difference distribution of all mean times for the bars numbered '7' of the ToF1 and ToF2 walls. These bars are the ones directly above the beam axis (c.f. fig. 4.8). A Breit-Wigner distribution has been fitted and from the width a tentative time resolution of 593 ps ± 8 ps can be extracted. The data have been taken during the commissioning beam time in June 2014.

The error on a single mean time can thus be estimated as:

$$\Rightarrow \Delta t_{\text{mean time}} \approx \frac{1}{\sqrt{2}} \cdot \Delta\left(\delta t_{\text{mean}}\right)$$

This mean time is the interesting quantity for the physics analysis, since it is used to extract the time of flight of the detected particle, so $\Delta t_{\text{mean time}}$ is the determining time resolution of the detector. Using this approach, the time resolution of the system of scintillators, PMTs and electronics can be extracted independently from the remaining experimental setup.

The first result is displayed in fig. 4.33. As can be seen, only a poor time resolution of 593 ps ± 8 ps is achieved.

As explained previously, the 'jDisc' module basically is a simple leading edge discriminator. The signals produced by the ToF detectors naturally cause a wide pulse height distribution mainly by the effects of the attenuation length along the bar. A wide distribution of pulse heights means a variety of possible slopes for the rising part of the signals, which translates to a significant time walk effect even for low discriminator thresholds. Since the attenuation effect is exponential with regard to the distance the light has to travel along the bar, this effect does not cancel out in the meantime calculation.

To confirm the assumption that the time resolution is spoiled by time walk effects, the same data were analysed investigating the measured time difference between the single channels of one side of the two overlapping bars. This time difference is plotted versus the time over threshold

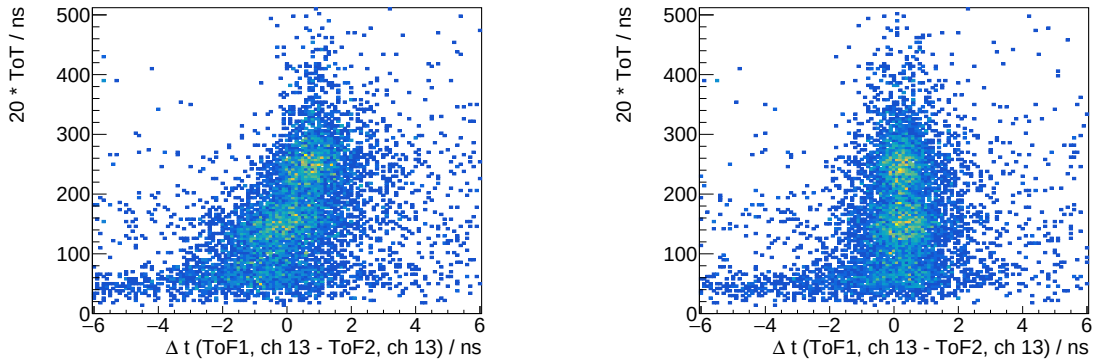

(a) Time walk before any correction

(b) Time walk after the correction described in section 4.8

Figure 4.34: Visualization of the time walk effect. Using the setup shown in fig. 4.32 which was also used for the extraction of the time resolution, the time difference between the leading edges of signals detected on one side of the setup is plotted. The vertical axis shows the corresponding time over threshold for the signal from the more upstream bar. The ToT has been scaled up to better visualize the time walk effect, which is strongly visible due to the dependence on the signal height and thus the time over threshold.

which is in turn related to the pulse height and thus should be related to the expected strength of the time walk effect.

The result is shown in fig. 4.34a. The time walk effect clearly stands out, which in turn also means that a correction can be applied without additional external information, since for this histogram, data recorded by the jDisc module has been used exclusively.

However, the actual correction itself will still be determined from a dataset of correlated sampling ADC and jDisc events for two reasons:

1. Using jDisc data alone for the correction might bias the correction if there is an unknown inherent correlation between the recorded quantities.

2. The sampling ADC offers much better pulse integral resolution and also allows to study both additional non-linearities and pulse shape stability for different amplitudes.

The correction is done based on the assumption that the time walk is dominated by the slope of the pulse and the threshold of the discriminator. Using the correlated dataset, a relation between the slope as fitted in the SADC feature extraction procedure (c.f. appendix A.3) and the time over threshold as measured by the jDisc module is extracted.

To do so, all correlated data points are binned by time over threshold and the mean and standard deviation are plotted for each bin. The resulting profile plot is shown in fig. 4.35. A polynomial of second order fits to the data points quite well. Applying this relation, the expected slope can be calculated for each hit from the time over threshold information. Using the set threshold value for the jDisc discriminator in millivolts and the known conversion of

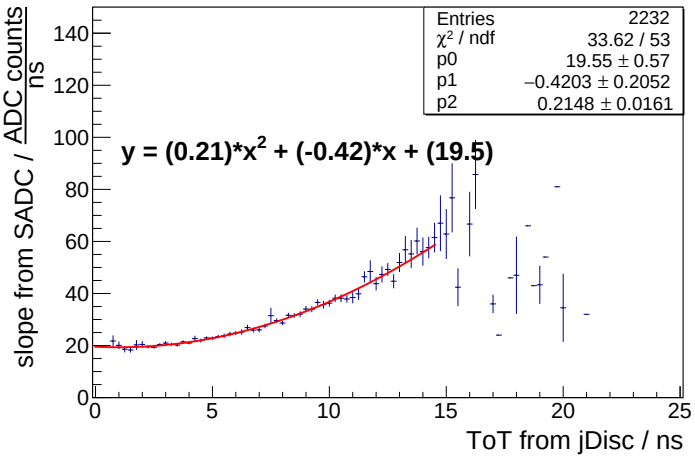

Figure 4.35: Correlating the time over threshold data from the jDisc module with the fitted signal slope from the sampling ADC reconstruction, a 'time over threshold to slope' relation can be extracted. The plotted data are from a single run for channel 13, bar 7, of the ToF 1 wall. The plot is binned by time over threshold, the points show the mean and standard deviation of the distributions which entered each bin.

SADC counts to millivolts, the calculated slope can be extrapolated to the baseline as visualized in fig. 4.36.

As shown, a time offset corresponding to the expected time walk can be extracted[14]. With this offset applied, fig. 4.34a is changed to fig. 4.34b using the same input dataset.

Using this correction technique for all channels of the ToF detector setup, the time resolution extraction can be re-performed. The result is shown in fig. 4.37 for which the same input dataset was used. Notably, a Gaussian fit now describes the data very well, and the width of the distribution is strongly reduced.

4.9 Clustering

In reconstruction terms, the information corresponding to one signal recorded by a readout electronics channel is stored in a so-called 'hit'. This combines all available types of information, e.g. time and energy, and may thus may contain the combination of information from several electronics modules. The association of two single 'hits' to a pair or set of hits is termed a 'cluster', which in the case of the ToF walls is the information related to the two readout channels belonging to one scintillator bar. For this reason, in terms of reconstruction, the mean time is an information belonging to a 'cluster'. The process of associating the two hits to one cluster is termed clustering and for the ToF walls will be outlined in this chapter, while a complete overview of the analysis framework and the processing stages will be given in chapter 5. For the

(14) This neglects any non-linear part of the rising slope or fluctuations of the baseline.

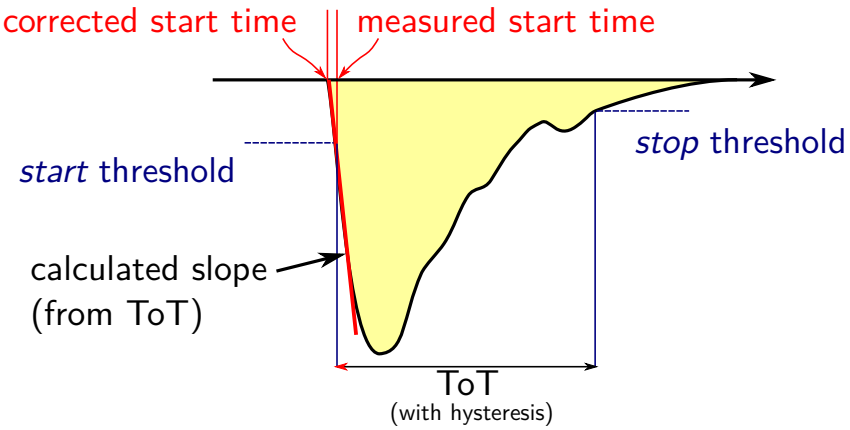

Figure 4.36: Schematic drawing to illustrate the time walk correction via the signal slope. The slope is calculated from the measured ToT using the determined 'time over threshold to slope' relation. Using the known 'start' threshold, which is slightly higher than the set threshold due to the hysteresis, a linear extrapolation to the baseline can be made which yields a corrected signal start time.

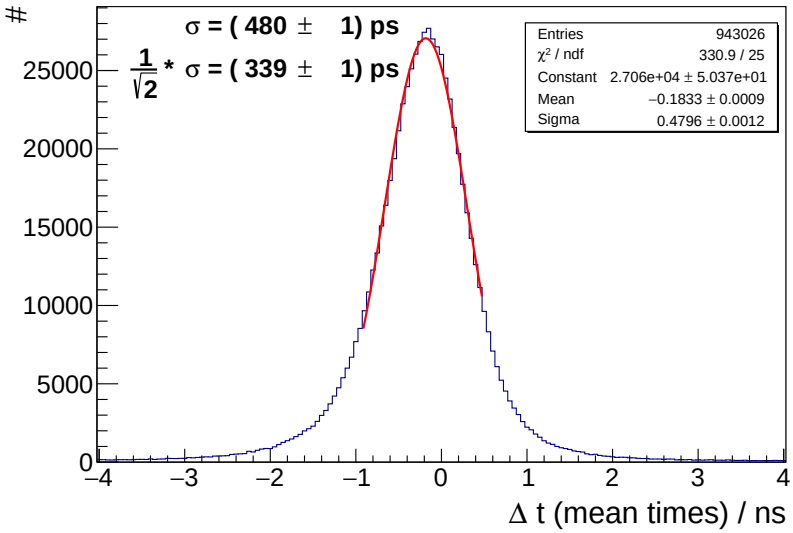

Figure 4.37: Mean time difference distribution of all mean times for the bars number '7' of the ToF1 and ToF2 walls after the ToT-based time walk correction technique has been applied. A Gaussian distribution can be fitted and from the width a time resolution of 339 ps ± 1 ps can be extracted.

online extraction of the mean time for trigger purposes, the corresponding hardware procedure is outlined in appendix A.2.

As described previously, the mean time is the main information provided by the ToF detectors for the physics analysis, since it allows to extract the β information. The cluster reconstruction can make use of the full time resolution including time walk corrections and additional information provided by the time over threshold to associate the signals produced by the two photomultiplier tubes at the end of the bars.

The general procedure can be outlined as follows:

1. Take one hit.
2. Iterate over all other hits.
   - a. Check if the index of the other hit was 'adjacent', i.e. for ToF matches the corresponding other end of the bar.
   - b. Check if time correlation is fulfilled. For ToF, a coarse cut of 20 ns is used.
   - c. If both conditions are fulfilled, construct a cluster and apply cluster-level calibrations.

There are several additional, ToF-specific details added to this clustering procedure to perform a basic cleaning of the data, which will be described in the following.

The very first cut which is used is the requirement of a time over threshold information for each hit. As explained in section 4.6.1, unpaired leading edges without associated ToT information are still kept as potential hits. However, these are usually caused by unwanted effects like a re-triggering of the system. For the ToF detectors for which all real signals produced by the photomultipliers are long enough to be detected with the jTDC, the time over threshold information is thus required for hits to enter the clustering stage.

The next step makes use of this information. As already mentioned in section 4.7.2, there are two techniques to calculate the position of the incident particle along the bar: the time difference, which is available with high resolution, and the ratio of the energy deposits, which can be used as a position information even without a time offset calibration due to the known attenuation effects.

The position from the energy information is much less resolved especially since it is provided by the ToT^2 and not a real pulse integral, but it can still be used to place a loose cut on the two sources of information to agree. As can be seen in fig. 4.38, the position information from the two different sources agree, but apparently the relation is not fully linear as can be seen from the 'spiralling' arms of the distribution towards the ends of the scintillator bars.

This is especially true for the ToF1 wall, which also shows a large number of hits outside of the selected band. This can be accounted to the closeness of the ToF1 inner bars to the beam (c.f. fig. 4.8) and the stronger contribution by the direct light close to the ends of the bar for geometric reasons. ToF3, on the other hand, is farther away from the beam and 'shielded' by

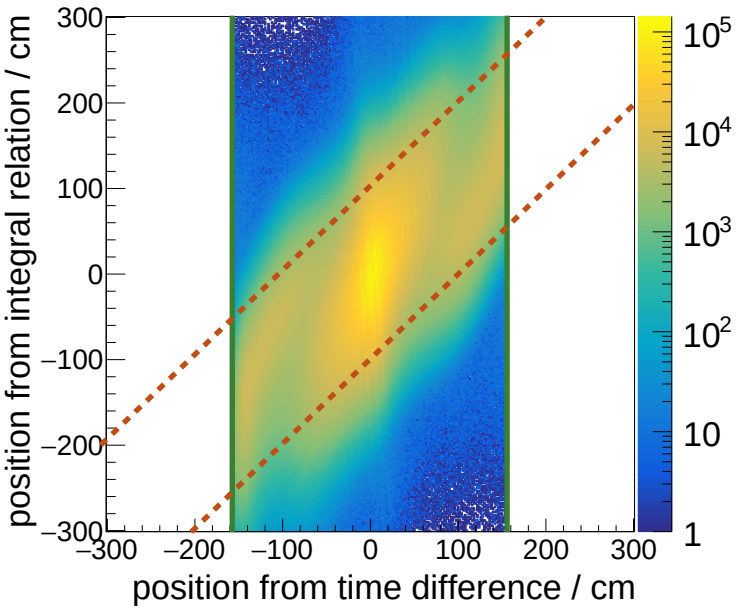

(a) Position correlation for ToF1.

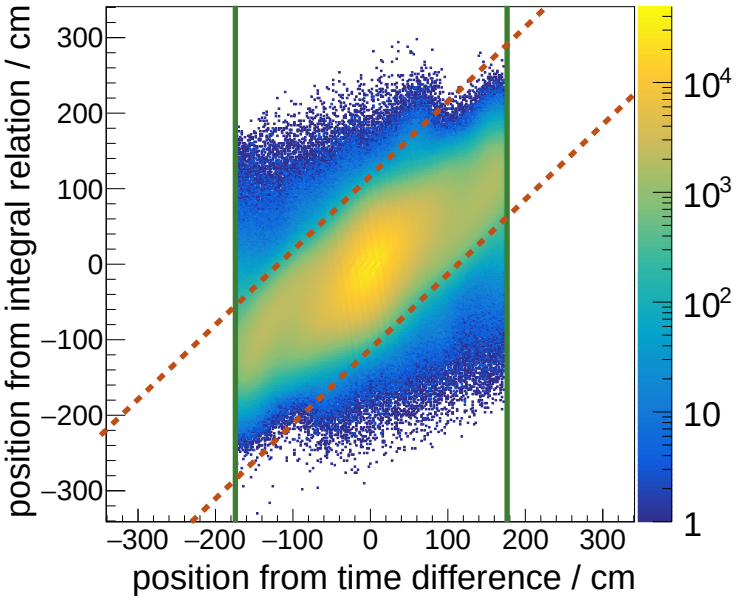

(b) Position correlation for ToF3.

Figure 4.38: Position from pulse integral relation versus position from time difference, extracted from the June/July 2015 dataset. The position from the pulse integral is calculated according to eq. (4.1) using the ToT information, while the position from the time difference uses the time walk corrected leading edge times and the effective speed of light in the bar. A cut on the time difference to constrain the possible clusters within the bar is already applied as is indicated by the green, solid lines. An additional cut on the red, dashed lines enforces a loose agreement between the two position values.

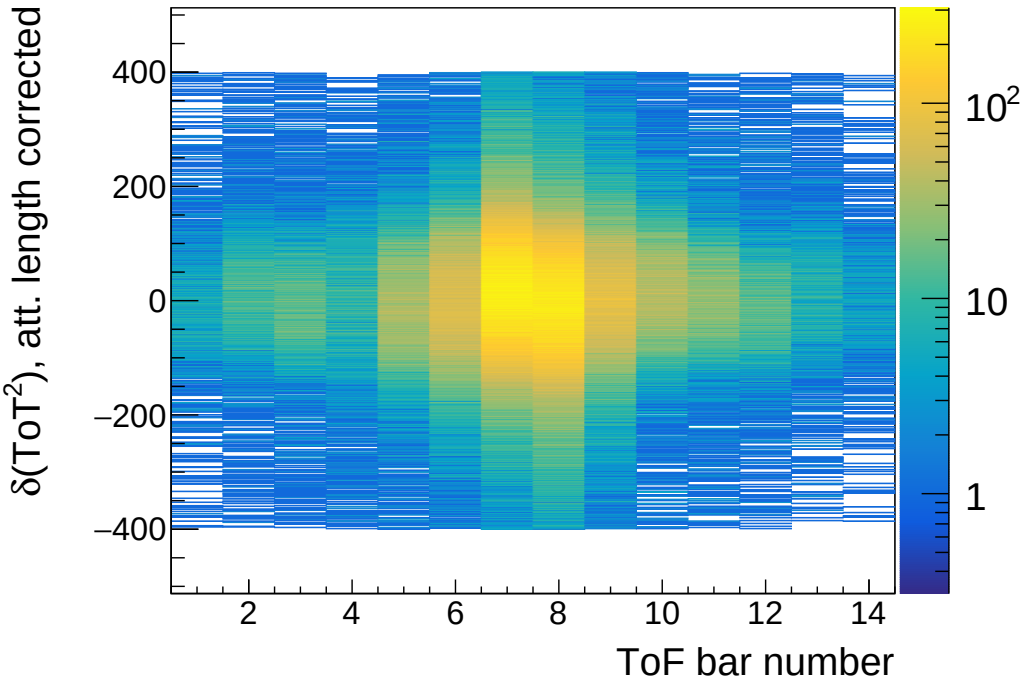

Figure 4.39: Difference distribution of the attenuation-length corrected ToT^2 values for each ToF bar of ToF1. The data used are from a single run of the October / November 2015 data-taking (run number 31213) after gain matching of the detector. A lose cut at a value of $\left|400\,\mathrm{ns}^2\right|$ of the ToT^2 can be seen, which corresponds to approximately 5σ of a Gaussian fit to the measured distribution.

the ToF1 and ToF2 walls, so most of the low energetic, close to the beam particles like electron and positron pairs which spoil the clustering algorithm have already been stopped in the walls in front.

For this reason, it can be assumed that the hits outside the selected region are caused by accidental coincidences and low energetic background, while the nonlinear shapes within the selected region more likely correspond to real signal events.

As next step, the attenuation-length corrected energy deposits are calculated separately for the two hits, using the position calculated from the time difference. A loose cut is then placed on the two corrected energies to agree with each other. This difference and the applied cut are plotted in fig. 4.39. It is very sensitive to the quality of the gain matching, which is why it can additionally be used as a final cross check for gain stability if all time calibrations are already done.

Finally, the calculated values for the single hits are combined to the cluster information. For this, the mean time and mean corrected energy information are calculated and the errors on these quantities as measured by the single channels are Gaussian propagated to combined errors of the cluster. Naturally, the position information from the time difference is used due to the

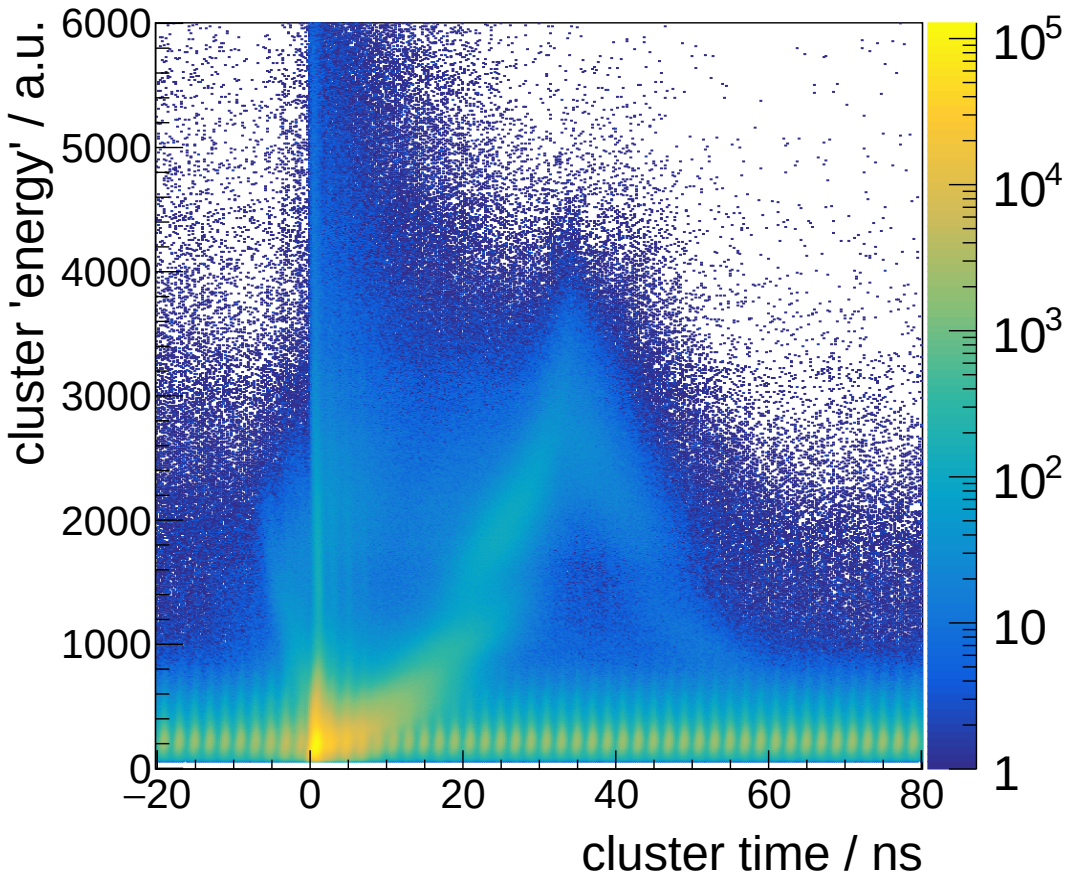

Figure 4.40: Information from reconstructed clusters of ToF1. The histogram shows the cluster 'energy', which is calculated from the mean of the attenuation length corrected ToT^2 values, versus the time of the cluster, which is the mean time of the hits after time walk correction. A t_0 calibration has been applied. The data are from the full October/November 2015 dataset, selecting events with trigger on BGO and Tagger.

higher resolution.

As a very last step, high-level calibrations on the position along the bar and time of the cluster are applied, if available. These are extracted from a full reconstruction combining the forward tracking with the information reconstructed with the ToF walls.

A distribution displaying the two defining quantities of the reconstructed clusters is shown in fig. 4.40. The effect of the t_0 calibration (c.f. section 3.5) can be clearly seen: relativistic particles related to the experimental trigger are pulled to 0 ns.

Offside this prompt time, the bunch structure of the accelerator can be seen, especially for low energy deposits, which again match with relativistic electrons reaching the detector. Since this cluster time convolves the time resolutions of the ToF detector and the start time detector, it can already be concluded that the convolution of both resolutions is sufficient to resolve the

2 ns bunch structure, albeit not fully disentangle the bunches.

Additionally, two distinct shapes can be made out:

1. A 'banana'-shaped structure before the prompt peak. This can be explained e.g. by e^+-e^--pairs both reaching a bar and being detected, thus creating a false mean time which actually is not from a single incident particle, but created by two differently charged particles. Such clusters can easily be neglected in later analysis and are also suppressed in the β reconstruction procedure as will be shown in section 4.10.

2. The strongest visual feature is the shape after the prompt region. This is created by protons which are stopped within the ToF wall for the region between 35 ns and 60 ns and punch-through protons depositing their $^{dE}/_{dx}$ for the region before 35 ns.

This structure matches well with results obtained in simulation and from a Bethe-Bloch calculation with protons. Furthermore, a non-linearity in the time over threshold can be seen slightly disrupting this structure.

The events with trigger conditions including forward detectors such as SciFi2 or even ToF have not been used for this histogram, since they contain a relatively prominent contribution from e^+-e^--pairs spoiling the visible shape. The same analysis for the June/July 2015 dataset does not yield any visible bunch structure. This is caused by a much worse start time resolution of approximately 700 ps, and underlines the importance of the interplay of both resolutions and the necessary focus on the quality of the start time determination for the resolution of the reconstructed time of flight. An in-depth explanation of the reconstruction of the start time has been provided in section 3.5, while more details on the interplay of the time resolutions combining the several ToF walls will be provided in the next section.

For completeness, it should be noted that apart from the general time calibrations described in chapter 3 and detector-specific energy calibrations which are done for each single channel, there are some high-level calibrations in use which apply to reconstructed information usually involving more than the information from one channel. For the ToF walls, there are two quantities which can be refined on the cluster level: the position along the bar and the time of the cluster.

Both these were fitted using higher level reconstruction, i.e. the tracking through the magnetic field is performed, and the difference in position from the extrapolated track and a time difference to the expected arrival time for relativistic particles are determined. The calibration constants yield corrections for ToF1 on the order of 5 cm and 0.3 ns, respectively, which matches about the expected resolution of the detector.

Consequently, these high level calibrations mainly correct for small variations of the mean time and position per bar, which may still remain due to the single channel time calibration procedure and due to the precision of the horizontal alignment of the full detector setup.

Since these calibrations mainly depend on the performance of the track finding and tracking procedure which are not part of this thesis and still under optimization, they are not presented in more detail here.

4.10 Reconstruction of β Information

The next step in the software reconstruction relevant for the ToF detectors is the reconstruction of a forward track through the magnetic field using information from the fibre tracking detectors, the drift chambers and also taking energy loss in the material into account. Using the known resolutions on position along the bar and the geometry, these tracks are then associated to clusters in the ToF walls[(15)]. More details on the tracking algorithms will be provided within the framework description in section 5.2.3.

After all candidate clusters of all ToF walls are associated to a track, an additional cleanup of these clusters is performed before the β is calculated:

1. All ToF clusters are ordered *descending* in time.
2. For each ToF cluster, a comparison with all other clusters is performed:
   - **a** The expected Gaussian error on the time difference is calculated:
     $\Delta(\delta t) = \sqrt{(\Delta t_{\text{cluster}})^2 + (\Delta t_{\text{other cluster}})^2}$
   - **b** If the time difference between the two clusters is smaller than 5σ of this error, the original cluster is kept.
   - **c** If the time difference is larger and more than one cluster is left, the original cluster is removed.

Using this technique, all 'late' clusters without matching partner are discarded. This easily suppresses remaining artefacts which could not be discarded by the clustering algorithm. An example for this are 'reflections' observed approximately 20 ns after a real cluster which could for example be caused by a real light reflection at the end of the bars, which creates an additional cluster with such a time delay within the same bar if the former incident hit was mostly central. Another explanation could be after-pulses created by luminous reactions, i.e. light emitted by electrodes due to electron bombardment. The typical timescale for this effect is between 20 ns and 100 ns as described in [Pho07]. Furthermore, false clusters created by e^+-e^--pairs (c.f. section 4.9) are strongly suppressed by this algorithm.

The β itself is then calculated using the following relations for each cluster separately:

$$t = t_{\text{cluster}} + t_0$$
$$v = \frac{l_{\text{track}}}{t}$$
$$\beta = \frac{v}{c}$$

(15) An additional tracking technique starting from the ToF clusters and detectors in front of the spectrometer magnet, only then adding the drift chamber clusters, is also available. In that case, the ToF clusters from the several walls are associated first with much more loose position correlation cuts and also applying a time difference cut.

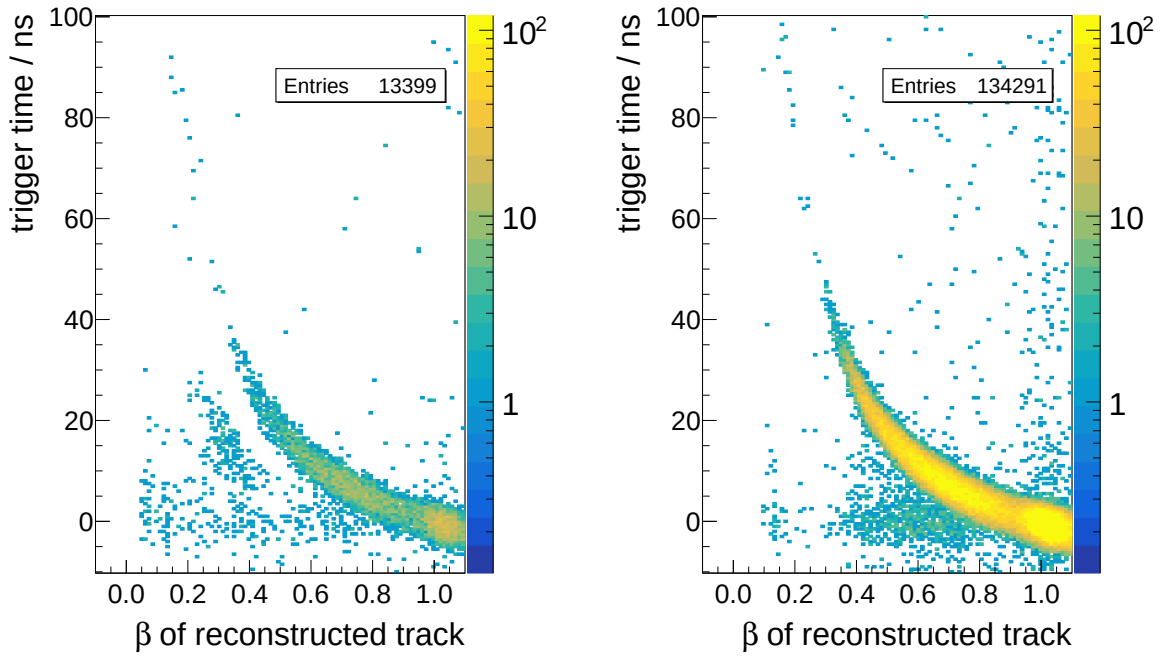

(a) Trigger time versus β before the changes to the β reconstruction.

(b) Trigger time versus β after the described changes.

Figure 4.41: Trigger time of the mean timer trigger from one of the ToF walls versus the β of the reconstructed track. Different input datasets have been used which explains the difference in statistics.

with t_0 being the time of flight expected for a straight track with speed of light and l_{track} being the length of the complete curved track from target to the corresponding ToF wall. The t_0 needs to be added back here, since any real time of flight offset for relativistic particles is removed by the t_0 calibration (as described in section 3.5). Only afterwards, the β for the complete track is calculated. For this, the error-weighted mean of all the β values of the clusters is used. This also highlights the importance of the cleanup algorithm: any clusters which are outliers in time would not produce a sharp line in any β versus momentum plot, but would spoil it in a 'smoothed' way, thus also spoiling any mass calculation from momentum and time of flight.

A visualization of the effect from the cleanup procedure can be easily seen in fig. 4.41. The shown plots are from before and after the implementation of the 'cleanup' technique and display the time of the mean timer trigger signal versus the β of the reconstructed track. Different datasets have been used, so only a qualitative comparison is possible, which is accommodated for by fixing the range of the colour palettes to the same maximum.

As can be seen, the trigger time and the reconstructed β can be correlated rather well, especially taking into account the limited 5 ns resolution of the trigger versus the high complexity of the full track reconstruction. Most uncorrelated entries are at almost zero trigger time, which is expected 'background' e.g. from electrons which may still cause a ToF trigger signal but

will usually not be found by the tracking algorithm which requires hits in the other tracking detectors.

The difference between these two plots is the shifted 'banana' structure visible at $\beta \approx 0.35$ for 15 ns to 20 ns of trigger time. This could be traced back to the described issue of clusters caused by additional reflections about 20 ns after an initial cluster. These are already suppressed in the trigger time spectrum due to the deliberate dead time of 35 ns (c.f. appendix A.2) on all clipped input signals, but are only removed from the track reconstruction by the described technique.

4.11 Additional Time over Threshold Functionality

In addition to the described advantages of the time over threshold based readout, the recorded information can also be used to study effects like dead time, time walk, reflections or correlated signal artefacts in a statistical manner by investigating correlated information. Such information is usually only available using a sampling ADC or an oscilloscope capable of event recording, but with the time over threshold readout can be accessed without additional effort for the full dataset since both the *time* and *time over threshold* is available for each single signal.

It should be noted for all these examples, that the histograms are the result of a statistical analysis, which is why also small effects which do not affect most signals but only a very small subset will be very pronounced. Additionally, all presented information is recorded during standard data-taking.

An example for this is shown in fig. 4.42. Several structures can be identified:

linear correlation The linear correlation between ToT and δt is caused by a re-triggering of the system shortly after the trailing edge of a signal, for example by fluctuations on the falling slope of the signal leading to additional threshold crossings, as outlined already in section 4.6.

reflection Approximately 132 ns after a leading edge, another leading edge mostly uncorrelated to the ToT is observed. This time delay matches twice the 10.4 m of cable length between the photomultipliers and the readout electronics assuming a signal propagation time of $5\,\mathrm{ns\,m^{-1}}$. For this reason, it can be safely assumed that this artefact is caused by a reflection of some signals or signal components by imperfect impedance matching. This is furthermore supported by the fact that it occurs more pronounced for high ToT, which corresponds to large signals and thus larger reflections barely passing the threshold.

reflection Approximately 108 ns after a leading edge, another leading edge (uncorrelated to the ToT) is observed. The interesting observation as compared to the previously described reflection is that it also occurs for higher time over threshold values and is hidden within the cable length. Actually, the cables from the photomultipliers are first connected to a patch panel to which the readout electronics is connected via shorter cables with a smaller cross section. The length of these patch cables is approximately 2.5 m which matches the time difference between these two reflections.

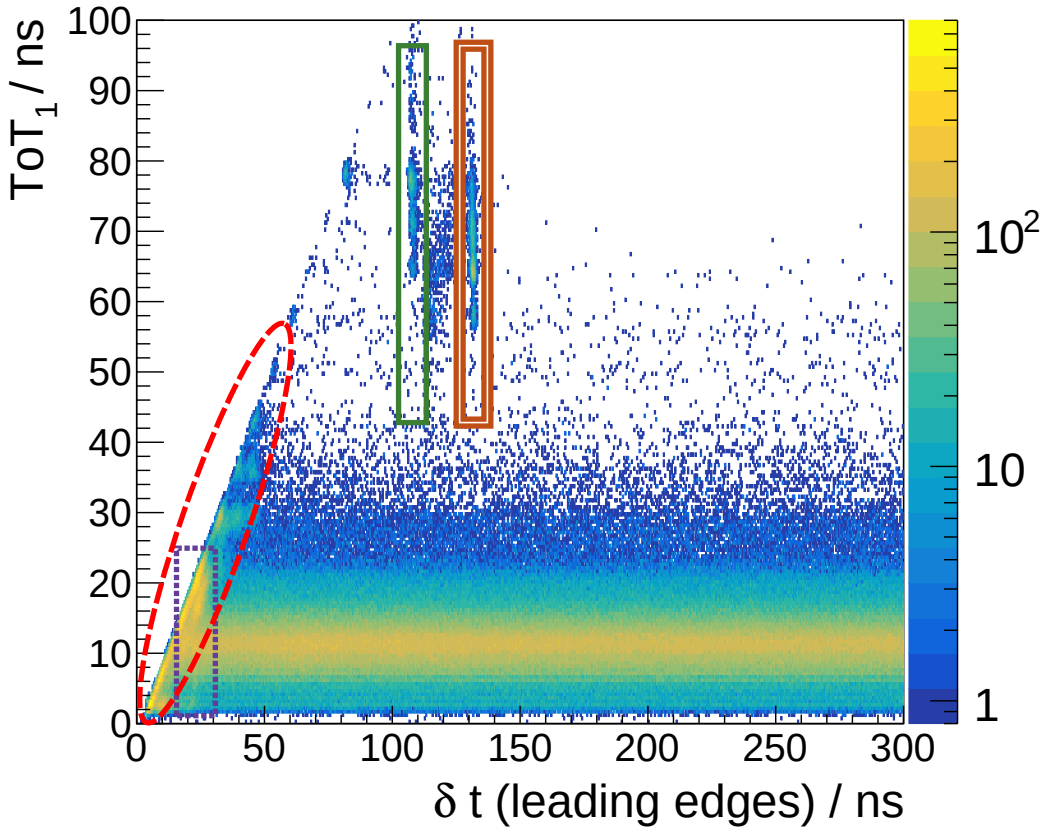

Figure 4.42: Example for the additional information available combining the time over threshold and time information. The data shown were recorded for one channel of the ToF1 detector. On the horizontal axis, the time difference between the leading edges of all pairs of consecutive signals is plotted. Correlated to this information, on the vertical axis the corresponding time over threshold of the earlier signal of the pair is shown. The histogram is filled for all recorded digitizations with valid ToT without applying any time cut before. Several structures can be identified which are discussed in the text.

reflection Approximately 24 ns after a leading edge, another leading edge, uncorrelated to the ToT, is observed. This again matches with the length of the cables between the jDisc module and the patch panel.

Obviously even small effects such as rare reflections due to a slight impedance mismatch due to cable connections can be identified with this technique in the high statistics data. For this reason, it is very much suited to monitor for issues also online during data-taking.

Another example for the additional information provided by correlating time and time over threshold in a statistical manner is shown in fig. 4.43. The diagonal correlations between the time over threshold difference and the time difference of the leading edges of consecutive signals persist through the full time difference range. The upper diagonal area is naturally excluded, since all time over thresholds are positive and for minimal ToT_2 the ToT_1 determines the region in which no additional leading edge is detected. The diagonal itself is filled more prominently due to remaining high frequent noise on the signal as described in section 4.6.4, since a moderate hysteresis setting is used. The most pronounced structure, however, is the repeating pattern of 2 ns of time differences which is also indicated by the black lines. This pattern matches the bunch structure of the accelerator ELSA.

The fact that this structure is so cleanly visible allows to conclude that the time resolution of the system of scintillator, photomultiplier and electronics is sufficient to resolve, albeit not fully separate, the 2 ns bunch structure. This conclusion is straightforward, since all information which enters the histogram is deduced from time differences recorded by the very same electronics, so no trigger effects are involved at all. The time walk effects are directly accessible from the slope of the diagonal correlation. Additionally, the width of the distribution of time over thresholds and even the average incident rate can be estimated by projecting to the vertical and horizontal axis, respectively.

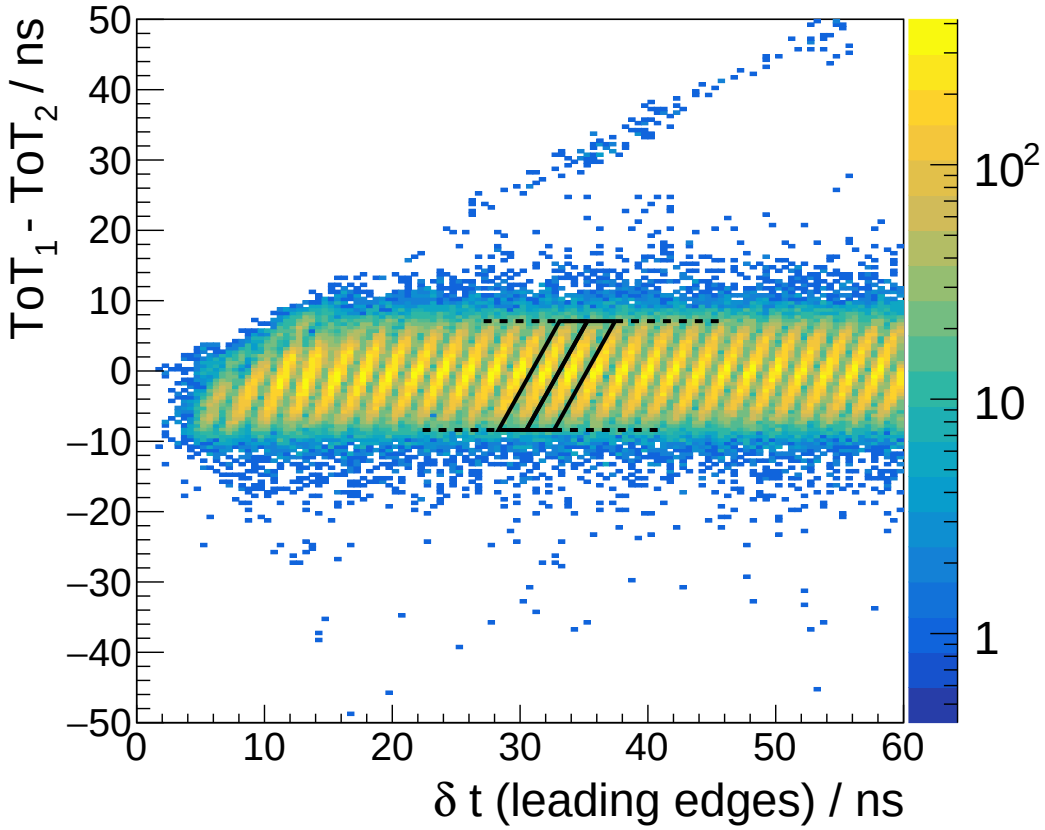

Figure 4.43: Example for the additional information available combining the time over threshold and time information. The data shown were recorded for one channel of the FluMo detector. On the horizontal axis, the time difference between the leading edges of all pairs of consecutive signals is plotted. Correlated to this information, the vertical axis shows the corresponding difference of the time over threshold of the earlier signal minus the time over threshold of the later signal of the pair. The histogram is filled for all recorded digitizations with valid ToT without applying any time cut before. The black lines highlight the bunch structure of the accelerator ELSA which is dominantly visible in this plot.

Chapter 5

Analysis Framework

The data acquisition of the BGO-OD experiment takes care of reading out all required electronics modules if a trigger occured, collecting the data and constructing one so-called *event* by combining all related information (c.f. [Ham16]). Basic validity checks of the data are made, but no special pre-processing or data modification is done online by the DAQ. The constructed events are then stored on disk in the file format of ROOT (c.f. [BR97]) and additionally made available for online analysis via a network data stream. On this level, the data structure in the file contains the raw data directly as they were read from the electronics modules. The analysis software deals with all further steps of data processing up to the physics analysis and additionally allows to simulate the expected detector response to generated physics events. To accommodate the very diverse requirements of the various analysis steps, a large flexibility of the framework is needed.

In the first part of this chapter, the general structure of the analysis framework and the major extensions implemented and used throughout this thesis are discussed (c.f. section 5.1). Secondly, the preanalysis steps common to the two analyses presented in this work are described in section 5.2. Subsequently, the cuts employed for the analysis of the $\gamma p \to p\pi^0$ reaction are presented in section 5.3. This reaction is analysed with the aim of testing the reliability of the developed software and to exploit the capabilities of the framework. Finally, the chapter is concluded by presenting the technique to extract the beam asymmetry for the π^0 photoproduction reaction in section 5.4.

5.1 Framework Structure

The analysis framework ExPlORA[1] was originally developed by the CBELSA/TAPS collaboration for use at the CBELSA/TAPS experiment in Bonn [S+11].

In 2011, a reduced version has been forked for use at the BGO-OD experiment. Apart from the introduction of experiment specific parts, several fundamental changes and extensions to the structure of the framework have been implemented. The basic design of an extensible, plugin-based structure, the underlying programming languages and the strong coupling to the ROOT framework (c.f. [BR97]), which is the standard framework used in particle physics experiments around the world, has been kept and was extended.

The analysis framework is designed using the technologies around which the underlying ROOT framework was built. ROOT is an object oriented framework featuring the ability to combine compiled and interpreted code, similar to its predecessor PAW[2]. The major technical improvements of the new C++-based framework over its predecessor which was written in Fortran were the self-documentation of the framework and the possibility to store and transport complicated object-oriented structures.

The same features defined the design of ExPlORA. First off, a schematic of the consecutive analysis steps is provided in section 5.1.1. The analysis is structured into configurable objects called 'plugins' each dealing with a dedicated task of the analysis, creating and exchanging specialized objects which encapsulate the physics information. This structure is detailed in section 5.1.2. These building blocks are set up and configured to form the full analysis chain in an interpreted configuration language which is described in more detail in section 5.1.3.

Building on the structural layout, several new developments were implemented to allow for flexible definition of physics cuts and storage of preprocessed data. These features are shortly described in section 5.1.4 and section 5.1.5, respectively.

5.1.1 Analysis Chain

A schematic overview of the generic blocks of the event-based data analysis framework ExPlORA is shown in fig. 5.1. This general schematic is common to many event based particle physics experiments. In the very first stage, the data acquisition system takes care of reading out the raw data and combining all data from the various detectors to one event. At the BGO-OD experiment, the data are stored on disk without further modifications.

The analysis software starts from this level. For this reason, the very first step is the decoding of the raw data. In the next step, a calibration database is used to map the raw channel numbers to the detector channels and apply the calibration constants and time corrections. At this point, the information from different readout modules belonging to one detector channel is grouped together.

(1) **Ex**tended **P**luggable **O**bjectoriented **R**OOT*ified* **A**nalysis
(2) '**P**hysics **A**nalysis **W**orkstation', a software tool for data analysis and visualization in high energy physics developed starting in 1986 (c.f. [Bru+89])

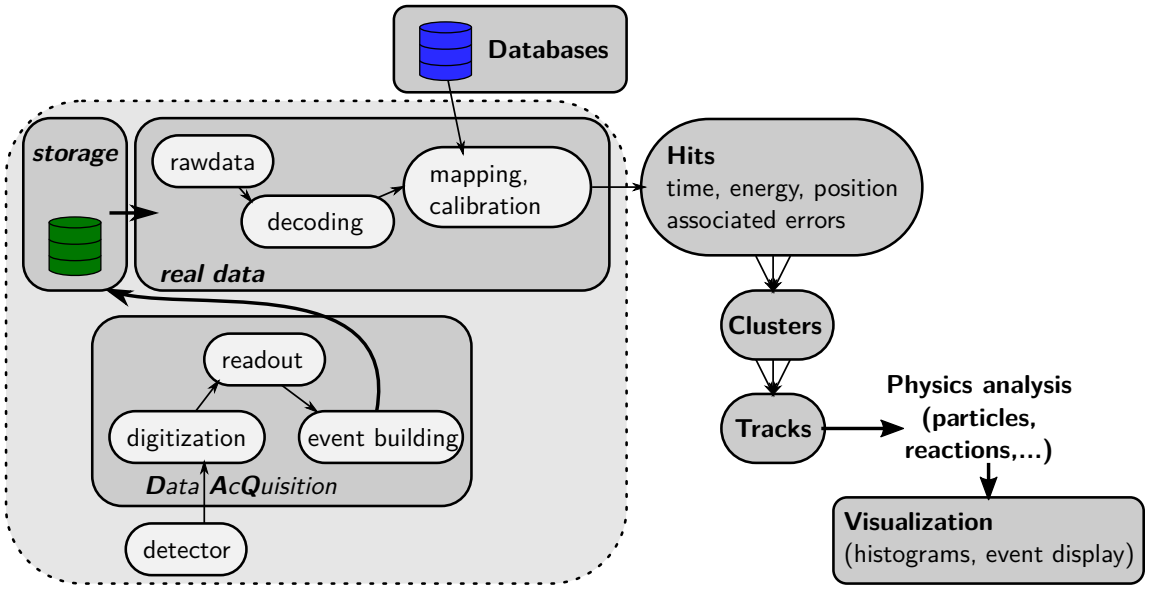

Figure 5.1: Schematic overview of the building blocks used in the event-based data analysis at the BGO-OD experiment.

Finally, the first stage of the reconstruction extends this information with the associated detector geometry and error information, still encapsulating all information of a single detector channel only. This level of information is termed *hit* at the BGO-OD experiment. Further steps combine several *hits* which were created by the same incident particle in one detector to *clusters*. In the end, the *clusters* from several detectors ascribed to the passage of the same particle are combined to form a *track*. It must be noted that this labelling is generically used also for neutral particles and even if just a single *cluster* and the target origin define such a *track*. In this way, it is unlike the concept of a physical track which is limited to charged particles.

At this point, only basic selection cuts for example on time and energy information have been applied, but no physics reconstruction was done yet. For this reason, the level of *tracks* provides a common input to any physics analysis which then constructs the corresponding *particles* and finally combines several *particles* to a *reaction candidate*. At all stages, but especially after the final physics reconstruction, a visualization via histograms or in an event display is possible.

5.1.2 Plugin and Container System

An object oriented data analysis is based on several concepts which are facilitated by the structuring of correlated data and defined algorithms into *data objects* and *plugins*, respectively. This encapsulation of data and algorithms into blocks allows for easy reuse, especially in a collaborative environment. An example for this would be a generic clustering algorithm, which combines *hits* in detectors by their geometric adjacency. Such a generic algorithm might be applicable to a large set of detectors if only the definition of geometric adjacency is specialized.

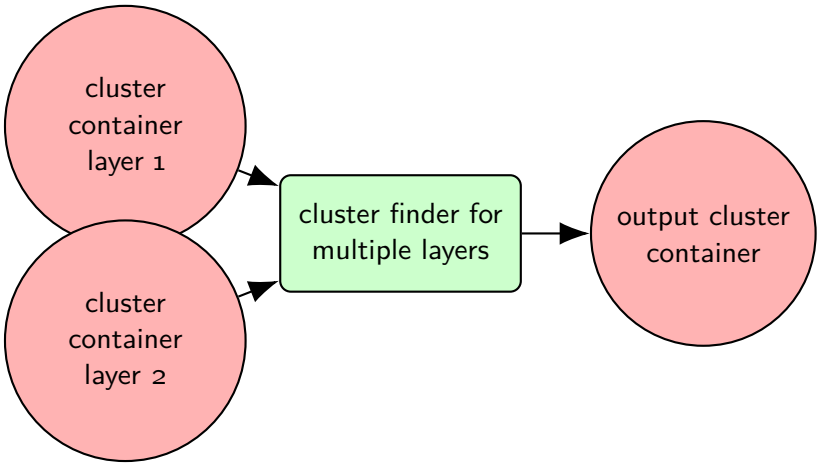

Figure 5.2: Visualization of the plugin and container structure for an example clustering algorithm.

In an object oriented framework, the details of such implementations are usually accessible via a common *interface*. This abstraction simplifies the usage of specialized implementations, since specifics are only exposed if necessary. An example for this would be a *cluster* reconstructed for a detector. General information necessary in the analysis such as the position or the energy and the associated resolutions are accessible via a common interface for all kinds of *clusters* of any detector, while each implementation may internally extract and store this information in a very different way. In other words, a common interface means that all kinds of *clusters* share a common list of methods, while each *cluster* provides the implementation specialized for the corresponding detector.

All event-based objects are stored in so-called *containers* for exchange of data between the various plugins. The containers are handled by the framework and take care of managing the storage of the objects in memory. Additionally, they integrate tightly with the mechanism of ROOT to store the objects on disk, if requested.

A simple visualization of such a chain of containers and plugins is shown in fig. 5.2. It shows the structure of the *cluster* finder algorithm as implemented for example by the `BTSciFiReconstruct` plugin. As input, *cluster* objects which are from the single layers of the SciFi2 detector (c.f. section 2.5.2) are used. As output, new, combined *cluster* objects are created. The important structural feature is that all the *clusters* are data objects encapsulating their relevant information, while the *cluster* finder algorithm only needs to know the common interface. Based on this framework structure, the full analysis chain can be constructed, combining dozens of plugins and containers to form an 'assembly line' to process the data.

In many situations at all stages of this assembly line, very common functionality is necessary. As part of this work, the necessary generic building blocks for data filtering, data storage and visualization have been implemented and used. They are interfacing with the structural

description language XML[3] which is presented in the following.

5.1.3 Configuration Language XML

To facilitate a logical and technical decoupling of the physics analysis and the more algorithmic analysis code itself, it is common to use a language for the structural description which is both machine- and human-readable on top of the more low-level programming language of the framework. The physics cuts and the visualization of the analysis are expressed in this structural language, while the dedicated programming language is used for any algorithmic part of the physics analysis.

```
<BTSciFiReconstruct
  sourcehorizontal="SciFi2_H_cluster"
  sourcevertical="SciFi2_V_cluster"
  dstcontainer="SciFi2_final_cluster"
  debug="0"
  />
```

Listing 1: Simple example for the instantiation of a single analysis plugin using the configuration language XML.

For ExPlORA, the structural description language is XML with many custom extensions. XML defines a structure based on elements and attributes as shown in listing 1. The example corresponds directly to the structure shown in fig. 5.2. The full block is called *element*. It is enclosed by a *tag* `BTSciFiReconstruct` which is configured via the contained *attributes*, which in this example are `sourcehorizontal`, `sourcevertial`, `dstcontainer` and `debug`. In case of the analysis framework ExPlORA, the element names an analysis plugin and the attributes name configuration parameters, in this case the names of the input and output containers the plugin uses. Furthermore, parameters like a debug-level can be set. The framework takes care to instantiate the corresponding C++ plugin `BTSciFiReconstruct` and set it up using the provided attributes.

XML additionally allows to nest such elements, i.e. the element `BTSciFiReconstruct` could contain an element of its own. The framework instantiates the plugins corresponding to all elements. Any outer level plugin is provided with access to all the contained plugins. An example for such nesting will be provided in section 5.1.4.

For the use in ExPlORA, this structural description has been extended with several dynamic features which strongly enhance the convenience of the otherwise static XML description. These enhancements contain the possibility to conditionally include other blocks of XML and set and pass on variables. Within the course of this thesis, the language has been extended with more dynamic features such as support for complex calculations and iterations.

(3) e**X**tensible **M**arkup **L**anguage

5.1.4 Data Filtering and Visualization

The most abundant task in data mining is the filtering of data by applying selection criteria, or physics *cuts*. In an object oriented framework, such cuts can be applied to the information stored within the objects, for example, a time selection or an energy cut.

```
<BTFilterContainer
  name="Forward_Tracks_Selection"
  srccontainer="ForwardTracks"
  dstcontainer="SelectedForwardTracks">
  <BTInterpretedConditionRange
    method="fGetTime"
    valuefrom="-2"
    valueto="8"
    />
</BTFilterContainer>
```

Listing 2: Example for filtering data, in this case reconstructed *tracks* in forward direction, by applying a time cut within XML syntax.

A realistic example for such a selection is shown in listing 2. The generic `BTFilterContainer` plugin developed in the course of this thesis accepts an input container and creates an output container. Each element stored in the input container is copied to the output container if a filter condition is fulfilled. This condition is defined inside the same XML-element, making use of the nesting functionality of the markup language. In the provided example, a selection based on the time information of the objects contained in the `ForwardTracks` container is performed. Only the objects passing this cut will be copied to the `SelectedForwardTracks` output container.

It should be noted that this example is fully contained within the structural description language XML and can be used for any object and container within the analysis framework, not requiring additional programming nor adaptions of the `BTFilterContainer` plugin. The conditions which are used for filtering can again be nested as necessary, for example combining a time and energy selection. A similar generic plugin exists to accept or discard a full event, acting like a software trigger mechanism.

From the technical point of view, care was taken in the development of this system that the performance is similar to or even exceeds that of compiled code which would otherwise be reimplemented in many different analysis plugins. This was achieved by leveraging the interpreter of the ROOT framework, which necessarily extends the underlying programming language C++ with reflection capabilities(4). This includes access to the full list of all the methods any data object offers to access the underlying information at runtime. Making use of

(4) *Reflection* is the functionality of a program to examine and modify its own structure at runtime, commonly also called *introspection*.

this mapping, the given method `fGetTime` can be resolved to an address in memory where the instructions to access the corresponding information are stored. In turn, the interpreting capabilities are only needed once when the analysis is set-up, while afterwards, the performance of compiled code can be achieved by directly jumping to the corresponding instructions. In all common cases, this is even significantly faster than calling any analysis plugin, since the overhead of going through the abstraction of a generic interface is avoided(5). An explanation of the complicated technical internals and the different implementations which were needed to integrate well with the ROOT 5 and ROOT 6 framework, which feature vastly different interpreters, would exceed the scope of the explanation given here.

Another advantage of such a generic filtering system is that it is simple to extend with common functionality. As an example, the generic `BTFilterContainer` can provide a list of cuts, counting the fraction of objects which passed each condition, both while the analysis is still running and also for a final result. Many operators are available, so for example, a cut on angle differences including a $\pm 180°$ wraparound can be defined. All available functionality has been documented with appropriate examples and is available within the collaboration (c.f. [Fre16]).

The underlying mechanism to extract information from any analysis object at runtime can also be leveraged for visualization. For this, a flexible histogramming mechanism was implemented, which allows to specify the containers, the information to extract from each object stored in the container, the histogramming axes and the order in which the containers should be iterated over. Again, this can be instantiated completely in the structural XML language and full documentation is available (c.f. [Fre16]).

5.1.5 Data Storage

A major complication in an object oriented framework is the storage of data objects. This follows from the complex structural layout of objects themselves: they may contain information of various different data types, vary in their effective size or even reference other objects. Looking at the connectivity shown in fig. 5.3, such interconnections are needed in both directions during analysis, for example, to compare a reconstructed *cluster* energy in simulation against the originally simulated particle and its energy deposit in the material.

Most of the complexity of storing object oriented structures is handled well by the ROOT framework. In a process termed *streaming*, objects of similar kind are split into their components and these are stored in an efficient way on disk or may be sent over network. The streaming mechanics even takes care if the structure of an object is changed or extended later by implementing a versioning system and migration procedures.

However, the issue of interconnected objects remains problematic. If only a selected part of higher level information is to be stored as an intermediate analysis output, for example only *clusters* or *tracks* without their original associated *hits* or even the raw data, the connections need to be broken in a safe manner. This problem was solved for the ExPlORA framework in

(5) The generic interface of objects and plugins implies a small runtime overhead, since the specific implementation which the machine must execute has to be determined at runtime.

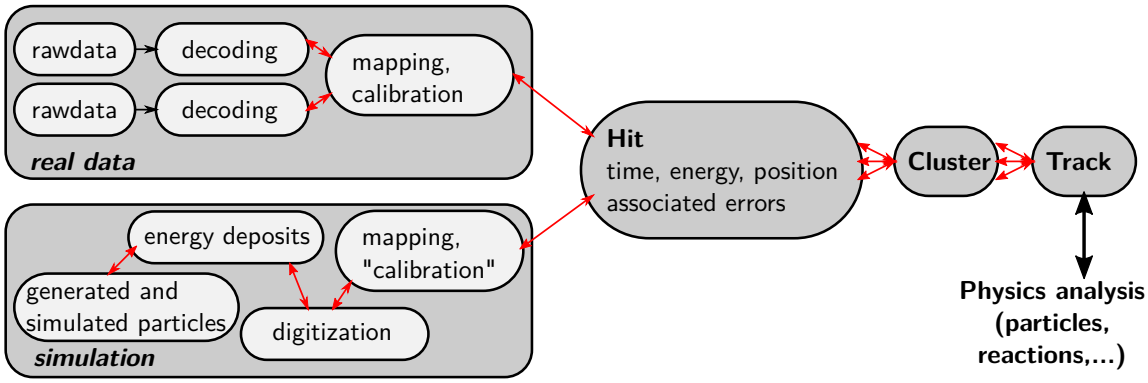

Figure 5.3: Schematic view of the data flow for both real data and simulation. The steps of analysis are arranged from left to right. The connecting arrows between the various stages indicate how the information is linked together: during analysis, all information is linked in both directions so for example, a simulated energy deposit can be accessed from a *track* walking back through the clustering, *hit*-finding and digitization levels.

the course of this thesis, now allowing to define which level of data should be 'cut off' from the interconnected information. This feature has been heavily used in this thesis to produce preprocessed data for physics analysis and also a reduced set of extracted information required for the determination of the beam asymmetry.

To implement this solution, a deep integration into the mechanisms employed by the ROOT framework was needed. Since in C++ *links* between objects are usually made by storing pointers to addresses in live memory which are not useful for storage on disk, ROOT already provides a mechanism to instrument all the pointers in data objects by assigning ascending numbers to all referenced objects, then storing this number instead of the pointer. When an object is restored from disk, the new memory address can be found back by using the link provided by this unique number. This technique solves part of the problem, but necessarily fails in two cases:

- If the referenced object is not read back from disk, the reference will be broken. This will occur if only a reduced set of information, for example only *tracks* and higher level objects, should be stored.
- If the unique number overflows and / or is reused, the reference will suddenly point to a different object.

Since ExPlORA is made for event-by-event analysis, it already employs the trick of resetting this unique counter after each event to prevent overflowing, which however does not solve the problem of potential reuse of the unique number[(6)]. To solve these issues, two techniques were employed by hooking into the reference mechanism of ROOT. After an event is finished, a

(6) This kind of re-use of the unique numbers across events is a problem if only a reduced set of information is read back. Then, the references in one event may be resolved to an invalid memory location, left over from a previous event.

	min. pulse length / ns	artificial dead time / ns	max. pulse length / ns
ARGUS	✗	✗	✗
barrel	2.5	2.5	✗
SciRi	✗	✗	✗
ToF	5.5	8.0	✗
FluMo	✗	✗	✗
GIM	✗	✗	✗

Table 5.1: Overview of the selection cuts applied during the *hit* reconstruction. The only cuts applied at this step are the time over threshold reconstruction cuts.

check is performed that each of the references is still valid, i.e. pointing to an existing object. Afterwards, a user-defined storage level is used to decide which data should not be written out, and the corresponding objects are marked as invalid. Finally, all references are re-checked and those pointing to invalidated objects are 'pruned', i.e. explicitly marked as invalid, such that if the objects are read back later, no attempt to resolve this reference will be made. After this, it is safe to store all objects on disk and re-read them again in a different analysis process.

Additionally, a second approach to protect against remaining pitfalls was implemented. This is achieved by supervising each single plugin in regular intervals, and checking for data corruption introduced for example by reusing an old unique number. Furthermore, it is checked that a plugin does not modify its input nor modify any other data objects apart from those listed in the output containers.

Employing these techniques, the analysis can be safely split into several parts, mainly the preanalysis part extracting the *tracks* from the raw data, and the physics analysis part starting from the *track* level. This allows to easily test several physics analyses on a common preanalysis dataset without introducing the huge overhead of always starting from the raw data. Consequently, the preanalysis will be described in the following section.

5.2 Preanalysis Steps

The first part of the analysis after the technical data decoding, mapping and calibration is the reconstruction of *hits*, *clusters* and *tracks* as was already sketched in section 5.1.1. On this level, the first selection cuts may be applied to the data.

In the following paragraphs, the several steps and the cuts applied to the data recorded from the various detectors are covered in more detail.

5.2.1 Hit Reconstruction

The conversion of the decoded information into *hits* in any case extends the digitized information with the geometric mapping, i.e. the position of a *hit* is defined by the known geometry of the

detector.

Additionally, at this stage, the time over threshold information for the detectors with jDisc readout is extracted by pairing the recorded leading and trailing edges. As was outlined in the algorithmic description which was given in section 4.6.1, the association between leading and trailing edges also allows to apply the first cuts to the data. This is also the only kind of cut already applied at this level of the analysis.

As shown in the overview in table 5.1, this functionality is only used for the scintillator barrel and ToF reconstruction. Both these detectors need to be operated with low threshold to maximize the efficiency and the quality of the time over threshold information, so they are susceptible to catch high frequency electronics noise. The scintillator barrel is a single-layer detector and is used as chargedness veto in the central region, thus reflections or noise could produce false physics information. For the ToF detectors, the clustering which is described in detail in section 4.9 necessarily has to use a large time window due to the effective speed of light in the scintillator bars, so any noise could produce wrong *clusters*. As already shown in section 4.6.1 in the detailed discussion of the time over threshold reconstruction, such structures are indeed observed in the data. The cuts which have been chosen are well below the minimum pulse lengths the photomultipliers produce, while the artificial dead time was chosen to also suppress reflections of the signals due to a small impedance mismatch along the signal cable lines (c.f. section 4.11).

For the other detectors, such a cleanup is either not necessary or even unwanted. The ARGUS detector features three layers which will allow the clustering algorithm to remove unwanted *hits*. Furthermore, it is only used in correlation with the tagger detector. The SciRi detector which is equipped with APDs (**A**valanche **P**hoto **D**iodes) and subsequently amplifier boards produces clean, long signals which are approximately 50 ns long, so a further cleanup is not necessary. For the FluMo and GIM detectors, dedicated efficiency studies are performed using time correlation with other detectors.

The step after the *hit* reconstruction is the clustering stage, which is described in the following.

5.2.2 Cluster Reconstruction

The clustering combines the *hits* of one detector or sub-detector via geometric and time correlation cuts to identify those *hits* which have been caused by the passage of the same particle. An overview of all the algorithms employed at the BGO-OD experiment is given in table 5.2.

Most detectors share a common base algorithm. This base algorithm checks for each *hit* whether a geometrically adjacent partner, possibly with a time correlation cut, is found. In this case, it becomes part of the *cluster*, unless the maximum *cluster* size is exceeded. Afterwards, the next unused *hit* is checked.

In this basic algorithm, only the definition of geometric adjacency needs to be reimplemented separately for each detector. As can be seen from the overview in table 5.2, while for the drift chambers and the ToF walls a variation of the basic algorithm is used, the BGO calorimeter (c.f. section 2.3.2) is the major exception. Inside the calorimeter, the electromagnetic shower

detector	algorithm
Tagger	default, min. 2 *hits*, $\Delta t < 1.2\,\text{ns}$
ARGUS	default, min. 2 *hits*, max. 6 *hits*, $\Delta t < 2.7\,\text{ns}$
barrel	clustering at later stage when combining with the BGO
BGO	local maxima clustering algorithm with time and energy cuts
SciRi	default, no cuts
MOMO	default for all 6 modules, $\Delta t < 20\,\text{ns}$
SciFi2	default for both layers, $\Delta t < 20\,\text{ns}$
Drift Chambers	dedicated: only the earliest *hit* in an adjacent channel is considered
ToF walls	dedicated algorithm already described in section 4.9

Table 5.2: Overview of the first stages of clustering algorithms in use at the BGO-OD experiment. The base algorithm which is used for most detectors is labelled with 'default' in this table.

which is induced by a photon or electron expands up to several crystals, which may lead to directly adjacent hits caused by different incident particles. Using the basic algorithm, all these *hits* would become part of one single *cluster*. A dedicated algorithm called 'local maxima' clustering was developed, which considers the crystals with the highest energy deposit first and then associates adjacent crystals to these, which allows to better separate *clusters*. Furthermore, the energy of crystals at the boundaries of two *clusters* is distributed to both, thus improving the effective energy and position resolution of the calorimeter. The algorithm is described in full detail and compared to other possible approaches in [Sch15]. For this clustering, two additional cuts are made. For each *hit* to be considered at all, at least 1.5 MeV of energy is required. After the clustering is finished, only *clusters* with at least 25 MeV are stored. These choices have been made to suppress electronic noise effects which may cause low energy deposits and partially suppress uncorrelated physics background such as energy deposits caused by unrelated particles scattered off the beam dump.

For the detectors which are constructed from multiple layers, an additional clustering stage combining the single-layer *clusters* is added. This applies to the MOMO detector consisting of six trapezoidal layers and the two-layered SciFi2 detector. Both use a dedicated *cluster*-combinatorics algorithm.

For the MOMO detector (c.f. section 2.5.1), the six trapezoidal modules are arranged such that the full detector area is covered by three layers of scintillating fibres. The multi-layer clustering algorithm reconstructs the intersections for both the cases that only two layers or all three layers have seen a matching *hit* within a time window smaller than 20 ns.

For the SciFi2 detector (c.f. section 2.5.2), the multi-layer clustering has to take the different lengths of fibres[(7)] into account. Using a time correlation cut of Δt smaller than 10 ns and taking the effective speed of light into account, the separate horizontal and vertical *clusters* are

(7) As illustrated in the setup-description in section 2.5.2, SciFi2 has a central hole left for the main beam.

associated to a *cluster* with two-dimensional information. Any single-layer *cluster* for which no corresponding *cluster* in the other layer has been found is discarded.

After the clustering steps, the information is already fully reconstructed per single detector. The next step is the combination of the clusters from the various detectors related to the passage of the same particle into *track* objects.

5.2.3 Track Reconstruction

Tracks are the base ingredient for the physics analysis. It must be noted that the terminology *track* in this case is used as a generic name for the next level of analysis: a track can either contain a combination of *clusters* from several detectors ascribed to the passage of one particle, but it may also contain not associated clusters from a single detector. Four types of *tracks* are reconstructed at the BGO-OD experiment: for the tagger-ARGUS system, the central detector region, the intermediate detector region and the forward spectrometer region.

The most straightforward tracking algorithm is that of the tagger-ARGUS system. In this case, the tagger defines the 'seed' of the tracking, i.e. it provides the time and initial energy information. The *clusters* found in the ARGUS detector are then used to refine the energy information extracted with the tagger. For this, a tight cut of the time difference between a tagger and ARGUS cluster to be smaller than 2.5 ns is used, which is dominated by the time resolution of the ARGUS detector. A cut on the energy difference between the two clusters to be less than 30 MeV resulting from the energy resolutions of the two detectors (c.f. section 2.1.3) further reduces the probability to pair accidental coincidences. For performance reasons, this tracking is only performed for *cluster* times which are ± 20 ns around the prompt peak.

The tracking in the central detector region is more complex. The software to include the two MWPCs in the central region is still under development and was not used in the course of this thesis, so the description provided here will be limited to the association procedure of the BGO and barrel detectors. For this algorithm, the BGO *clusters* are used as the 'seed' due to the finer granularity of the BGO calorimeter. For each BGO *cluster*, all barrel *hits* are checked. Since the barrel detector does not provide any information on the polar angle, the angle of the BGO *cluster* must be used to correct the time of the barrel *hit* using the effective speed of light in the material, as shown already in the study of the barrel energy information in section 4.6.2. All combinations between BGO *clusters* and barrel *hits* after a time difference cut of 10 ns and a $\Delta\phi$ cut of 20° are considered as potential *tracks*. To not create multiple *tracks* for a single BGO *cluster*, in case a *cluster* was associated with multiple barrel *hits*, the barrel *hits* are merged into a *cluster*. This handles the case in which a particle passed through the scintillator barrel and deposited energy in two neighbouring scintillator bars.

However, this algorithm actually allows for multiple association of scintillator barrel *hits* to different BGO *clusters*. For this reason, the algorithm requires care at the level of the final analysis and in terms of particle interpretation. In real data, the case of the passage of a charged and an uncharged particle through the same barrel scintillator bar can not be distinguished from

that of two charged particles without additional information, as could be provided for example by the MWPC detectors. In simulation, a particle mis-identification study will be presented for the $\omega \to \pi^+\pi^-\pi^0$ decay in section 6.4.

After the central tracking has been performed, a higher level time correction using the tagger *cluster* time and the times of the BGO and barrel *clusters*[8] is attempted. As outlined in the discussion of the global trigger (c.f. section 3.1.2), the time gates used for the BGO trigger are wide, while the tagger trigger is used with the smallest possible gate setting and thus defines the timing of the event. However, due to the high rate of tagger triggers it might happen that the tagger trigger which caused the event does not correspond to the footprint of the hadronic reaction recorded in the central detector region. In this case, another tagger *cluster* should be chosen to provide the event timing. The time information available from the BGO and barrel detectors after the clustering is sufficient to disentangle between the tagger *clusters* from different electron bunches. This correction is described in more detail in appendix B.1.

In the intermediate detector region, the *tracks* are defined by SciRi *clusters* and the target centre, i.e. the change from *cluster* to *track* is a purely technical conversion of the information. In the future, the MRPC which is still under commissioning will provide a superior angular and time resolution.

The tracking in the forward direction is the most complex part of the reconstruction algorithm, since it involves combinatorics between a manifold of detector layers, energy loss calculations and step-wise tracking through the magnetic field of the open dipole. Two approaches for the *track*-finding part are in use, which will be shortly described in the following.

The very first step is the combination of the *clusters* from the front tracking detectors, MOMO and SciFi2. All combinations are assembled and several cuts are enforced:

- The maximum time difference between the *clusters* from the two detectors is 9 ns.
- The average time of the two *clusters* has to range between −4.5 ns to 10.5 ns as compared to the reconstructed trigger time.
- The position extrapolated to the target origin (assumed at $z = 0\,\text{cm}$) must be within a 3 cm radius around the target centre (assumed to be $x = y = 0\,\text{cm}$). Detector resolutions are not taken into account for this cut, but the target cell has a diameter of 3 cm which is safely below this cut (c.f. section 2.2).

Behind the tracking detectors, the open dipole magnet deflecting charged particles in the horizontal plane is placed. To reconstruct and combine the *tracks* behind the magnet with those found in the front part, two techniques are in use:

(8) This includes single-bar *hits* in the barrel which have been associated with a BGO *cluster* such that a time correction could be performed in the central tracking stage.

1. The first technique is to start with a combinatorics algorithm making use of all drift chamber *clusters*. This technique will in the following be called 'drift chamber tracking' approach.
   a) It combines those drift chamber *clusters* for which the distance in the vertical plane normalized by the target distance matches up to a maximum absolute difference of 0.003, estimated from simulation studies.
   b) The direction of the assembled *track*-segments is allowed to change no more than 8° from one drift chamber detector to the next.
   c) Subsequently, the front and rear *tracks* are combined by propagating the *tracks* straight to the magnet centre plane, and cutting on a maximum difference in the horizontal and vertical direction and the angles projected in these planes.
   d) A uniform field is assumed to extract a first guess on the momentum, the *track* length and the charge sign.
   e) The selected *tracks* are extrapolated to the ToF walls and matched with *clusters* found in all ToF walls by employing a position difference cut and the requirement that the calculated β ranges between 0.1 and 1.2.
2. The second technique starts with information from the ToF walls and only afterwards picks up the matching *clusters* found in the drift chambers. This technique will in the following be called 'ToF tracking' approach.
   a) The first step is to combine the ToF *clusters* from the several walls by a 4σ cut based on the position and time resolutions, constructing a ToF *track*.
   b) These ToF *tracks* are directly combined with the *tracks* from the front tracking detectors. For these combinatorics, a maximum time difference ranging between −10 ns and 70 ns is imposed. Additionally, the front *track* is extrapolated to the ToF walls and a maximum difference of the position in the vertical plane, i.e. the plane orthogonal to the deflection plane of the magnet, of 20 cm is allowed.
   c) Using the difference of the extrapolated position of the front *track* and the ToF *track* in the horizontal plane and the known field strength, a first guess of the momentum using a relation extracted from simulation with protons is made and the charge sign is deduced.

After any of the *track*-finding procedures, a first fitting of the momentum is performed. For this, a particle with the mass of a proton and negative or positive charge, as assigned previously, is assumed. The *track* is then propagated through the spectrometer, starting from the *cluster* measured in SciFi2 to the last *cluster* found in the ToF walls (if any), taking a simulated magnetic field map and the energy losses in the material calculated using the Bethe Bloch formula into account. Algorithmically, this propagation is discretized using sequential small steps of dynamic size. According to the distance between the track position at these steps and the

measured *cluster* positions with associated uncertainties, a χ^2 is calculated which is minimized by varying the start momentum using Brent's method as implemented in the [BR97] framework. Finally, the *track* is propagated back to the target position, correcting for the energy loss such that a start momentum can be extracted. Additionally, the average momentum calculated along the stepping procedure is stored which will be needed for the particle identification via the measured β versus momentum relation.

In case the 'ToF tracking' approach was used, the procedure is repeated additionally checking for drift chamber *clusters* which are not farther than 10 cm away from the *cluster* position in the corresponding layer of each chamber. The *clusters* are then added to the *track*.

The notable difference between the two approaches is that the 'drift chamber tracking' strongly depends on the efficiency of the drift chamber detectors, but on the other hand is able to reconstruct the passage of a charged particle even if the ToF walls have not been reached by it. On the contrary, the 'ToF tracking' approach explicitly requires that the charged particle was also measured in at least one of the ToF walls, but strongly reduces the dependency of the *track* reconstruction efficiency on the efficiency of the drift chambers. A study of these differences will be provided in the analysis of the ω photoproduction in section 6.3.

Finally, all central, intermediate and forward *tracks* undergo an additional step in which a hypothesis for several possible particle types is created which is described in the next section.

5.2.4 Track Hypothesis Creation

In the last step of the preanalysis, the *tracks* are reinterpreted assuming a set of possible particle types, creating a so-called hypothesis for each of these interpretations.

For all central, intermediate and forward *tracks*, hypotheses for proton, charged pions and charged kaons are constructed[(9)], while a hypothesis for photons is constructed in the central region only. For forward tracks, the hypotheses with mismatching charge sign are excluded.

The hypotheses allow for a different treatment of the *tracks* depending on the particle type. In the central region, this translates into particle-type dependent energy loss corrections. The corrections have been extracted by checking the simulated detector response to different particle types with the simulation package GEANT4 (c.f. [Ago+03]). The resulting correction factors for photons and charged particles have been crosschecked with real data (more details are described in [Jud16]).

In the intermediate region, no special treatment of the different hypotheses is done.

In the forward region, a dedicated refitting of the initial *track*-fit, which was performed in the assumption of a particle with the mass of a proton, is performed for each particle type, taking the corresponding energy loss in the material into account. This means a complete re-fitting including the stepping and minimization procedure through the magnetic field is performed with the different particle masses. In the case of the 'ToF tracking' approach, this will now automatically take the associated drift chamber *clusters* into account in the fit.

(9) Additionally, a hypothesis for neutrons was added for the central region, but it is not used throughout this work.

Probability	Applicable to	Source of Information
Central Chargedness	Central *Tracks*	Central *track* with barrel *hit*
BGO Cluster Size	Central *Tracks*	Number of crystals / *hits* in corresponding BGO *cluster* with measured energy
Forward Chargedness	Forward *Tracks*	Charge and charge sign of reconstructed forward *track*
ToF	Forward *Tracks*	Expected β vs. measured β
Invariant Mass	*Composed* Particle	Invariant mass of a reconstructed particle, e.g. π^0 from two measured photons
Energy Conservation	Reaction	Reconstructed initial and final state energies

Table 5.3: Overview of the probabilities used for physics cuts throughout this thesis work. Furthermore, probabilities making use of the $^{dE}/_{dx}$ in the barrel detector and ToF walls and a dedicated probability for K^+ identification within the BGO ball are under development.

It must be noted that any modification performed at this stage on the momentum or energy is also reflected in an update of the associated uncertainties. Additionally, at this stage of hypotheses creation, probabilities which depend on the particle type are added to each individual hypothesis. These are described in the following.

5.2.5 Probabilities

Based on the corresponding particle hypothesis, a fine-grained probability for this particle to match a certain assigned *role* is calculated. A list of the probabilities used in the analyses performed in this thesis is given in table 5.3. The concept and their definition is shortly outlined as follows, they will be covered in more detail alongside the example analysis in section 5.3.

The term 'probability' encapsulates the expected detector response of such a particle in reality. The most straightforward example is the probability defined from the forward chargedness. As the name suggests, it is based on the charge and charge sign of a *track* reconstructed in the forward spectrometer. For any charged particle hypothesis, for example a proton, if the charge sign of the reconstructed *track* matches, i.e. in this case is positive, the probability is set to 100 % since the response of the apparatus in terms of *charge and charge sign* matches the one expected for a p. It should be noted that this probability for the very same *track* in the hypothesis of a π^+ is also 100 %, i.e. there can be no overall normalization in this concept, since the different hypotheses are investigated independently. In the case of not matching charge, i.e. a π^-, the probability is set to 0 %, while for neutral particles, no dedicated tracking is implemented yet.

The probability from central chargedness is defined in a very similar way. Since no information on the sign of the charge is available, no difference is made between positively and negatively charged particles. In addition, a small conversion probability calculated from the probability for pair production inside the scintillator material is taken into account for photons, slightly

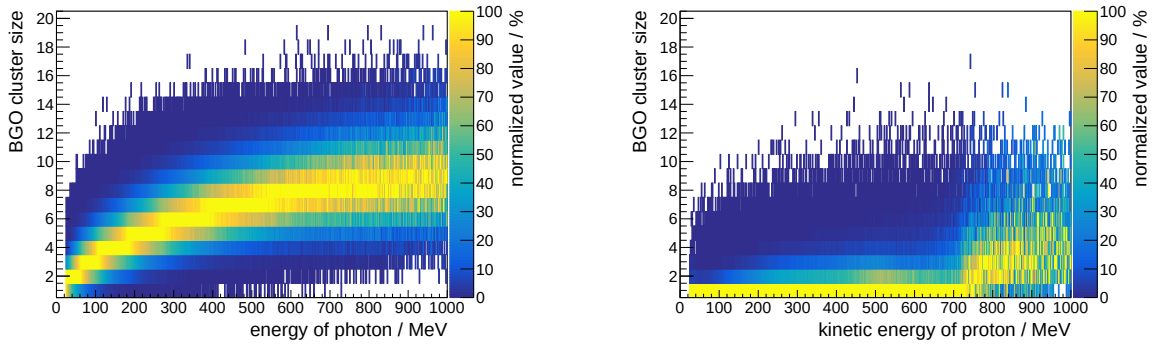

(a) Distribution of BGO *cluster* sizes for reconstructed photons of different energies, normalized per energy bin to 100 % in the maximum.

(b) Distribution of BGO *cluster* sizes for reconstructed protons of different energies, normalized per energy bin to 100 % in the maximum.

Figure 5.4: These plots provide the input data for the definition of the probability from BGO *cluster* size for a cluster with measured energy. They were extracted from real data taken in June / July 2015, applying the same analysis as described in section 5.3, naturally excluding the cut on the probability from BGO *cluster* size itself.

modifying the discrete value of 0 % for uncharged particles depending upon the thickness of scintillating material which was crossed by the central *track*. The 100 % value for charged particles is also modified by taking the efficiency of the barrel detector of 94 % into account (as determined in [Jud16]).

The probability from BGO *cluster* size uses the fact that the electromagnetic showers produced by photons are usually not contained within a single BGO crystal as the energy deposition of charged hadrons are. Using $\gamma p \to p\pi^0$ reactions which have been reconstructed without the use of this probability value[(10)], an energy- and particle-type-dependent *cluster* size distribution can be extracted. A normalization of the extracted distributions in bins of energy allows to define a probability for a particle hypothesis with measured energy and BGO *cluster* size. The plots resulting from this normalization procedure are shown in fig. 5.4. At the upper end of the energy scale, the distributions are slightly distorted: for photons, this is mainly due to the smaller statistics, while for protons with kinetic energies above 500 MeV, the shower may not be fully contained anymore until finally the proton punches through for even higher energies. Simulation was *not* used to extract these data, since the correct modelling of the shower development in BGO crystals is complicated and mistakes in the simulation procedure may introduce unknown systematics into the definition of this probability for each particle type.

The probability from time of flight encapsulates the particle identification in the forward spectrometer. This is performed by calculating the expected β of a particle starting from its

(10) The analysis described in section 5.3 has been used for this purpose.

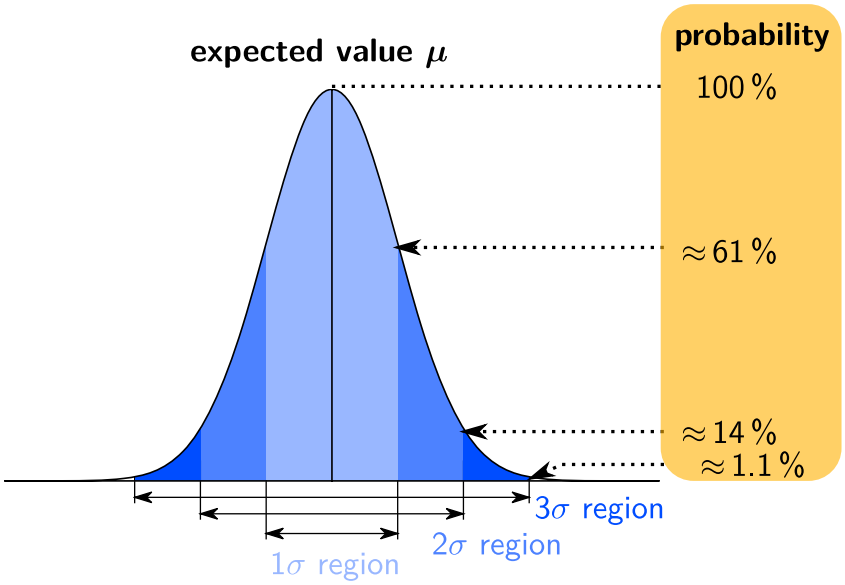

Figure 5.5: General illustration of the definition of the probabilities based on an expectation value and a Gaussian with defined width. As an example, for the probability from time of flight, the 'expectation value μ' would be the expected β. The width 'σ' of the Gaussian would correspond to the known uncertainty. The probability is then extracted by evaluating the Gaussian at the measured value β. Every selection cut is defined based on this probability value. In turn, this value can also be expressed in terms of accepted standard deviations σ as illustrated in the figure.

measured momentum and forcing its mass to the nominal PDG value:

$$\beta_{\text{expected}} = \frac{p_{\text{meas}}}{\sqrt{p_{\text{meas}}^2 + m^2}}$$

The error on the β_{expected} is calculated by Gaussian error propagation from the measured momentum. The probability of the particle hypothesis is then defined by using a Gaussian distribution centred on the expected β, The width of the Gaussian is calculated by error propagation from the expected β, which contains the momentum error, and the measured β, which contains the time resolution of the detectors. The probability value is then extracted by evaluating the Gaussian distribution for the measured β, i.e. if the measured beta is exactly the expected one, a probability value of 100 % would be assigned. A generic illustration of this definition is shown in fig. 5.5.

It must be noted that this probability is different from the percentage of the population of values which are found within the bands of standard deviations of a *normal distribution*. Within this thesis, most cuts will be made by requiring a probability value larger than 0.3 %, corresponding to approximately 3.4σ.

5.2.6 Time Selection of Tracks

At this point, the highest level of information in the preanalysis stage has been reached. The last step of the preanalysis is the application of the first major selection cut, the selection of the *tracks* in time.

In this thesis, two datasets have been studied. The first one was recorded in June / July 2015 and will be discussed in the following. It will be used both for the analysis of the $\gamma p \to p\pi^0$ reaction and the reconstruction of $p\omega \to p\pi^+\pi^-\pi^0$ events as will be performed in section 6.3. The second dataset recorded in October / November 2015 will be used for the ω reconstruction only. Accordingly, the differing experimental conditions and the pre-selections will be discussed in section 6.2.

During the data-taking period in June/July 2015, an electron beam energy of 2.9 GeV was used. A selection of runs after tuning of all detector components, excluding periods of data-taking with known issues, was done. Only data taken with physics trigger conditions and after optimization of the linear polarization was used. Over the full beamtime, data with different intensities with beam currents ranging between 900 pA and 1300 pA was taken and included for this analysis. The open dipole magnet was turned on at half field value of 0.216 T.

In the following investigation, only data analysed using the drift chamber tracking approach will be shown, since the ToF tracking is mainly of interest to overcome a lack of drift chamber efficiencies, but might come with a larger contamination of false tracks unless additional cuts are performed.

In total, 250.4 hours of data acquisition time are taken into account for this analysis. This set also includes a few hours of alignment data which was recorded with turned off magnetic

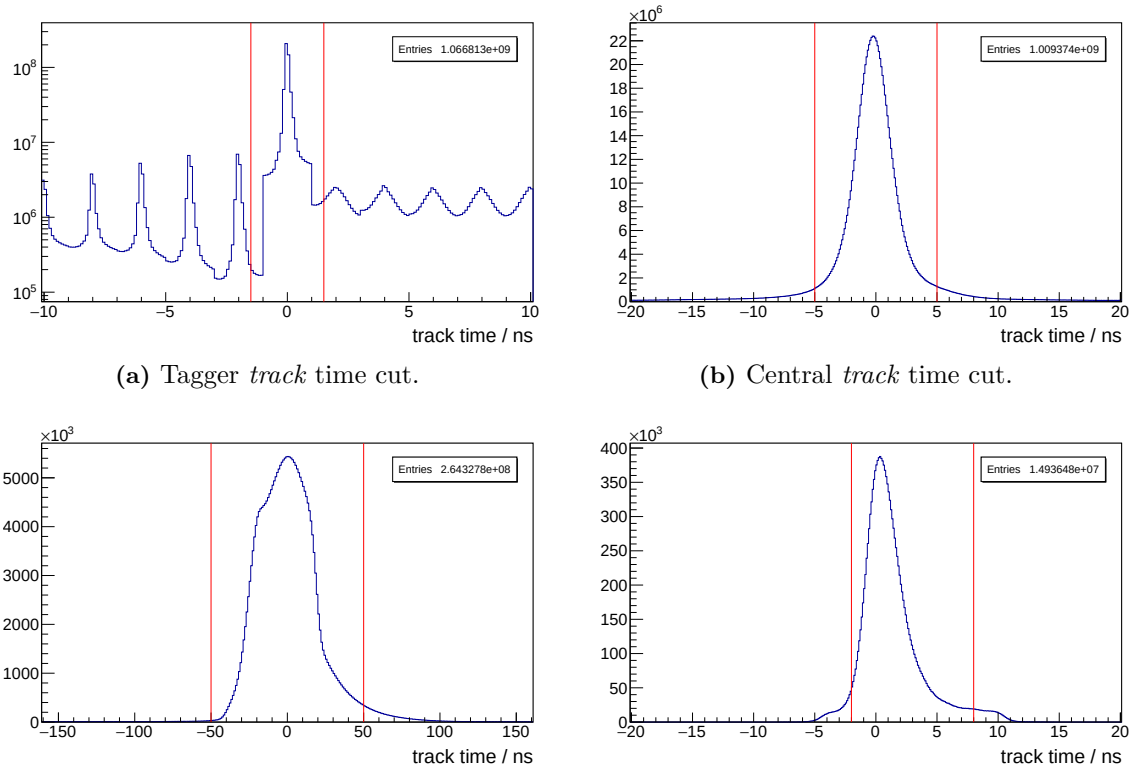

(a) Tagger *track* time cut.

(b) Central *track* time cut.

(c) Intermediate *track* time cut.

(d) Forward *track* time cut.

Figure 5.6: Time distributions of the reconstructed *tracks* in the different detector regions. The applied cuts are indicated by the red, solid lines.

field of the open dipole magnet. For these data, only straight tracks can be reconstructed which are not taken into account for physics analysis.

The applied cuts for the four kinds of tracks are visualized in fig. 5.6.

The tagger defines the time difference and provides a time resolution sufficient to disentangle the bunches, which is why the bunch structure of the accelerator can clearly be seen in fig. 5.6a. The additional rectangular cutoff around the central peak is induced by the clustering time cut described in section 5.2.2. It must be noted that for the beam time in June / July 2015, the electronics of the tagger detector was plagued by technical issues with the discriminator thresholds, namely a variation of the thresholds with ripple from the supply voltage. This effect shifts the measured time information due to variation of the time walk effect. Since all channels on the same electronics discriminator undergo the same variation, the time resolution of adjacent channels are not affected for almost all coincidence pairs[11]. For this reason, the high cross-channel resolution shown in section 3.5.2 is only reached for the October / November 2015 beam time data, while in the June / July 2015 dataset, the *cluster* time difference cut becomes visible. Consequently, for the analysis, a slightly wider cut on the tagger *track* time is chosen as indicated.

In fig. 5.6b, the distribution of the time of the central *tracks* is shown. This time distribution is mostly Gaussian due to the start time extraction with the sampling ADCs of the BGO detector which minimize any energy dependent time walk effect.

In fig. 5.6c, the time distribution of the intermediate *tracks* provided by the SciRi detector is shown. A peak and a shoulder can be seen, which is likely caused by a trigger gating effect. It should be noted that no time walk correction has been used in this analysis. As the time information does not need to be accurate since the detector is not used for time of flight measurements, but only as a binary detection information, a large cut is used to include almost the complete distribution.

For the forward *track* time shown in fig. 5.6d, which is provided by the error weighted mean of the times measured by the MOMO and SciFi2 detectors[12], an asymmetric cut is used such as not to cut out slow particles.

The *tracks* selected in this way are then used for the reconstruction of reactions as will be explained in the subsequent analysis section.

5.3 Example Analysis: $\gamma p \to p\pi^0$

For a study of the analysis technique especially in view of the extraction of the beam asymmetry, the reaction $\gamma p \to p\pi^0$ is studied.

This reaction is the best characterized channel in photo production off proton. It dominates the first resonance region and thus is almost free from contributions by background channels in close to threshold production. Additionally, high statistics data and model fits for the beam

(11) Of course, a few coincidences of channels are made across different discriminator boards.
(12) If the *track* was built with only MOMO or SciFi2, the corresponding time information is used.

asymmetries are readily available, so the analysis and treatment of uncertainties can be tested.

In this section, the full physics analysis chain and cuts are presented. Finally, the incremental effect of all cuts will be summarized in an overview table (table 5.4).

5.3.1 Reconstruction of $\gamma p \rightarrow p\pi^0$ Events

The very first stage of the physics analysis after the initial pre-selection of data is the combinatorics of all selected *tracks* to identify the reaction footprint. At this stage, no particle identification cuts are applied yet such as not to bias the investigated data sample.

To accommodate this, the reaction to be investigated is defined looking at all initial and final state particles. For the $\gamma p \rightarrow p\pi^0$ reaction, the incoming photon and the target proton define the initial state, while the final state consists of a proton and a π^0. The π^0 itself is a short-lived meson with a live time below 1×10^{-16} s and can thus not be detected directly in the BGO-OD experiment. The dominant decay mode of the π^0 is into two photons.

For this reason, the footprint to be identified in the detector system consists of the initial photon, which corresponds to one tagger *track* made by the corresponding electron to reconstruct the initial state, and one proton and two photons to characterize the final state for a total of three particles in the final state.

Only events with at least one track in the tagging system and exactly three total tracks in the central, intermediate or forward region are considered. Each track in the tagging system is interpreted as a possible post-bremsstrahlung electron associated to the incoming photon. Each of the other tracks is interpreted as the final proton or one of the photons from the π^0 decay.

Via a combinatorics algorithm, all possible combinations of the *tracks* are assembled, making use of the existing hypotheses for each track[13]. Following the design concept of the framework, this reaction-finding procedure produces an object-oriented structure called *reaction* which encapsulates all information. The *reaction*-object marks the highest level of information in the framework. It contains the initial and the final *state*, which in turn contain the initial and the final state *particles*, respectively. These are also organized in a similar, tree-like structure. In the reaction $\gamma p \rightarrow p\pi^0$ which is investigated in this example, the final state contains the p and the π^0, while the π^0 itself is, in software terms, a *composed particle* object consisting of two γ particles.

The advantage of this concept is the fact that it is possible to treat both the information that can be calculated dynamically on the level of the complete reaction, for example, the missing mass to one of the final state particles which can only be derived taking also the initial state into account, and all the information related to each individual particle or composed particle in one common structure. At this point, all *tracks* have been assigned a *role*, i.e. which particle they might be, for each explicit combination which was built. This allows to perform a probability-based particle identification in the following, making use of the previously calculated hypotheses and eventually discarding some of the combinations.

(13) This naturally means that only central tracks are considered as potential photons from the π^0 decay, since only for these, a photon hypothesis is reasonable as described in section 5.2.4.

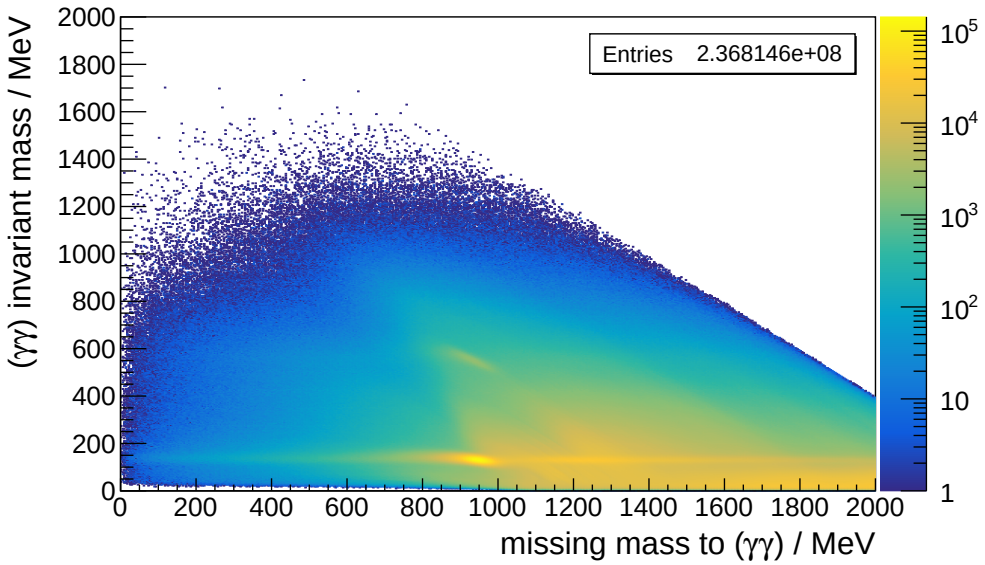

Figure 5.7: Distribution of the invariant mass of the $(\gamma\gamma)$-system versus the missing mass to it before any cuts. Peak structures at the mass of the π^0 and the η mesons are found on the invariant mass axis at the missing mass corresponding to the proton mass. The η mesons also has a decay mode into two photons and thus shares the same final state, which is why the process $\gamma p \rightarrow p\eta$ is part of the reconstructed reactions up to this point.

It must be noted that in principle the outlined technique would also work if one particle was missing, calculating its four momentum from the initial state and the other measured particles by employing momentum conservation. This was indeed investigated, however, as will be demonstrated in the subsequent analysis steps, the resolutions of the detectors are currently insufficient to allow for a reconstruction without requiring exclusive detection of all final state particles.

Already at this point, the distribution of the invariant mass of the reconstructed π^0 candidates versus the missing mass to the π^0 for all the combinations displays the expected correlation for π^0 and η production as shown in fig. 5.7. The following steps of the analysis make use of the probabilities and constraints given by the conservation laws for momentum and energy to remove false combinations from this set.

For this purpose, the last two probabilities listed in table 5.3, namely the probability defined from the invariant mass and the one defined by energy conservation, are also added at this level of assembled *reactions*. The invariant mass probability is applied to the previously explained *composed particles*, i.e. intermediate particles which can be reconstructed from the four momentum of their decay products, and could also be used for single particles if a reliable invariant mass information can be measured. This probability is based on a Gaussian with adjustable width, i.e. 'resolution' centred at the PDG mass value of the corresponding particle, such that later a cut in terms of σ can be defined. Similarly, the energy conservation probability

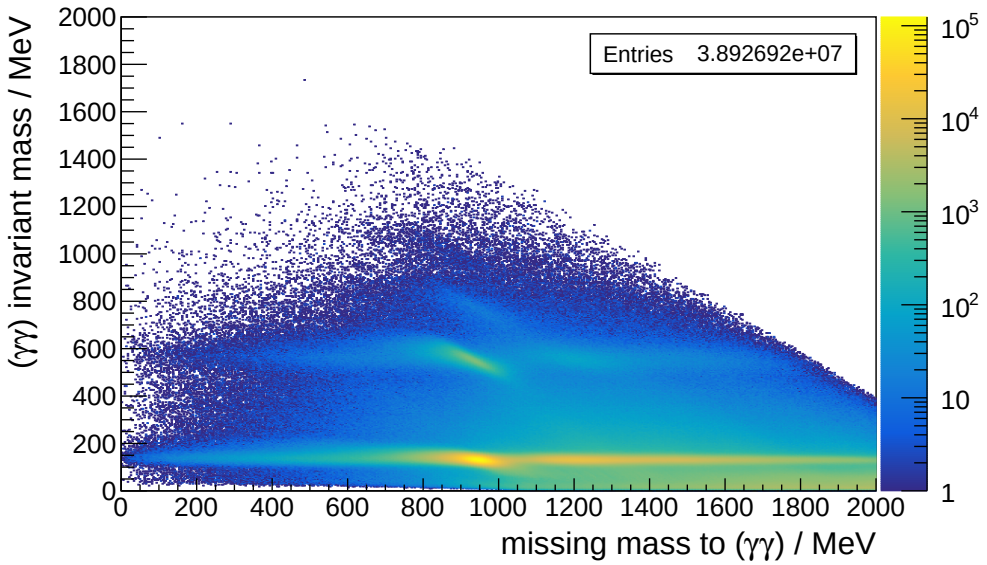

Figure 5.8: Distribution of invariant mass of the $(\gamma\gamma)$-system versus the missing mass to it after the cut on the central chargedness probability, i.e. the barrel detector. The number of reaction candidates is strongly reduced from 2.37×10^8 to 3.89×10^7 and the peak structures from the π^0 and the η mesons are much better separated from the background.

is defined on the difference between the reconstructed total energy of the initial and the final state by using a Gaussian centred around 0 MeV, again with adjustable width.

5.3.2 Selection of Combinations by Probability and Conservation Laws

The first cut in the performed selections is to make use of the barrel detector, i.e. the 'Central Chargedness' probability (c.f. section 5.2.5). This cut acts like a 'veto': technically, it is required that the multiplicative product of all the central chargedness probabilities of all central *tracks* is above 10 %, which is only fulfilled if all *tracks* of uncharged particles were not observed in the barrel detector, while all *tracks* of charged particles were seen in the barrel detector. The effect of this cut is shown in fig. 5.8, reducing the number of total combinations down to about 16 %.

The next cut commonly termed 'coplanarity cut' makes use of the conservation of the x and y component of the momentum. Since the initial state has zero transverse momentum[(14)], this must also hold for the final state. For a final state consisting of two bodies, a meson and a baryon, this can also be expressed as the azimuthal angle of these two partners to differ by 180°. In case of the π^0p final state, a cut on $\Delta\phi$ to be $\pm 180° \pm 15°$ as illustrated in fig. 5.9 is used which is well above the expected angular detector resolutions.

The next cut is commonly termed 'colinearity cut', making use of the conservation of the four momenta of the final state particles. This is expressed by calculating the expected four momentum

(14) It consists of the photon, which in first approximation only has a momentum component in z direction, and the target proton at rest.

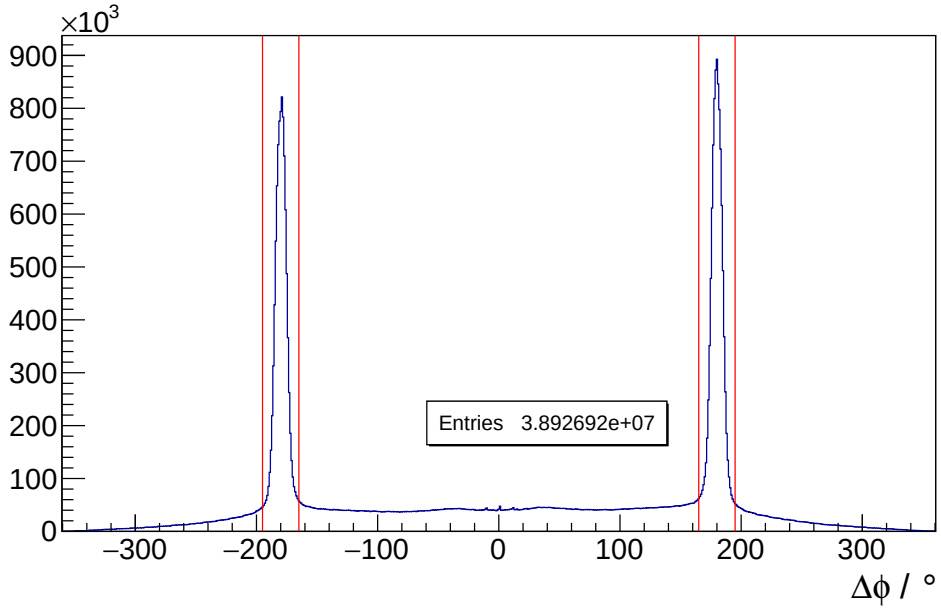

Figure 5.9: Distribution of the azimuthal angle differences between the reconstructed final state meson and the measured final state baryon. The cut indicated by the red, solid lines reduces the number of combinations from 3.89×10^7 (c.f. fig. 5.8) down to 2.04×10^7.

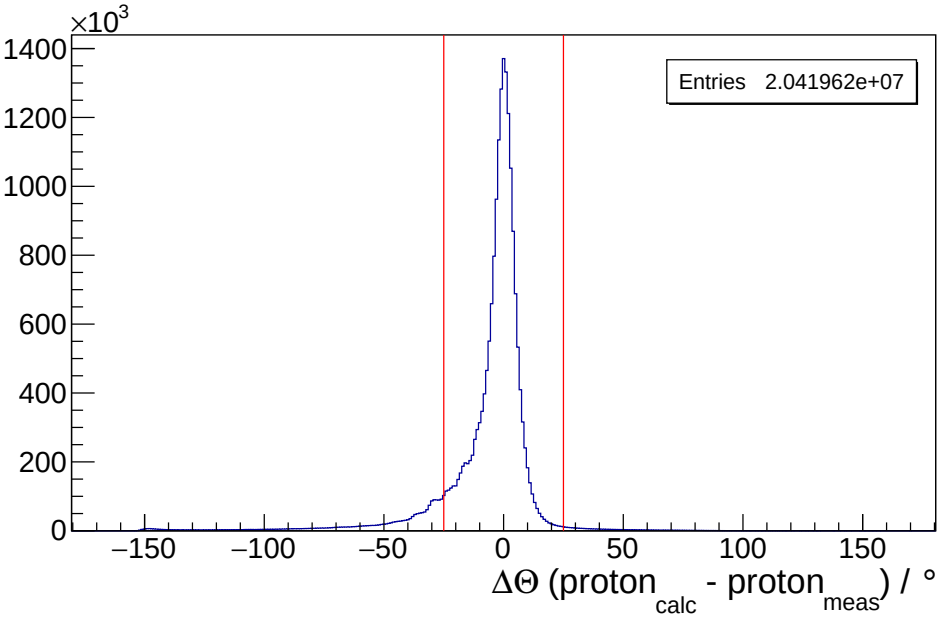

Figure 5.10: Illustration of the cut placed on the polar angle difference in the laboratory frame between the expected and measured proton direction, indicated by cut indicated by the red, solid lines. The number of total candidate reaction combinations is reduced from 2.04×10^7 (c.f. fig. 5.9) to 1.83×10^7 by this cut.

of the final state proton only from the measured initial state and from the reconstructed π^0. The cut is then placed on the polar angle difference between the expected proton momentum and the measured one. To prevent early biasing of the selected subset, the cut has been chosen sufficiently large ($\Delta\Theta = \pm 25°$) to be well above any detector resolution as illustrated in fig. 5.10.

The next cut is based on a particle identification by the size and reconstructed energy of the *clusters* in the BGO detector. As already outlined in section 5.2.5, the size of *clusters* created in the BGO detector varies for photons and charged particles, additionally showing an energy dependency. This has been modelled as a probability which was extracted using the very same $p\pi^0$ analysis outlined here without the use of this cut providing distributions for protons and photons depending on *cluster* size and energy.

In the use of this cut, 3.4σ of the expected distribution from the histograms which have been normalized for each energy bin separately are accepted. Consequently, following the definition of the probability, values below 0.3 % are discarded. The effect is visualized in fig. 5.11.

The next step is the cut on the probability from ToF. This probability is defined using the β and momentum information from the forward spectrometer as described in section 5.2.5, thus yielding a smooth probability distribution with peaks at the maximum and minimum possible value. A cut of 3.4σ corresponding to a probability value larger than 0.03 % is applied. The total number of reaction candidates is only reduced from 1.80×10^7 to 1.79×10^7 by this cut, since the contribution of forward going protons to the reconstructed reactions is low already from the expected kinematics. This is reflected in the total number of candidate reactions with forward protons being 174 486 before the cut, and being reduced to 141 762 after.

For the following cuts based on the energy or momentum of the measured particles, it must be considered that the BGO-OD setup lacks a reliable momentum or energy measurement of final state baryons for most detector regions. In the cases of the baryon being detected in the central region, the momenta are not well defined for kinetic energies higher than about 500 MeV. For baryons detected in the SciRi detector, no energy information is available at all. For the forward spectrometer, the resolution of the momentum information is expected to be sufficient over the full detected energy range, but no systematic study of the actually achieved resolution has been performed yet.

Since in this exclusive analysis, all initial and final state particles are required to be detected, the absolute value of the proton momentum can be calculated from momentum conservation using the initial photon energy, the mass of the initial proton, the direction and momentum of the reconstructed final state π^0 and the measured direction and nominal mass of the final state proton.

The calculation has already been documented in greater detail for the $\omega \to \pi^+\pi^-\pi^0$ decay (c.f. [Sch15]). In case of the $\gamma p \to p\pi^0$ reaction, the application of momentum conservation yields three possible solutions, of which the mean value is used.

The most important effects of the momentum recalculation are obviously the ones on the candidate proton detected in SciRi. In this case, the detector does not measure the energy of the particle, but an arbitrary value of 1234 MeV is assigned in software as its total energy. As a

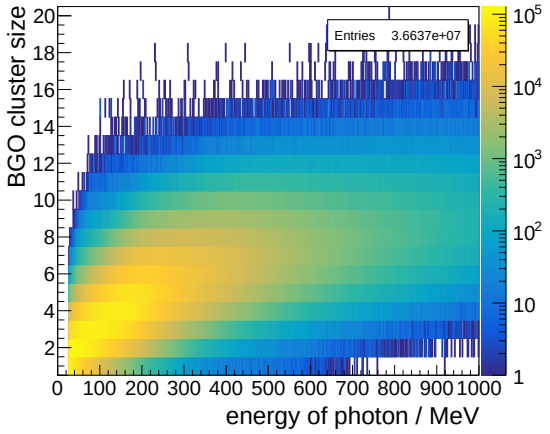

(a) Distribution of BGO *cluster* size vs. *cluster* energy for candidate photons **before** applying the *cluster* size cut.

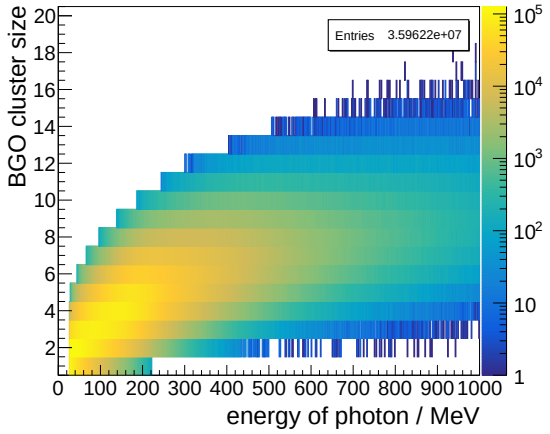

(b) Distribution of BGO *cluster* size vs. *cluster* energy for candidate photons **after** applying the *cluster* size cut.

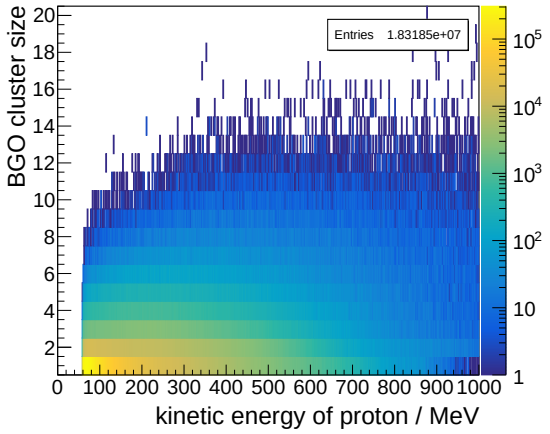

(c) Distribution of BGO *cluster* size vs. *cluster* energy for candidate protons **before** applying the *cluster* size cut.

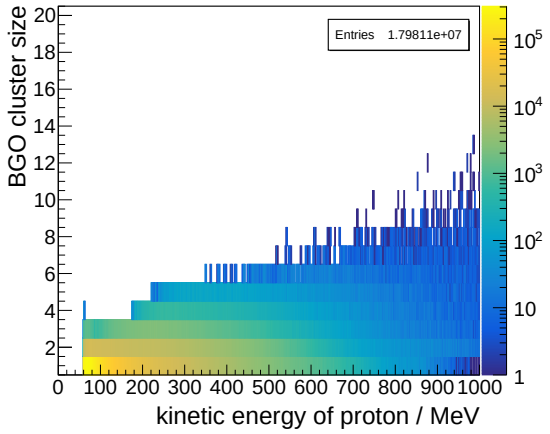

(d) Distribution of BGO *cluster* size vs. *cluster* energy for candidate protons **after** applying the *cluster* size cut.

Figure 5.11: Distribution of BGO *cluster* size vs. *cluster* energy for the different particle candidates before and after cut. The cut is energy dependent as described in section 5.2.5.

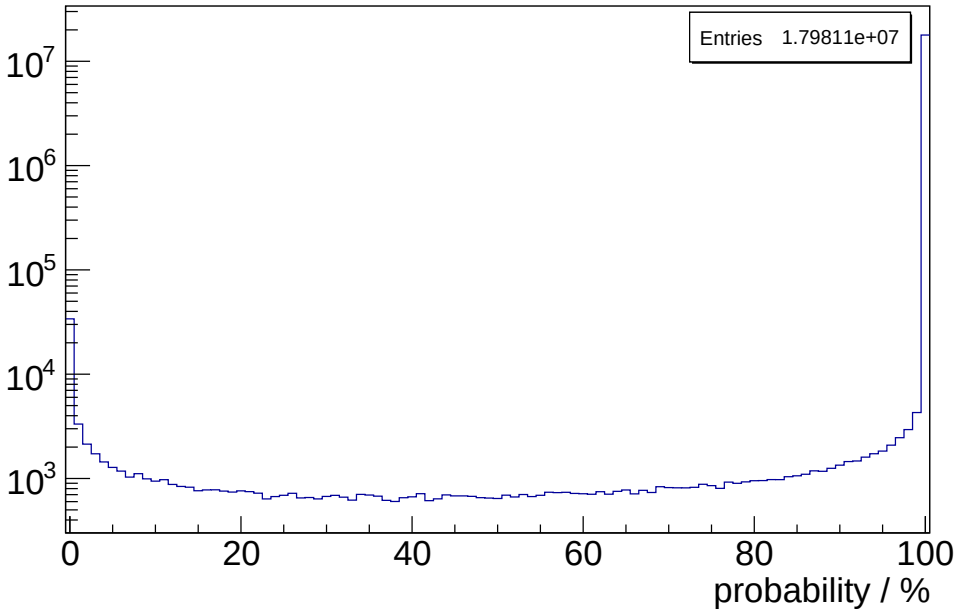

Figure 5.12: Distribution of the probability from ToF for all reaction candidates.

consequence, all the candidate protons in SciRi are considered having the same momentum. This shows up clearly in fig. 5.13a which displays the correlation between the incoming photon energy and the mass of the particle missing to the final state proton. Three clearly distinguishable bands show up corresponding to protons in SciRi which have the same attributed energy and three different possible values for their polar angle.

The bands disappear in fig. 5.13b, where the recalculated momentum (and then energy) of the candidate proton is used for the calculation of the mass of the missing particle. Obviously, the effects of a corrected proton momentum become strongly visible also when the energy balance of the reaction is considered. Figure 5.13c and fig. 5.13d show the difference between the initial and final state energies, for arbitrary assigned and properly calculated proton momenta, respectively.

On the base of this observation, the next cut is placed on the energy conservation. The difference between the initial and final state energy should be zero and is smeared out by detector resolution effects, yielding a Gaussian distribution with long tails from false combinations of initial state tagger electrons and final state reactions. A cut of ± 147 MeV corresponding to about 3σ is effectively applied by cutting on the probability from energy conservation (c.f. section 5.2.5), reducing the number of total reaction candidates from 1.79×10^7 to 1.30×10^7, mainly removing these long tails of the energy difference distribution.

Figure 5.14 shows a side-effect of the momentum recalculation procedure which actually allows for an additional cut. In some kinematically forbidden combinations, the recalculated momentum for the proton ends up being negative, resulting in a flip of the direction of the four-momentum vector in three dimensional space. In terms of laboratory angle, this relates to

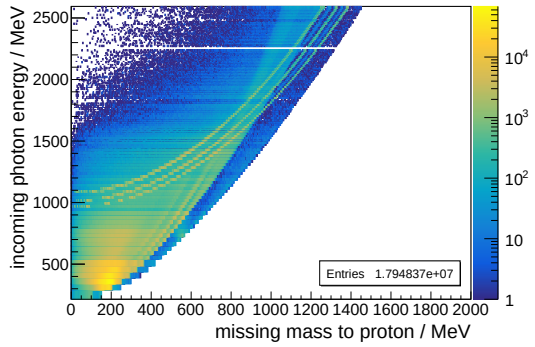

(a) Photon energy vs. missing mass to the proton **before** momentum recalculation, containing non-physical values for the candidate protons detected in SciRi.

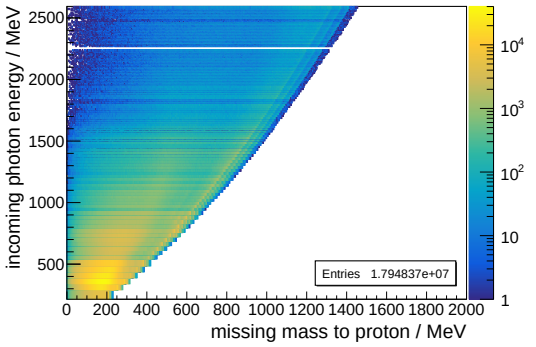

(b) Photon energy vs. missing mass to the proton **after** momentum recalculation.

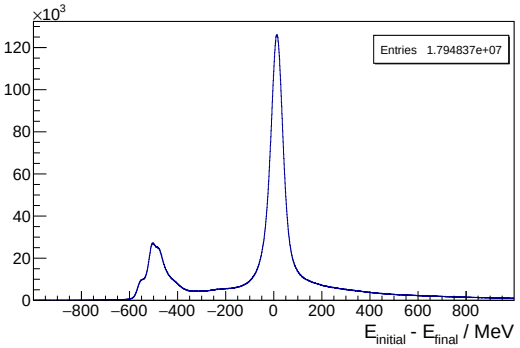

(c) Difference of total initial state vs. total final state energies **before** momentum recalculation.

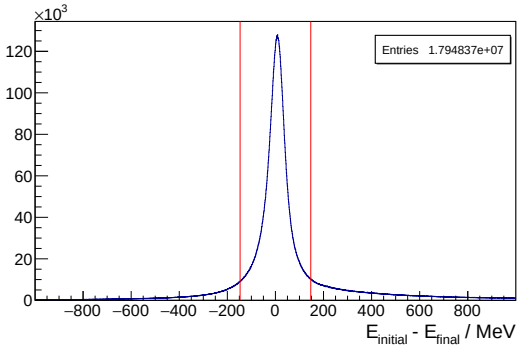

(d) Difference of total initial state vs. total final state energies **after** momentum recalculation. The red, solid lines indicate the bounds of the energy conservation cut.

Figure 5.13: Visualization of the effects of the momentum recalculation procedure. The distribution of the photon energy vs. missing mass to the proton in fig. 5.13a shows three clearly distinguishable bands corresponding to the three rings of the SciRi detector, for which no energy information is available and a fixed number is used in the analysis code, leading to non-physical values. The same issue is also observed in the energy difference plot before recalculation which shows a pronounced peak structure far from the expected position (c.f. fig. 5.13c). These artefacts vanish after the recalculation procedure as shown in fig. 5.13b and fig. 5.13d.

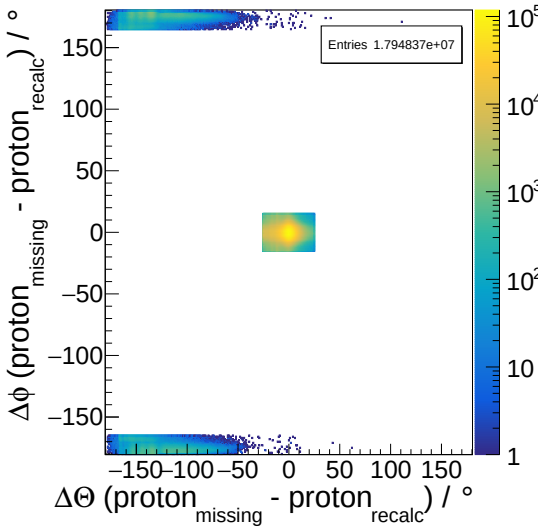

(a) Distribution after momentum recalculation, before energy conservation cut.

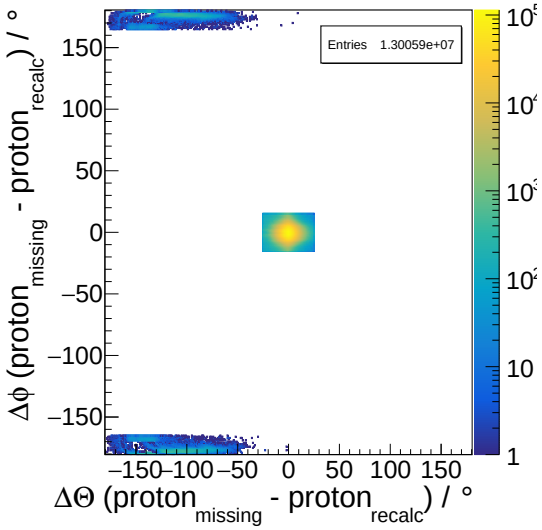

(b) Distribution after energy conservation cut.

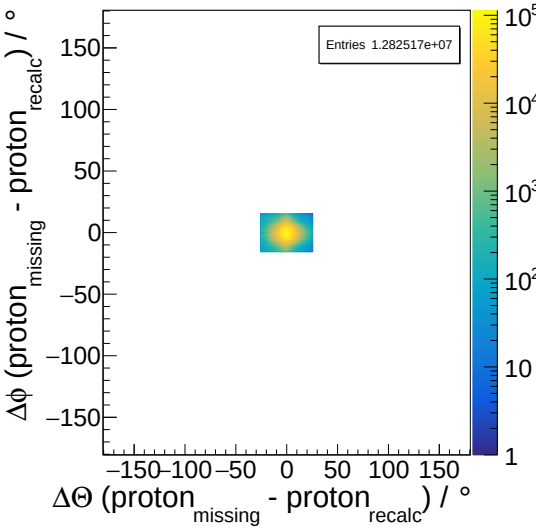

(c) Distribution after repeating the coplanarity cut.

Figure 5.14: Distributions of the azimuthal angle difference vs. the polar angle difference for the measured proton candidate vs. the expected proton as calculated from the initial state and the measured π^0. The distribution is displayed directly after the momentum recalculation procedure (c.f. fig. 5.14a), after the application of the energy cut (c.f. fig. 5.14b) and after repeating the azimuthal angle cut (c.f. fig. 5.14c).

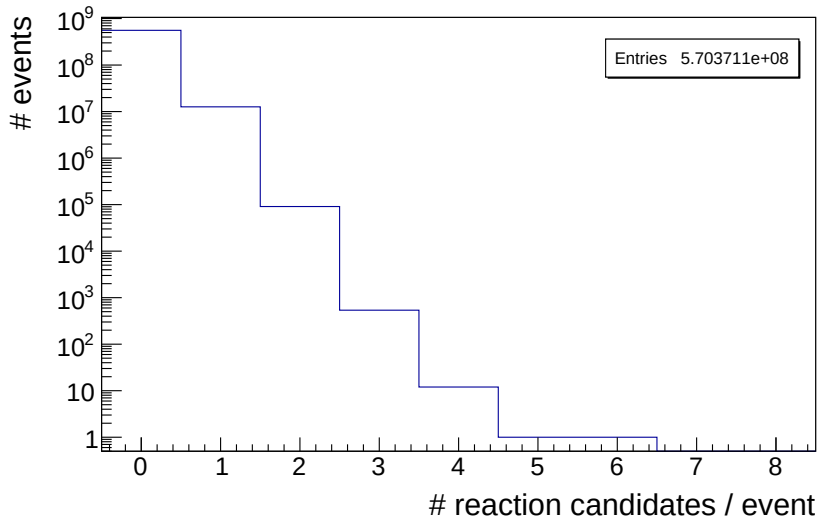

Figure 5.15: Distribution of the number of reaction candidates per event after application of all previous cuts.

the following change expressed in the coordinate system employed at BGO-OD:

$$\phi_{\text{recalc}} = \phi + 180°$$
$$\Theta_{\text{recalc}} = 180° - \Theta$$

This effect is visualized in fig. 5.14. As can be seen, after the momentum recalculation procedure, entries in an area at azimuthal angle differences of about 180° laboratory angle difference between the expected proton (from the 'missing to the $(\gamma\gamma)$-system') and the recalculated proton angle shows up.

These entries are not removed by the energy conservation cut — indeed, after the energy conservation cut, structures in these areas appear which can be correlated to the angular granularity of the SciRi and BGO detectors. These structures show up for negative polar angle differences between 'missing' and 'recalculated' proton direction in the laboratory. This matches the described issue of a proton in reality found in more forward polar angles, which was then recalculated with a negative value.

The combinations with these false momenta are less than 2 % of the total combinations and are safely removed by repetition of the coplanarity cut.

5.3.3 Kinematic Fit and Selection of best Combination

After all these cuts are applied, the number of reaction candidates per event is strongly reduced. As shown in fig. 5.15, in most cases, no reaction is reconstructed. The events with only one reconstructed reaction are predominant and the number of events with higher numbers of

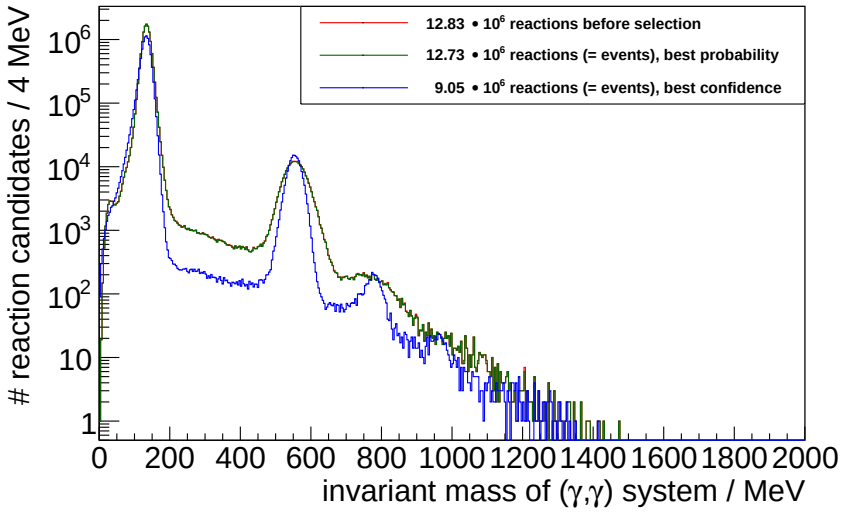

Figure 5.16: Invariant mass distributions for the $(\gamma\gamma)$ system of reconstructed reaction candidates. The uppermost distribution in red shows the situation before any selection, i.e. with a low contribution from multiple reaction candidates per event. The distribution in green which is almost indistinguishable from this distribution is the result of selecting a single reaction per event by 'best probability'. It must be noted that in this case, the recalculated momenta are still used. The lowest distribution in blue shows the result from the kinematic fit after employing a minimum confidence level and selection of the reaction candidates with the highest confidence level per event.

combinations is a factor of 100 smaller. It must be noted that this set can still include any other reaction leading to the $p\gamma\gamma$ final state, since no cut on the invariant mass of the reconstructed π^0 was performed.

In case of multiple reconstructed combinations in one event, the most probable reaction for this event must be chosen. Two techniques have been investigated:

1. Selecting the reaction by best probability, including all the previously described probabilities.

2. Applying a kinematic fit, employing a minimum confidence level, and choosing the reaction with highest confidence for the events with multiple combinations.

The effect of the two different approaches is shown in fig. 5.16. As can be seen, the selection of the 'best' candidate by highest probability does not change the end result significantly. The kinematic fit, on the contrary, performs an additional cut, since it takes all measured information with associated errors into account. In particular, it has to be pointed out that for the proton momentum, the value used by the kinematic fit is the one measured either in the forward spectrometer or in the BGO, or the one assigned in software $\left(E_\mathrm{p} = 1234\,\mathrm{MeV}\right)$ for SciRi[15].

(15) In case of detection of the candidate proton in SciRi, a large uncertainty is assigned to the momentum to leave it free for variation by the kinematic fit.

step of analysis	# of RC	# events with at least 1 RC	# events with at least 1 RC / %
no cuts applied	236 814 577	102 924 565	18.05
barrel veto	38 926 924	36 409 410	6.38
coplanarity	20 419 622	19 192 903	3.36
colinearity	18 318 502	17 512 371	3.07
cluster size in BGO	17 981 101	17 189 749	3.01
particle ID in ToF	17 948 371	17 159 087	3.01
momentum recalculation	17 948 371	17 159 087	3.01
energy conservation	13 005 903	12 913 256	2.26
coplanarity (repeated)	12 825 168	12 733 089	2.23
kinematic fit	12 825 168	12 733 089	2.23
min. confidence 0.01 %	9 074 914	9 045 658	1.59
selection by best CL	9 045 658	9 045 658	1.59

Table 5.4: List of the number of reaction candidates (RC) and events with at least one reconstructed reaction candidate at each stage of the analysis. The indicated percentage relates to the total number of data trigger events (570 371 094) of the analysed dataset.

For each event, the solution with the highest confidence level of at least 1 % from all converging fits is selected. This allows to strongly suppress the background and at the same time improve the resolution of the reconstructed mass for both the observed π^0 and η signal.

It must be noted that the kinematic fit start from the measured values again, not using the recalculated momentum. The fit was configured in the most basic way, only employing the conservation of the four-momenta.

Employing these constraints, the fit varies the combined set of measured quantities belonging to the particles reconstructed as one reaction within their errors. In the fitting procedure, the constraints are evaluated and their error is checked against a termination condition after each iteration. Additionally, the χ^2 and a confidence level are calculated, making use of the known degrees of freedom of the fit.

This variation procedure is essential if information from detectors with very diverse resolutions is combined to give the correct weight to each of the measurements. The technique and the underlying algorithm which relies on the minimization of an error matrix is described in more detail in [Ave99] and has been implemented within the analysis framework used at the BGO-OD experiment (c.f. [Sch16]).

A complete overview of all the analysis steps and their effect on the number of events with reconstructed candidate reactions and total number of combinations is shown in table 5.4.

5.4 Beam Asymmetry Extraction for $\vec{\gamma}p \rightarrow p\pi^0$

After the reactions have been selected, they are stored together with all physics information. This follows the scheme of the data processing as laid out in section 5.1.5: apart from the information about the events such as event numbers and beam current, only the reconstructed objects of *particles*, *composed particles* and the *reactions* are kept, extended by the associated *probabilities*. This means the stored information includes all the reconstructed 4-momenta, associated particle types, information about which detector was involved in the reconstruction of each particle and also the information about the confidence level of the kinematic fit.

Technically, these data are still kept in separate files for each analysed run, not only to allow for studies of changes over time and to simplify a potential selection a posteriori, but also to easily separate the runs taken in different polarization conditions. The files also include the summed scaler data recorded by the tagger hodoscope, which will be needed for a normalization of the relative flux between the datasets for the two polarization planes.

To facilitate the following analysis steps, a change of paradigm is necessary. Up to this point, all data analysis took place on an event-by-event basis, not correlating any event with one another and not using any information integrated over the full data-taking period. The data were only added together for visualization in histograms. For the extraction of physics results from the full dataset, however, access to the full set of events at once is helpful to allow for application of more elaborate statistical analysis techniques.

For this reason a tool was developed in the course of this thesis which accepts the output data from the analysis framework ExPlORA and gathers only the physics observables needed for the extraction of polarization observables or cross sections. It also accepts output from simulation for the study of background channels and is able to easily handle the reduced information from one or several beam times at once.

In this work, it is employed for the extraction of the beam asymmetry, while it is also used for first cross section studies in the collaboration. The tool allows to define the various steps of the analysis which can be tuned or exchanged by using a configuration file format as necessary for the investigated reaction.

In the following, a short description concerning the beam asymmetry as a physics observable and how it can be extracted from experimental data is provided in section 5.4.1. The detailed procedure to assemble the necessary physics information from the data is then explained in sections 5.4.2 to 5.4.5. Finally, the results are shown and commented on in section 5.4.6.

5.4.1 The Beam Asymmetry and its Extraction

Fixing the orientation of the polarization plane using linearly polarized photon beams, the photo-produced mesons may be produced with a preferred azimuthal direction. This is described by a polarization observable, the 'beam asymmetry'. It can be experimentally accessed as an asymmetry by performing two sets of measurements in two polarization planes which are orthogonal to each other. The normalized count rate difference measured within bins of azimuthal

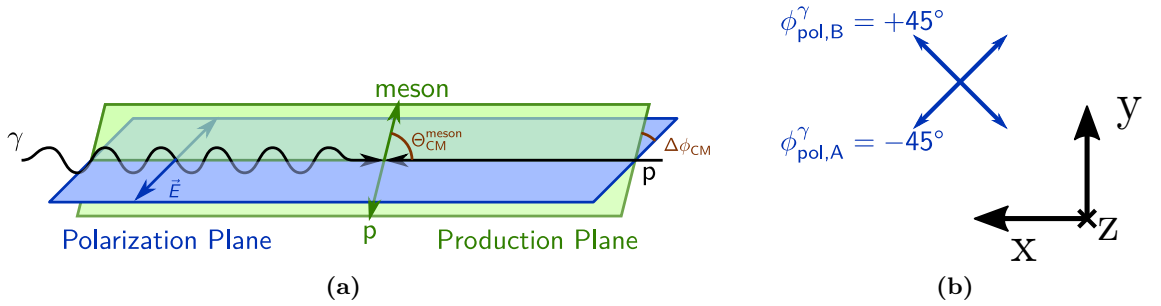

(a) (b)

Figure 5.17: Illustration of the involved angles in the extraction of the beam asymmetry. As shown in fig. 5.17a, the azimuthal angle ϕ is always defined as the angle between the reaction plane and the polarization vector of the photon, the polar angle Θ_{CM}^{meson} is the angle between the meson and the z direction in the centre of momentum system. Figure 5.17b shows the alignment of the two polarization planes set up during data-taking.

angle for the two polarization planes then allows to extract the beam asymmetry.

The differential cross sections of any photoproduction process via linearly polarized photons can be written as a function of the unpolarized cross-section as follows:

$$\left(\frac{d\sigma}{d\Omega}\right)_{pol} = \left(\frac{d\sigma}{d\Omega}\right)_{unpol} \cdot \left(1 - P\left(E_\gamma\right) \cdot \Sigma\left(E_\gamma, \Theta_{CM}^{meson}\right) \cdot \cos\left(2 \cdot \Delta\phi_{CM}\right)\right)$$

with $P\left(E_\gamma\right)$ being the degree of polarization of the photon beam, $\Sigma\left(E_\gamma, \Theta_{CM}^{meson}\right)$ being the beam asymmetry, and $\Delta\phi$ being the angle between the reaction plane and the polarization vector of the photon:

$$\Delta\phi = \Delta\phi_{CM} = \phi^{meson} - \phi^{\gamma}_{pol,A|B}$$

Due to the choice of reference frame having the photon beam direction in z, the azimuthal angles of the meson and baryon are the same for both the centre of momentum and the laboratory system. At BGO-OD, the two polarization planes are set orthogonal to each other and correspond to azimuthal angles of the polarization vector in the laboratory reference system of $\pm 45°$. In the following, the convention $\phi^{\gamma}_{pol,A} = -45°$ and $\phi^{\gamma}_{pol,B} = +45°$ is used (c.f. fig. 5.17) and the corresponding polarization planes are referred to using the shorthand of 'A' and 'B', respectively. Using this scheme, we derive:

$$\left(\frac{d\sigma}{d\Omega}\right)_{pol,A} = \left(\frac{d\sigma}{d\Omega}\right)_{unpol} \cdot \left(1 + P_A\left(E_\gamma\right) \cdot \Sigma\left(E_\gamma, \Theta_{CM}^{meson}\right) \cdot \sin\left(2 \cdot \phi^{meson}\right)\right)$$
$$\left(\frac{d\sigma}{d\Omega}\right)_{pol,B} = \left(\frac{d\sigma}{d\Omega}\right)_{unpol} \cdot \left(1 - P_B\left(E_\gamma\right) \cdot \Sigma\left(E_\gamma, \Theta_{CM}^{meson}\right) \cdot \sin\left(2 \cdot \phi^{meson}\right)\right)$$

The differential cross sections within a given bin of E_γ, Θ_{CM}^{meson} and ϕ^{meson} are related to the

expected count rate by the flux, the solid angle element, the number of scattering centres and the reconstruction efficiency within this bin. Since the number of scattering centres of the target, the solid angle element and the reconstruction efficiency do not depend on the polarization plane, they cancel out if the ratio of count rates is used. The factor for the flux and the extracted degree of polarization do not cancel out, since they both vary for the different planes and may also vary time.

Using this, we can calculate the normalized difference as follows:

$$\frac{\left(\frac{\mathrm{d}\sigma}{\mathrm{d}\Omega}\right)_{\text{pol.,A}} - \left(\frac{\mathrm{d}\sigma}{\mathrm{d}\Omega}\right)_{\text{pol.,B}}}{\left(\frac{\mathrm{d}\sigma}{\mathrm{d}\Omega}\right)_{\text{pol.,A}} + \left(\frac{\mathrm{d}\sigma}{\mathrm{d}\Omega}\right)_{\text{pol.,B}}} = \frac{\left(P_{\mathrm{A}}\left(E_\gamma\right) + P_{\mathrm{B}}\left(E_\gamma\right)\right) \cdot \Sigma\left(E_\gamma, \Theta_{\mathrm{CM}}^{\text{meson}}\right) \cdot \sin\left(2 \cdot \phi^{\text{meson}}\right)}{2 + \left(P_{\mathrm{A}}\left(E_\gamma\right) - P_{\mathrm{B}}\left(E_\gamma\right)\right) \cdot \Sigma\left(E_\gamma, \Theta_{\mathrm{CM}}^{\text{meson}}\right) \cdot \sin\left(2 \cdot \phi^{\text{meson}}\right)}$$

As can be seen from this expression, after binning the experimental data in E_γ and $\Theta_{\mathrm{CM}}^{\text{meson}}$, a variation in ϕ^{meson} is expected. The necessary ingredients for the extraction of the beam asymmetry are:

- The number of $\gamma\mathrm{p} \to \mathrm{p}\pi^0$ events within a bin of E_γ, $\Theta_{\mathrm{CM}}^{\text{meson}}$ and ϕ^{meson}, described in section 5.4.2.
- The degree of polarization depending on E_γ, described in section 5.4.3.
- A scaling factor for the flux to normalize the count rates determined for the two polarization planes, described in section 5.4.4.

Finally, the formula will be rewritten in terms of effective count rates in section 5.4.5.

5.4.2 Selection of $\gamma\mathrm{p} \to \mathrm{p}\pi^0$ Events

The first step is the selection of the events which should be counted for the extraction of the beam asymmetry within a bin of E_γ, $\Theta_{\mathrm{CM}}^{\text{meson}}$ and ϕ^{meson}. As shown at the end of the reconstruction in section 5.3.3, the $\gamma\mathrm{p} \to \mathrm{p}\pi^0$ reaction can be reconstructed almost background-free, applying a cut on the $(\gamma\gamma)$ invariant mass as shown in fig. 5.18.

In preparation of the analysis of the beam asymmetry for ω photoproduction which will be discussed in chapter 6, the cut is expressed as a *weighting factor* which is stored for each single reconstructed event. In this simple case, the factor (which is termed w_{signal} in the following) is just '1' if the reconstructed invariant mass of the meson is inside the cut, and '0' otherwise.

The numbers of selected π^0 events are shown fig. 5.18 both for the extraction from integrating the contents of the histogram between the bounds defined by the cut, and for the sum of the assigned weights. The numbers show exact agreement as expected if the histogram binning is chosen to match the bounds of the cut. The histograms are presented both for the full set of events from the June / July beamtime in polarization setting A and for the subset of events in one special binary with E_γ between 1100 MeV and 1150 MeV, $\Theta_{\mathrm{CM}}^{\text{meson}}$ between 80° and 90° and ϕ^{meson} between 0° and 45°.

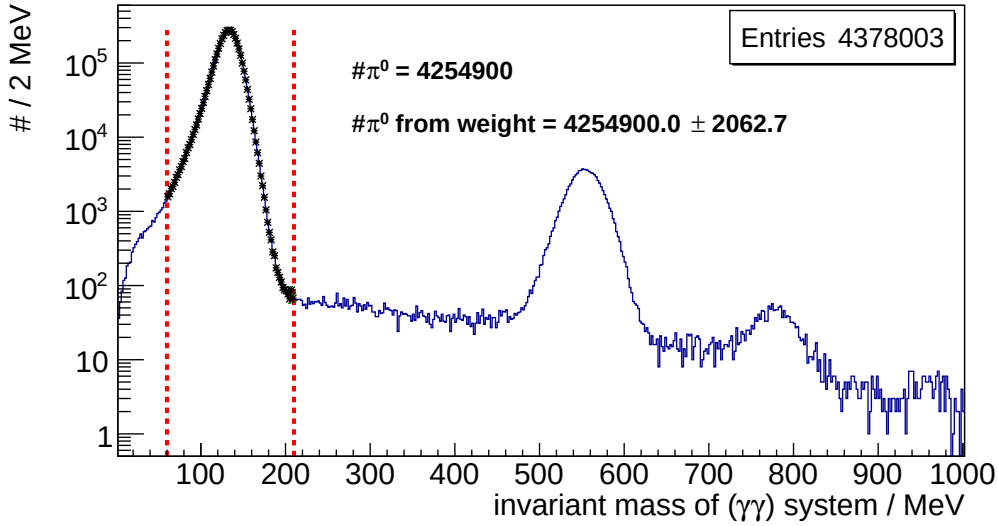

(a) Distribution of invariant masses of the $(\gamma\gamma)$-system for all the events collected in polarization plane A.

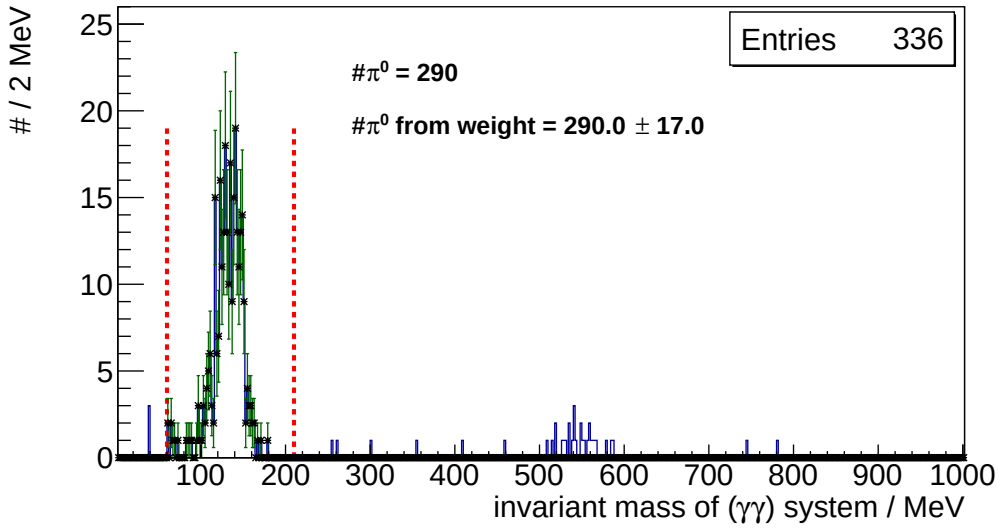

(b) Distribution of invariant masses of the $(\gamma\gamma)$-system for the sub-sample of events with polarization plane A, with E_γ between 1100 MeV and 1150 MeV, $\Theta_{\mathrm{CM}}^{\mathrm{meson}}$ between 80° and 90° and ϕ^{meson} between 0° and 45°.

Figure 5.18: Visualization of the selection of π^0 for all the reconstructed events with polarization plane 'A' for the June / July 2015 data-taking. Figure 5.18a shows the distribution from the full sample. The red, dashed lines indicate the ±75 MeV cut around the PDG mass of the π^0. For comparison, fig. 5.18b shows the distribution within one single bin in E_γ, $\Theta_{\mathrm{CM}}^{\mathrm{meson}}$ and ϕ^{meson}. The upper label in each plot indicates the number of accepted π^0 if the histogram would be integrated between these cut boundaries, while the lower label indicates the sum of the assigned weights for each single reaction. The markers with error bars visualize the weights and the associated statistical errors.

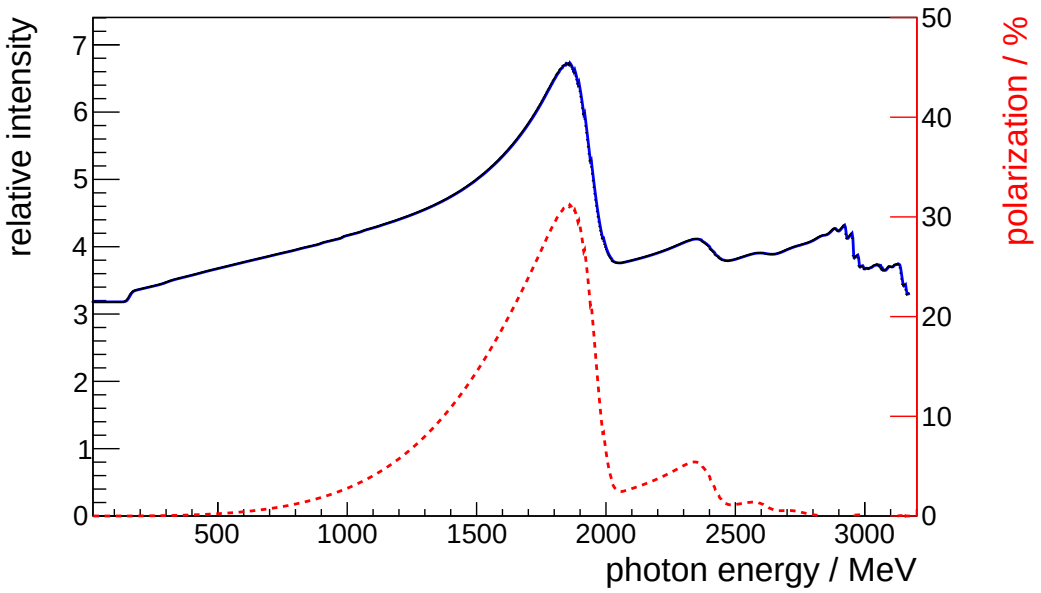

Figure 5.19: Relative intensity spectrum and corresponding degree of polarization extraction was done for the runs 29900 to 30059 of the October / November 2015 beamtime. The upper, blue, solid line shows the fit to the relative intensity of the spectrum recorded with the diamond radiator for the polarization plane 'A' divided by the spectrum recorded using the amorphous radiator. The lower, red, dashed line, is the degree of polarization extracted from the result of the fit.

5.4.3 Extraction of the Degree of Polarization

The extraction of the polarization is performed using the tool COBRIS[(16)] (c.f. [Bel11] and [Bel16]), This utility applies a fit which describes the ratio of the spectrum recorded with the diamond radiator in one polarization plane and the spectrum recorded with an amorphous radiator, which can be either of equivalent thickness or scaled accordingly. According to [Bel16], a relative uncertainty of 1 % can be estimated for the result of this fit. An example for such a graph including the fitted relative spectrum and the extracted degree of polarization is shown in fig. 5.19.

Due to limited available statistics of normalization data in the June / July 2015 dataset, a single extraction of the degree of polarization has been performed over the full beam time, averaging over both polarization planes. The result is shown in fig. 5.20. In October / November 2015, regular taking of dedicated data for normalization allowed to extract the degree of polarization for each day and each polarization plane separately.

For each $\gamma p \to p\pi^0$ reaction, a polarization weight w_{pol} is set from this plot. For a given photon energy, this weight is the inverse of the extracted degree of polarization. It must be noted that the photon energy used in this case is the measured one, not the one which might have been modified by the kinematic fit.

(16) **C**alculation **o**f **Br**emsstrahlung **I**ntensity **S**pectra

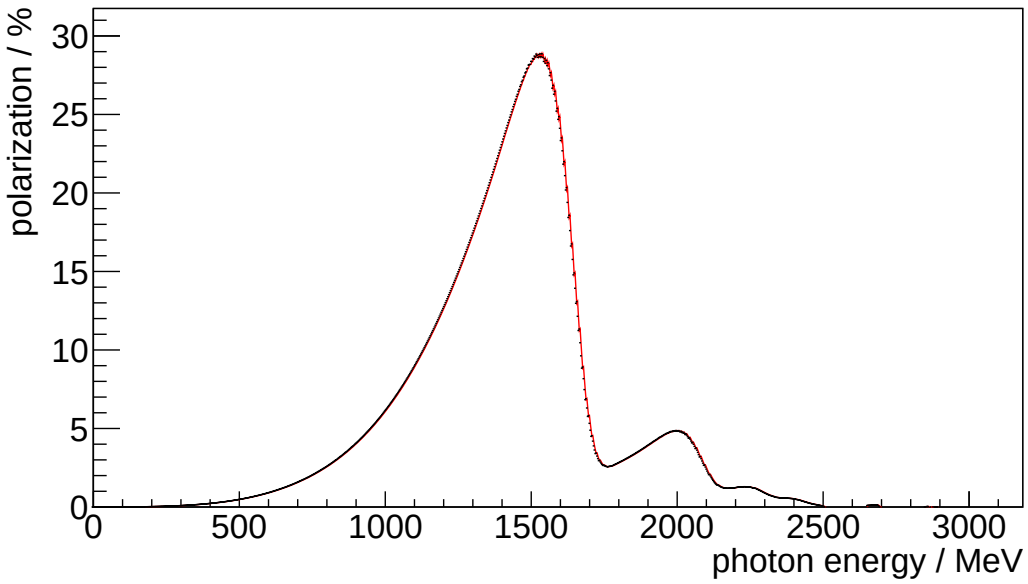

Figure 5.20: Degree of polarization for the June / July 2015 beamtime. Due to the limited available statistics, only a single extraction for both polarization planes over the full beam time is performed.

5.4.4 Photon Flux Normalization

The count rates of the reconstructed $\gamma p \rightarrow p\pi^0$ reactions per polarization plane have to be normalized for the corresponding flux.

Usually, this normalization should be performed using the rate of photons impinging on the experimental target, which could be reconstructed using the tagger detector and the detector setup for flux monitoring. However, the flux normalization procedure has not yet been finalized within the collaboration, such that a more basic approach is chosen. Since for the extraction of the beam asymmetry, any scaling factor which cancels out in the ratio of the count rate difference over the sum of the count rates for the two polarization planes can be neglected, the incident rate of tagged photons measured by the tagger detector can be used. This assumes that any collimation effects or pair production of photons would affect the two polarization settings in the same way for all photon energies, which for sure introduces an additional systematic uncertainty.

The energy-dependent tagged photon rate is provided by the tagger detector via scalers, which are recorded in parallel to normal data-taking and read out in so-called scaler events as already mentioned in section 3.1.2. The tagger electronics provides this information both for each single channel of the hodoscope and for the coincidence channels corresponding to geometrically adjacent scintillators which are used to define the trigger condition. The scalers are gated to count only during the live time of the experiment's data acquisition. Since a counter to measure the active time of the system is included, a rate can be extracted.

To ensure that the information provided by the scalers matches the expectation, a two-fold

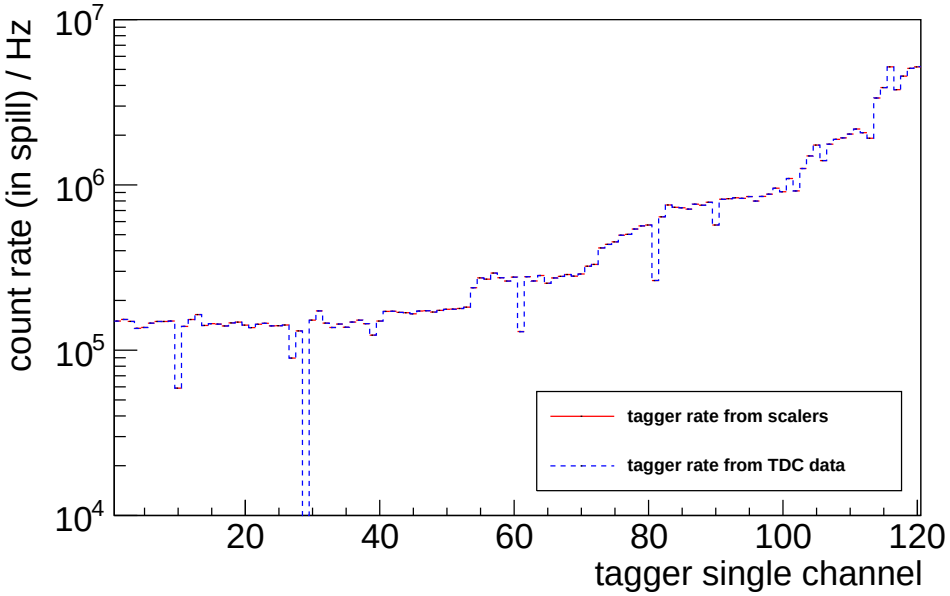

(a) Average count rates for the single channels of the tagger detector.

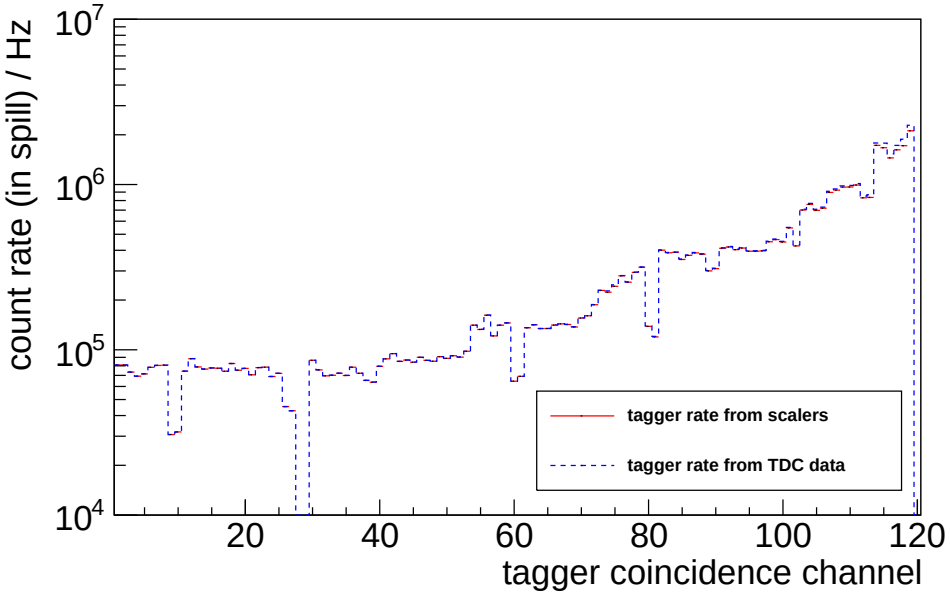

(b) Average count rates for the coincidence channels of the tagger detector.

Figure 5.21: The histograms visualize the average count rates recorded for the tagger detector, once directly taken from the scaler data, and once reconstructed from the TDC information (see text). The full dataset from June / July 2015 has been used.

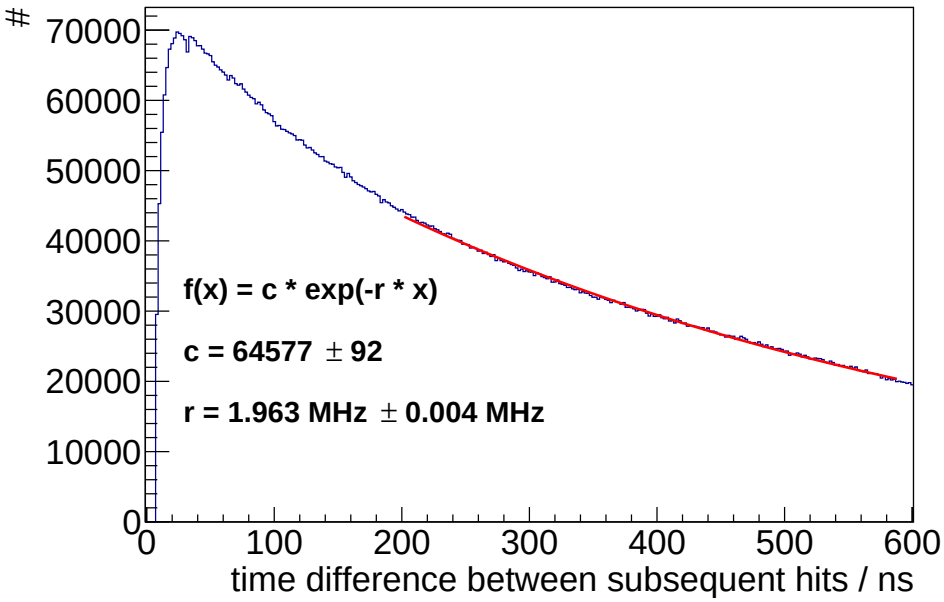

Figure 5.22: Inter-arrival times of hits recorded with one single tagger channel (109) for the June / July 2015 dataset without any event selection. An exponential is fitted and the rate extracted from the slope is shown.

study has been performed, attempting to extract the rate from the time information recorded by the TDC modules. It must be noted that this is only useful as a cross-check: the individual *hits* are only recorded within the time windows of the TDC modules when a trigger event has occured, while the scalers are free-running during the full live time of the acquisition, thus providing superior statistics.

Additionally, the TDC data have to be treated to prevent any biasing as much as possible. For this reason, the prompt peak and the edges of the TDC time window are excluded from all further analysis. Furthermore, the analysis is explicitly limited to events within the extraction period of the accelerator for both scalers and TDC time information.

The first technique consists in the investigation of the distribution of the time differences between subsequent *hits* in one channel, i.e. the 'inter-arrival times'. This distribution shows an exponential fall-off. For a Poisson-like statistics and an on average constant rate, the slope of this exponential allows to extract the rate. One example for the distribution of inter-arrival times and a corresponding fit is visualized for one single tagger channel in fig. 5.22. It should be noted that the fit range must be chosen carefully due to dead time effects for short inter-arrival times. However, it is found that the statistics provided within the time windows recorded by the TDCs only allows a successful extraction of this rate for the channels which are exposed to the highest intensity part of the beam, which is the reason why the second technique described in the following will be used in this study.

The second technique consists in summing the total number of TDC *hits* within the selected

time windows, and divide that by the length of the time window. Both these numbers are accumulated over all events before the division is performed to reduce the numerical error. This is done for each channel individually, taking the different offsets for each TDC channel into account in the removal of the prompt peak region and the TDC window edges. The result of this division yields sufficient statistical significance over the full range of the tagger channels. The comparison between the scaler data and these results for the full June / July 2015 dataset is shown in fig. 5.21a, yielding an almost perfect agreement.

Furthermore, the coincidences between adjacent channels are re-built from the TDC data, employing the known gates used in the FPGA firmware. These coincidences are treated in the same way as the single channel *hits* and are compared against the scalers for the coincidence channels. The result for the full June / July 2015 dataset is displayed in fig. 5.21b. The agreement is perfect for almost all channels, but with increasing intensity, a small difference in rate is observed, pointing to a detected rate which is lower from the scalers than the one reconstructed with the TDC data.

There are several possible explanations for this small disagreement which affects the coincidences only:

- The FPGA uses a slightly different time information than is used for the software reconstruction of the coincidences. While in the software reconstruction, the gate is applied to the time information after the time calibrations are performed (c.f. section 3.3), the FPGA necessarily uses the uncalibrated time information. This includes both the treatment of the integral non-linearity and the t_0 alignment (c.f. section 3.5.2), which in hardware is only possible by the trigger time alignment providing inferior time resolution (c.f. section 3.4.1).

- The gate used to construct the coincidences is set to $\pm 7.2\,\mathrm{ns}$, while the coincidences counted by the FPGA scalers are additionally affected by a dead time of 10 ns. This is not the case for the coincidences reconstructed from the TDC data in software.

It is expected that the first effect mostly cancels out statistically, while the second effect is the dominant contribution to the observed rate-dependent disagreement. This is reflected by the fact that the rate extracted with the scalers, if different, is always lower and shows a rate dependency. The effect is small, since the dead time imposed by the frontend discriminators is also of the order of 10 ns. Furthermore, it should be noted that the coincidences counted by the scalers during the live time are exactly those which could cause a trigger event by design of the firmware, which is not the case for the software reconstructed ones.

From these considerations, it follows that the count rates from the scalers are more reliable and hence they will be used for the normalization of the reconstructed count rates of the $\gamma p \rightarrow p\pi^0$ reactions. Systematic errors which may enter if the rates recorded for the two different polarization planes would differ strongly are of course not excluded by this simple study.

For the following analysis steps, the w_{flux} weights are assigned to each single reconstructed reaction. The sum of all scaler counts for the energy bin (c.f. fig. 5.23a) corresponding to the

measured energy of the incoming photon (i.e. not the one after the kinematic fit) is divided by the bin width to yield a number of counts per MeV. The w_{flux} is then assigned as the reciprocal value of this number.

It must be noted that the ratio of the total counts per energy bin for both polarization planes is not flat, as shown in fig. 5.23b. The major feature in this figure is the shape around 1550 MeV which corresponds to the position of the coherent edge. This indicates that the position of the polarization maximum was on average slightly different for the two polarization planes. Since only a single extraction of the degree of polarization is performed due to the limited statistics, this issue has to be taken into account in the discussion of systematic uncertainties.

5.4.5 Azimuthal Distributions for the Extraction of the Beam Asymmetry

At this point, all the components are ready to calculate the normalized asymmetry of count rates in bins of photon energy, azimuthal and polar angle. The information is stored in the factors w_{pol}, w_{signal} and w_{flux} for each single event.

We define the flux-normalized count rates as:

$$N_{A|B}\left(E_\gamma, \Theta, \phi\right) = \sum_{i=0}^{N} (w_i)$$

with w_i being the weight of each single reaction:

$$w_i = w_{\text{signal}} \cdot w_{\text{flux}}$$

We can now replace the differential cross sections shown in section 5.4.1 with these effective count rates:

$$\frac{N_A - N_B}{N_A + N_B} = \frac{(P_A + P_B) \cdot \Sigma \cdot \sin\left(2 \cdot \phi^{\text{meson}}\right)}{2 + (P_A - P_B) \cdot \Sigma \cdot \sin\left(2 \cdot \phi^{\text{meson}}\right)}$$

Approximating $P = P_A = P_B$, the expression simplifies to:

$$\frac{N_A - N_B}{N_A + N_B} \approx P \cdot \Sigma \cdot \sin\left(2\phi^{\text{meson}}\right) \tag{5.1}$$

As described in section 5.4.3, the extracted degree of polarization is determined and stored for each single reaction. Hence, defining:

$$N_{\text{pol},A|B}\left(E_\gamma, \Theta, \phi\right) = \sum_{i=0}^{N} \left(w_{\text{tot},i}\right)$$

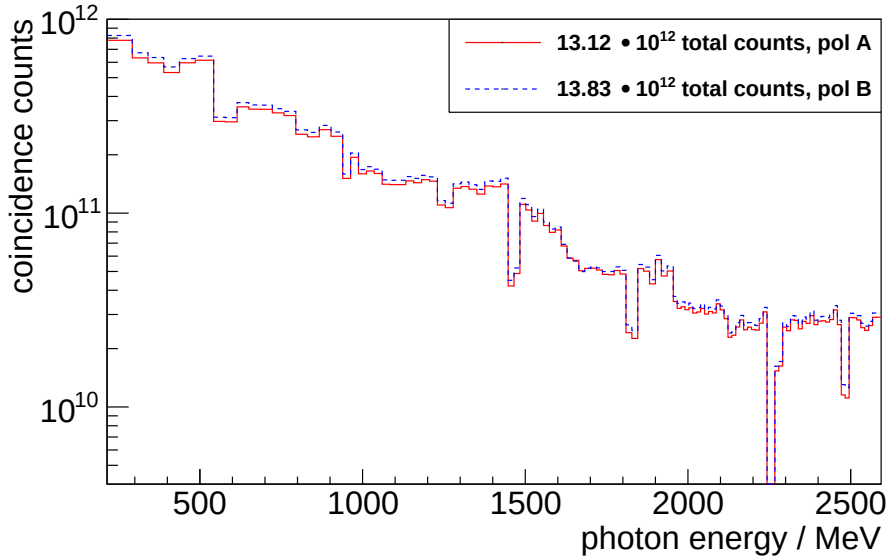

(a) Total coincidence counts recorded by the tagger scalers for the full selected June / July 2015 dataset, separately for the two polarization planes.

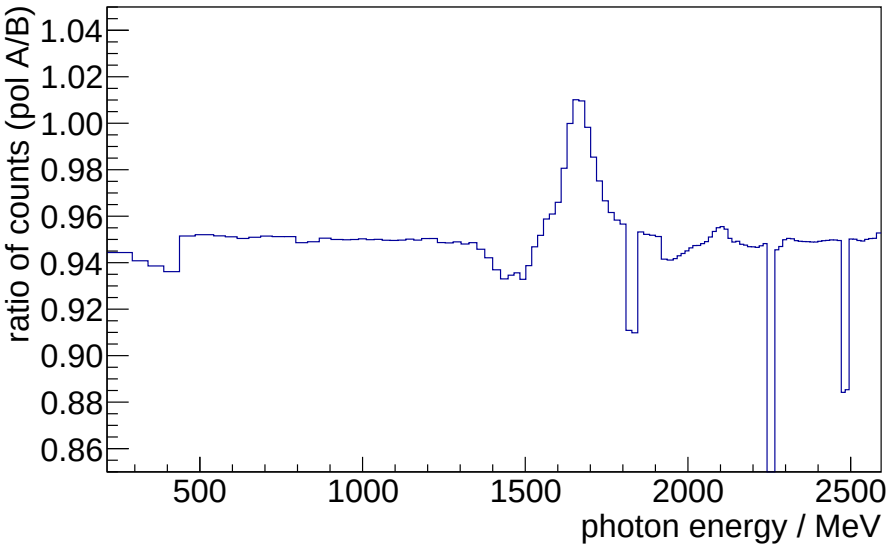

(b) Ratio of the total coincidence counts recorded by the tagger scalers for the two polarization planes.

Figure 5.23: The histograms show the comparison between the total coincidence counts recorded by the tagger scalers for the two different polarization planes over the full analysed June / July 2015 dataset. In fig. 5.23a, the total coincidence counts per polarization plane are plotted together versus the photon energy. In fig. 5.23b, the ratio of coincidence counts for plane 'A' divided by the number of counts for plane 'B' versus the photon energy is displayed.

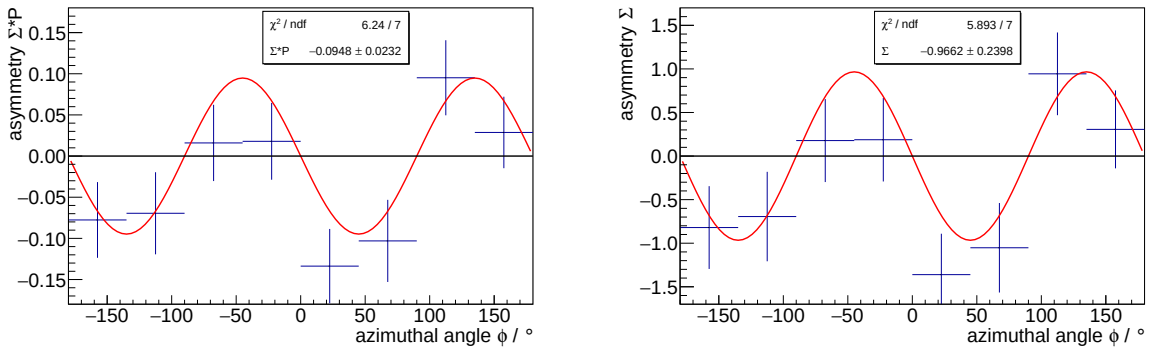

(a) **(b)**

Figure 5.24: Azimuthal distribution of the normalized count rate difference of π^0 photoproduction events for the extraction of the beam asymmetry, including statistical uncertainties. The data refer to the bin with E_γ between 1100 MeV and 1150 MeV and $\Theta_{\mathrm{CM}}^{\mathrm{meson}}$ between 80° and 90°. The result from the fit to the data points is also shown. The differences between the two panels illustrate the impact of the weighting for the degree of polarization.

with $w_{\mathrm{tot},i}$ being the weight of each single reaction, now including the degree of polarization:

$$w_{\mathrm{tot},i} = w_{\mathrm{pol}} \cdot w_i = w_{\mathrm{pol}} \cdot w_{\mathrm{signal}} \cdot w_{\mathrm{flux}}$$

the polarization can be absorbed into the effective count rates, yielding the final expression:

$$\frac{N_{\mathrm{pol},A}\left(E_\gamma,\Theta\right) - N_{\mathrm{pol},B}\left(E_\gamma,\Theta\right)}{N_A\left(E_\gamma,\Theta\right) + N_B\left(E_\gamma,\Theta\right)} \approx \Sigma\left(E_\gamma,\Theta\right) \cdot \sin\left(2 \cdot \phi^{\mathrm{meson}}\right) \tag{5.2}$$

It must be noted that in this expression, different extracted degrees of polarization may be used for the two polarization planes entering $N_{\mathrm{pol},A|B}$. This partially compensates the initial approximation of $P_A = P_B$ by scaling the effective count rates with the corresponding degree of polarization. Notably, it still allows to make use of the degrees of polarization for an unbinned weighting, avoiding artefacts from applying an energy binning beforehand. A small systematic error is introduced by the approximations, which should be far below the statistical error of the presented data. For the dataset recorded in June / July 2015 for which only a single extraction of the degree of polarization is performed, this technique even applies no modification at all, since $P = P_A = P_B$ has to be assumed in any case. The error bars shown in the following are purely statistical, since also any errors on the extraction of the polarization are far below the current statistical uncertainties (c.f. section 5.4.3). A short discussion of the systematic uncertainties will follow at the end of this section.

An example for the ratios of count rates in eight bins of azimuthal angle ϕ^{meson} within a single bin in E_γ and $\Theta_{\mathrm{CM}}^{\mathrm{meson}}$ is shown in fig. 5.24. The data points show an oscillating behaviour

with azimuthal angle which can be described by fitting $\Sigma \sin\left(2 \cdot \phi^{\text{meson}}\right)$ if the large statistical uncertainties of the data points are considered. In the fitting procedure, neither an offset nor a phase shift is allowed, which is why the number of degrees of freedom of the fit to the eight data points shown in fig. 5.24 is exactly seven. It should be noted that the reduced χ^2 for this fit to the data is in general close to '1', i.e. the data points with their associated large statistical uncertainty do not contradict the fitted sinusoidal shape. For illustration, fig. 5.24a shows the extracted $\Sigma \cdot P$ using only the effective count rate ratios without taking the polarization into account (c.f. eq. (5.1)), while fig. 5.24b includes the weighting by the $w_{\text{tot},i}$ factors (c.f eq. (5.2)). Since for this dataset, only a single set of extracted degrees of polarization for one plane is available, the usage of the weights effectively only re-scales the vertical axis.

This fitting procedure is performed in the same way for each bin in E_γ and $\Theta_{\text{CM}}^{\text{meson}}$. The extracted values for $\Sigma\left(E_\gamma, \Theta_{\text{CM}}^{\text{meson}}\right)$ from the fits include only the propagated statistical uncertainties. All corresponding fits to the azimuthal distributions are shown in appendix C.1.

5.4.6 Results of the Beam Asymmetry for the Reaction $\vec{\gamma}p \rightarrow p\pi^0$

The results from the extraction of the beam asymmetry are shown in fig. 5.25 in comparison with already published model descriptions. The points extracted in this work are shown with their statistical error only, i.e. it should be expected that 66 % of the extracted points agree with previous results within 1σ of uncertainty indicated by the error bars.

Comparing the extracted data points with the most recent solutions from the Bonn-Gatchina partial wave analysis, this expectation is indeed fulfilled. However, as can be seen especially for the lowest bin in $\Theta_{\text{CM}}^{\text{meson}}$, the result is too poor in some bins to deduce any statement on the beam asymmetry at all. Furthermore, values which are larger than 1 or smaller than -1 are extracted for some bins. This is a direct consequence of the low statistics within the bins that had to be used for the extraction, and is propagated to the error bars.

The beam asymmetry extraction is performed in 50 MeV wide bins in E_γ ranging from 1100 MeV to 1550 MeV, in twelve 10° wide bins in $\Theta_{\text{CM}}^{\text{meson}}$ covering from 50° to 170°, and in and eight bins in azimuthal angle ϕ with the constraints of zero phase and no offset of the sinusoidal fit.

Variations of this choice of binning especially in the direction of using less angular or energy bins were tested, but the overall results did not change significantly. Any reduction of the number of bins in azimuthal angle ϕ is not considered appropriate, if a $\sin(2\phi)$ modulation has to be observed and fitted. A reduction in the number of bins in photon energy or polar angle would effectively merge the dependent structures in the beam asymmetry.

The statistical uncertainties are all well above 30 %. Taking these large errors into account, the systematic uncertainties play a secondary role. As already discussed in section 5.4.4 where the flux normalization is shown, a disagreement between the count rate in the two polarization planes is observed at the position of the maximum of the polarization. In turn, this leads to a systematic error on the extracted degree of polarization which must be larger than the originally assumed value of 1 % deduced from the fitting procedure. Assuming a worst-case estimate of 5 %

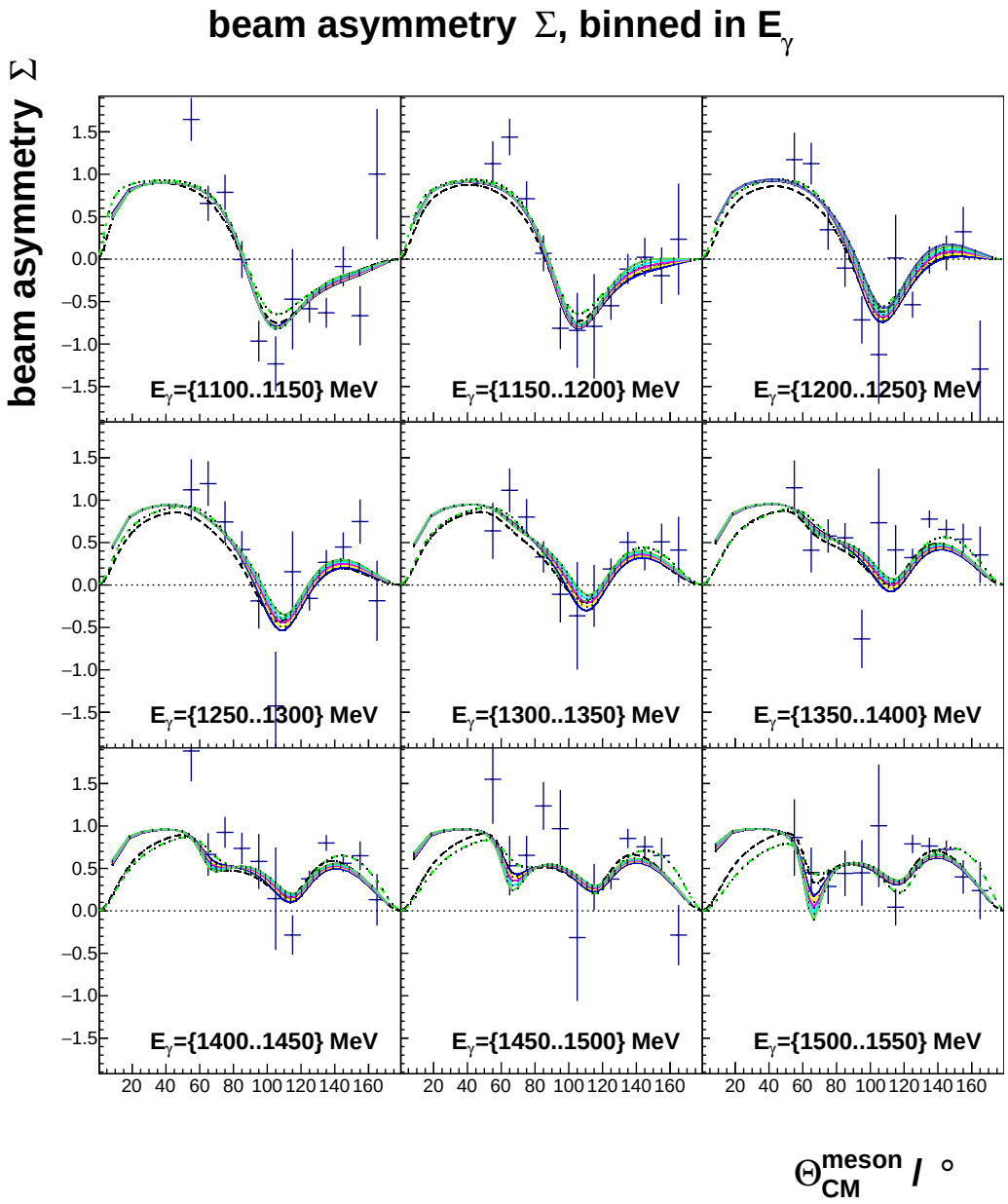

Figure 5.25: Extracted beam asymmetries Σ in bins of E_γ. The blue crosses are the data with statistical errors from this work, while the coloured lines show theoretical descriptions available in literature. The black, dashed line is from the Chew-Mandelstam parametrization published in 2012 (c.f. [Wor+12]), evaluated at the photon energy corresponding to the centre of each displayed bin. The green, dash-dotted line is from the MAID 2007 fit (based on [Dre+99]), again evaluated at the centre of each energy bin. All solid lines are from the Bonn-Gatchina partial wave analysis '2014–02' (c.f. [Gut+14]). This analysis provides solutions in energy bins of 10 MeV, all five solutions contained within one bin of the analysis performed in this thesis are plotted.

absolute on the polarization, which would be caused by an $\approx 10\,\mathrm{MeV}$ shift of the coherent peak and hence the degree of polarization at the steepest part of the distribution (c.f. fig. 5.20) and a degree of polarization of about 20 % absolute, the systematic uncertainty from the extraction of the degree of polarization would be 25 %. This estimate is a worst-case assumption, since the data analysed for the beam asymmetry used the events with photon energies below the steep fall-off of the polarization which only starts at the end of the uppermost extracted bin in E_γ. Furthermore, since the position of the coherent peak was not fully stable over the full beam time, this effect is smoothed statistically.

The systematic error on the relative flux determination is regarded as negligible: using the TDC reconstruction, the values from the scalers could be confirmed with a small rate effect resulting in a less than 5 % count rate difference for the channels hit by the highest intensity part of the photon beam. Since these channels correspond to an incoming photon energy region not investigated in the π^0 analysis (and below the ω photoproduction reaction threshold), any systematic effect on the photon flux determination can not affect the results of this analysis.

Summarizing the results, it has been shown that the extraction of the beam asymmetry of the model channel $\gamma\mathrm{p} \to \mathrm{p}\pi^0$ yielded results which agree with published model descriptions of the beam asymmetry within large statistical errors. The dataset recorded in October / November 2015 is also analysed, but does not yield a high statistical impact for the $\gamma\mathrm{p} \to \mathrm{p}\pi^0$ reaction. This is expected, since the maximum of the polarization was set to 1850 MeV far beyond the threshold for π^0 production, and the lowest photon energies were not tagged since the channels of the tagger detector exposed to the highest intensity were turned off.

The following analysis on the $\omega \to \pi^+\pi^-\pi^0$ reaction will be affected by significantly larger statistical uncertainties due to the lower cross section and competing 'background' channels with the same final state, which is why additional studies on the systematic uncertainties from the data are not performed. However, the analysis will provide a comparison between simulated data and the implemented reconstruction to investigate the effects of the reconstruction and the various cuts, and a short outlook on remaining issues and potential improvements will be given.

Chapter 6

Photoproduction of ω Mesons

In 2012, the BGO-OD collaboration proposed a campaign of measurements of ω photoproduction off proton and neutron target. While the detector setup is still missing foreseen components for the tracking of charged particles, this thesis exploits the existing possibilities of performing the intended measurement of the beam asymmetry.

Following this programme, the first step is indeed the reconstruction of ω photoproduction events via the dominant ω meson decay mode to $(\pi^+\pi^-\pi^0)$. The dataset recorded in June / July 2015, with the maximum of the polarization degree set to 1550 MeV, could allow to measure the beam asymmetry in the energy range already covered by GRAAL (c.f. [Veg+15]), albeit with lower statistics. In a second data taking performed in October / November 2015, the maximum of the polarization degree was adjusted to 1850 MeV which could allow for measurements at higher energy.

In this thesis, both datasets are analysed and the obtained results are assessed and compared to each other. As first step, kinematic studies are described in section 6.1 to guide the later analysis. Secondly, the preanalysis of the datasets is discussed in section 6.2, before the main reconstruction performed on the two datasets is presented in section 6.3. The reconstruction is also applied to simulated events to gain a better understanding of the experimental distributions and the achievable resolutions, as explained in section 6.4. Finally, the number of reconstructed ω photoproduction events is counted for each bin used to extract the beam asymmetry. The developed event weighting technique used for this task is described in section 6.5. The extraction of the beam asymmetry is presented in section 6.6. The chapter is concluded by a short outlook given in section 6.7, which summarizes the hardware issues that make the proposed measurement not yet feasible with the current BGO-OD setup.

6.1 Kinematic Studies

For an exclusive reconstruction of the $p\omega \to p\pi^+\pi^-\pi^0$ reaction, in total five final state particles have to be detected: the proton, the π^- and π^+, and the two photons from the decay of the π^0. While the photons are detectable only in the central BGO calorimeter, the other particles can be detected in all angular regions covered with detectors. An initial study of the expected kinematics of this reaction is performed using simulation to assess the expected angular distributions of the final state particles.

The simulation starts from a fixed accelerator energy setting E_0, from which a photon beam with a $1/E_\gamma$ intensity spectrum is generated by a dedicated event generator. Based on the photon beam energy, the ω-photoproduction events are generated using the ω-photoproduction cross-section. The kinematic of the final state ω and p is generated according to the differential cross-section[(1)]. The event generation does not take any polarization of the photon beam into account. For the results presented in the following, the ω mass has been fixed to 782.65 MeV neglecting the natural width of 8.49 MeV ± 0.08 MeV (c.f. [Pat+16]). Starting from the generated ω and p, the software package GEANT4 (c.f. [Ago+03]) takes over to generated the decay products of the ω meson, propagate them through the geometry of the experiment and simulate energy losses in insensitive material, energy deposits in sensitive detector material and subsequent physics processes such as multiple scattering. In the case of the ω decay, GEANT4 uses a phase-space distribution for the decay particles.

Combining the information from the event generator and the decay products simulated by GEANT4, the expected kinematics for a given condition of the experiment can be extracted. For the data presented in the following, the energy of the incident electron beam was set to 2.9 GeV matching the setting used in the June / July 2015 beam time, apart from the coherent peak in the bremsstrahlung spectrum, which is not reproduced in simulation.

As can be seen in fig. 6.1 which displays the final state signatures created for 1 000 000 generated ω events, GEANT4 reproduces the expected branching ratio of 89.2 % ± 0.7 % for the three-pion decay $\omega \to \pi^+\pi^-\pi^0$ within the uncertainty provided by the PDG, while the radiative decay is accounted for a branching ratio which is slightly higher than the PDG value of 8.28 % ± 0.28 % (c.f. [Pat+16]). With reduced statistics, also the decays to $\omega \to \pi^+\pi^-$ and additional final states via the rare $\pi^0 \to e^-e^+\gamma$ decay are included. It must be noted that GEANT4 does not simulate any other decay modes apart from the three listed ones, so a small difference from the PDG provided values must be expected for normalization reasons. For reference, GEANT4 version 10.1 patchset 02 was used in this thesis work, and the simulated branching ratios are also found back in the physics tables embedded in this version of GEANT4.

For the analysis performed in this thesis, only the $p\omega \to p\pi^+\pi^-\pi^0$ channel will be studied. Apart from the fact that the branching ratio for the radiative decay is lower, the exclusive reconstruction of this channel would require the detection of three photons in the final state.

As indicated in fig. 6.2 which shows the polar angle distribution of the higher energetic photon

(1) The cross-section data were extracted by combining results published in [Kle+08; Bar+03; ABB68; Bal+73; Han96].

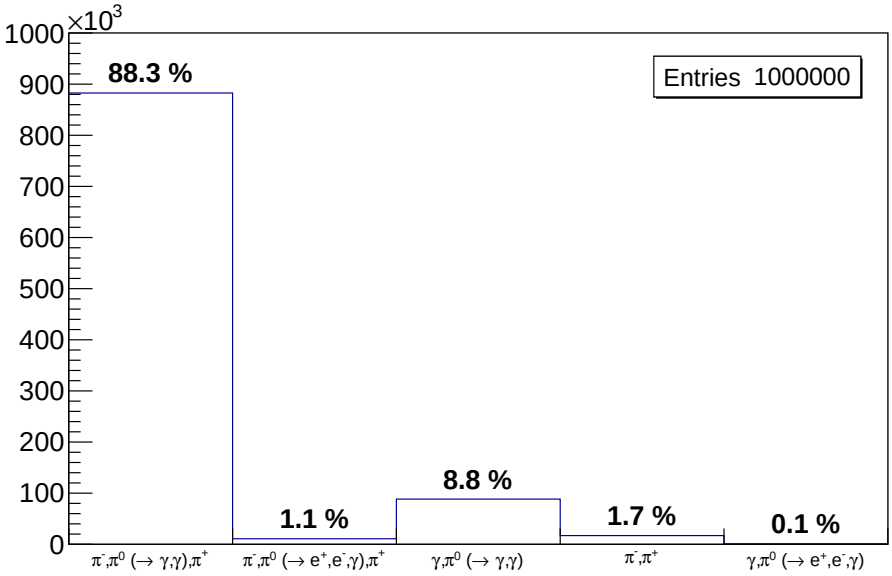

Figure 6.1: Branching ratio of the ω meson as simulated by GEANT4. Adding up the different subsequent π^0 decay signatures, the values 89.4 % for the decay to three pions, 8.9 % for the radiative decay and 1.7 % for the decay into two charged pions are found back. These are the branching ratios which are part of the physics table included in the GEANT4 10.1 patchset 02 release.

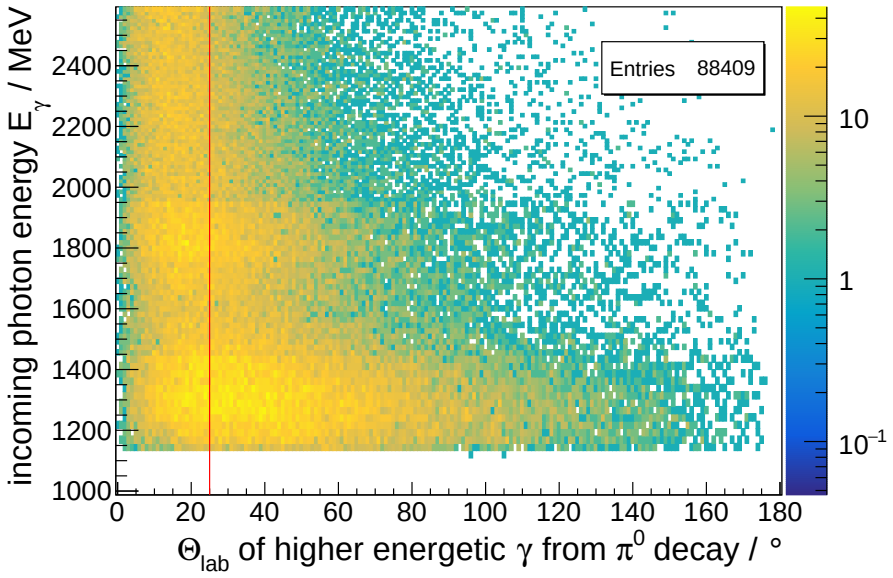

Figure 6.2: Polar angle of the higher energetic photon from the subsequent π^0 decay for the radiative decay of the ω versus the incident photon energy. The distributions are qualitatively similar for the two other decay photons. The red, solid line indicates the 25° below which photons can not be detected in the BGO-OD setup.

from the π^0 in the radiative decay of the ω versus the energy of the incoming photon, the lower polar angles are predominantly covered. However, only the photons emitted with a Θ angle above 25° in the laboratory system can be detected at the BGO-OD experiment within the BGO electromagnetic calorimeter. On the contrary, all photons emitted with a polar angle less than 25° in the laboratory system can not be detected by the experimental setup if they don't undergo pair production. Taking this into account, already about half of these higher energetic photons from the π^0 in the radiative decay of the ω could not be detected. Due to the forward boost, this affects also the two other photons which need to be detected. For this reason, the BGO setup is not well suited for the detection of the final state of the ω radiative decay.

Considering the $\omega \to \pi^+\pi^-\pi^0$ decay, the expected angular distributions of the final state particles are depicted in fig. 6.3. The charged pions shown in fig. 6.3a and fig. 6.3b are in the region covered by the SciRi detector. The angular distributions of the photons from the π^0 decay are shown in fig. 6.3c and fig. 6.3d, while the former plot corresponds to the higher energetic photon and the latter to the lower energetic one. It should be noted that especially the higher energetic photon is often found to be emitted in the direction below 25° in the laboratory system where it can not be detected. Still, the situation is considered less problematic as compared to angular distribution of the photons from the radiative decay of the ω, which would require three photons for an exclusive detection. As shown in fig. 6.3e, the proton is emitted mainly in the direction covered by the SciRi detector and the forward crowns of the BGO calorimeter.

For the analysis performed in this thesis, this implies that the energy information of the charged particles will in most cases not be well defined, since the SciRi detector provides no energy information. For the photons, however, the central electromagnetic calorimeter will be used in any case. The following analysis takes these implications into account and makes use of all detectors in the reconstruction procedure.

6.2 Preanalysis of Datasets

For the analysis of the $p\omega \to p\pi^+\pi^-\pi^0$ decay, both the datasets recorded in June / July 2015 and October / November 2015 are studied. The selections performed for the June / July 2015 data on the preanalysis level are the same as already described in section 5.2.6.

For the October / November 2015 beamtime, important parameters of the setup have been chosen differently: the electron beam energy provided by the accelerator was set to 3200 MeV, and the maximum of the polarization was adjusted to 1850 MeV. Both these changes do not affect the preanalysis in general, so the same clustering and tracking algorithms and the same time selection cuts have been used.

Additionally, a few notable changes have been performed on the hardware side between the two beam times:

- The ARGUS detector was only half available during June / July 2015, providing an improvement of the photon energy resolution in the region 1050 MeV and 1610 MeV, while

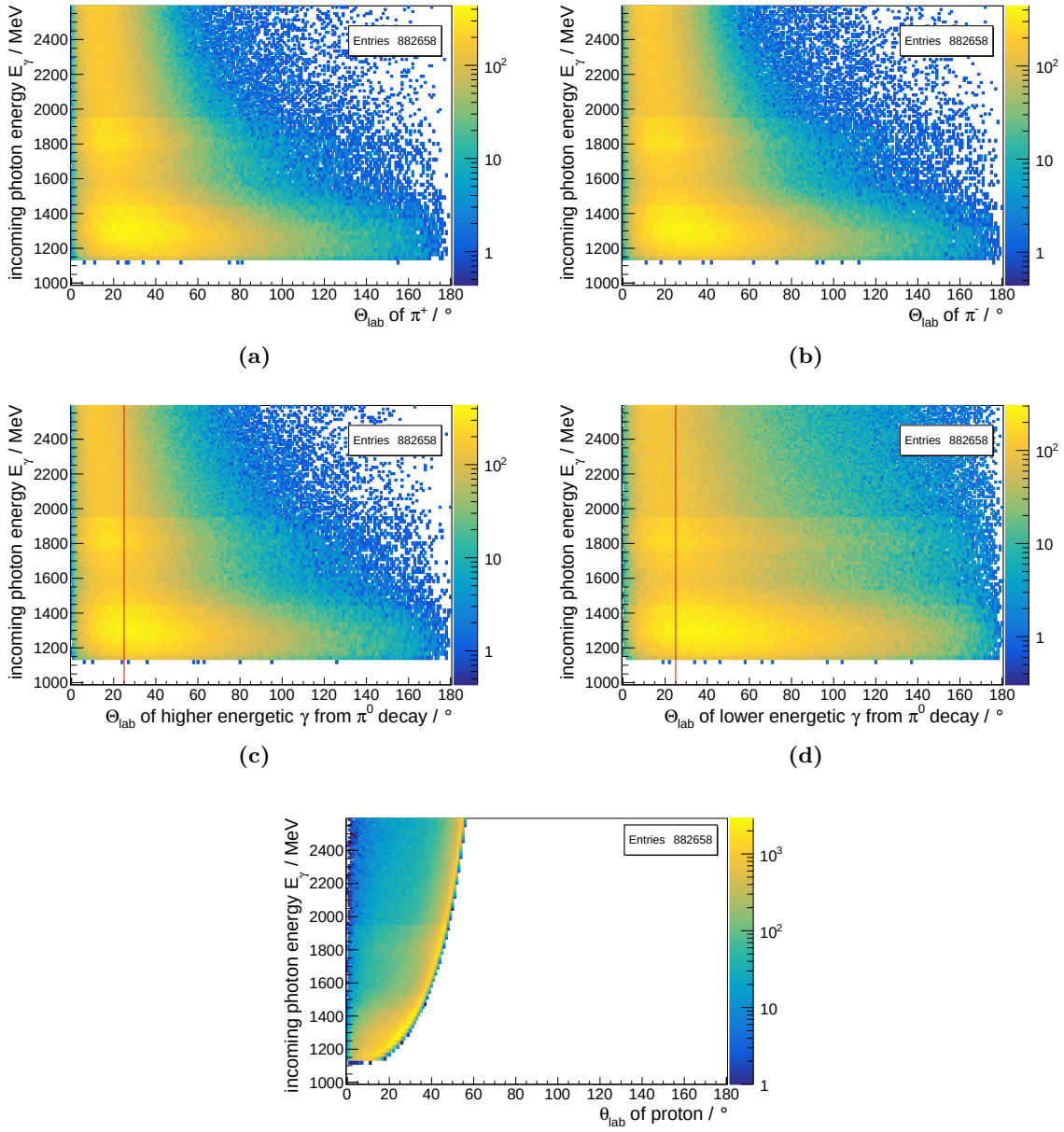

Figure 6.3: Angular distributions expected for the final state products of the reaction $\gamma p \to p\omega$ with $\omega \to \pi^+\pi^-\pi^0$ and $\pi^0 \to \gamma_1\gamma_2$. The ω meson and the proton are generated according to the known total and differential cross-section of the photoproduction process, while the angular distribution of the decay products are generated via phase-space distributions. The red, solid lines indicate the 25° below which photons can not be detected in the BGO-OD setup.

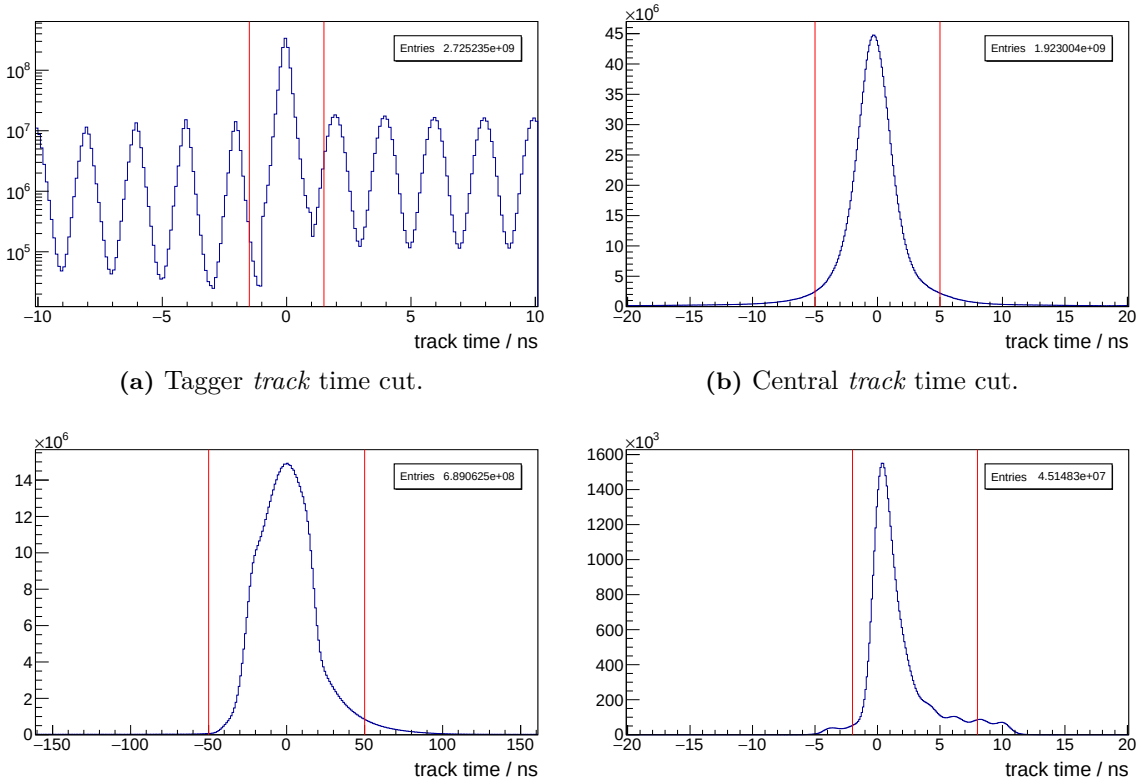

(a) Tagger *track* time cut.

(b) Central *track* time cut.

(c) Intermediate *track* time cut.

(d) Forward *track* time cut.

Figure 6.4: Time distributions of the reconstructed *tracks* in the different detector regions. The applied cuts are indicated by the red, solid lines.

it covered the range of 950 MeV and 2100 MeV in photon energy for October / November 2015.

- An electronics issue with the discriminators of the tagger detector was resolved, leading to an improvement of the start time resolution. Previously, only about 800 ps could be achieved due to fluctuations of the discriminator thresholds, while now the design value of approximately 200 ps is achieved for all channels (c.f. [Bel16]). This also has a strong effect on the quality of the flux determination, as will be shown in section 6.6.
- The efficiency of the drift chambers was significantly lower due to a mistake in the high voltage configuration.
- The experimental target was realigned in longitudinal direction, which will slightly change the polar angles covered by the detector elements as reconstructed when assuming the target centre as the reaction vertex.

Especially the improvement of the time resolution of the tagger is visible in the time selection of the tagger *tracks*. The reduced drift chamber efficiency and its effect on the reconstruction will be shortly discussed at the end of the following analysis section.

Over the full beamtime, data with a beam current of about 1200 pA were recorded, including short tests at half of this current. The open dipole magnet was turned on at half field value of 0.216 T to allow for momentum reconstruction in the forward spectrometer. The complete dataset for all 342 hours of data acquisition time is taken into account for this analysis. This also includes a few hours of alignment data which were recorded with the magnetic field of the open dipole magnet turned off. For this subset of the data, only straight *tracks* can be reconstructed in the forward direction which are not used for this physics analysis.

The selections applied to this dataset are shown in fig. 6.4.

6.3 Reconstruction of $\gamma p \to p\pi^+\pi^-\pi^0$ Events

For the reconstruction of the $\gamma p \to p\omega$ reaction with the ω decaying via $\omega \to \pi^+\pi^-\pi^0$, the five final state particles p, π^+, π^- and two photons have to be identified. The same combinatorics approach as already described in section 5.3.1 is used. This means that *tracks* from all detector regions are used and each of them is interpreted as a proton, a charged pion or a photon according to the available particle hypotheses with associated probabilities.

An exclusive detection of all five final state particles is required. The analysis is performed twice: once only analysing events with exactly five selected *tracks*, and once allowing for up to seven selected *tracks* within the event. The photons from the π^0, in the following termed γ_1 and γ_2, are regarded as identical under exchange in the combinatorics. Already for the case of exactly five reconstructed *tracks* in one event, up to 60 combinations are possible[(2)].

(2) This number is effectively a bit lower, since the forward spectrometer can identify the charge sign and photons are only hypothesized in the central calorimeter.

Additionally, for the October / November 2015 dataset, both the analyses are performed twice for the different approaches for the forward tracking (c.f. section 5.2.3).

In the following, all the histograms which are shown will be from the June / July 2015 dataset for the exclusive analysis requiring exactly five reconstructed *tracks* in the final state. Unless explicitly noted, they will be from data analysed using the drift chamber tracking approach. A comparison between the (in total) six different approaches will be performed.

The analysis steps are similar to the example analysis discussed in section 5.3.1 with some adaptations. The first step again is the usage of the barrel detector as a chargedness-veto in the central region. The cut is technically expressed as enforcement of the corresponding probability to be above 10 %, corresponding to the requirement that all charged particles in the central region were indeed detected in the barrel, while all uncharged particles were not.

The next information on which a cut is performed is the selection by cluster size in the BGO. This is based on the energy-dependent histograms extracted previously from the $p\pi^0$ reconstruction. As a reminder, the probability which is defined using these histograms employs the distribution extracted for protons for any charged particles in the central detector, i.e. in this case, it is used for the final state proton and the two charged pions. A 3.4σ cut which effectively attacks two issues showing up in the dataset is used.

First of, there is an unexpectedly high contribution of charged particles at large polar angles in the laboratory frame. As shown in fig. 6.6 which displays the distribution of the polar angles of the proton candidate, these angles are strongly affected by the cut on the BGO cluster size. As already shown when the kinematics was discussed (c.f. fig. 6.3e), such angles are not expected for the proton by pure kinematics. In fact, these proton candidates observed in real data are likely caused either by particles produced at the second photon collimator or scattering off the beam dump and depositing their energy in the BGO in coincidence with a barrel hit. The size of the corresponding BGO cluster is then usually larger, since the particles traverse the BGO material transverse to the crystal orientation.

The second effect is the rejection of very low energy neutral 'tracks' for which the reconstructed π^0 mass is significantly below the expected mass, as shown in fig. 6.7. This is effectively caused by the selection technique, since the BGO cluster size versus energy relation defining the probability was extracted from reconstructed $p\pi^0$.

Afterwards, a 3.4σ cut on the probability from time of flight, i.e. the particle identification with the ToF walls, is performed. The effect of this cut is minimal, since the statistics of forward going protons due to the kinematics is low as already visible in fig. 6.6 and also demonstrated in the cut overview table (c.f. table 6.1).

Subsequently, the re-scaling of the momenta of all charged particles is performed. Employing the calculation already discussed in section 5.3.2 for this reaction with three charged final state particles with measured angles, the three components of the momentum can be calculated by employing momentum conservation, keeping the angles unchanged. The energy of each charged particle is then derived from its calculated momentum, fixing the mass to the corresponding nominal PDG value.

Furthermore, in the $p\pi^+\pi^-\pi^0$ final state, the invariant mass of the π^0 reconstructed from the

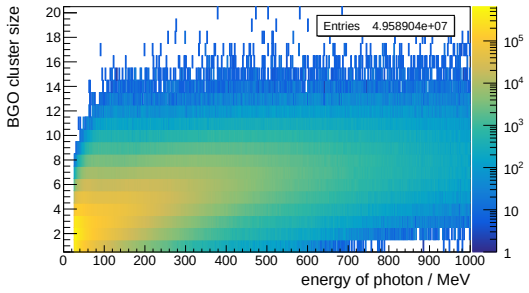

(a) Candidate photons, *before* cut.

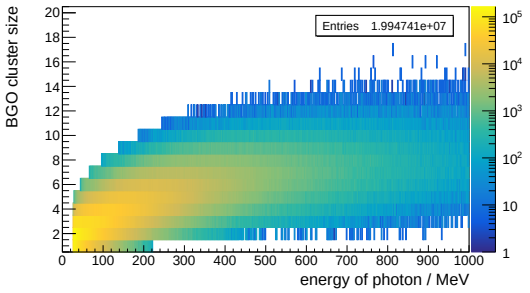

(b) Candidate photons, *after* cut.

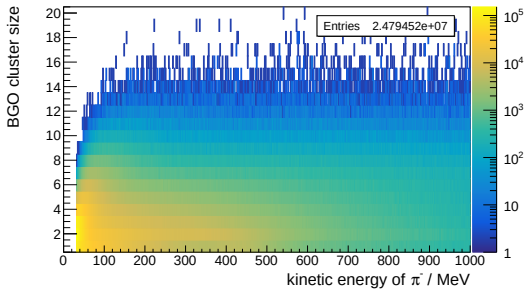

(c) Candidate π^-, *before* cut.

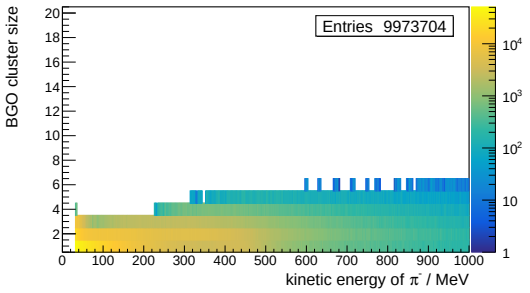

(d) Candidate π^-, *after* cut.

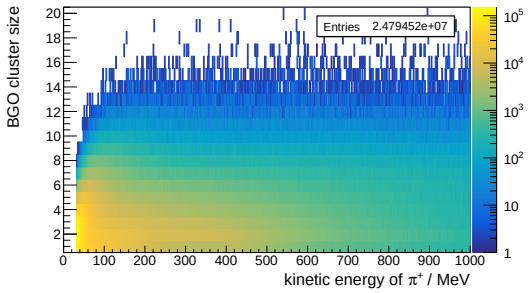

(e) Candidate π^+, *before* cut.

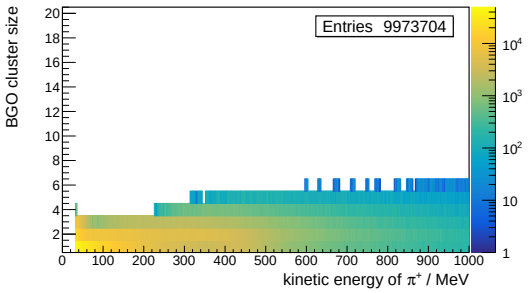

(f) Candidate π^+, *after* cut.

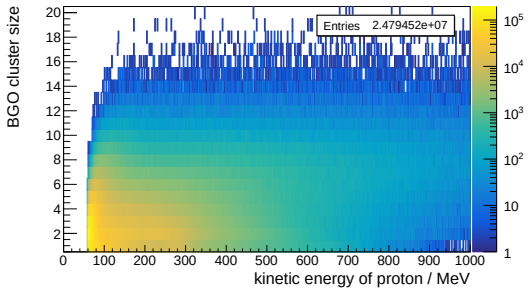

(g) Candidate protons, *before* cut.

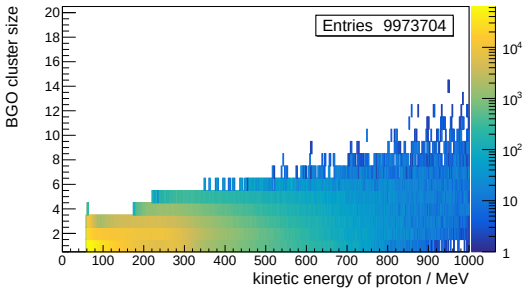

(h) Candidate protons, *after* cut.

Figure 6.5: Visualization of the effect of the energy and particle type dependent BGO cluster size cut. The left column shows the situation before, the right column the situation after application of the cut.

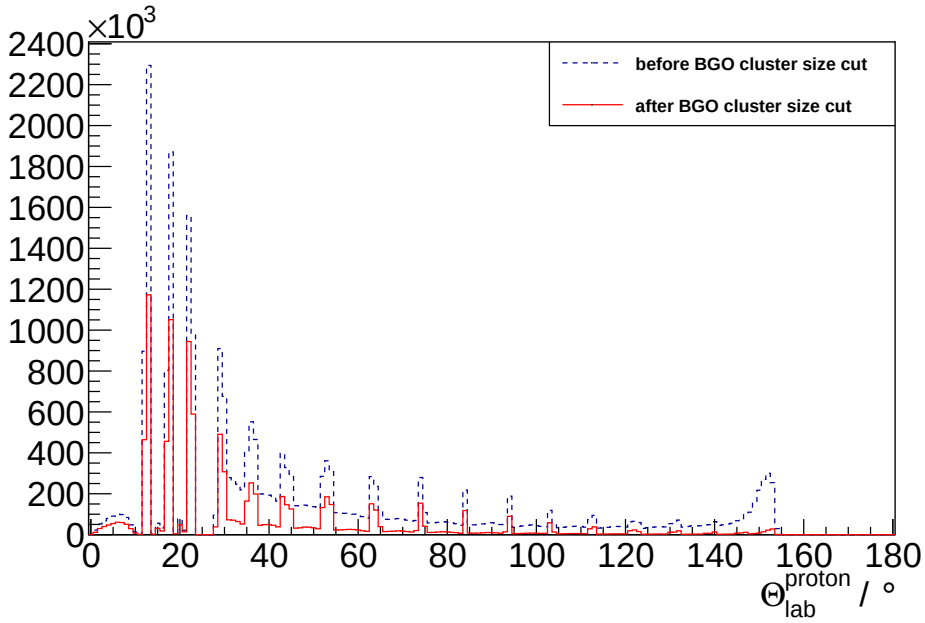

Figure 6.6: Effect of the BGO cluster size cut on the angular distribution of proton candidates of considered reactions.

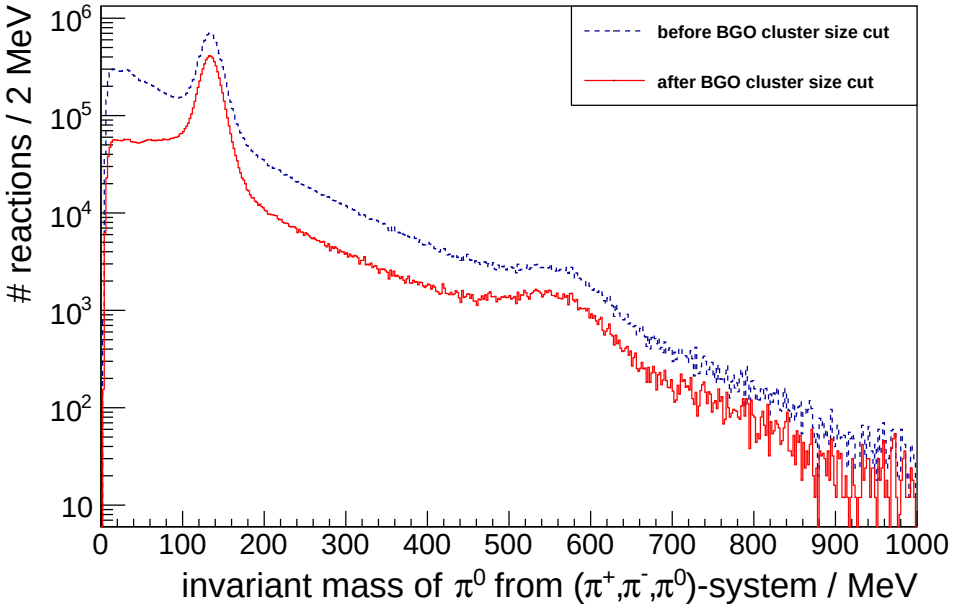

Figure 6.7: Effect of the BGO cluster size cut on the distribution of π^0 candidates of the reaction candidates' $(\pi^+\pi^-\pi^0)$ system.

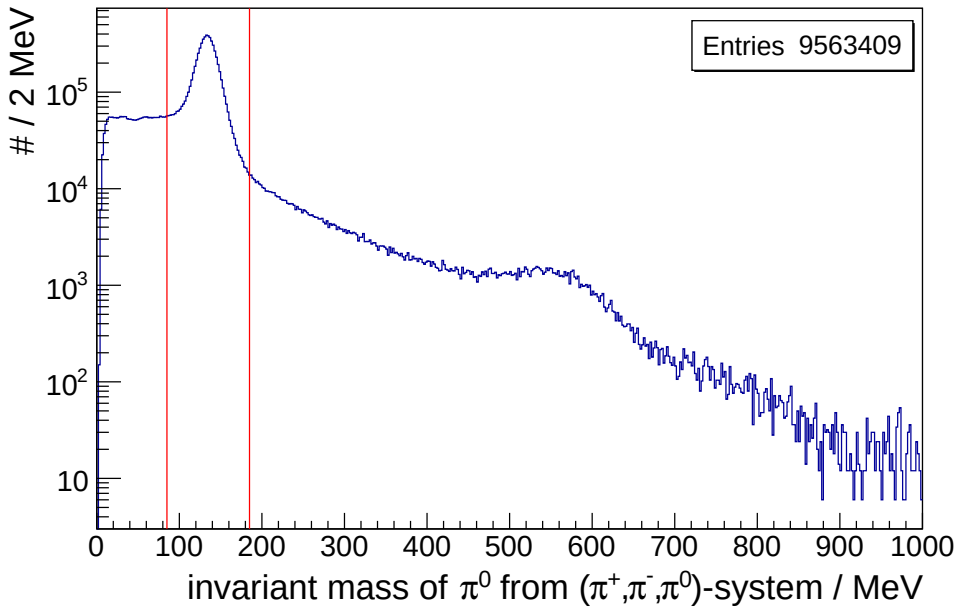

Figure 6.8: Distribution of invariant masses of π^0 candidates from the $(\pi^+\pi^-\pi^0)$ system. The red, solid lines indicate the limits of the applied cut which are ± 50 MeV around the nominal π^0 mass.

two photons detected in the BGO can be constrained to remove wrong combinations from the reconstructed candidate reactions. The cut is defined to accept invariant masses reconstructed from the two photons lying between the nominal π^0 mass ± 50 MeV as indicated in fig. 6.8.

The next constraint is put on the energy conservation. The limit is applied to the energy balance of the full initial state from the incoming photon and the target proton and the reconstructed final state. The difference between these two energies is allowed to be at maximum 300 MeV. While this value matched a 3σ cut for the real data of the $p\pi^0$ reconstructed previously, it is more constraining for the $p\pi^+\pi^-\pi^0$ final state, for which it corresponds approximately to a 2σ cut. However, the higher combinatorics background visible in fig. 6.9 is strongly reduced by this requirement. As will be shown in table 6.1, while the number of candidate reactions is strongly reduced, the number of events with at least one reconstructed reaction is not affected as dominantly.

Finally, before the reaction candidates are handed to the kinematic fitter, they are filtered by their photon energy to be between 500 MeV and 2100 MeV. For higher photon energies, the degree of polarization is negligible and the data can not be used for the extraction of the beam asymmetry. The lower photon energies below the threshold for ω photoproduction are kept such that the $p\eta$ channel is not removed from the set of reconstructed reactions but is kept for cross-checking of a potential signal-biasing of the analysis.

At this stage before the kinematic fit, the missing mass to the proton and the invariant mass of the $(\pi^+\pi^-\pi^0)$ still show different distributions as visible in fig. 6.10. On the contrary, after

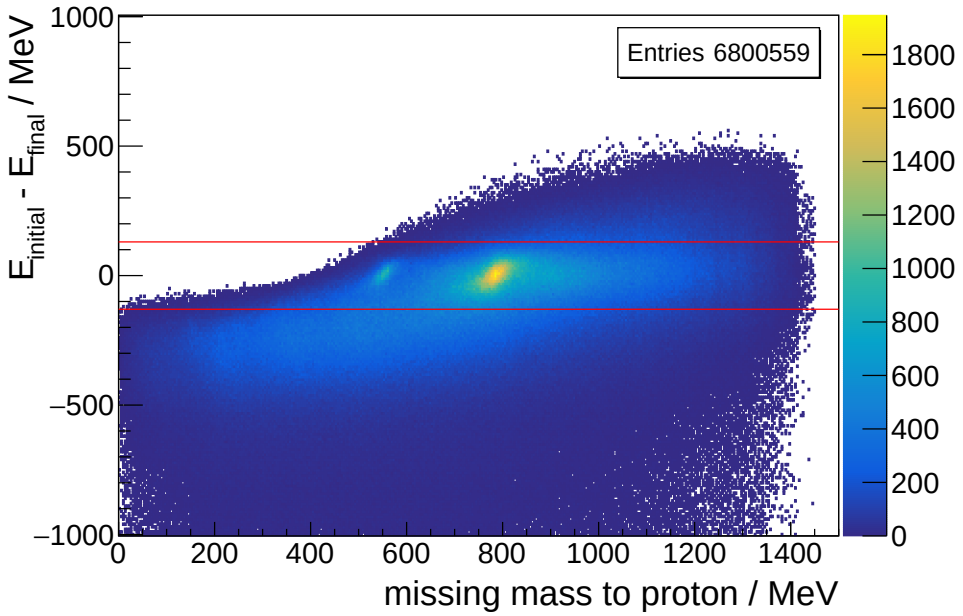

Figure 6.9: Difference between the energy of the initial state minus the energy of the final state versus the missing mass to the proton of each candidate reaction. The red, solid lines indicate the cut on the energy balance to be between ±130 MeV.

the kinematic fit, the two distributions are forced to be identical. Figure 6.10 displays both the distribution of the reconstructed meson mass after the kinematic fit after enforcing a minimum confidence level (CL) of 1 % and the result after selecting the reaction candidate with the highest confidence for each event. This selection of the best combination by confidence level reduces the number of combinations by slightly more than a factor of two, which reduction is fully expected: in the central and intermediate detector region, the charge sign and thus the π^+ and π^- can not be distinguished, thus duplicating the combinatoric possibilities.

It should be noted that even after the kinematic fit procedure, which relies on Gaussian errors, the effect of the granularity of the detectors in polar angle can not be fully overcome. This is visualized in fig. 6.11. The three bands corresponding to the three 'rings' of the SciRi detector are found back as structures in the reconstructed mass for all incoming photon energies. The same effect is also seen for the most forward crowns of the BGO. This effect will be further discussed in the comparison to simulation in section 6.4and in the extraction of the number of ω mesons in section 6.5.

The effect of all selections on the total number of reaction candidates and number of events with at least one reaction candidate is shown in table 6.1. As can be seen, the barrel veto and the BGO cluster size cut have a strong impact on the percentage of events for which a candidate reaction can be reconstructed.

Taking this into account, the analysis has been performed again analysing events with up to two additional *tracks* over the minimum of five, constructing the complete necessary combinatorics.

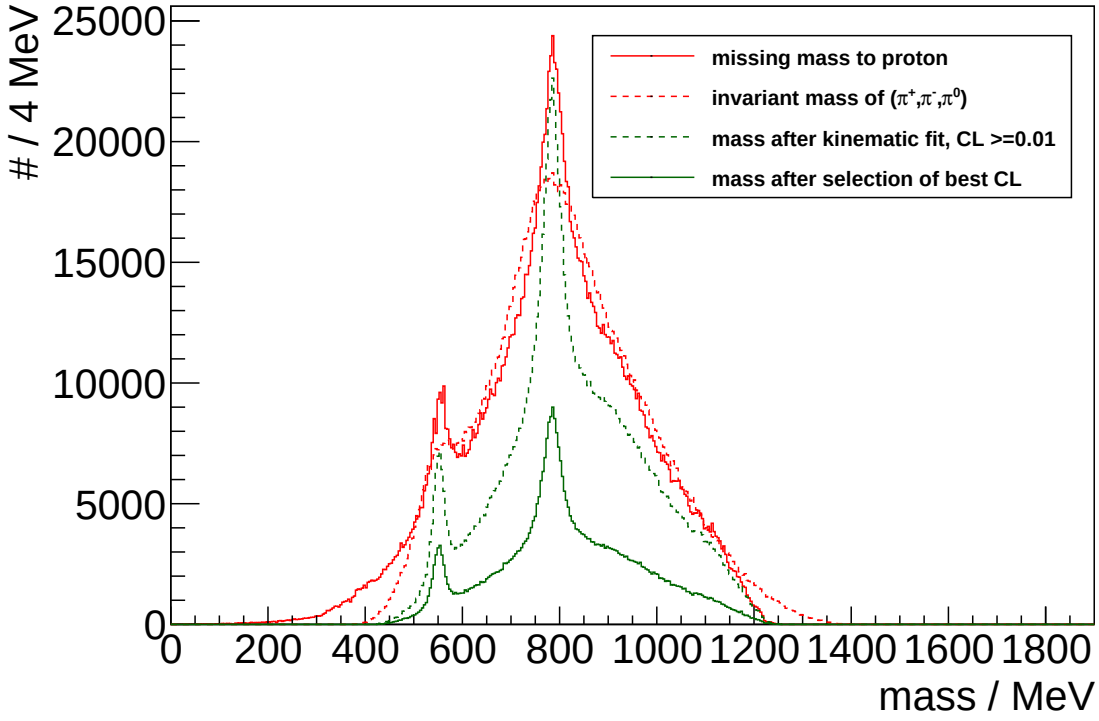

Figure 6.10: Distribution of invariant mass of the candidate $(\pi^+\pi^-\pi^0)$ system and the missing mass to the proton before and after kinematic fitting. The solid, red line indicates the missing mass to the proton, the dashed, red line shows the invariant mass of the $(\pi^+\pi^-\pi^0)$ system before fitting. The distributions are differently shaped, the missing mass to the proton is notable more peaked in the signal regions. After the kinematic fit has been applied, both the masses agree by design. The result from the kinematic fit after requiring a minimum confidence level (CL) of 1 % is indicated by the dashed, green line. The lowest distribution described by the solid, green line is the result of selecting the reaction candidate with the highest confidence level from the kinematic fitting procedure for each event.

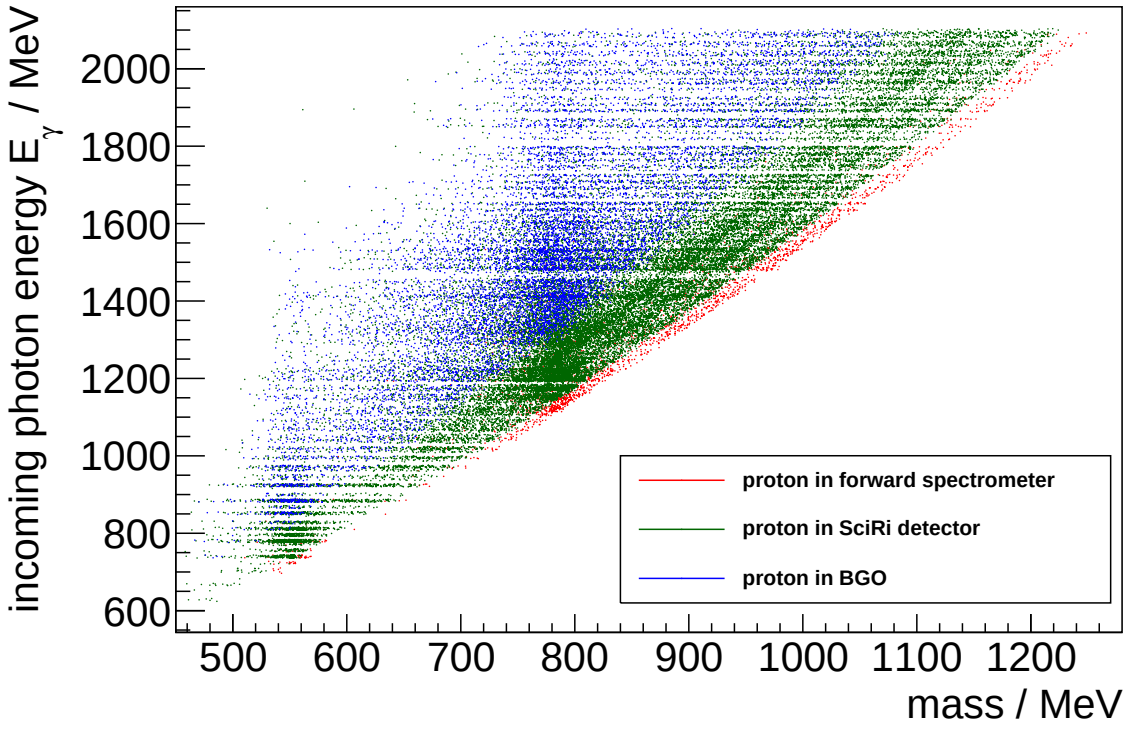

Figure 6.11: Incoming photon energy versus the reconstructed meson mass depending on the angular region in which the proton was detected. The effect of the granularity of the detectors in terms of polar angle can be found back in form of band structures in this histogram.

step of analysis	# of RC	# events with at least 1 RC	# events with at least 1 RC / %
no cuts applied	614 937 472	15 324 242	2.69
barrel veto	24 794 520	4 002 693	0.70
cluster size in BGO	9 973 704	1 652 070	0.29
particle ID in ToF	9 563 409	1 586 894	0.28
momentum recalculation	9 563 409	1 586 894	0.28
invariant mass of π^0	6 800 559	1 140 119	0.20
energy conservation	2 166 431	704 653	0.12
photon energy 500 MeV to 2100 MeV	1 762 220	575 136	0.10
kinematic fit	1 577 753	535 368	0.09
min. confidence 0.01 %	1 195 694	445 113	0.08
selection by best CL	445 113	445 113	0.08

Table 6.1: List of the number of reaction candidates (RC) and events with at least one reconstructed reaction candidate at each stage of the analysis. The dataset used in this case is the data recorded in June / July 2015, limiting the number of *tracks* in one event to exactly five. The drift chamber tracking approach is used. The indicated percentage relates to the total number of data trigger events (570 371 094) of the acquired dataset.

step of analysis	# of RC	# events with at least 1 RC	# events with at least 1 RC / %
no cuts applied	3 113 410 052	21 868 860	3.83
barrel veto	116 246 036	6 835 201	1.20
cluster size in BGO	44 344 648	3 258 676	0.57
particle ID in ToF	42 635 570	3 142 461	0.55
momentum recalculation	42 635 570	3 142 461	0.55
invariant mass of π^0	24 547 416	2 210 084	0.39
energy conservation	5 343 703	1 268 933	0.22
photon energy 500 MeV to 2100 MeV	4 064 602	975 638	0.17
kinematic fit	3 508 459	896 825	0.16
min. confidence 0.01 %	2 299 392	707 543	0.12
selection by best CL	707 543	707 543	0.12

Table 6.2: List of the number of reaction candidates (RC) and events with at least one reconstructed reaction candidate at each stage of the analysis. The dataset used in this case is the data recorded in June / July 2015, allowing for up to seven *tracks* in one event. The drift chamber tracking approach is used. The indicated percentage relates to the total number of data trigger events (570 371 094) of the acquired dataset.

While this increases the computational effort since more than five times as many combinations are considered in total, this allows to study 43 % more events for the analysis right from the beginning, while even 59 % more events with a reaction candidate are reconstructed after all selections (c.f. table 6.2).

However, this improvement in number of reconstructed events effectively corresponds to a larger contamination of 'background' events, as can be deduced from fig. 6.12. Both the signal regions of η and ω and the continuous distribution over the full mass range are enhanced if events with up to seven selected *tracks* are considered. Nevertheless, the ratio of the distributions which is plotted in fig. 6.12b shows that the increased number of reconstructed events is minimum at the η and ω mass, i.e. the signal to background ratio is decreased. For this reason, in the extraction of the beam asymmetry and for the comparison to simulation, only the 'cleaner' reconstruction requiring exactly five *tracks* will be studied in detail.

As already discussed, the same analysis is also applied to the data recorded in October / November 2015. It is expected that the tracking approach based on the drift chambers as initial seed for the tracking behind the magnet is adversely affected by the reduced drift chamber efficiency. A study was performed within the collaboration (c.f. fig. 6.13) checking this efficiency for the several drift chamber layers by making use of the surrounding chambers. The results have been binned in terms of β of the corresponding reconstructed *track* and cross-checked with simulation. A similar study has also been performed for the June / July 2015 data. The efficiency for the same chamber was found to be well above 80 % over the full range in β with only slightly lower efficiencies for the other chambers.

This effect has direct influence on the reconstruction in the forward region as can be seen in fig. 6.14. The diagram shows the polar angle distribution of the final state protons of reconstructed $\gamma p \to p\omega$ with $\omega \to \pi^+\pi^-\pi^0$ reactions for the analyses performed in the two different beam times with the different tracking approaches. Several features can be noted:

- The reconstructed statistics is higher for the October / November dataset, especially for larger $\Theta_{\text{lab}}^{\text{proton}}$. This shift of the distribution towards higher $\Theta_{\text{lab}}^{\text{proton}}$ is expected due to the increased beam energy and position of coherent edge and can also be deduced from the kinematic studies shown in section 6.1. The higher overall statistics is mainly caused by the October / November 2015 data-taking period being longer and being performed with a higher average beam intensity. This is also reflected by the total number of analysed events (570 371 094 for June / July 2015 versus 1139 808 898 for October / November 2015).

- Even though the overall statistics is higher, the number of forward protons from the reconstructed reactions in the October / November is almost the same as in the June / July dataset if the drift chamber tracking approach is used. This can be explained by the reduced efficiency of the drift chambers.

- Making use of the ToF *track*-finding algorithm, the statistics in the forward region is almost doubled nearly matching the other detector regions.

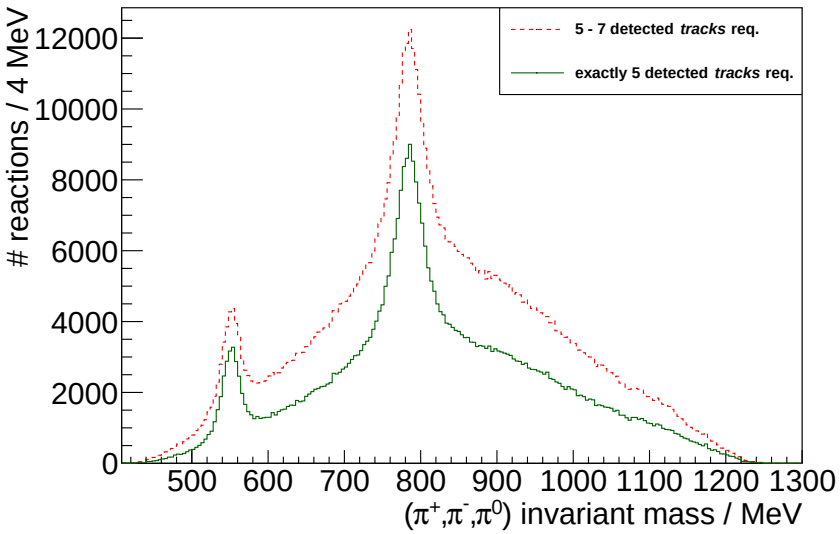

(a) Distribution of invariant masses of the $p\pi^+\pi^-\pi^0$ system for the two different analyses.

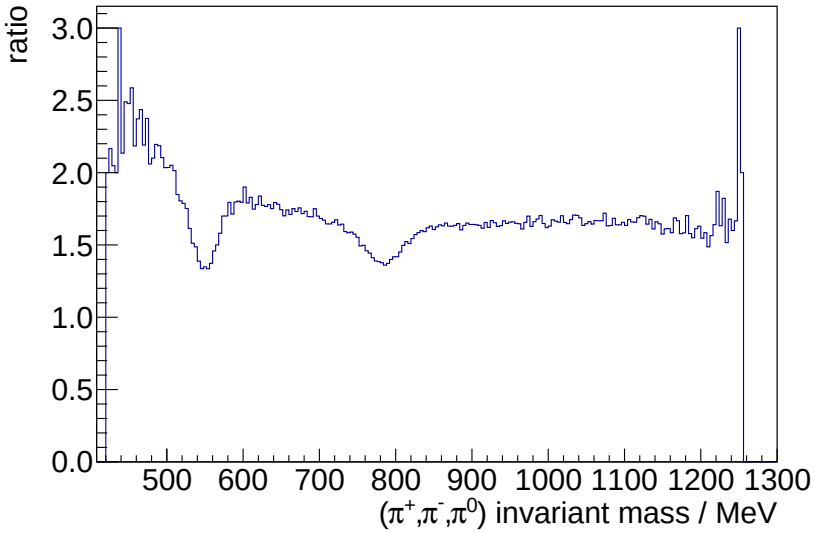

(b) Ratio between the invariant mass distributions reconstructed using events with five to seven *tracks* and only events with exactly five *tracks*.

Figure 6.12: Comparison between the two approaches of selecting events with exactly five reconstructed *tracks* in the final state, and allowing for up to seven reconstructed *tracks*. The comparison is performed via the invariant mass distributions at the end of the analysis chain, i.e. the 'best' reaction candidate per event has already been selected. Figure 6.12a shows the two distributions in direct comparison, while fig. 6.12b shows the distribution allowing for up to seven reconstructed *tracks* in the event divided by the more constraining analysis requiring exactly five *tracks*.

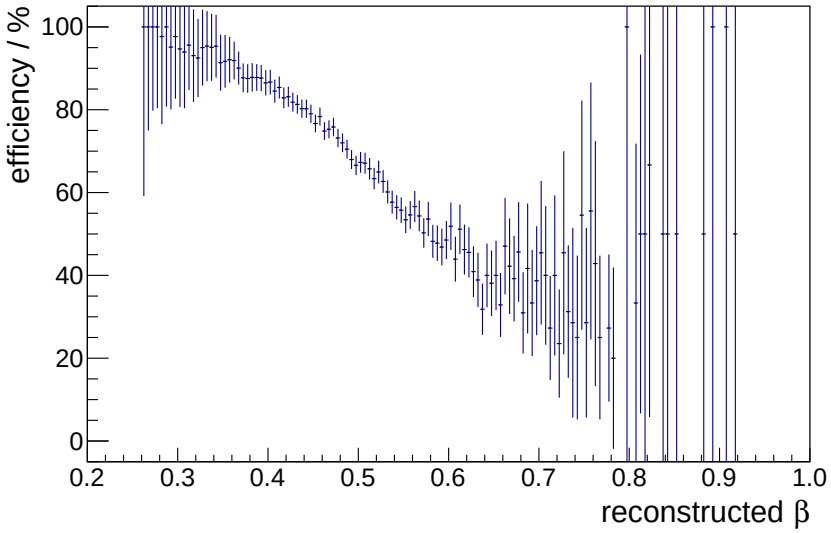

Figure 6.13: The drift chamber efficiency determined for one layer of one chamber (following the BGO-OD internal naming convention, X11) in the October / November 2015 beamtime for protons ([Jud17]). The reconstructed efficiencies obtained for other chambers and layers are very similar. More details about the general technique are described in [Zim17].

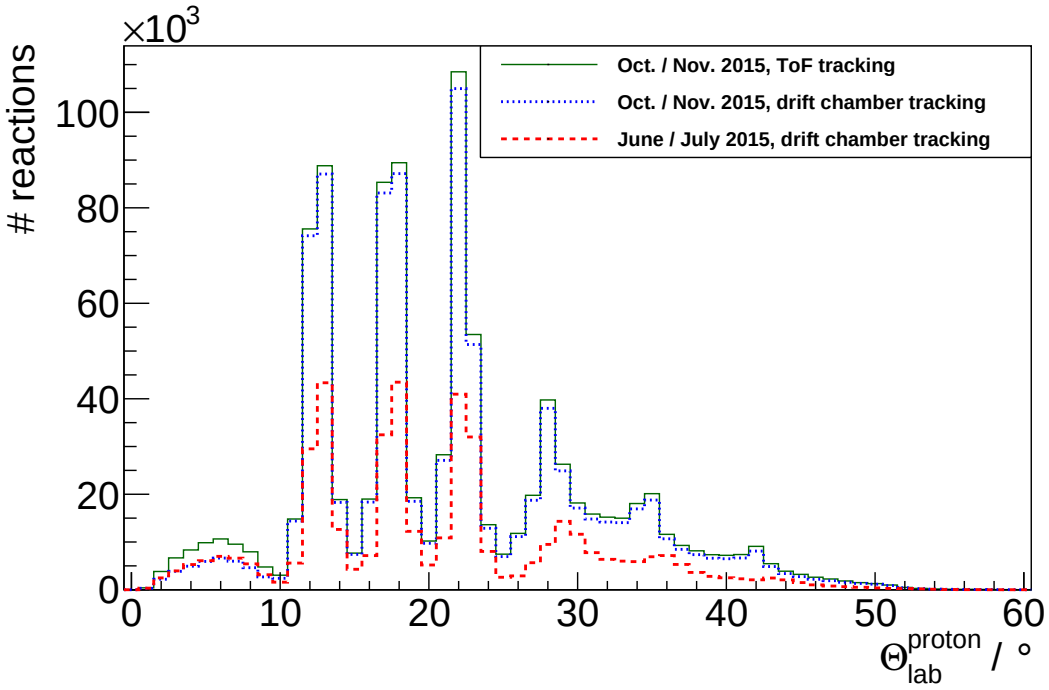

Figure 6.14: Polar angle distribution of the final state protons of reconstructed $\gamma p \to p\omega$ reactions for the analyses performed in the two different beam times with the different tracking approaches.

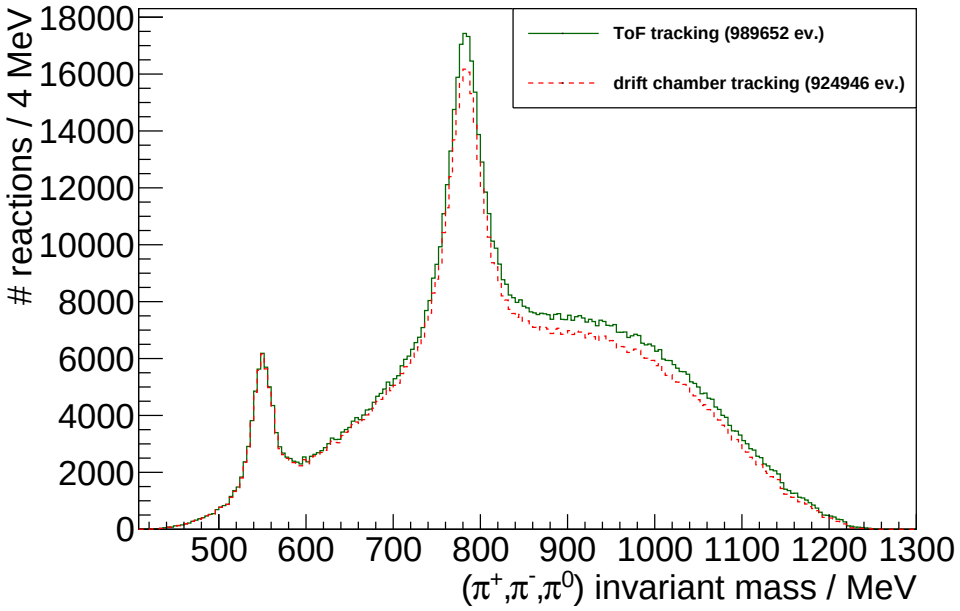

(a)

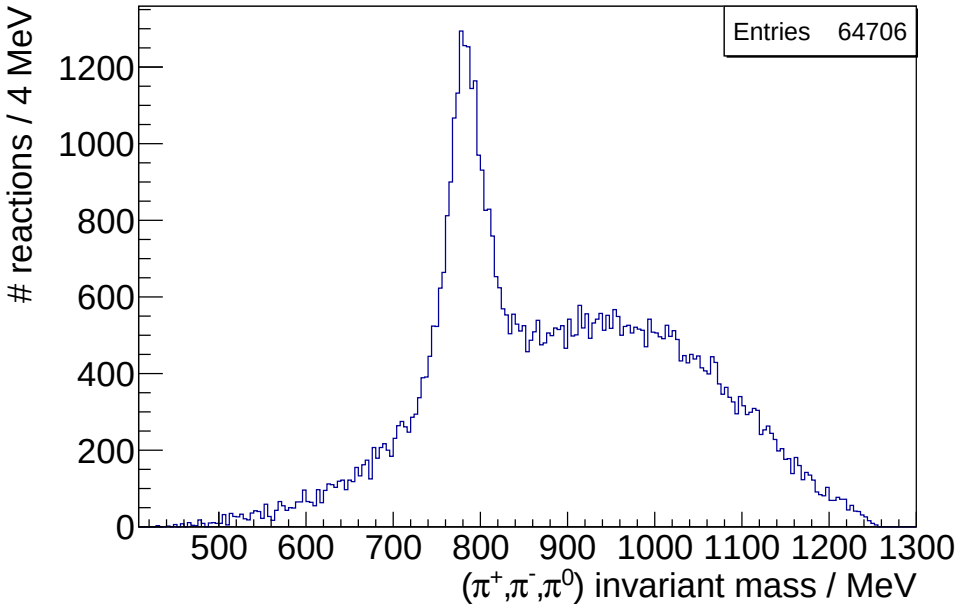

(b)

Figure 6.15: Comparison of the distributions of invariant masses of the $(\pi^+\pi^-\pi^0)$ system obtained at the last stage of the analyses of the October / November 2015 data using the two different tracking approaches. Figure 6.15a shows the two distributions plotted together, while fig. 6.15b displays the enhancement obtained by using the ToF tracking approach over the drift chamber tracking approach.

step of analysis	# of RC	# events with at least 1 RC	# events with at least 1 RC / %
no cuts applied	1 471 695 320	37 481 577	3.29
barrel veto	61 051 592	9 751 285	0.86
cluster size in BGO	25 107 256	4 127 202	0.36
particle ID in ToF	23 595 827	3 859 973	0.34
momentum recalculation	23 595 827	3 859 973	0.34
invariant mass of π^0	16 631 368	2 749 756	0.24
energy conservation	5 441 042	1 735 545	0.15
photon energy 500 MeV to 2100 MeV	3 971 733	1 269 345	0.11
kinematic fit	3 564 371	1 185 638	0.10
min. confidence 0.01 %	2 719 737	989 652	0.09
selection by best CL	989 652	989 652	0.09

Table 6.3: List of the number of reaction candidates (RC) and events with at least one reconstructed reaction candidate at each stage of the analysis. The dataset used in this case is the data recorded in October / November 2015, limiting the number of *tracks* in one event to exactly five, and employing the ToF tracking approach. The indicated percentage relates to the total number of data trigger events (1 139 808 898) of the acquired dataset.

- A peaked structure is found between 10° and 25°. These very high count rates are already expected from the kinematic studies performed in section 6.1, the peaking is caused by the granularity of the SciRi detector.
- Peaked structures are also found in the central region (above 22.5°) matching the granularity of the BGO crystals. They are slightly shifted between the June / July 2015 and October / November 2015 dataset. This is caused by a misalignment of the target in longitudinal direction in the June / July data-taking period, which is taken into account in the reconstruction and hence changes the laboratory angles effectively covered by the detector elements.
- Additionally, also more reactions with protons found in the other detector regions can be reconstructed, which is expected for kinematics with a charged pion going into the forward region.

It must be noted that the ToF tracking approach could be further improved to achieve a better resolution in the extraction of the momentum and does not efficiently suppress badly reconstructed *tracks* which could be created for uncorrelated hits in the front and rear part of the experiment. These issues do not affect the analysis performed here, since the momentum information is only accessed to identify the proton. Apart from this, only the measured angles of the proton are used.

step of analysis	# of RC	# events with at least 1 RC	# events with at least 1 RC / %
no cuts applied	5 177 178	184 342	18.43
barrel veto	498 360	91 502	9.15
cluster size in BGO	293 622	55 338	5.53
particle ID in ToF	278 600	54 461	5.45
momentum recalculation	278 600	54 461	5.45
invariant mass of π^0	249 695	49 148	4.91
energy conservation	134 877	41 037	4.10
photon energy 500 MeV to 2100 MeV	117 010	34 482	3.45
kinematic fit	107 391	32 706	3.27
min. confidence 0.01 %	81 201	27 624	2.76
selection by best CL	27 624	27 624	2.76

Table 6.4: List of the number of reaction candidates (RC) and events with at least one reconstructed reaction candidate at each stage of the analysis. The indicated percentage relates to the total number of generated events with $p\omega$ in the final state (1 000 000). In this analysis, only events with exactly five reconstructed *tracks* have been accepted. It must be noted that of these only the subset of 882 658 events decayed to the $p\pi^+\pi^-\gamma\gamma$ final state according to the branching ratios.

As a cross-check, the invariant mass distributions obtained using the two tracking approaches after the full analysis chain including the kinematic fit are compared in fig. 6.15. The increased number of ω events clearly makes the ToF tracking approach preferable for the October / November 2015 dataset. Subsequently, the same reconstruction is applied to simulated data to understand the appropriate technique to distinguish the ω signal from the competing background channels.

6.4 Simulation Studies on the Event Reconstruction Procedure

The same reconstruction is applied to the event-generated reactions with their corresponding simulated final states and digitized energy deposits in the detector material. Using the generated information, the quality of the reconstruction can be tested and a better understanding of how the experimentally obtained signal distribution can be better distinguished from competing background channels with the same final state signature will be gained.

Running the analysis with the very same cuts on a set of 1 000 000 generated $\gamma p \to p\omega$ events, of which for 882 658 events the $p\pi^+\pi^-\gamma\gamma$ final state is generated, the results presented in table 6.4 and table 6.5 are obtained.

It must be noted that the simulation has some known deficits. Notably, the cluster size versus energy relation in the BGO differs in the GEANT4 simulation versus the experimentally observed relation and the thresholds for the digitization are not optimized yet, while adaptions of the

step of analysis	# of RC	# events with at least 1 RC	# events with at least 1 RC / %
no cuts applied	26 897 368	260 689	26.07
barrel veto	1 890 388	140 054	14.01
cluster size in BGO	863 074	86 894	8.69
particle ID in ToF	822 019	85 286	8.53
momentum recalculation	822 019	85 286	8.53
invariant mass of π^0	611 591	73 414	7.34
energy conservation	238 813	58 364	5.84
photon energy 500 MeV to 2100 MeV	207 674	49 341	4.93
kinematic fit	187 368	46 650	4.67
min. confidence 0.01 %	129 869	38 122	3.81
selection by best CL	38 122	38 122	3.81

Table 6.5: List of the number of reaction candidates (RC) and events with at least one reconstructed reaction candidate at each stage of the analysis. The indicated percentage relates to the total number of generated events with pω in the final state (1 000 000). In this analysis, events with up to seven reconstructed *tracks* have been accepted. It must be noted that of these only the subset of 882 658 events decayed to the p$\pi^+\pi^-\gamma\gamma$ final state according to the branching ratios.

energy and time resolutions are implemented in the simulation. For these reasons, differences in the effect of the BGO cluster size cut and the effect of allowing for more *tracks* in the event are expected.

As shown in fig. 6.16, even for the 'clean' situation of simulated signal events, the main peak which is found back at the mass of the ω meson is lying on a wide, smooth background shape. Indeed, this shape corresponds to the reaction candidates for which the proton has been misidentified as a charged pion and vice-versa.

This can be checked particle by particle by comparing the kinematic variables produced by the event generator and GEANT4 with the one 'reconstructed' at the end of the analysis. the generated particles and the particles identified at the end of the analysis are associated to each other based on their angular correlation.

The difference between generated and reconstructed total energy is visualized in fig. 6.17 for the different kinds of particles. The second peak found for all charged particles corresponds to the misidentification of a charged pion as a proton and vice-versa.

The frequency of the pion-proton misidentification is visualized in fig. 6.18, which allows to see how many times a generated particle is interpreted as a photon, as a charged pion or as a proton in the analysis of the event. As expected, the two charged pions can not be distinguished, while the photons are rarely mistaken for charged particles. The most common misidentification is the interpretation of the proton as one of the charged pions and vice-versa.

The efficiency of the event reconstruction is also studied as a function of the angular coordinates

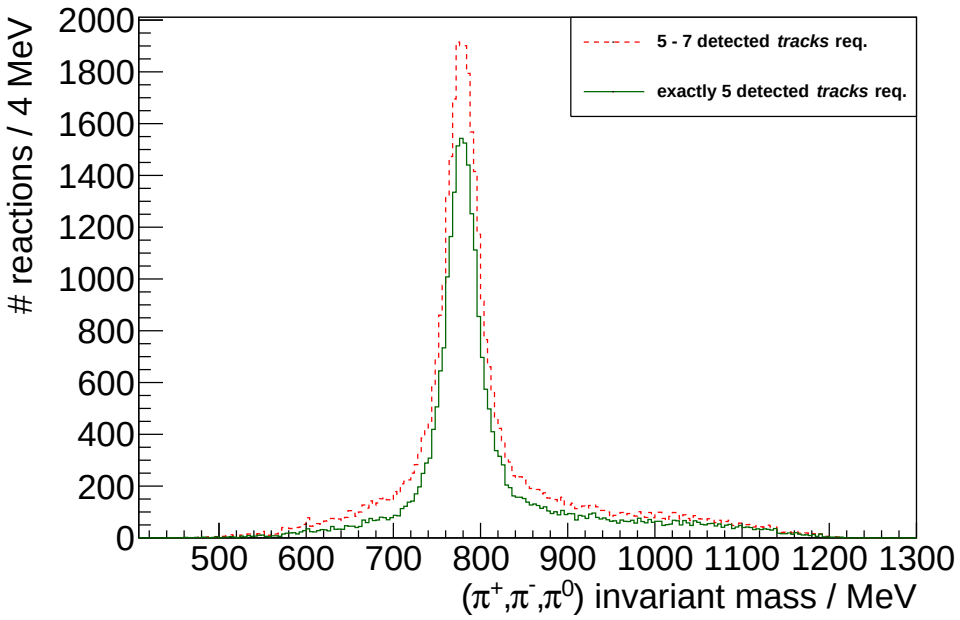

Figure 6.16: Distribution of reconstructed invariant masses of the $(\pi^+\pi^-\pi^0)$-system from generated pω events. One analysis has been performed requiring exactly five reconstructed *tracks* in the event, the other analysis allowed for up to seven reconstructed *tracks*.

of the generated particles. The overview shown in fig. 6.19 visualizes the combined effects of the detector acceptance in case of detection of all the final state particles and the reconstruction efficiency in the laboratory frame.

The left column of histograms shows the angular distributions of the final state particles of the reconstructed reactions. Apart from the previous effects being more pronounced, the effect of the angular granularity of the detectors can be clearly seen by the dotted structures in the BGO and intermediate regions. In the BGO, these structures are more smooth for the neutral particles, since the larger cluster sizes allow for an increased angular resolution more fine than the granularity of the detector elements. The central column displays the angular distributions of the final state particles of those generated reactions only which could be reconstructed. As can be seen, the neutral photons can not be reconstructed in the polar angle region below about 21° corresponding to the forward opening of the BGO calorimeter. Additionally, the protons with higher polar angles above approximately 50° are lost even though the BGO calorimeter covers this area well. This is caused by the loss of forward photons, which constrain the kinematics of the reactions which can be reconstructed such that only lower polar angles are allowed for the proton. Furthermore, two less populated regions for the azimuthal angles of approximately −100° and 80° are visible, which are caused by the two halves of the BGO calorimeter not being completely closed. This also affects the intermediate detector region covered by SciRi, but not the forward spectrometer. The rightmost column of histograms shows the angular distributions

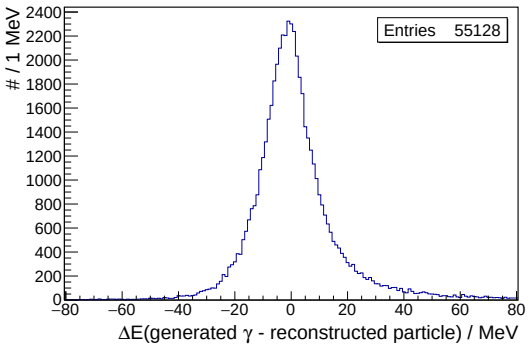

(a) Total energy difference between generated photons and corresponding reconstructed particle.

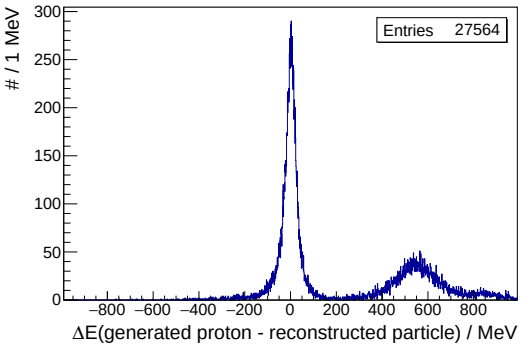

(b) Total energy difference between generated proton and corresponding reconstructed particle.

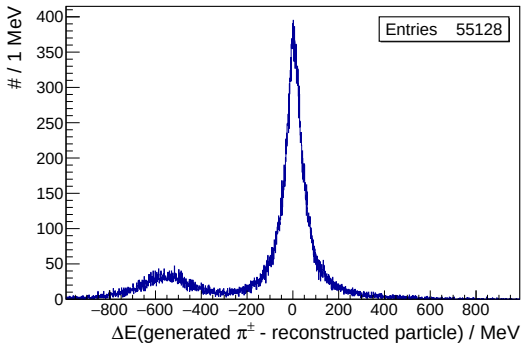

(c) Total energy difference between generated charged pion and corresponding reconstructed particle.

Figure 6.17: Difference in total energy between the generated particle and the particle that was reconstructed in a similar angle. Apart from the expected strong peaking at 0 MeV, for all charged particles, a second bump is found. This corresponds to the misidentification of a charged pion as proton and vice-versa. Since no such bump is observed for the photon, the energy-difference scale has been zoomed.

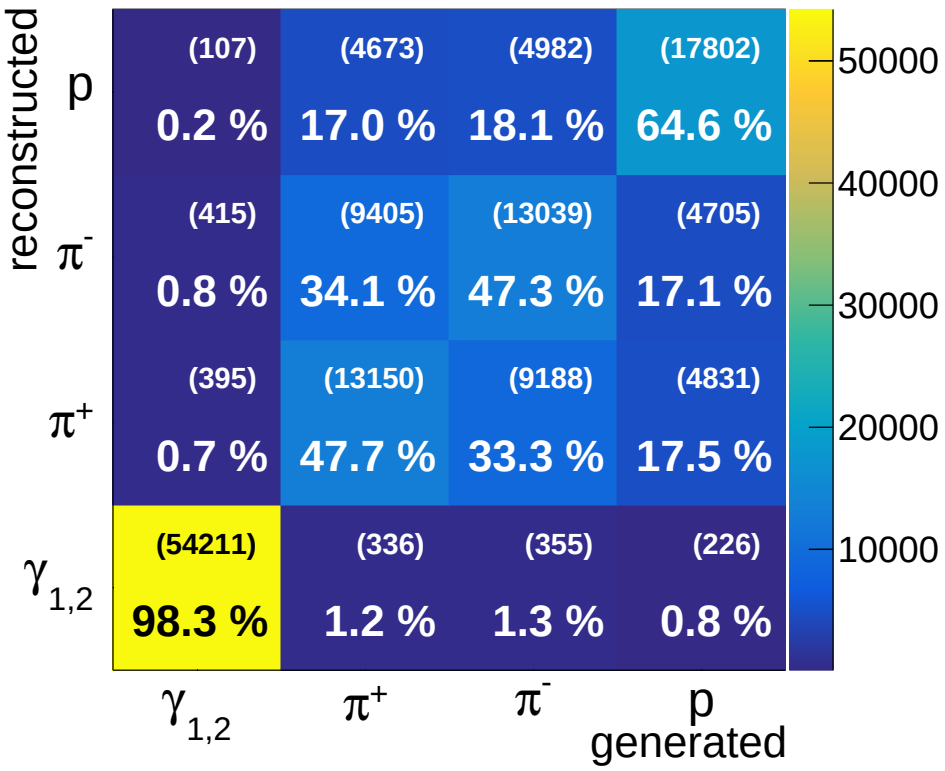

Figure 6.18: Statistics concerning correct and false particle identification for the reaction $\gamma p \to p\omega$ with $\omega \to \pi^+\pi^-\gamma\gamma$. The horizontal axis indicates the type of generated particle, while the vertical axis shows how the particle was reconstructed at the end of the analysis. The two photons are merged into one bin.

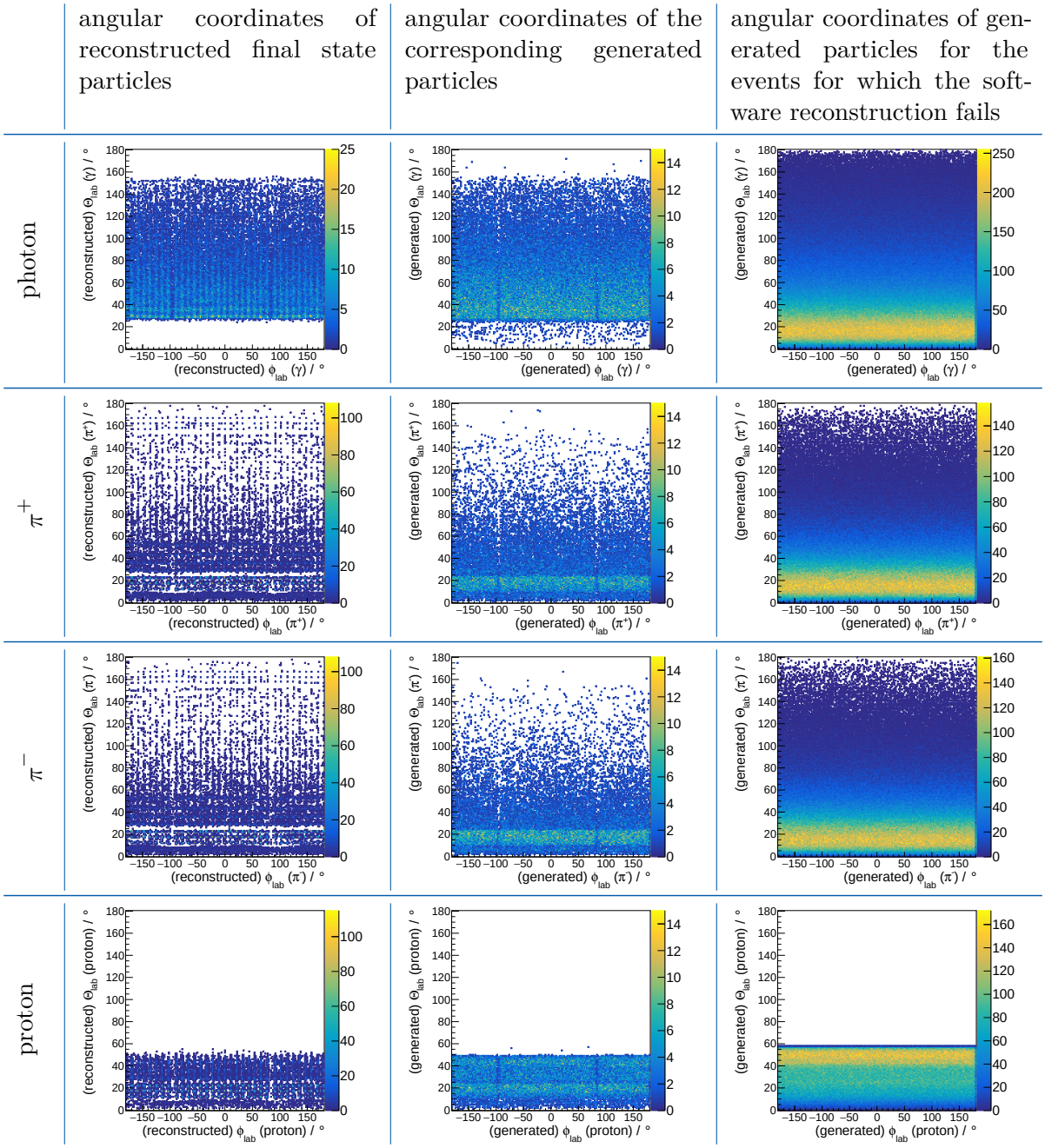

Figure 6.19: Angular distributions of generated and reconstructed particles in simulation. Each row corresponds to one final state particle type. The leftmost column contains the angular distributions of the reconstructed particles matching the generated ones for this subset of events. The central column of histograms shows the angular distributions in the laboratory frame for the corresponding generated particles. The rightmost column of histograms finally displays the angular distributions in the laboratory frame for the generated particles which could not be reconstructed.

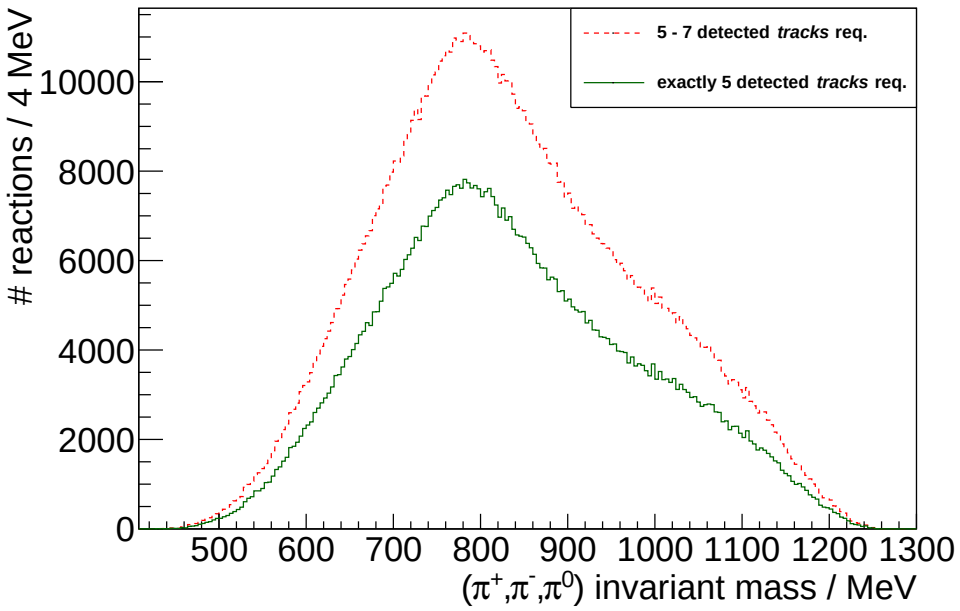

Figure 6.20: Distribution of reconstructed invariant masses of the $(\pi^+\pi^-\pi^0)$-system from generated $p\pi^+\pi^-\pi^0$ phase-space events. One analysis has been performed requiring exactly five reconstructed *tracks* in the event, the other analysis allowed for up to seven reconstructed *tracks*.

of the generated final state particles which have not been reconstructed.

The most predominant background is the non-resonant production of $p\pi^+\pi^-\pi^0$, which is only limited by the available phase space, i.e. it has a strong kinematical overlap with the analysed signal. The major distinction can only be made by identifying the smooth shape of this phase-space channel versus the peak structure of the ω signal in the distribution of invariant masses. This can be visualized in simulation by comparing the distribution of invariant masses of the $(\pi^+\pi^-\pi^0)$-system from the ω decay (c.f. fig. 6.16) with the distribution obtained after applying the same reconstruction on phase-space generated $p\pi^+\pi^-\pi^0$ events (c.f. fig. 6.20). It should be noted that the reconstructed invariant masses of the phase-space distribution show a peaking overlapping with the region of the reconstructed signal.

Understanding the interplay of these distributions and also the behaviour after binning the selected events in photon energy is crucial for the extraction of the number of reconstructed ω photoproduction reactions, which is the necessary input for the extraction of the beam asymmetry. For this reason, after the major background channels[(3)] had been simulated and reconstructed using the same analysis which had been applied to the real data, a template fit to the reconstructed invariant mass distribution is performed. This fit is based on the `TFractionFitter` code implemented in the ROOT-framework (c.f. [BR97]), which in turn was

(3) For completeness, simulations for $(K^0\Sigma^+)$, $(K^+\Lambda)$, $(K^+\Sigma^0)$ and $(\pi^+\pi^+\pi^-n)$ have also been performed, but only a negligible number of events were accepted by the cuts discussed previously.

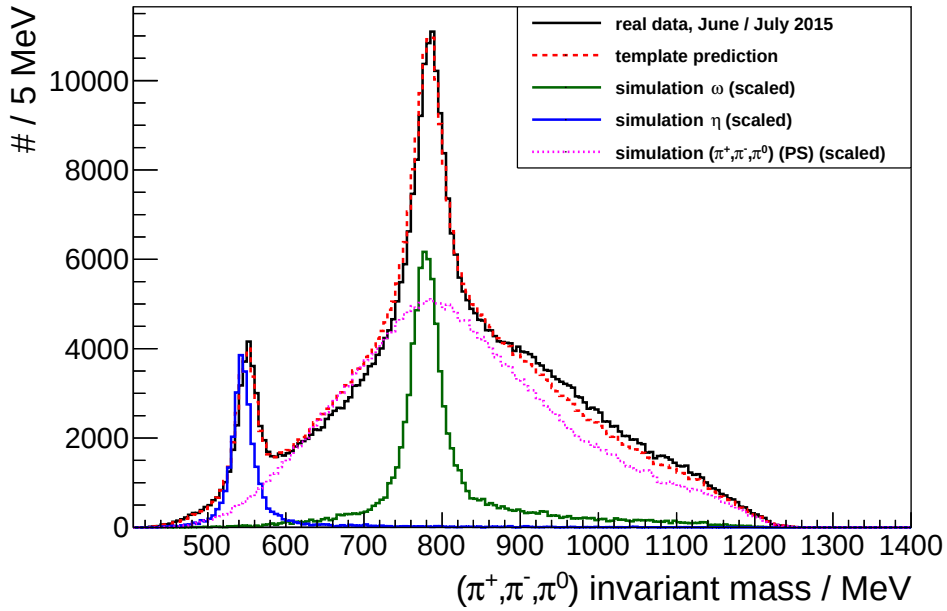

Figure 6.21: Distribution of the invariant masses of the $(\pi^+\pi^-\pi^0)$ system for real data from the June / July 2015 beam time and the reconstruction from simulated channels (scaled). The simulation is performed for pω, pη and a p$\pi^+\pi^-\pi^0$ phase-space distribution. A photon energy spectrum matching the one from real data is employed (see text). Via a fitting technique (see text), a template fit is performed and used to extract the scaling factors. The overall fit result is shown as the template prediction for comparison with the data.

modelled after the HMCMLL algorithm described in detail in [BB93]. This algorithm uses the invariant mass distributions of the simulated channels and scales each of them in order to reproduce the invariant mass distribution obtained with the real data. the scaling is performed simultaneously applying a global scaling parameter to the full invariant mass distribution, and allowing the number of events per invariant mass bin to range within the statistical error.

It must be noted that the monte-carlo datasets used for the fit have been weighted with the corresponding relative bremsstrahlung intensity spectrum of the tagger (c.f. e.g. fig. 5.19). This is necessary since the event generator only models a $1/E_\gamma$ bremsstrahl-spectrum, while in real data, a coherent peak and inefficiencies for some of the tagger channels modified the $1/E_\gamma$ distribution.

The result of the template fit is shown in fig. 6.21. As can be seen, the fit matches the real data surprisingly well. However, it must be taken into account that the template prediction is not exactly the sum of the scaled monte-carlo templates, but each single point was allowed to be modified within the corresponding statistical uncertainty as prescribed by the HMCMLL algorithm. For comparison, the plotted monte-carlo contributions themselves have been scaled by the extracted overall weight from the fit, but are otherwise not modified, which is why the sum of these contributions would not exactly reflect the shape of the template prediction.

Even though the overall agreement is astonishingly good, several features can be made out in the distribution:

- Especially the signal peaks of the reconstructed ω and η from simulated signal events seem to be shifted to slightly lower invariant masses. This can likely be explained by a mismatch in the energy-calibration especially for simulated data, for which no optimization has been performed yet.
- The natural widths of the mesons are not taken into account in simulation yet, as already mentioned in section 6.1 This is mainly visible for the signal peak of the η.
- The efficiency of the SciRi detector is not yet well modelled in simulation. Since the majority of protons is expected and found in the SciRi detector region, this may change the distribution especially close to the upper end of the kinematically allowed invariant masses (c.f. fig. 6.11).

In this work, the template fit is used as a guidance on the expected shape of the invariant mass distributions of the 'background' channels for the extraction of the number of ω mesons in the various energy bins. On the contrary, it is not used to extract the number of reconstructed mesons, since the simulation is not yet considered mature enough due to the previously described reasons, and any estimate on uncertainties would be impossible.

This is shown in fig. 6.22. For these histograms, only the scaling with the global parameter is used for each simulated channel and no variation within the statistical error is allowed. This global scaling simultaneously embeds the averaged ratios of the cross-sections of the simulated channels and the averaged relative acceptance and efficiency[4] for each simulated channel. This

(4) The efficiency in this case embeds both the 'hardware' efficiency and the 'software' efficiency.

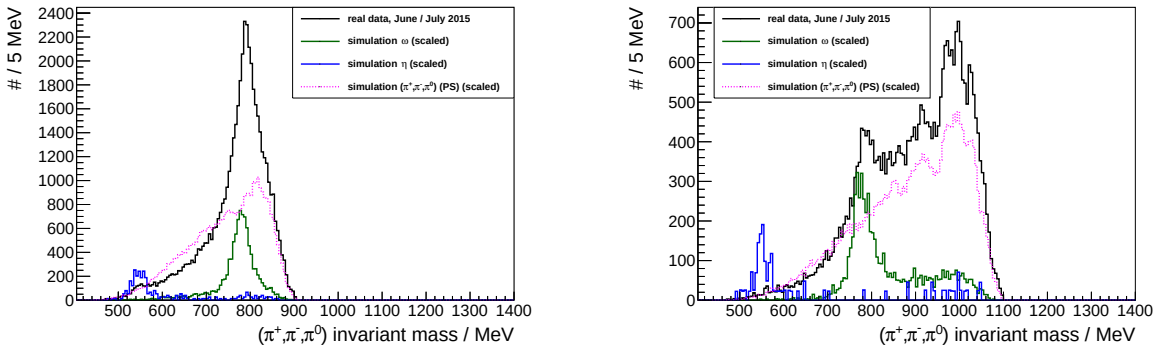

(a) Invariant mass distribution in a bin of E_γ between 1250 MeV and 1350 MeV.

(b) Invariant mass distribution in a bin of E_γ between 1650 MeV and 1750 MeV.

Figure 6.22: Distribution of the invariant masses of the $(\pi^+\pi^-\pi^0)$ system for real data and for the simulated channels (scaled), within bins in photon energy. The scaling factors as extracted from the overall template fit (c.f. fig. 6.21) have been applied.

notably means that additional differences due to energy-dependent cross-sections, acceptances and efficiencies are not yet modelled. Still, the globally scaled distributions are sufficiently realistic for the qualitative study performed here.

Two energy bins are chosen to illustrate the behaviour of the 'background' channels. The first one shown in fig. 6.22a corresponds to events with incoming photon energies between 1250 MeV and 1350 MeV, thus being close to the threshold for ω production. As can be seen, the peaking of the phase-space background and the ω signal can not be distinguished at all without any assumptions about their proper invariant mass distribution.

The second bin shown in fig. 6.22b corresponds to events with incoming photon energies between 1650 MeV and 1750 MeV. Also in this case, the ω signal can not be clearly identified: the real data distribution shows a peaked structure reflecting the granularity of the SciRi and BGO detectors in polar angle. This is found back in the reconstructed events both for the simulated ω events and for the phase-space $p\pi^+\pi^-\pi^0$ production and spoils any clear identification of the ω signal peak. Additionally, the issue of confusing the proton with one of the charged pions produces a significant number of ω with a wrongly reconstructed, smoothly distributed invariant mass. Both these issues are present across the whole energy range and could only be overcome by an improvement in the detector resolutions. On a side-note, the contribution of η is overestimated in this case mainly due to low statistics in the simulated dataset. It can be neglected in this energy range.

Taking all these effects into account, the standard technique of fitting a Gaussian distribution to the signal region with a simple linear background function is not feasible. Since the template model itself is not considered reliable yet, the following chapter will explain a newly developed technique based on an analytical description of the background shape which allows to recover also a part of the signal which is not within the expected invariant mass region.

6.5 Extraction of Number of ω Mesons

For the extraction of the number of ω mesons per polarization plane in bins in energy, polar and azimuthal angle, an analytical description of the $(\pi^+\pi^-\pi^0)$ invariant mass (x_{inv}) distribution is employed to attempt to distinguish between signal and background. The mass distributions are visualized and stored in a histogram bin by bin and for each of them, the following analytical description is fitted:

$$f\left(x_{\text{inv}}\right) = s\left(x_{\text{inv}}\right) + b\left(x_{\text{inv}}\right) \tag{6.1}$$

with $s\left(x_{\text{inv}}\right)$ and $b\left(x_{\text{inv}}\right)$, for the signal and background distributions respectively, being defined as:

$$s\left(x_{\text{inv}}\right) = \mathbf{N} \cdot (\text{binwidth}) \cdot \text{gausn}\left(x_{\text{inv}}, \mathbf{m}, \boldsymbol{\sigma}\right) \tag{6.2}$$

$$b\left(x_{\text{inv}}\right) = \mathrm{e}^{\mathbf{S} \cdot x_{\text{inv}}} \cdot \left(1 - \text{erf}\left(\left(x_{\text{inv}} - \mathbf{k}\right) \cdot \mathbf{w}\right)\right) + \mathbf{C} \tag{6.3}$$

All the parameters printed in bold are fit parameters. The fit function for the signal events $\left(s\left(x_{\text{inv}}\right)\right)$ consists of a normalized Gaussian for the signal peak, scaled with the bin width of the histogram such that the variable $\mathbf{N}$ allows direct access to the number of potential signal events in the Gaussian component of the fit. For reference, the normalized Gaussian is defined as:

$$\text{gausn}\left(x_{\text{inv}}, \mathbf{m}, \boldsymbol{\sigma}\right) = \frac{1}{2\pi \cdot \boldsymbol{\sigma}} \cdot \mathrm{e}^{-\frac{1}{2}\left(\frac{x_{\text{inv}} - \mathbf{m}}{\boldsymbol{\sigma}}\right)^2}$$

The mean $\mathbf{m}$ of the Gaussian corresponds to the mass of the meson and for the fit is bound to $\pm 40\,\text{MeV}$ around the nominal ω mass. The width $\boldsymbol{\sigma}$ is empirically bound between $6.7\,\text{MeV}$ and $30.0\,\text{MeV}$.

Additionally to the Gaussian mimicking the distribution of ω events, the 'background' is modelled by an exponential function. This functional form was found to provide the most stable description of the background distribution with the least possible parameters, for example as compared to higher order polynomials. The slope parameter $\mathbf{S}$ is empirically bound to small values of $0.001\,\text{MeV}^{-1}$ and $0.01\,\text{MeV}^{-1}$. Furthermore, an additive constant $\mathbf{C}$ is left free for variation by the fit to model the offset of the exponential distribution.

The cutoff at high invariant mass following from the kinematical restrictions of the available phase-space at a given photon energy is modelled by a Gaussian error function which is multiplied with this exponential. The Gaussian error function is defined as:

$$\text{erf}\left(x_{\text{inv}} - \mathbf{k}\right) = \frac{2}{\sqrt{\pi}} \int_0^{x_{\text{inv}} - \mathbf{k}} \mathrm{e}^{-t^2}\,\mathrm{d}t$$

The parameter $\mathbf{k}$ can be varied by the fit within a range defined independently for each histogram,

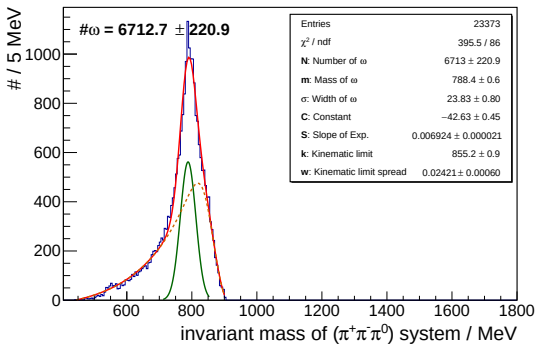

(a) Invariant mass distribution in a bin of E_γ between 1250 MeV and 1350 MeV, pol. plane 'A'.

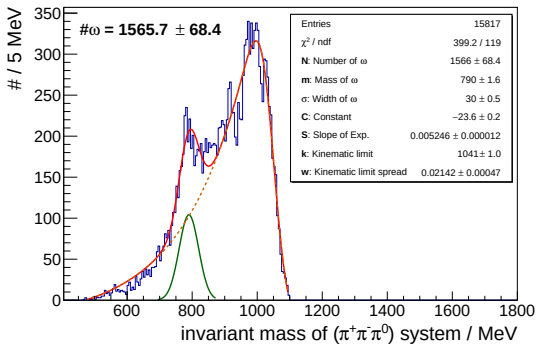

(b) Invariant mass distribution in a bin of E_γ between 1650 MeV and 1750 MeV, pol. plane 'A'.

Figure 6.23: Analytical fit to the reconstructed distributions of invariant masses of the $(\pi^+\pi^-\pi^0)$ system, June / July 2015 data. The fit is indicated by the red, solid line describing the full distribution, while the green, solid line shows the Gaussian component of the fit function. For completeness, the remaining part of the fit function is indicated by a brown, dashed line. The number of ω shown in these histograms is extracted directly from the integral of the Gaussian component of the fit function.

according to the procedure described in the following. At first, the histogram bin with the maximal population of counts $n_{\max}$ is identified. Then, the histogram bin for which the number of counts exceeds 20 % of $n_{\max}$ is selected as the centre of the range of allowed values for **k**. The width of this range is empirically bound to ± 30 MeV. The smoothness of the cutoff, which is a consequence of the detector resolution, is described by the width of the error distribution modelled by the fit parameter **w**. It is empirically bound between $0.001\,\mathrm{MeV}^{-1}$ and $0.2\,\mathrm{MeV}^{-1}$.

Additionally, the range of the fit is constrained to prevent distortions of the fitted function. At smallest values of the invariant mass distribution, the fit is performed starting from the first non-empty bin of the histogram of the $(\pi^+\pi^-\pi^0)$ invariant mass distribution. At highest values of the invariant mass, the fit is performed up to the last histogram bin whose entries are at least 1 % of $n_{\max}$ or for invariant mass values up to the nominal mass of the ω meson plus 20 MeV, depending on which of these two constraints yields the higher invariant mass limit.

Figure 6.23 shows the result of the fit to the $(\pi^+\pi^-\pi^0)$ invariant mass distribution for the data recorded in June / July 2015 for polarization plane 'A' and the same energy bins as presented in fig. 6.22. As can be seen, the distributions are described well by the fit function, albeit especially for the higher energetic bin, the analytical function is necessarily *smoothing* over the artefacts induced by the granularity of the detectors. The Gaussian component, for reference, is plotted separately and the number of signal events by its integration including the error from the fit is shown.

By comparing the analytical description to the experimental distribution of the $(\pi^+\pi^-\pi^0)$ invariant masses, it is observed that for the higher energetic bins (c.f. fig. 6.23b) the 'background' component of the analytical description slightly overestimates the distribution for invariant

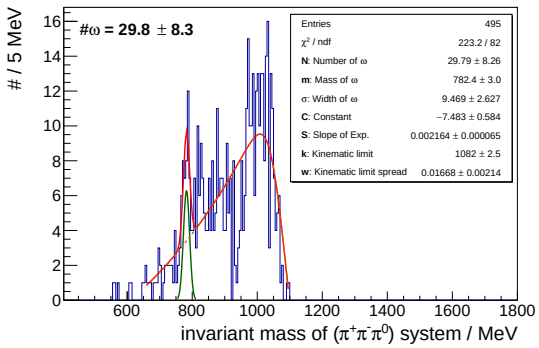

(a) Invariant mass distribution in a bin of E_γ between 1650 MeV and 1750 MeV, $\Theta_{\text{CM}}^{\text{meson}}$ between 36° and 72° and ϕ^{meson} between −135° and −90°, pol. plane 'A'.

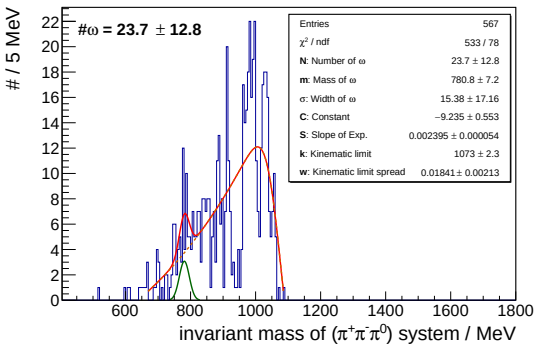

(b) Invariant mass distribution in a bin of E_γ between 1650 MeV and 1750 MeV, $\Theta_{\text{CM}}^{\text{meson}}$ between 36° and 72° and ϕ^{meson} between −180° and −135°, pol. plane 'A'.

Figure 6.24: Analytical fit to the reconstructed distributions of invariant masses of the $(\pi^+\pi^-\pi^0)$ system within the bins in photon energy, azimuthal and polar angle as they are used for the extraction of the beam asymmetry, using the dataset from June / July 2015. Similar to the complete energy bins shown in fig. 6.23, the fit is indicated by the red, solid line describing the full distribution, while the green, solid line shows the Gaussian component of the fit function. For completeness, the remaining part of the fit function is indicated by a brown, dashed line. The number of ω shown in these histograms is extracted directly from the integral of the Gaussian component of the fit function.

masses below 750 MeV and slightly underestimates the distribution for invariant masses above 850 MeV.

Taking inspiration from this observation, if the 'background' component of the fit is considered reliable and anything exceeding this background is considered signal, some of the substructures observed above the signal region would be accepted as signal. This region matches the one for which in simulation (c.f. fig. 6.22b) the signal events from protons misidentified as charged pions are found.

Additionally, taking into account that the distributions shown here are for the full energy bin and no binning in polar and azimuthal angle has been applied yet, the expected statistics in a bin which is to be used to extract the number of ω mesons for the measurement of the beam asymmetry is by orders of magnitude lower. The stability of the fit of the Gaussian component is dominated by the few histogram bins between 750 MeV and 850 MeV, while the fit to the 'background' distribution takes the full invariant mass range into account, resulting in a higher stability of the fit within the available statistics.

As an example, the $(\pi^+\pi^-\pi^0)$ invariant mass distribution is shown for two selected E_γ, $\Theta_{\text{CM}}^{\text{meson}}$ and ϕ^{meson} bins in fig. 6.24, which displays a subset of events from fig. 6.23b. The employed binning is already tuned on the minimum number of bins to maximize the statistics per bin available for the extraction:

- in azimuthal angle, at least eight points are considered necessary to allow for a reliable fit

of the sinusoidal function to extract the beam asymmetry;

- in polar angle, only five bins with a width of 36° in the centre of momentum frame of the ω meson have been used;
- in incoming photon energy, already the bin width of 100 MeV could smear out energy-dependent effects.

Comparing the shape of the Gaussian signal component in fig. 6.24a with the one in fig. 6.24b, it can be seen that width and amplitude of the Gaussian vary strongly due to the very limited statistics. The fit of the 'background' shape, however, is more stable since almost the full invariant mass range is taken into account.

Inspired by this observation, a technique based on the extraction of the number of ω mesons making use of the analytical description of the fitted 'background' distribution is developed. For each event, the w_{signal} (c.f. section 5.4.5) is calculated in the following way:

1. The $b\,(x_{\text{inv}})$ part of the fitted analytical function (c.f. eq. (6.3)), is evaluated for the reconstructed invariant mass of the reaction.
2. The result is divided by the number of entries found in the corresponding invariant mass bin of the very same histogram to which the analytical function was fitted.
3. The resulting fraction, from now on termed $w_{\text{background}}$, is interpreted as the 'background-probability' of the reaction. Notably, this number may be larger than 1. This will be the case if the fit function exceeded the reconstructed invariant mass distribution.
4. If the reconstructed invariant mass is outside of the fit range, $w_{\text{background}}$ is forced to a value of exactly 1.
5. The signal probability w_{signal} is now defined as $w_{\text{signal}} = 1 - w_{\text{background}}$. Notably, this value is exactly 0 outside of the fit range, and is negative for values of $w_{\text{background}}$ larger than 1.

The weights w_{signal} calculated in this way are then assigned to each of the reconstructed events. Furthermore, employing Gaussian error propagation from the involved fit parameters and the statistical error of the entries in the histogram bin, a statistical error on the weight is calculated and stored. Before explaining how the weights and associated uncertainties are employed in the procedure for the extraction of the beam asymmetry (c.f. section 6.6), a short discussion of the approach to define the w_{signal} is presented in the following.

Comments on the Technique for the Extraction of the Number of ω Mesons

The data shown already in fig. 6.24 are now compared with the corresponding weighted histogram, in which each event is included depending on the assigned weight w_{signal}. This comparison is presented in fig. 6.25, where the black points with the associated error bars represent the result

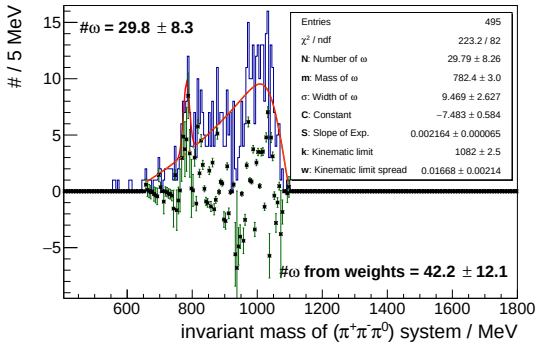

(a) Invariant mass distribution in a bin of E_γ between 1650 MeV and 1750 MeV, $\Theta_{\mathrm{CM}}^{\mathrm{meson}}$ between 36° and 72° and ϕ^{meson} between −135° and −90°, pol. plane 'A'.

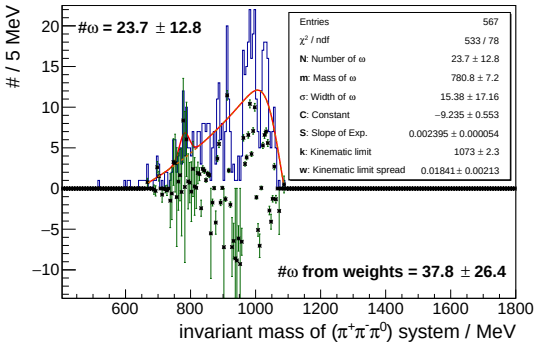

(b) Invariant mass distribution in a bin of E_γ between 1650 MeV and 1750 MeV, $\Theta_{\mathrm{CM}}^{\mathrm{meson}}$ between 36° and 72° and ϕ^{meson} between −180° and −135°, pol. plane 'A'.

Figure 6.25: The same analytical fits already shown in fig. 6.24 are displayed again (June / July 2015 data). In this case, the summed up signal-weights within the same invariant mass binning are plotted on top, including the propagated associated uncertainties from the fit parameters and the statistics within each of the invariant mass bins (see text). In addition to the number of ω extracted directly from the integral of the Gaussian component of the fit function which was already shown before, the number of ω obtained from the sum of all signal-weights is shown. It is calculated by summing up all the w_{signal} in all invariant mass bins within the full bin in photon energy, azimuthal and polar angle, again propagating the individual uncertainties.

of summing the weights per histogram bin including the corresponding statistical error bar. As can be seen especially in fig. 6.25a, the points follow a Gaussian-like shape in the region between 750 MeV and 850 MeV and fluctuate strongly below 750 MeV and above 850 MeV. For both plots, the sum of the weighted events for invariant masses above 850 MeV is positive, corresponding to a positive number of reconstructed ω events also for invariant mass values higher than the nominal ω mass. As shown in figs. 6.25a and 6.25b, the number of ω reconstructed with this background subtraction procedure is slightly larger than the one extracted from the integral of the Gaussian fit, and the same holds for the statistical error.

This observation matches with the expectation: the smoothing of the artefacts achieved by this technique attempts to reproduce the tail of the $(\pi^+\pi^-\pi^0)$ invariant mass distribution observed in simulations for ω events in case of $\pi^\pm$ / proton misidentification.

Indirectly, the smoothing effect is caused by the fitting algorithm, which is based on the minimization of the overall χ^2. This means that integrating over the differences between the experimental distribution and the fitted function, which is done by calculating the weights per bin and summing them up, is expected to produce a close-to-zero result. The observed small excess accounted for as ω events is caused by the analytical function being unable to describe a smooth, smeared component of signal and / or background which is underneath the dominant background distribution, such that it is necessarily recovered by the sum of the differences between distribution and fit function. In other bins, however, the result obtained by using the weighting technique is lower. This is observed mainly for those $\Theta_{\mathrm{CM}}^{\mathrm{meson}}$ bins for which the invariant mass distribution of the $(\pi^+\pi^-\pi^0)$ phase-space background is peaking in correspondence to the ω mass value, thus falsely increasing the signal count extracted with the Gaussian fit. However, it should also be noted that even this background subtraction technique, which is less affected by reduced statistics, is not completely able to overcome the lack of statistics in many bins.

As a cross-check, the data shown already in fig. 6.23 are now compared with the corresponding weighted histogram as displayed in in fig. 6.26. As can be seen for the low photon energy bin shown in fig. 6.26a, the technique fails in distinguishing between signal and non-signal components, similar to the behaviour of the Gaussian component of the fit as shown in fig. 6.23a. However, for the high photon energy bin shown in fig. 6.26b, the situation is different: the shape of the signal is reproduced as expected, and further contributions for higher invariant masses also included in the ω dataset.

It must be pointed out that fig. 6.23 and fig. 6.26 show $(\pi^+\pi^-\pi^0)$ invariant mass distributions integrated over the full polar and azimuthal angular ranges. This is done for the written thesis to show the main features and discuss the most important aspects of the fitting procedure. The shown statistics still has to be divided into 40 bins (8 bins in ϕ^{meson} and 5 bins in $\Theta_{\mathrm{CM}}^{\mathrm{meson}}$) in order to estimate the number of ω photoproduction events for the extraction of the beam asymmetry. As already pointed out, the lower statistics affects the stability of the Gaussian fit significantly, while the fitting procedure of the complete invariant mass distribution proves more stable even for most of the low statistics bins. The shown large statistical uncertainty of the results necessarily reflects the overall insufficient statistics.

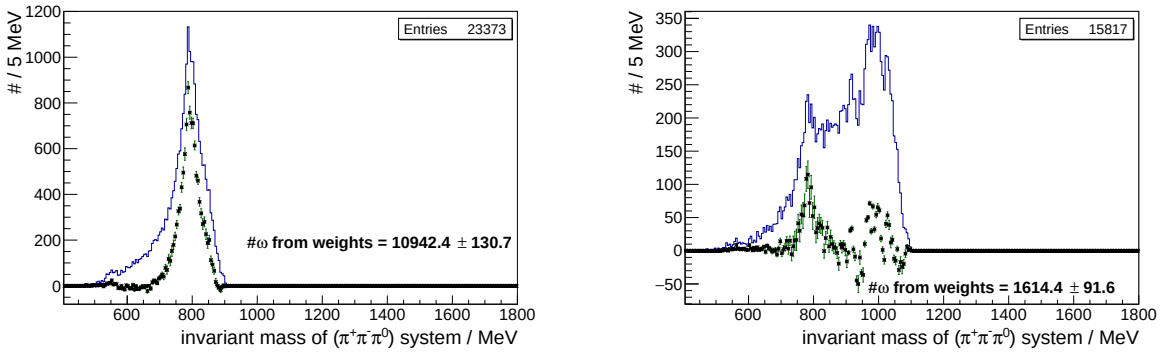

(a) Invariant mass distribution in a bin of E_γ between 1250 MeV and 1350 MeV, pol. plane 'A'.

(b) Invariant mass distribution in a bin of E_γ between 1650 MeV and 1750 MeV, pol. plane 'A'.

Figure 6.26: Display of the summed w_{signal} weights within the complete energy bins already presented in fig. 6.23 for a cross-check of the weighting technique (June / July 2015 data). The weights themselves have been extracted within the corresponding bins in photon energy, azimuthal and polar angle and been summed up to match the displayed energy and invariant mass binning.

6.6 Extraction and Fitting of the Beam Asymmetry

For the extraction of the beam asymmetry from the determined count rates, the exact same procedure as already discussed in section 5.4.5 is applied.

The notable difference at this point is made for the data recorded in October / November 2015. In this case, the degree of polarization has been extracted on a daily basis, for both polarization planes separately. Comparing the ratio of the total coincidence counts recorded by the tagger scalers for the two different polarization planes for June / July 2015 (c.f. fig. 5.23b) and for October / November 2015 (c.f. fig. 6.27), it can be observed that the issue of the shifted position of the intensity peak from the coherent bremsstrahlung between the two polarization planes persists. However, the displayed ratio is significantly smoother due to the improvements on the tagger detector, and the total counts recorded per energy bin per polarization plane are closer to unity. For this reason, it is expected that the systematic uncertainties from the extraction of the polarization and from the flux normalization are significantly lower as compared to the June / July 2015 dataset. Since the statistical uncertainties strongly outweigh the systematics, as will be pointed out in the following paragraphs, a more detailed discussion of the systematics would not be meaningful.

In the following, the data from October / November 2015 will be shown as an example due to the higher available statistics and expected lower systematic uncertainties. An example for the effect of including the degree of polarization extracted on a daily basis is shown in fig. 6.28, where the normalized count rate difference (introduced in section 5.4.5) is shown. Figure 6.28a presents the normalized count rate difference without taking the polarization degree into account (c.f. eq. (5.1)), while fig. 6.28b includes the weighting by the $w_{\text{tot},i}$ factors (c.f. eq. (5.2)) using

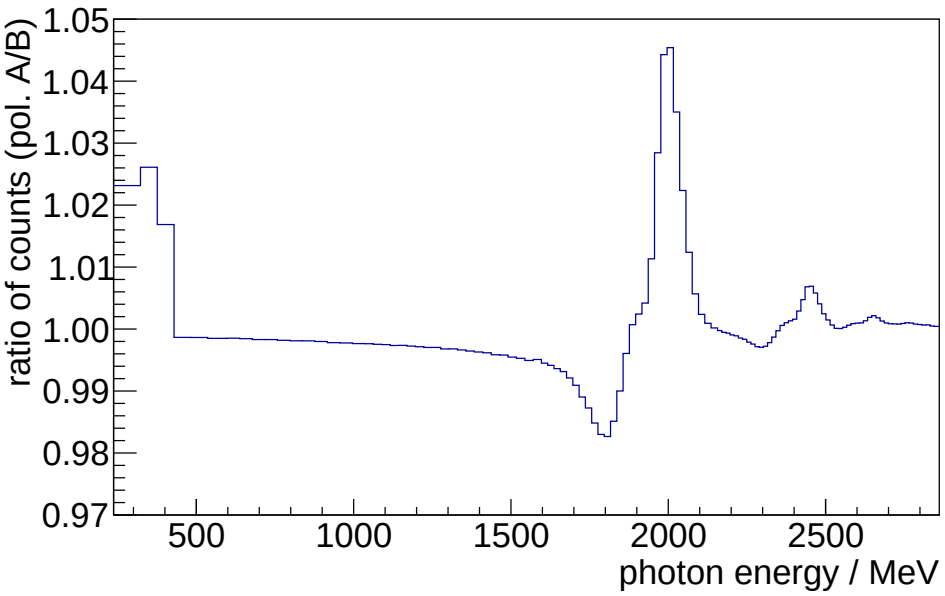

Figure 6.27: The histogram shows the ratio of the total coincidence counts recorded by the tagger scalers for the two different polarization planes over the full analysed October / November 2015 dataset.

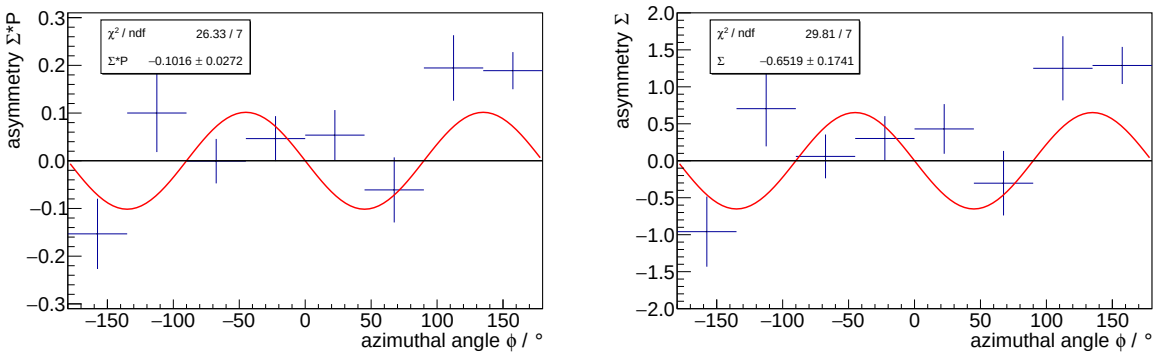

(a) **(b)**

Figure 6.28: Azimuthal distribution of the normalized count rate difference of ω photoproduction events for the extraction of the beam asymmetry, including statistical uncertainties. The data refer to the bin with E_γ between 1450 MeV and 1550 MeV and $\Theta_{\mathrm{CM}}^{\mathrm{meson}}$ between 72° and 108° recorded in the October / November 2015 beamtime. The result from the fit to the data points is also shown. The differences between the two panels illustrate the impact of the weighting for the degree of polarization.

the individual extracted degree of polarization for each daily period.

The two plots show really small differences (except for the scale factor of the vertical axis) which are minimal compared with the statistical uncertainties. For this reason, the systematic uncertainties introduced by the approximation described in section 5.4.5 can be regarded as negligible compared to the current statistical uncertainties.

The more striking issue is that the data plotted in fig. 6.28 do not show the expected sinusoidal behaviour. On the contrary, within the error bars, they are even compatible with a flat distribution. As a consequence, the fit of the sinusoidal function results in high values of the reduced χ^2, usually larger than 3, which reflects the bad quality of the fit.

This can be clearly illustrated by comparing the datasets from the two data-taking periods as shown in section 6.6, which displays the azimuthal distributions for all bins in polar angle belonging to one bin in incoming photon energy from 1450 MeV to 1550 MeV. In none of these plots, the data points show any clear indication of the expected sinusoidal fluctuation, and the fit is essentially influenced by the few points with the smallest uncertainties. This issue is reflected in high values of χ^2 indicating that the fit function can not describe the data.

It must be stated that also the uncertainties of the data points can not be regarded as reliable: They are based on the extraction of the number of ω mesons discussed in section 6.5 according to the fitting procedure. The fitting procedure itself is not regarded as reliable yet, considering the unknown effect of the artefacts traced back to the granularity of the detectors and the reduced available statistics. For this reason, neither the uncertainties nor the values entering the azimuthal distributions should be trusted.

In summary, the fit function does not describe the behaviour of the experimental distribution and the parameter extracted from the fit, together with the corresponding error, can not be regarded as reliable.

As an example for the extracted beam asymmetries, the results for the energy bin between 1450 MeV and 1550 MeV are shown in fig. 6.30. It must be noted that for the dataset recorded in June / July 2015 (c.f. fig. 6.30a), this energy corresponds to the maximum degree of polarization of about 30 %[5], while for October / November 2015 the degree of polarization in this energy bin is about 15 %. Still, the degree of polarization and the uncertainty of its determination has a small effect as compared to described problems due to the insufficient angular resolution for charged particles and the reduced statistics.

As a consistency check, the signal weights can be inverted (i.e. $w'_{\text{signal}} = 1 - w_{\text{signal}}$ is used) and the beam asymmetry extraction is performed for 'background' events. Assuming that the major contribution below the ω signal stems from the phase-space production of $\pi^+\pi^0\pi^-\text{p}$, the extracted beam asymmetry should be compatible with zero if the procedure to identify the signal events is correct.

The results of this analysis are shown in fig. 6.31 for the same energy bin, again for both the analysed beam times. As can be seen, indeed four out of the five data points agree with

(5) This also implies a slightly larger uncertainty of the degree of polarization due to the instability of the position of the polarization peak in energy.

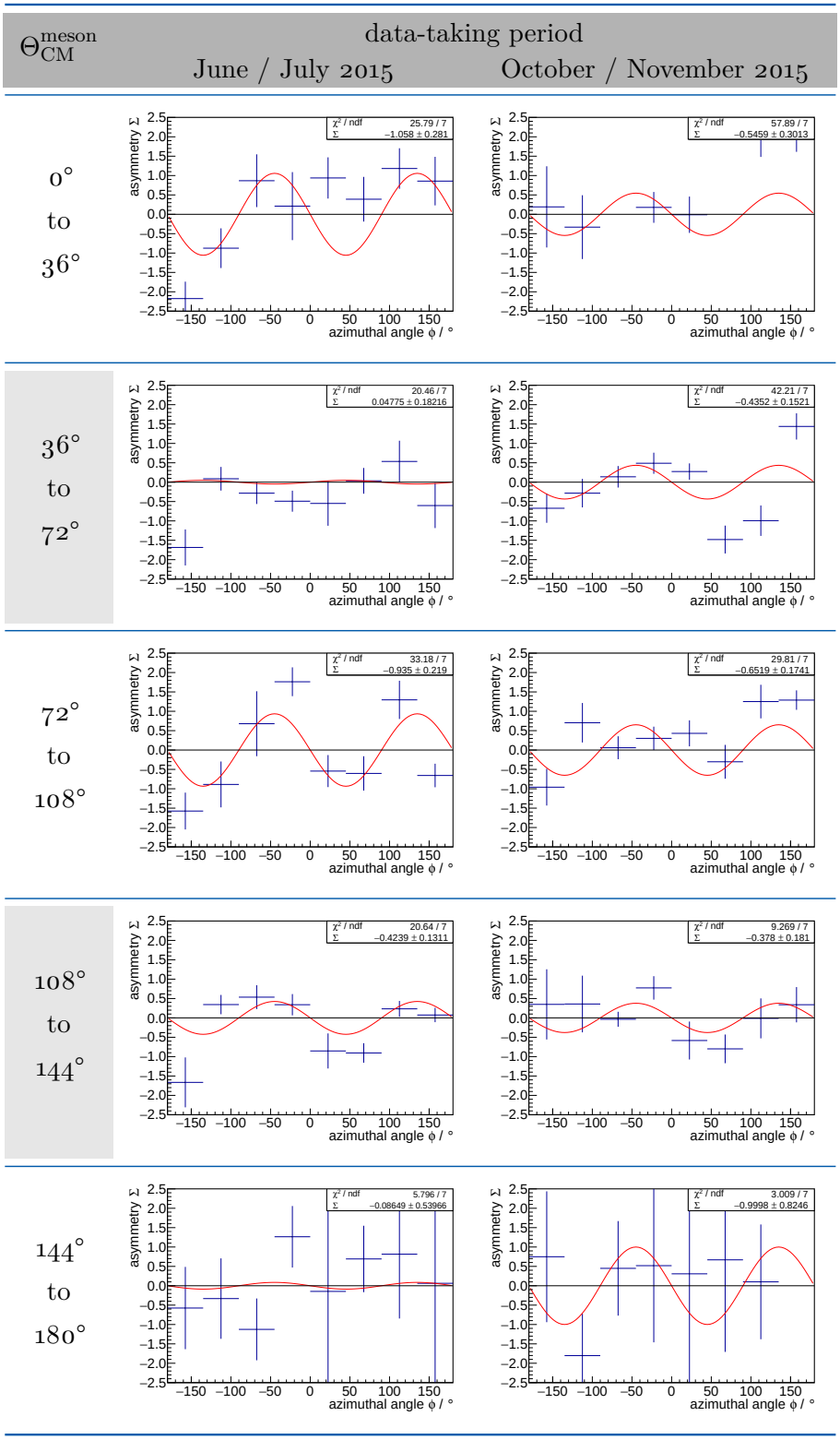

Figure 6.29: Azimuthal distribution of the normalized difference of ω photoproduction events for the extraction of the beam asymmetry, including statistical uncertainties. The results shown have been extracted from the June / July 2015 and October / November 2015 data sets for incoming photon energies E_γ between 1450 MeV and 1550 MeV in different bins of $\Theta_{\mathrm{CM}}^{\mathrm{meson}}$. Of all the energy bins, this region is considered the 'best' in terms of available statistics, degree of polarization and background separation for both the data-taking periods.

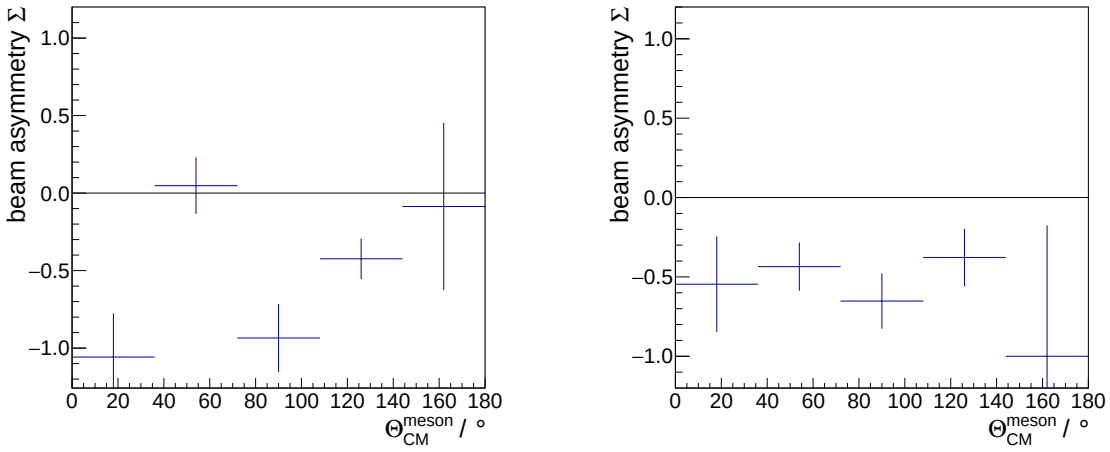

(a) **(b)**

Figure 6.30: Extracted beam asymmetries Σ for the reconstructed $p\omega \to p\pi^+\pi^-\pi^0$ within the energy bin E_γ between 1450 MeV and 1550 MeV. The values have been extracted for the June / July 2015 beam time (c.f. fig. 6.30a) and the October / November 2015 beam time (c.f. fig. 6.30b).

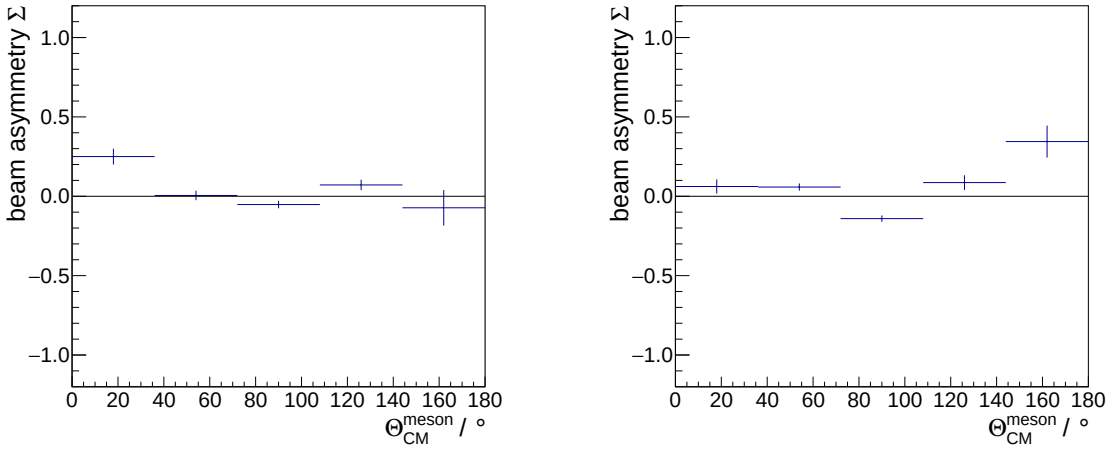

(a) **(b)**

Figure 6.31: Extracted beam asymmetries Σ from the non-signal part of the reconstructed $p\omega \to p\pi^+\pi^-\pi^0$ within the energy bin E_γ between 1450 MeV and 1550 MeV. The extraction has been performed by inverting the meaning of the w_{signal} weights as described, i.e. the beam asymmetry from the expected non-signal part is extracted. The values have been extracted for the June / July 2015 beam time (c.f. fig. 6.30a) and the October / November 2015 beam time (c.f. fig. 6.30b).

a beam asymmetry of zero for the June / July 2015 dataset in the energy bin displayed in fig. 6.31a. A similar agreement is also found throughout the remaining energy bins and in the October / November dataset 2015 (c.f. fig. 6.31b), while some points only agree with the expected asymmetry of zero within 2σ of the calculated uncertainty.

The tendency of the data points to a zero beam asymmetry for the incoherent $(\pi^+\pi^-\pi^0)$ photoproduction is in agreement with the expectation and does not reveal a significant flaw in the implemented analysis technique. However, the results can still not be considered reliable enough to extract a physics result: the insufficient statistics combined with the coarse granularity of the detectors can not be overcome by the analysis techniques presented here.

Nevertheless, in the following, the extracted beam asymmetries for ω photoproduction employing the data from both the beam times are presented in fig. 6.32. As discussed in section 6.5, bins of 100 MeV in E_γ and 36° in $\Theta_{\mathrm{CM}}^{\mathrm{meson}}$ have been chosen. The asymmetry is extracted by fitting a sinusoidal function to eight bins in azimuthal angle. All corresponding fits to the azimuthal distributions are collected in appendix C.2 and appendix C.3.

The extraction has been limited to those bins in incoming photon energy for which the degree of polarization is at least 10 %. For the June / July 2015 beam time, this translates into photon energies between 1150 MeV and 1650 MeV. Additionally, it must be considered that the highest energetic bin from 1550 MeV to 1650 MeV includes the steep falloff of the degree of polarization, and hence is affected most by an instability of the polarization peak.

For the October / November 2015 beam time, the requirement of a degree of polarization of at least about 10 % translates into bins in photon energy between 1350 MeV and 1950 MeV. Again, the last bin from 1850 MeV to 1950 MeV is affected most by any instability of the polarization peak.

In fig. 6.32, the red points correspond to the extracted beam asymmetry values for the June / July 2015 data taking, the blue points correspond to the results for the October / November 2015 beamtime. Comparing the two sets of results in the overlapping energy bins, it can be found that only for the bin from 1450 MeV to 1550 MeV and the bin from 1550 MeV to 1650 MeV, some of the points indeed agree within the huge statistical uncertainties. However, no overall agreement is found. Once again, it is important to underline that the results can not be regarded as reliable, especially when checking the fits to the azimuthal distributions one by one which are collected in appendix C.2 and appendix C.3.

Taking the large and not fully characterizable uncertainties into account, the only overall statement which can be extracted is that a tendency towards a small beam asymmetry with negative sign as measured with high precision at the GRAAL experiment (c.f. [Veg+15]) can be confirmed.

6.7 Necessary Improvements and Outlook

As outlined in detail in the analysis of the $\gamma p \to p\omega$ with $\omega \to \pi^+\pi^-\pi^0$ reaction, the BGO-OD experiment with its currently incomplete hardware setup can not fulfil the necessary requirements

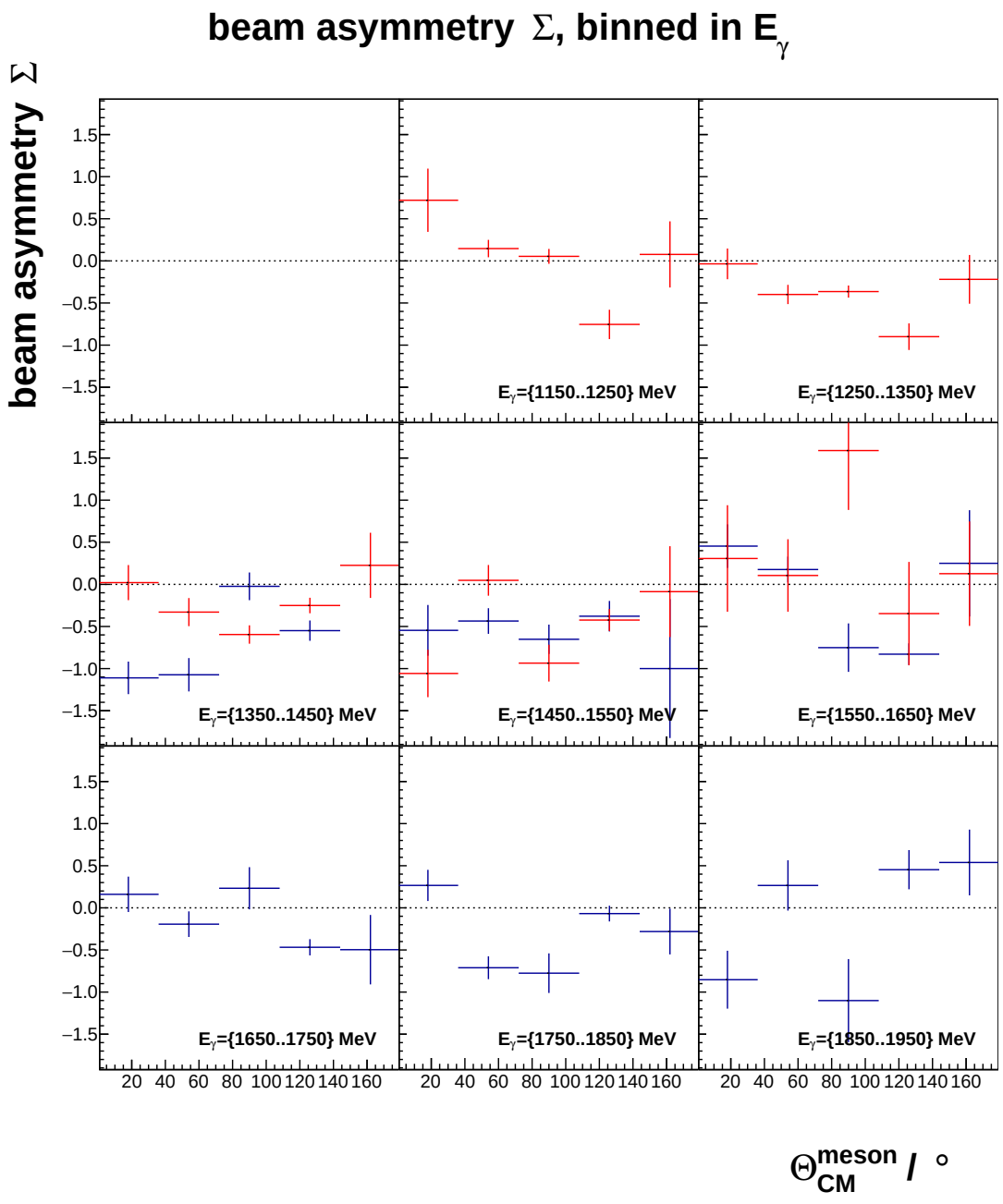

Figure 6.32: Extracted beam asymmetries Σ for ω photoproduction in bins of E_γ using the datasets from June / July 2015, in red, and October / November 2015, in blue. The shown error bars for the extracted points are purely by propagated statistical uncertainties, while they are still underestimated due to the bad quality of the sinusoidal fit (large χ^2).

for a reliable identification of ω photoproduction events and consequently, a reliable extraction of the beam asymmetry can not be performed.

Several reasons were discussed and are summarized as follows:

- Due to the lack of tracking detectors, the angular resolution for charged particles reduces to the granularity of the central BGO calorimeter and the intermediate SciRi detector. As a consequence, artefacts in the $(\pi^+\pi^-\pi^0)$ invariant mass distribution (or equivalently, in the missing mass to the proton distribution) appear, making the distinction between signal and background distributions impossible.
- The measurement of the photon flux is not yet possible, due to still not understood collimation effects and not fully known performances of the photon flux detectors (FluMo and GIM). As a consequence:
  - the extraction of the effective photon flux on the target is not possible,
  - the determination of the effective degree of polarization of the photon beam after collimation is not possible.
- Neither energy information nor particle ID is available in the intermediate angular region, and in the case of the proton being detected in the central region, the momenta are not well measured for kinetic energies higher than about 500 MeV. As a consequence, the exclusive detection of all final state particles becomes essential.
- From simulation studies (c.f. table 6.5), it has been found that geometrical acceptance and detector efficiency reduce the number of detected ω photoproduction events to about 30 %, and only about 10 % of them is reconstructed and selected by the presented analysis.

The issues related to the coarse detector granularity and the lack of statistics are regarded as the primary issues, since the remaining systematic effects are expected to be well below the current statistic uncertainties.

It is unclear how the analysis technique could be improved taking the known issues into account. The lack of overall energy and angular resolution means that even for an exclusive reconstruction, as it was performed, a kinematic fit can not recover a resolution of the reconstructed $(\pi^+\pi^-\pi^0)$ invariant mass sufficient to distinguish the ω signal from competing background channels.

The usage of a template fit to better describe and subtract the contributions from competing channels is not considered safe as of yet (c.f. section 6.4): the uncertainties of the cross section implemented in the event generator, the acceptances, the detection efficiencies and the flux normalization would in this case all affect the extraction of the number of reconstructed ω photoproduction events and none of them has been studied systematically within the collaboration.

In summary, it can be concluded that the primary issue for the study of mixed charged and neutral final states is the poor angular resolution for charged particles which could be overcome by taking the MWPC and MRPC detectors into operation. This would remove the artefacts in the mass distributions and would allow for a safer background subtraction procedure.

As secondary issues for the beam asymmetry, systematic studies of the effective photon flux on the target and the extraction of its degree of polarization still have to be performed.

Concluding, a further study of the beam asymmetry for ω photoproduction off proton with the existing setup of BGO-OD before full commissioning of the MWPC and MRPC detectors is not desirable.

Chapter 7

Summary and Conclusion

Experiments with high energy photon beams are nowadays one of the tools for the study of the underlying mechanisms responsible for the production of hadrons. In 2012, measurements of the photoproduction of ω mesons in statistically not highly exploited energy regions have been proposed to the PAC of ELSA by the BGO-OD collaboration. A polarized photon beam with known degree of polarization is requested to perform the foreseen measurements of the beam asymmetry.

The then newly installed BGO-OD experiment located at the accelerator ELSA uses an energy-tagged photon beam which is produced via bremsstrahlung and impinges on a central proton target. The setup combines a central electromagnetic calorimeter covering almost the full solid angle and a forward tracking spectrometer to reconstruct the momentum of charged particles. It is complemented by time of flight walls for charged particle identification. The BGO-OD setup is still missing tracking detectors for charged particles in the region above 12° polar angle, leading to a poorer angular resolution than the one foreseen in the proposal for the measurement of the beam asymmetry of ω photoproduction.

In the course of this thesis, the procedures for the time alignment of the more than 800 trigger signals have been optimized such that the necessary preparation of the setup for data-taking can now be efficiently performed in about 1 hour. The implemented method is also employed for the time calibration of the almost 6000 channels of the full setup and the high control achieved by this procedure serves as a tool for online diagnosis of hardware problems in the setup phase. Improvements of the event time reconstruction permit to identify the particular bunch of the electron beam from the accelerator that contained the electron which gave rise to the trigger signal. This will allow to increase the event time resolution to the bunch length of approximately 80 ps, depending on the configuration of the accelerator.

Furthermore, two time of flight walls have been installed and commissioned, equipped with a newly developed readout electronics. The idea of making use of the time over threshold measured by the new electronics allowed to improve the time resolution of the detector by a factor of two via a time walk correction technique and to equalize the gain of the several channels of the time of flight walls and to monitor their stability online. By now, the same electronics is in successful use for four other sub-detectors at BGO-OD.

Alongside these improvements, software development has been performed implementing functionalities for the filtering and visualization of data, focusing both on an increased performance compared to the use of customized code for all analyses and offering a fully documented, easy-to-use set of tools to the full collaboration. A recompilation of the framework is not necessary anymore, which allows to test different selection criteria quickly. This is complemented by an extension of the framework which permits to start the physics analysis from a common, pre-processed and reduced dataset instead of from the raw data.

As a test case of the not yet completed setup and of the complete analysis chain, a reconstruction of π^0 photoproduction events is performed, checking also the techniques for the extraction of the relative fluxes in two polarization planes and of the degree of polarization of the photon beam. After a selection based on the reconstructed invariant mass of the decay products of the π^0 $\left(\pi^0 \to \gamma\gamma\right)$, the beam asymmetry is extracted and confirmed to agree with published data within the statistical uncertainties.

Based on this experience, a first reconstruction of $\gamma p \to p\omega$ is attempted, identifying the ω meson via its decay $\omega \to \pi^+\pi^-\pi^0$. An exclusive detection of all final state particles is required. Since the contamination from non-resonant three-pion production prevents a clean event selection, the use of a fitting procedure to subtract the competing background channels is necessary. The major issue in the application of this procedure is found to be the limited angular resolution of the BGO-OD setup for charged particles with polar angles Θ above $12°$ in the laboratory frame, due to the fact that tracking detectors covering this region are still missing. This generates artefacts in the mass distributions of the reconstructed $(\pi^+\pi^-\pi^0)$-system which can not be fully overcome even by a kinematic fit, both for the events from the ω decay and for the incoherent three-pion production events. Still, a separation of 'signal' and 'background' events is attempted using a dedicated weighting technique. Considering the low statistics and the inability to cross-check systematic uncertainties for this approach, it can not yet be regarded as a procedure which is fully under control. The results are used to tackle the extraction of the beam asymmetry for $\vec{\gamma}p \to p\omega$ for two data-taking periods (June / July and October / November 2015) independently.

Finally, it can be concluded that the current status of the experimental setup, which is still missing two tracking detectors for charged particles, is not yet appropriate for a proper identification of ω photoproduction events and, as a consequence, is not yet ready for the proposed measurements of the beam asymmetry.

Bibliography

[ABB68] ABBHHM: Aachen–Berlin–Bonn–Hamburg–Heidelberg–München Collaboration. 'Photoproduction of Meson and Baryon Resonances at Energies up to 5.8 GeV'. In: *Phys. Rev.* 175 (5 Nov. 1968), pp. 1669–1696. DOI: 10.1103/PhysRev.175.1669 (cit. on p. 174).

[Ago+03] S. Agostinelli et al. 'GEANT4: A Simulation toolkit'. In: *Nucl. Instrum. Meth.* A506 (2003), pp. 250–303. DOI: 10.1016/S0168-9002(03)01368-8 (cit. on pp. 139, 174).

[Ale15] S. Alef. 'Scintillating Fibre detector and kinematic fitting for the BGO-OD experiment'. master thesis. Rheinische Friedrich-Wilhelms-Universität Bonn, Sept. 2015. URL: https://www.hsag.physik.uni-bonn.de/forschung/diplom-doktorarbeiten/diplom-masterarbeiten/Masterarbeit_Stefan%20Alef.pdf (cit. on p. 17).

[Ave99] P. Avery. *Applied Fitting Theory VI: Formulas for Kinematic Fitting*. CBX 98-37. Apr. 1999. URL: http://www-f9.ijs.si/~matevz/docs/EaveryFitting/fitting.html (visited on 6th Mar. 2017) (cit. on p. 157).

[Bal+73] J. Ballam et al. 'Vector-Meson Production by Polarized Photons at 2.8, 4.7, and 9.3 GeV'. In: *Phys. Rev. D* 7 (11 June 1973), pp. 3150–3177. DOI: 10.1103/PhysRevD.7.3150 (cit. on p. 174).

[Bar+03] J. Barth et al. 'Low-energy photoproduction of ω-mesons'. In: *The European Physical Journal A - Hadrons and Nuclei* 18.1 (2003), pp. 117–127. ISSN: 1434-601X. DOI: 10.1140/epja/i2003-10061-y (cit. on pp. 4, 174).

[Bau14] P. Bauer. 'Aufbau und Test eines schnellen Flugzeitspektrometers für das BGO-OD-Experiment'. German. bachelor thesis. Rheinische Friedrich-Wilhelms-Universität Bonn, Aug. 2014. URL: https://www.hsag.physik.uni-bonn.de/forschung/diplom-doktorarbeiten/bachelorarbeiten/BachelorThesis_PatrickBauer.pdf (cit. on pp. 67, 72, 82).

[BB93] R. Barlow and C. Beeston. 'Fitting using finite Monte Carlo samples'. In: *Computer Physics Communications* 77.2 (1993), pp. 219–228. ISSN: 0010-4655. DOI: 10.1016/0010-4655(93)90005-W (cit. on p. 201).

[BBS00] J. Berger, B. Boyer and P. Stassi. *Relative Gain Measurement for the 280 Go PMTs, PHOTONIS XP2282B/04 type*. Tech. rep. Institut des Sciences Nucléaires, Service Détecteurs et Instrumentation, 2000. URL: http://lpscwww.in2p3.fr/hadrons/go/gopostscripts/PMT_Relative_gain_measurement.pdf (visited on 6th Mar. 2017) (cit. on p. 107).

[Bel11] A. Bella. 'Setup of a Goniometer System for the Production of Linearly Polarised Photons for the BGO-OD Experiment at ELSA'. diploma thesis. Rheinische Friedrich-Wilhelms-Universität Bonn, 2011. URL: https://www.hsag.physik.uni-bonn.de/forschung/diplom-doktorarbeiten/diplom-masterarbeiten/Diplomarbeit_AndreasBella.pdf (cit. on p. 162).

[Bel16] A. Bella. 'Linearly polarised photons at the BGO-OD experiment at ELSA'. PhD thesis. Rheinische Friedrich-Wilhelms-Universität Bonn, 2016. URL: http://nbn-resolving.de/urn:nbn:de:hbz:5n-44930 (cit. on pp. 15, 16, 162, 179).

[Bie] J. Bieling. *The jTDC, an FPGA based high resolution TDC implemented on Xilinx Spartan 6 and compatible FPGAs*. URL: https://github.com/jobisoft/jTDC/wiki (cit. on pp. 232, 281).

[Bie+12] J. Bieling et al. 'Implementation of mean-timing and subsequent logic functions on an FPGA'. In: *Nuclear Instruments and Methods in Physics Research Section A: Accelerators, Spectrometers, Detectors and Associated Equipment* 672 (2012), pp. 13–20. ISSN: 0168-9002. DOI: 10.1016/j.nima.2011.12.104 (cit. on p. 234).

[Bie11] J. Bieling. 'FPGA module and firmware descriptions'. BGO-OD-008-2011 (internal). Aug. 2011 (cit. on pp. 33, 44, 60, 234).

[Bla+92] T. Blaich et al. 'A large area detector for high-energy neutrons'. In: *Nuclear Instruments and Methods in Physics Research Section A: Accelerators, Spectrometers, Detectors and Associated Equipment* 314.1 (1992), pp. 136–154. ISSN: 0168-9002. DOI: 10.1016/0168-9002(92)90507-Z (cit. on p. 104).

[Bös16] S. Böse. 'Aufbau und Test eines neuen Szintillationsfaser-Detektors für das neue Vorwärtsspektrometer an ELSA'. German. PhD thesis. Rheinische Friedrich-Wilhelms-Universität Bonn, 2016. URL: http://nbn-resolving.de/urn:nbn:de:hbz:5n-43001 (cit. on pp. 23, 77).

[BR97] R. Brun and F. Rademakers. 'ROOT: An object oriented data analysis framework'. In: *Nucl. Instrum. Meth.* A389 (1997), pp. 81–86. DOI: 10.1016/S0168-9002(97)00048-X. URL: http://root.cern.ch (cit. on pp. 125, 126, 139, 199, 282).

[Bru+89] R. Brun et al. 'PAW, a general-purpose portable software tool for data analysis and presentation'. In: *Computer Physics Communications* 57.1 (1989), pp. 432–437. ISSN: 0010-4655. DOI: 10.1016/0010-4655(89)90257-9 (cit. on pp. 126, 282).

[Büc+12] M. Büchele et al. 'The GANDALF 128-Channel Time-to-Digital Converter'. In: *Physics Procedia* 37 (2012), pp. 1827–1834. ISSN: 1875-3892. DOI: 10.1016/j.phpro.2012.02.504 (cit. on p. 230).

[CAE16] CAEN – Tools for Discovery. *Technical Information Manual Mod. V1190-VX1190 A/B, 128/64 Ch Multihit TDC*. Rev. 14. Nov. 2016. URL: http://www.caen.it/servlet/checkCaenManualFile?Id=12130 (visited on 6th Mar. 2017) (cit. on p. 78).

[CAM79] R. A. Cecil, B. D. Anderson and R. Madey. 'Improved predections of neutron detection efficiency for hydrocarbon scintillators from 1 MeV to about 300 MeV'. In: *Nuclear Instruments and Methods* 161.3 (1979), pp. 439–447. ISSN: 0029-554X. DOI: 10.1016/0029-554X(79)90417-8 (cit. on p. 100).

[Chr04] J. Christiansen. 'HPTDC high performance time to digital converter'. In: (Mar. 2004). URL: https://cds.cern.ch/record/1067476/files/cer-002723234.pdf (cit. on p. 78).

[Dre+99] D. Drechsel et al. 'A Unitary isobar model for pion photoproduction and electroproduction on the proton up to 1-GeV'. In: *Nucl. Phys.* A645 (1999), pp. 145–174. DOI: 10.1016/S0375-9474(98)00572-7 (cit. on p. 171).

[Ele] Elektroniklaboratorien Bonn UG. *ELB-MEZ-HSD16*. URL: http://www.elbonn.de/cms/item.php?theme=elb-mez-hsd16&language=de (visited on 6th Mar. 2017) (cit. on p. 80).

[Fre10] O. Freyermuth. 'Aufbau eines TDC auf einem FPGA–Board'. bachelor thesis. Rheinische Friedrich-Wilhelms-Universität Bonn, July 2010. URL: http://www.institut3b.physik.rwth-aachen.de/global/show_document.asp?id=aaaaaaaaaamlexe (cit. on p. 231).

[Fre12] O. Freyermuth. 'Development of a Dead Time Measurement System for the Compass Experiment using FPGA Technology'. master thesis. Rheinische Friedrich-Wilhelms-Universität Bonn, Oct. 2012. URL: http://www.institut3b.physik.rwth-aachen.de/global/show_document.asp?id=aaaaaaaaaamlakl (cit. on pp. 11, 236).

[Fre16] O. Freyermuth. 'Tutorial to Simplified Analysis using the ExPlORA Framework'. ExPlORA documentation (internal). Oct. 2016 (cit. on p. 131).

[Fro+16] F. Frommberger et al. *Electron Stretcher Accelerator (ELSA)*. Sept. 2016. URL: http://www-elsa.physik.uni-bonn.de/Beschleuniger/bilder/elsaplan_en.pdf (visited on 3rd Nov. 2016) (cit. on p. 9).

[GKR15] F. Gonnella, V. Kozhuharov and M. Raggi. 'Time over threshold in the presence of noise'. In: *Nuclear Instruments and Methods in Physics Research Section A: Accelerators, Spectrometers, Detectors and Associated Equipment* 791 (2015), pp. 16–21. ISSN: 0168-9002. DOI: 10.1016/j.nima.2015.04.028 (cit. on p. 98).

[GPW86] R. T. Giles, F. M. Pipkin and J. P. Wolinski. 'Tests of conventional and microchannel plate photomultipliers as components of a scintillation time-of-flight system'. In: *Nuclear Instruments and Methods in Physics Research Section A: Accelerators, Spectrometers, Detectors and Associated Equipment* 252.1 (1986), pp. 41–52. ISSN: 0168-9002. DOI: 10.1016/0168-9002(86)90934-4 (cit. on p. 67).

[Gut+14] E. Gutz et al. 'High statistics study of the reaction $\gamma p \to p\pi^0\eta$'. In: *Eur. Phys. J.* A50 (2014), p. 74. DOI: 10.1140/epja/i2014-14074-1 (cit. on p. 171).

[Ham08] D. Hammann. 'Test und Betrieb der Prototyp-Driftkammer für das B1-Spektrometer'. German. diploma thesis. Rheinische Friedrich-Wilhelms-Universität Bonn, 2008. URL: https://www.hsag.physik.uni-bonn.de/forschung/diplom-doktorarbeiten/diplom-masterarbeiten/Diplomarbeit_DanielHammann.pdf (cit. on p. 27).

[Ham16] D. Hammann. 'The data acquisition for the BGO-OD experiment'. PhD thesis. Rheinische Friedrich-Wilhelms-Universität Bonn, 2016. URL: http://nbn-resolving.de/urn:nbn:de:hbz:5n-44095 (cit. on pp. 35, 44, 52, 56, 125).

[Han96] J. Hannappel. 'Erste Messung der Reaktion γp $\to \omega$p bis zu Werten von $|t| = 1\,\mathrm{GeV}^2$ mit dem SAPHIR-Detektor'. German. BONN-IR-97-15. PhD thesis. Rheinische Friedrich-Wilhelms-Universität Bonn, 1996 (cit. on p. 174).

[Jud16] T. C. Jude. 'Alignments, energy corrections, efficiencies and resolutions applied to data at the preanalysis stage'. BGO-OD-027-2016 (internal). July 2016 (cit. on pp. 20, 139, 141).

[Jud17] T. C. Jude. *Private Communication*. 2017 (cit. on p. 190).

[Kle+08] F. Klein et al. 'Beam asymmetries in near-threshold ω photoproduction off the proton'. In: *Phys. Rev. D* 78 (11 Dec. 2008), p. 117101. DOI: 10.1103/PhysRevD.78.117101 (cit. on pp. 5, 174).

[Kna15] J. Knaust. 'Glasfasergestützte Synchronisation des BGO-OD Experiments mit den Strahlpaketen von ELSA'. German. master thesis. Rheinische Friedrich-Wilhelms-Universität Bonn, Sept. 2015. URL: https://www.hsag.physik.uni-bonn.de/forschung/diplom-doktorarbeiten/bachelorarbeiten/bachelorthesis-jensknaust.pdf (cit. on pp. 64, 244).

[Lev+96] P. Levi Sandri et al. 'Performance of a BGO calorimeter in a tagged photon beam from 260 to 1150 MeV'. In: *Nuclear Instruments and Methods in Physics Research Section A: Accelerators, Spectrometers, Detectors and Associated Equipment* 370 (1996), pp. 396–402. ISSN: 0168-9002. DOI: 10.1016/0168-9002(95)00839-X (cit. on p. 20).

[Max02] Maxim Integrated. *Dual ECL and Dual/Quad PECL, 500 ps, Ultra-High-Speed Comparators*. 19-2409; Rev 1; 9/02. 2002. URL: https://www.maximintegrated.com/en/products/analog/amplifiers/MAX9601.html (visited on 6th Mar. 2017) (cit. on p. 81).

[Mei13] P. Meiß. 'The Time Of Flight Spectrometer of the BGO-OD Experiment'. diploma thesis. Rheinische Friedrich-Wilhelms-Universität Bonn, Sept. 2013. URL: https://www.hsag.physik.uni-bonn.de/forschung/diplom-doktorarbeiten/diplom-masterarbeiten/Diplomarbeit_PeterMeiss.pdf (cit. on pp. 67, 70, 76, 79, 99, 102, 236, 239).

[Mes11] F. Messi. 'The AFA board (an active splitter for analog signals)'. BGO-OD-009-2011 (internal). July 2011 (cit. on p. 77).

[Mes15] F. Messi. 'The Tagging System of the BGO-OD experiment'. PhD thesis. Rheinische Friedrich-Wilhelms-Universität Bonn, 2015. URL: http://nbn-resolving.de/urn:nbn:de:hbz:5n-40284 (cit. on pp. 61, 77).

[Mes16] R. Messi. *Private Communication*. 2016 (cit. on p. 21).

[Pat+16] C. Patrignani et al. 'Review of Particle Physics'. In: *Chin. Phys.* C40.10 (2016), p. 100001. DOI: 10.1088/1674-1137/40/10/100001 (cit. on pp. 3, 174).

[PFH13] D. Proft, F. Frommberger and W. Hillert. 'Proceedings of IPAC2013: The Accelerator Control System at ELSA'. In: 2013, p. 3149. URL: https://accelconf.web.cern.ch/AccelConf/IPAC2013/papers/thpea002.pdf (visited on 6th Mar. 2017) (cit. on p. 10).

[Pho07] Photonis S.A.S. *Photomultiplier Tubes Catalogue*. 2007. URL: https://hallcweb.jlab.org/DocDB/0008/000809/001/PhotonisCatalog.pdf (visited on 6th Mar. 2017) (cit. on pp. 107, 118).

[Pic95] M. Picard. 'Entwurf, Entwicklung und Inbetriebnahme eines verteilten Rechnerkontrollsystems für die Elektronen-Stretcher-Anlage ELSA, unter besonderer Berücksichtigung der Extraktion im Nachbeschleunigungsbetrieb bis 3.5 GeV'. PhD thesis. Rheinische Friedrich-Wilhelms-Universität Bonn, 1995. URL: http://www-elsa.physik.uni-bonn.de/Publikationen/texte/picard_dr.pdf (visited on 6th Mar. 2017) (cit. on p. 11).

[Rei15] B.-E. Reitz. 'Coherent bremsstrahlung with the scintillating fiber detector of the BGO-OD tagging system'. master thesis. Rheinische Friedrich-Wilhelms-Universität Bonn, Oct. 2015. URL: https://www.hsag.physik.uni-bonn.de/forschung/diplom-doktorarbeiten/diplom-masterarbeiten/Masterarbeit_Bjoern-EricReitz.pdf (cit. on p. 17).

[Rit] S. Ritt. *DRS4: 9 Channel, 5 GSPS Switched Capacitor Array*. REV. 0.9. Paul Scherrer Institute. URL: https://www.psi.ch/drs/DocumentationEN/DRS4_rev09.pdf (cit. on p. 78).

[Rom12] M. Romaniuk. 'Target system'. BGO-OD-016-2012 (internal). Dec. 2012 (cit. on p. 18).

[S+11] C. Schmidt, A. Suele, U. Thoma et al. '**Ex**tended **Pl**uggable **O**bjectoriented **R**OOT(ified) **A**nalysis) for the CBELSA/TAPS experiment'. 2011 (cit. on p. 126).

[SB14] G. Scheluchin and J. Bieling. 'Spartan 6 firmwares (jTDC v6 and derivatives)'. BGO-OD-022-2014 (internal). Sept. 2014 (cit. on pp. 60, 234).

[Sch12] L. Schildgen. 'Charakterisierung des Antwortverhaltens der Time-of-Flight-Detektoren des BGO-OD-Experiments'. German. bachelor thesis. Rheinische Friedrich-Wilhelms-Universität Bonn, July 2012 (cit. on pp. 67, 70).

[Sch15] G. Scheluchin. 'Meson photoproduction on the proton using the BGO-OD detector complemented by a new Scintillating Ring (SciRi)'. master thesis. Rheinische Friedrich-Wilhelms-Universität Bonn, Aug. 2015. URL: https://www.hsag.physik.uni-bonn.de/forschung/diplom-doktorarbeiten/diplom-masterarbeiten/Masterarbeit_GeorgScheluchin.pdf (cit. on pp. 28, 135, 150).

[Sch16] G. Scheluchin. *Private Communication*. 2016 (cit. on p. 157).

[Str+15] I. I. Strakovsky et al. 'Photoproduction of the ω meson on the proton near threshold'. In: *Phys. Rev. C* 91 (4 Apr. 2015), p. 045207. DOI: 10.1103/PhysRevC.91.045207 (cit. on p. 5).

[Ugu+12] C. Ugur et al. 'A 16 channel high resolution (<11 ps RMS) Time-to-Digital Converter in a Field Programmable Gate Array'. In: *Journal of Instrumentation* 7.02 (2012), p. C02004. DOI: 10.1088/1748-0221/7/02/C02004 (cit. on p. 230).

[Veg+15] V. Vegna et al. 'Measurement of the Σ beam asymmetry for the ω photo-production off the proton and the neutron at GRAAL'. In: *Phys. Rev.* C91.6 (2015), p. 065207. DOI: 10.1103/PhysRevC.91.065207 (cit. on pp. 5, 173, 214).

[WIE11] W-IE-NE-R Plein & Baus GmbH. *W-Ie–Ne-R AVM16 / AVX16: 16 channel ADC, 160 MHz with features extraction, User's Manual*. V 2.0. Nov. 2011. URL: http://file.wiener-d.com/documentation/AVM16/WIENER_AVM16-Manual_2.0.pdf (visited on 6th Mar. 2017) (cit. on p. 20).

[Wil+09a] M. Williams et al. 'Differential cross sections and spin density matrix elements for the reaction $\gamma p \to p\omega$'. In: *Phys. Rev. C* 80 (6 Dec. 2009), p. 065208. DOI: 10.1103/PhysRevC.80.065208 (cit. on p. 5).

[Wil+09b] M. Williams et al. 'Partial wave analysis of the reaction $\gamma p \to p\omega$ and the search for nucleon resonances'. In: *Phys. Rev. C* 80 (6 Dec. 2009), p. 065209. DOI: 10.1103/PhysRevC.80.065209 (cit. on p. 5).

[Wil96] D. H. Wilkinson. 'Ionization energy loss by charged particles Part I. The Landau distribution'. In: *Nuclear Instruments and Methods in Physics Research Section A: Accelerators, Spectrometers, Detectors and Associated Equipment* 383.2 (1996), pp. 513–515. ISSN: 0168-9002. DOI: 10.1016/S0168-9002(96)00774-7 (cit. on p. 100).

[Wor+12] R. L. Workman et al. 'Unified Chew-Mandelstam SAID analysis of pion photoproduction data'. In: *Phys. Rev. C* 86 (1 July 2012), p. 015202. DOI: 10.1103/PhysRevC.86.015202 (cit. on p. 171).

[Yuk35] H. Yukawa. 'On the Interaction of Elementary Particles I'. In: *Proc. Phys. Math. Soc. Jap.* 17 (1935). [Prog. Theor. Phys. Suppl.1,1(1935)], pp. 48–57. DOI: 10.1143/PTPS.1.1 (cit. on p. 1).

[Zim12] T. Zimmermann. 'PhotonFluxMonitor for the BGO-OD experiment'. diploma thesis. Rheinische Friedrich-Wilhelms-Universität Bonn, Jan. 2012. URL: https://www.hsag.physik.uni-bonn.de/forschung/diplom-doktorarbeiten/diplom-masterarbeiten/Diplomarbeit_ThomasZimmermann.pdf (cit. on p. 17).

[Zim17] T. Zimmermann. 'Møller polarimetry for the BGO-OD experiment and cross section measurement of the reaction $\gamma p \to K^+\Lambda$ at the extreme forward angles'. PhD thesis. Rheinische Friedrich-Wilhelms-Universität Bonn, 2017. URL: http://nbn-resolving.de/urn:nbn:de:hbz:5n-45967 (cit. on p. 190).

APPENDIX A

Time of Flight Walls

In this appendix, additional technical descriptions related to chapter 4 is presented.

A.1 FPGA-based TDCs: The jTDC

The time to digital conversion is nowadays often achieved by the usage of customized ASICs or FPGAs. The main advantage of custom electronics as compared to commercial solutions is the fact that any preprocessing or preselection which needs to be done in real time can already be implemented in the hardware itself. Furthermore, the integration of the trigger logic into the very same hardware module as the TDC allows to remove a common source of errors.

For the BGO-OD experiment, the choice for FPGAs was made due to their high availability and flexibility: the company 'ELB'(1) located close-by produces ready to use, versatile FPGA boards, which could be easily integrated into the existing VME-based infrastructure. Additionally, close contact to the manufacturer was possible.

FPGAs are **F**ield-**P**rogrammable **G**ate **A**rrays. This means that these **i**ntegrated **c**ircuits (ICs) feature a set of logic elements like flip-flops, loadable LUTs(2) and inverters which can be flexibly interconnected by applying a user-defined hardware description. This is usually complemented by additional elements like phase-locked loops or delay-locked loops for clock generation and control, DSP(3) elements or configurable delays. The programmability of this IC allows to develop and test an algorithm or hardware logic directly on the silicon without

(1) Elektroniklaboratorien Bonn UG, www.elbonn.de
(2) **L**ook **U**p **T**ables
(3) **D**igital **S**ignal **P**rocessing

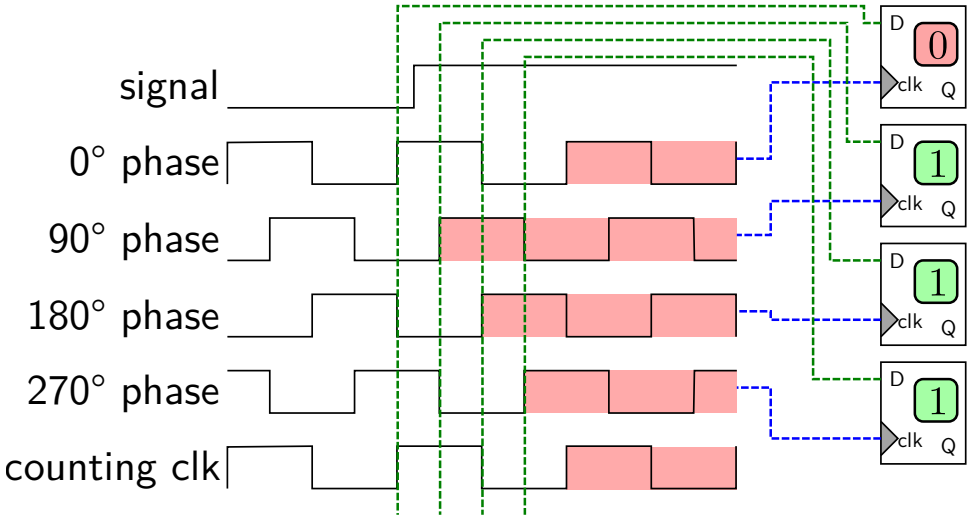

Figure A.1: Schematic illustration of signal sampling via phase-shifted clocks to measure a leading edge time with a resolution better than the period of a single clock.

manufacturing an expensive, dedicated ASIC if the offered resources are sufficient for the use case.

The boards manufactured by ELB feature connectors for three piggyback daughter boards ('mezzanines') to treat the analogue or digital input signals before they enter the FPGA. These mezzanines can be chosen flexibly depending on the use case (c.f. section 4.4.6).

For the implementation of a TDC on an FPGA, two techniques are common practice:

1. Shifted clock sampling (explained in more detail e.g. in [Büc+12])
2. Carry chain sampling (e.g. the jTDC presented here and the 'TRB3' implementation detailed at [Ugu+12])

The sampling technique with phase-shifted clocks is visualized in fig. A.1: a high frequency clock is used (usually below 500 MHz for technical reasons) to sample the signal. Commonly, special elements on the FPGA provide a configurable PLL(4) or DLL to derive this clock from an input clock, which may have a lower frequency. These elements also provide the possibility to produce phase-shifted variants of a common clock signal.

These clocks can then be distributed to the signal-sampling flip-flops in the FPGA. These flip-flops may even sample the signal at both rising and falling edge of the clock signal (⇒ **D**ual **D**ata **R**ate, short DDR) to further increase the sampling resolution.

Using this approach, the effective sampling rate of the incoming signal may be increased by a factor of 16, assuming double data rate and 8 shifted clocks. This technique was used in the 'The GANDALF 128-Channel Time-to-Digital Converter' (c.f. [Büc+12] and a time resolution of

(4) **P**hase–**l**ocked **l**oop

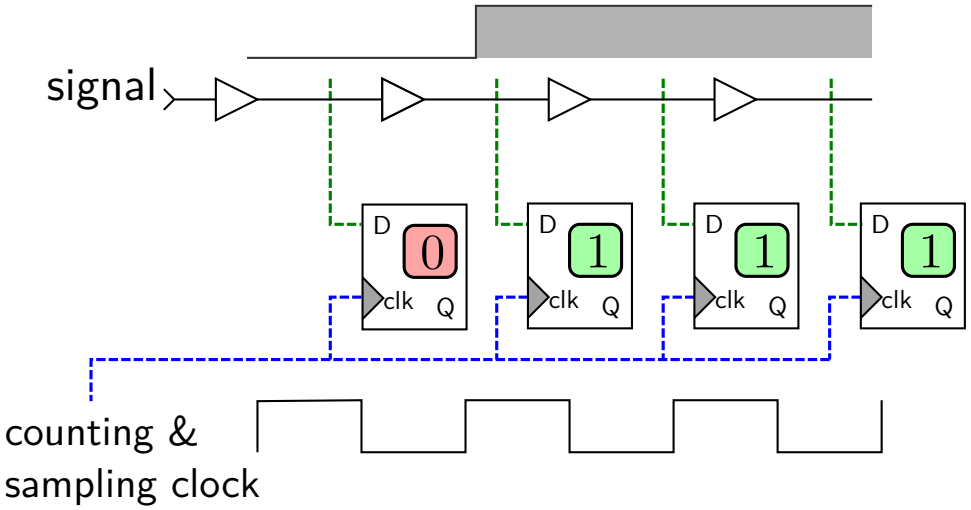

Figure A.2: Schematic illustration of signal sampling via the tapped delay line approach, i.e. passing the signal through an unclocked line sampled at several taps during each clock cycle. This allows to achieve a higher resolution than the clock period.

64 ps could be achieved using a base-clock of 500 MHz on an FPGA-board based on a Xilinx® Virtex®5 FPGA.

There are of course some advantages and downsides to this method:

1. For high resolution, expensive FPGA chips are necessary since the resolution directly scales with the maximum clock frequency.

2. The implementation has to be carefully optimized to minimize the input signal skew of the path for each channel to all sampling flip-flops.

3. The signals sampled in different clock domains have to be synchronized for leading edge detection and readout which usually proves complicated.

The main advantage is that the effective width of the bins is mostly equal and the resource-usage (in terms of flip-flops and slices on the FPGA) is minimal.

A simplified proof-of-concept of this technique (for a single channel) was also implemented in the course of my Bachelor thesis, making use of four phase-shifted 100 MHz clocks on a Spartan®3 based FPGA board [Fre10]. It proved to be more complex in the design details and by far less adequate for cheaper FPGA chips than the carry chain sampling which will be explained in the following paragraphs.

The sampling technique using carry chain elements is visualized in fig. A.2: the fastest segmented propagation path on the FPGA, the carry chain, is usually used to transport the carry bit in arithmetic operations. In each slice of the FPGA along a carry chain, the signal can be extracted and routed to the data-inputs of the flip-flops in the slice. Additionally, the

input-signal has to be routed directly from the input pad (not using any clocked path) into the carry chain.

If the propagation time through the full carry chain is longer than one clock cycle of the sampling clock which is used to trigger the flip-flops, this technique allows to sample the signal using the propagation time of one such 'step' of the carry chain (i.e. the path between two flip-flop inputs). Furthermore, the design has to fix the positioning and lengths of the used the carry-chains.

Using this approach, the bin-widths are defined by the lengths of the mentioned propagation delays through the carry chain between the flip-flop inputs, hence the name 'tapped delay line'. These bin widths need not be equal but only constant over time, since a calibration can accommodate for the spread in bin widths if the variation is not macroscopic. This variation in bin widths is called integral non-linearity, short 'INL'.

For this method, only one clock domain is used and no synchronization needs to be done. Since the minimum bin size is not determined by the minimum propagation delay between two 'taps', the clock frequency is not decisive for the resolution anymore(5) Naturally, this also comes with several downsides:

1. A calibration to correct for the integral non-linearity is needed, at least once for each board and firmware version.

2. The resource-usage is much larger, since many flip-flops for sampling across the whole chip have to be used, leaving less space for additional features.

3. Consequently, the power draw of such a design is higher.

The main advantage, however, is the fact that cheaper FPGA chips can be used, since the high clock frequency and the multiple clock domains which are needed for the phase-shifted clock sampling are not necessary for this sampling technique. In addition, the only fixed part of the design is the allocation (position and length) of the carry chains, while the phase-shifted clock approach requires careful positioning of all sampling flip-flops (either manually or assisted by self-developed, FPGA-model specific code). For this reason, the This allows for much easier porting of the design to different FPGA models.

Consequently, the jTDC was implemented by J. Bieling for the Spartan®3 boards produced by ELB (called VFB-2). The design was later also transferred to the successor FPGA board VFB-6 which is based on a Spartan®6 chip. The full details and implementation for the Spartan®6 based version are freely available in [Bie], while the key features are shortly summarized in table A.1.

The notable points from this feature list are the impressive rate stability and time resolution which are mainly limited by the used FPGA and not by the design of the TDC itself. In addition,

(5) Of course the maximum design clock frequency for an FPGA chip and the propagation time of the carry chain are usually correlated.

(6) approximate limit by the leading edge detection mechanism in the firmware — the limit imposed e.g. by the LVDS input mezzanines is about 3 ns

Number of channels per board	up to 100
TDC bin size	40 ps average, 30 ps RMS
32-bit scalers	for all channels, max. 200 MHz, can be gated
Maximum input rate (all channels)	200 MHz
Double pulse resolution	5 ns
Maximum hits per event	15 360 $\Rightarrow$ 775 ns time window at highest possible rate
Minimum signal length	400 ps[(6)]

Table A.1: Key features of the jTDC as implemented on a Spartan®6.

the jTDC features two event FIFOs which can be used alternatingly. This is optimized for the event-based acquisition system used at the BGO-OD experiment, since it allows to read out an event during the live time of the experiment, i.e. while the module is already ready to accept a new trigger.

In view of the discriminator mezzanine described in section 4.4.6, the very short minimum signal length and the pattern detection (to identify leading and trailing edges) will be discussed in more detail in section 4.6.1.

A.2 Mean-Timer Trigger

The key information from the time of flight walls is the actual arrival time of the particle in the sensitive volume with respect to the start time of the experiment. The start time is defined by the tagger detector, or, more refined, by the determination of the time of the bunch which contained the electron on which the tagger detector triggered, derived from the RF frequency signal of the accelerator.

In offline analysis, this start-time reconstruction can be arbitrarily complicated as will be discussed in section 3.5 and make use of calibrations made with high statistics data. Since the BGO experiment uses flexible hardware trigger logic and a high-level software trigger is not available, an 'online', hardware-based approach has to be used to allow for a trigger condition including the time of flight walls.

The determination of the incident time of the particle needs a basic reconstruction already on this hardware level, since the time information from the single channels of the two-sided readout is completely spoiled by the effective speed of light (c.f. section 4.2.3) along the several metres long bars. As an order of magnitude, an effective speed of light of about $15\,\mathrm{cm\,ns^{-1}}$ can be assumed. For a plastic scintillator of 3 m length, this already results in a time difference of 20 ns for a particle hitting close to the photomultiplier as compared to a particle impinging at the other end of the bar. To accommodate for this linear effect[(7)], the mean time of the two-ended

(7) The effect is linear since the effective speed of light is a material constant.

readout can be used as time of flight information and consequently, as the trigger time.

There are basically two possible ways to implement a mean-timer in hardware on an FPGA board:

1. Implementation using discrete logic: a cascade of LUTs, OR and AND blocks).
   A mean-timer based on this design is described in [Bie+12].

2. A mean-timer based on a sampling stage which uses internal clocked delay structures (such as shift registers) and checks for time overlaps of two neighbouring channels.
   This technique is used for the ToF-trigger implemented by J. Bieling and described in this thesis.

While the first technique for sure allows to achieve a higher time resolution of the trigger signal since all paths are unclocked, it requires a huge manual effort in the design process and the usage of additional analogue delay elements which are usually part of modern FPGAs.

However, the time resolution of the trigger signal does not need a high precision, since in any case, a wide time gate should be chosen to not discriminate the β too strictly (c.f. section 3.4.2). For the reconstruction, the digitized time information of all hits is anyways stored with full precision for all triggered events. For that reason, if the trigger rate and module buffers allow to record a sufficient time window around the trigger time, the second technique is by far the easier choice in terms of implementation, calibration and configurability and is also the one used at the BGO-OD experiment.

The detailed functionality of this mean-timer trigger is outlined in two internal notes on the hardware of the experiment (c.f. [Bie11] and [SB14]). Some modifications have since been made by J. Bieling to improve the propagation time of the trigger logic at the cost of routing resources, which will be taken into account in the following short description.

First, the same hit-detection mechanism of the jTDC appendix A.1 is used. For the mean timing, only the clock cycle in which the leading edge was found is decisive. In this clock cycle, a '1' is injected into a shift register which exists for each channel separately. This logic '1' is only injected for one single clock cycle, i.e. the signal is *clipped*. Furthermore, a deliberate dead time of 35 ns is enforced to prevent trigger signals caused by multiple combinations between consecutive hits.

The logic which is applied is shown schematically in fig. A.3. The signals are shifted through the shift-registers by one step with each clock cycle. Each time, the check which is illustrated for one pair is made for all pairs in parallel: if the corresponding partner register was also active at the same position, or the position shifted by one, this creates a trigger signal.

Before the trigger is ready to be used in beamtime, an alignment procedure is required first. This is already apparent from the definition of the mean time:

$$t_{\text{mean}} = \frac{t_1 + t_2}{2} \tag{A.1}$$

The main issue is the question on how t_1 and t_2 are extracted, since in this sum, the 'absolute'

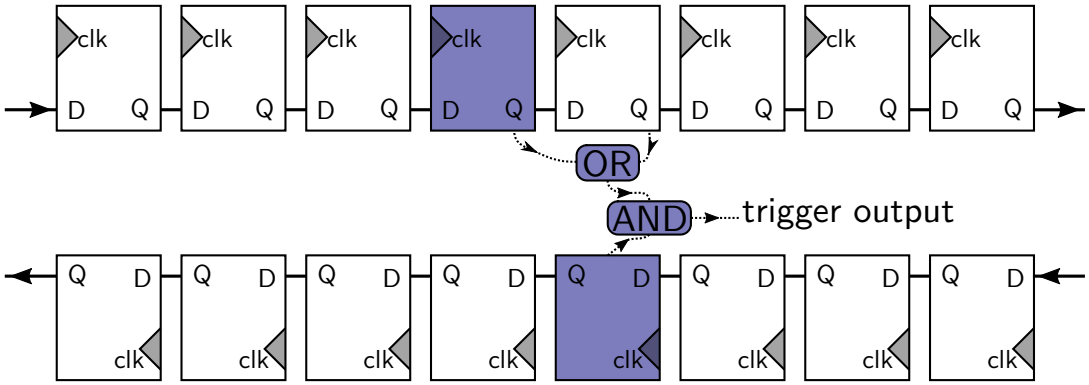

Figure A.3: Schematic illustration of the mean timer trigger logic. The picture shows the two shift registers for two neighbouring channels. The input signals are clipped to be one clock cycle long. Additionally, a deliberate dead time is applied so that only one flip flip for each channel will ever be active in the full registers. In order to simplify the scheme, the logic is only shown for one stage. In the real implementation, the illustrated condition is evaluated for all steps in parallel.

start time offset does not cancel out. This absolute offset is made by different delays for each channel by differing

- cable lengths from the PMT to the FPGA inputs,
- effective thresholds leading to time walk effects, e.g. due to different gain matching (c.f. section 4.7),
- variable routing path lengths inside the FPGA,
- delays introduced by the electronics before the FPGA.

For this reason, a calibration of the offset of these times (or rather, a time alignment) is always necessary already on trigger-level. This alignment procedure is performed using a special trigger condition, then afterwards using a partially automated tool to fit the time distributions and set the new delay parameters. The procedure itself will be detailed in section 3.4.

Additionally, for all single channels and the mean-timer channels, the firmware features scalers. 'Scalers' are simple counters which count up if a given signal is high. Usually, they check the signal with a fixed frequency (in this case, the clock frequency of 200 MHz) which also defines their maximum counting rate. In addition, one scaler counting each clock cycle is used to determine the total measurement time in terms of clock cycles. Combining these two pieces of information, the rate of a clock-synchronous signal can be measured. Furthermore, these scalers can be enabled / disabled by an additional gating signal which is usually chosen to limit the time in which the scalers are active to the live time of the experiment. The single-channel scalers and the clock scaler are actually already part of the jTDC-firmware (c.f. appendix A.1) relying upon the hit-detection capabilities of the jTDC.

The scalers used in the BGO-OD experiment are also a special implementation developed by J. Bieling, termed 'Slimfast Multioption Counter'[8]. A detailed description is given in the internal notes of the experiment and also summarized in [Fre12]. In short, a special design allows to minimize the number of paths for which strong routing constraints are necessary by imposing strong timing constraints only on the lowest bits of the counter. This strongly simplifies the routing and allows for better resource usage in the FPGA, since usually, the constraint for the maximum routing delay between subsequent flip-flops of a counter is one clock cycle of the counting clock. In the 'Slimfast Multioption Counter', this requirement is only applied for the connections between the flip-flops responsible for the lowest 4 bits. For all more significant bits of the counter, the constraint is loosened to $^1/_8$ of the counting clock. Consequently, the place-and-route process can distribute the used flip-flops more freely over the FPGA, thus simplifying these processes and usually improving the overall resource usage significantly which allows to fit more channels onto one FPGA module.

The performance of the mean-timer trigger is visualized in fig. 4.41b which displays the reconstructed β of the track versus the trigger time from the mean timer output. Taking into account the 5 ns inherent resolution, this demonstrates that a β range can be selected already on trigger level. The crucial point of this new trigger logic is that it was previously implemented on a separate FPGA module as shown in fig. 4.11a. With the jDisc module, it was possible to integrate the trigger logic on the very same FPGA, reducing the complexity of the electronics setup and ensuring that the measured time information and the trigger logic agree by design.

A.3 SADC Reconstruction

The raw data stream provided by the 'CAEN V1742' SADC (c.f. section 4.4.4) consists of the raw ADC values obtained by the digitization of the charges stored in the capacitors inside the *DRS4* chip. These samples need a calibration offset applied to overcome capacity fluctuations related to the manufacturing process. These offsets can be taken from a vendor-supplied table stored in the module. All samples need to be ordered in time before any feature extraction can be done. A simple visualization of this information is shown in fig. A.4.

The feature extraction is then done applying a baseline determination followed by a pulse detection technique based on differentiation to identify the rising slope. Afterwards, the slope is fitted to determine the start time from extrapolation to the baseline. Other parameters (pulse height, peak time, integral) can also be determined easily.

This reconstruction was already implemented in the thesis of P. Meiß [Mei13] and was extended and improved as part of this thesis, especially to correct for the measured trigger time and to allow for comparison with the time over threshold information from the jDisc device. For this, a simulation of the time over threshold for a given threshold was added which gives the necessary handle for the time walk correction (c.f. section 4.8).

(8) An alternate implementation based on usage of a dedicated DSP slice on the FPGA is by now also in heavy use in most of the firmwares.

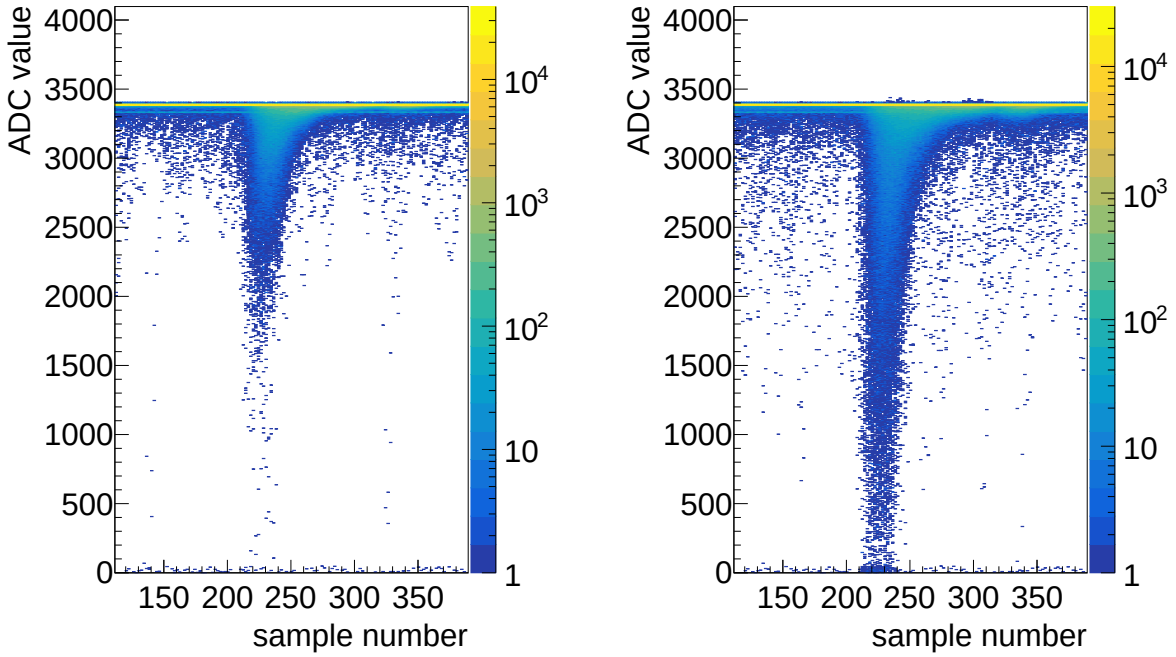

(a) SADC data for a single, central ToF2 channel with a high voltage setting of 1500 V

(b) SADC data for a single, central ToF2 channel with a high voltage setting of 1800 V

Figure A.4: Straightforward, oscilloscope-like visualization of the digitized samples. In this case, data taken during a test beamtime from a central channel of the ToF2 wall are shown. The horizontal axis corresponds to the sample number of the recorded data while the vertical axis corresponds to the raw ADC value for this sample. These histograms are filled once for each sample number and event with the digitized ADC value. Since the samples are first ordered in time and the trigger was on a correlated signal, this histogram corresponds to an oscilloscope display with an external trigger input and active persistence, since several pulses have been overlaid. For this reason, a prompt peak region is strongly visible. The full dynamic input range of this ADC is 1 V_{pp} corresponding to the shown 4096 raw values. The sampling rate has been set to 1 $GS\,s^{-1}$ which means that one sample corresponds to 1 ns in time. Some basic quality information about the signals can be roughly estimated, such as the pulse height distribution, minimum and maximum pulse widths and heights and correlated structures which may appear within the large time window. The data shown in fig. A.4a are from a data-taking with high voltage setting of 1500 V for the photomultiplier of this channel, while the data in fig. A.4b are from data-taking with a high voltage setting of 1800 V with similar beam conditions. It can immediately be seen that the large dynamic range of the SADC is often exceeded for the higher setting. Also, a correlated structure about 100 ns after the main peak shows up (which likely is a reflection of the large signals after twice the cable length of about 10 m corresponding to about 50 ns connecting PMT and module).

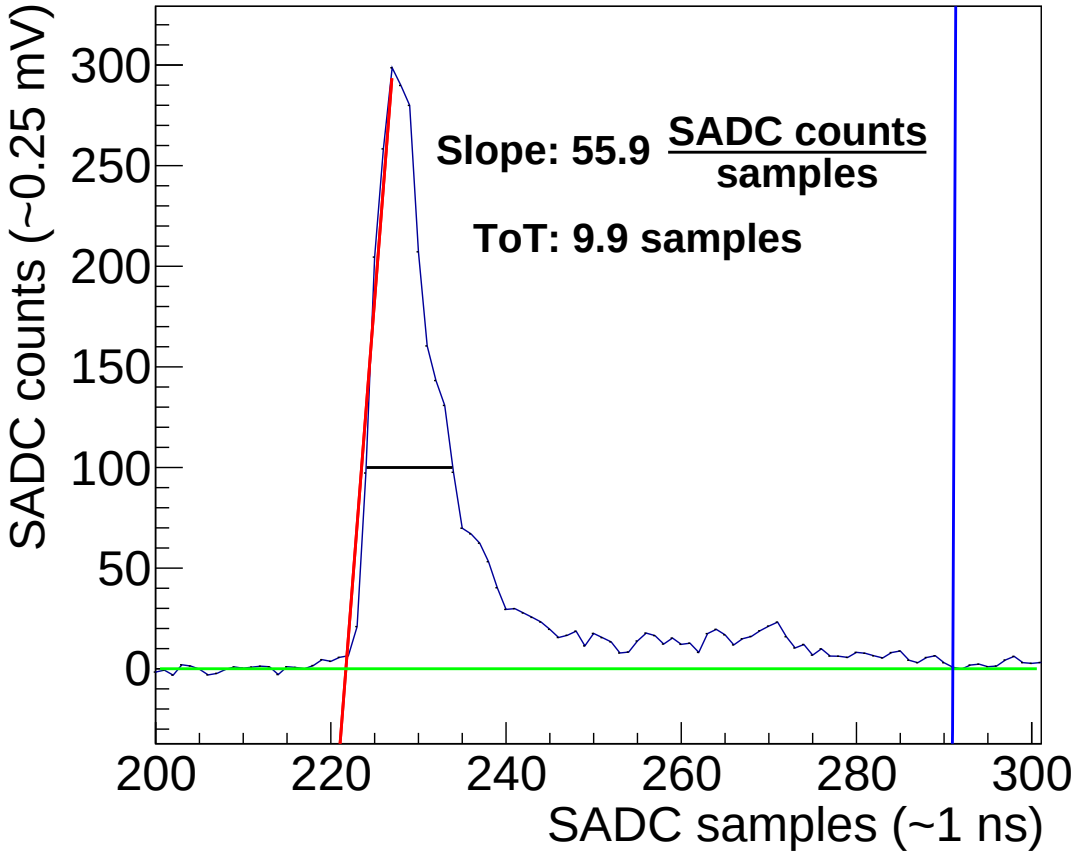

Figure A.5: Visualization of the implemented SADC feature extraction algorithm. The fitted baseline is shown in green and already subtracted so it appears to be exact at ADC value '0'. The fitted rising slope is drawn in red and the ToT in black. The blue line marks the end of the integrated pulse shape (used for extraction of the pulse integral).

An example for this reconstruction is shown in fig. A.5. The fitted functions are visualized and the extracted ToT and fitted slope are shown. The threshold used for the ToT calculation is configurable and in this case corresponds to 100 samples matching about 25 mV.

The pulse integral which was used in the initial high voltage tuning procedure and also compared against the time over threshold information is calculated by integrating the samples which are part of a signal after subtraction of the baseline. The exact procedure on how the the end of the signal for the integration is determined and in which way pileup is handled is described in the thesis of P. Meiß [Mei13]. All statements related to the integration procedure are still valid for the version of the code used in this thesis.

APPENDIX B

Analysis Framework

In this appendix, additional technical descriptions related to chapter 5 is presented.

B.1 Selection of the Correct Bunch

An additional, event by event correction on top of the timing already discussed in section 3.5 is possible using more high-level, reconstructed information. It has already been actively used in this thesis and relies on the achieved time resolution to be sufficient to disentangle the electron bunches from the accelerator.

The goal of this correction is attempt to select the actual bunch in which the hadronic event took place, which might differ from the bunch to which the electron causing the trigger signal by being detected in the tagger hodoscope belongs. This 'reaction time' correction was implemented by J. Hannappel and is also used for the analyses performed in this thesis. It is based on the following scheme:

1. Use the time information after all previously outlined corrections are already applied.
2. Create two histograms with a 2 ns binning, matching the time distance between bunches which is determined by the 500 MHz radio frequency used by the accelerator.
3. Fill one histogram with all cluster-times (within a large window around the prompt region) from the BGO and Barrel detectors, weighted with their respective time error. This should peak at the time of the hadronic event if the central detectors were involved.

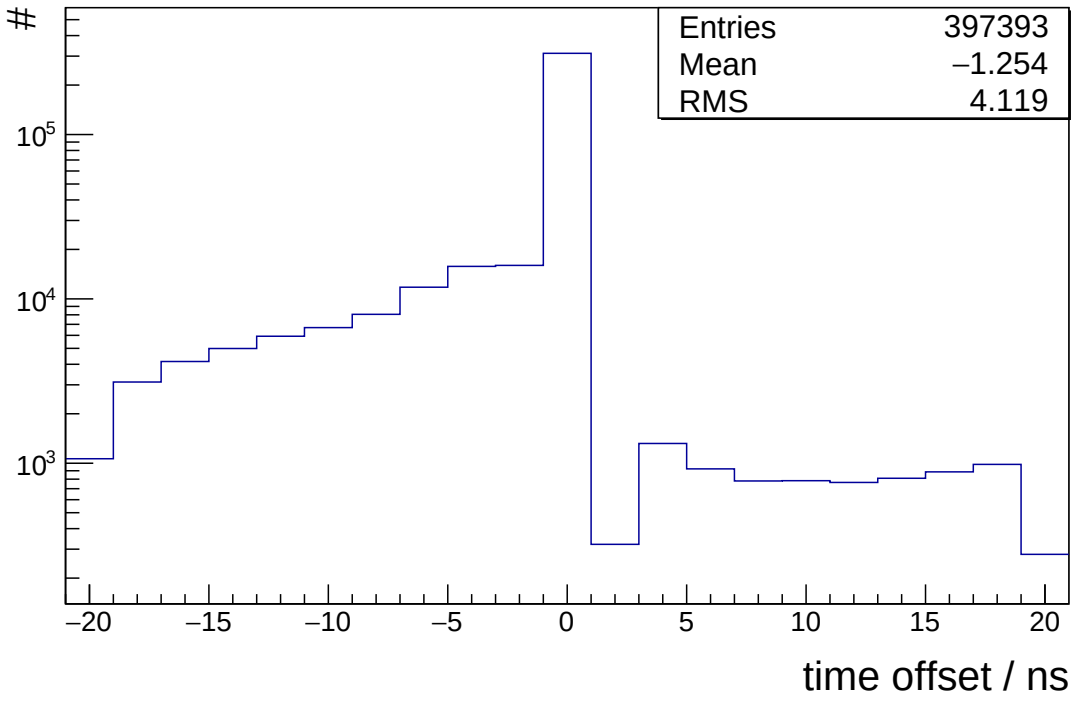

Figure B.1: This histogram shows the 'reaction time offset' finally applied for an example dataset, the bin widths are chosen such that they match the bunch period of the accelerator. As can be seen from the logarithmic scale, this correction is rarely used at all. The data shown are from a single run (number 31213) of the October / November 2015 beamtime.

4. Fill the other histogram with all times of all tagger clusters within a large window around the prompt region.

5. Multiply the resulting histograms bin-by-bin and find the bin with maximum content. This is the most probable offset (in 'number of bunches') for this event.

Again, this offset is applied globally to all time data so it will not affect any time differences, but simplify cutting on an 'absolute' time information.

A distribution of these time offsets (which are binned with the bunch distance by design, i.e. 2 ns) can be seen in fig. B.1.

This correction has direct impact on the physics information available at the end of the analysis chain (before the physics reconstruction). An example for this is shown in fig. B.2. The reaction time correction mainly influences the β axis, but also (indirectly) has a strong impact on the available events: time cuts on the prompt peak region for preselection of correlated events may discard events for which e.g. the tagger coincidence which caused the trigger did not match the hadronic event (which can occur since the gates on the central detectors are large). The

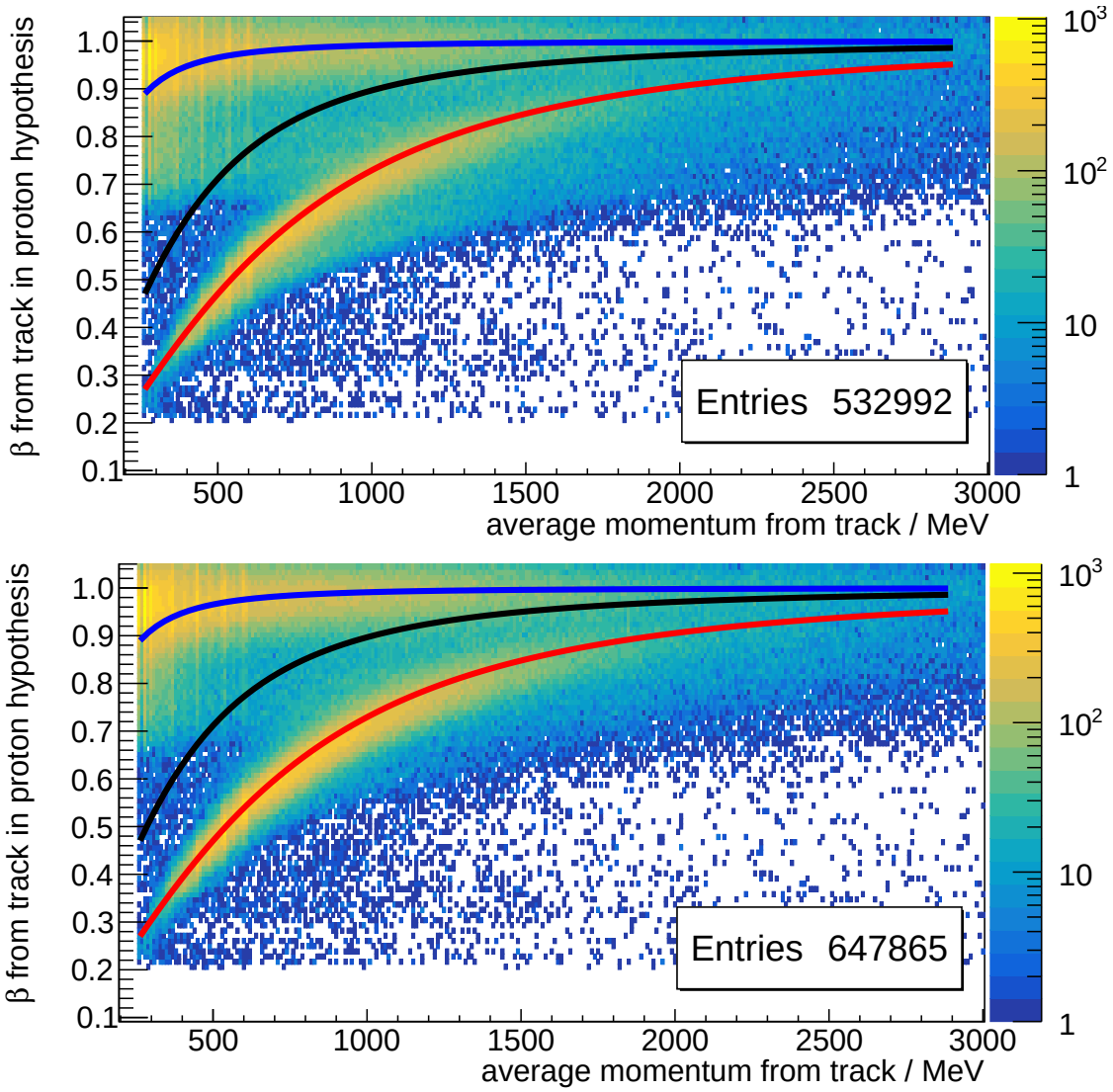

Figure B.2: Illustration of the effect of the reaction time correction on extracted physics quantities. These plots show the β as measured by the time of flight walls (c.f. section 4.10) and the start detector of the experiment on the vertical axis. The horizontal axis is the result of momentum reconstruction (the average momentum along the track is calculated using the energy losses in the material). The red line, black line and blue line corresponds to the characteristic loci of protons, kaons and pions, respectively. The only difference between the two plots is that the upper plot has been created with the reaction time correction turned off, while the correction was active for the lower histogram. The data used for this plot is a small subset of 82 runs with 41 232 304 total events in the June / July 2015 beamtime, corresponding to continuous data-taking of 17 h 35 min. The tracks were reconstructed using the 'ToF tracking' approach, for which a detailed description is given in section 5.2.3.

correction done by the event by event reaction time offset allows more tracks to survive and thus makes more events available for analysis.

Furthermore, a detailed look at the distributions reveals that a reflective structure of the expected loci of the several particles types becomes visible in β. In the worst case, parts of the bunch structure become visible which overlay e.g. the loci of pions with that of kaons. The reaction time correction strongly reduces this effect.

B.2 Time Correction with ELSA Radio Frequency

A further improvement of the time resolution seems only possible by choosing a time reference with even higher resolution. In fact, this better time reference is available: the radio frequency used by the acceleration cavities of the electron accelerator ELSA directly determines the macroscopic bunch structure. Thus, if the phase between the radio frequency signal and the global trigger can be determined event by event with a precision better than the time interval between two consecutive bunches as was already shown in appendix B.1, the start time resolution can be improved up to the bunch length in time (convoluted with the time resolution of the measuring TDC).

This has been investigated in a bachelor thesis [Kna15] and was first tested successfully in the October / November 2015 beamtime. In this bachelor thesis, a transmitter and receiver for an optical link was constructed to transport the 500 MHz signal from which the radio frequency of the accelerator is derived to the experimental area. The phase measurement was then performed by discriminating the output of the optical receiver with an FPGA, dividing the frequency by a factor of 2 for technical reasons and using the resulting signal as TDC clock. This special TDC then measures the global trigger signal and thus is able to directly determine the phase between the RF and trigger signals event by event. This finally allows to further improve the start time resolution from better than 250 ps to a value in the order of 80 ps to 100 ps which is only limited by the bunch length which depends on the accelerator configuration and the time resolution of the used TDC.

A few (solvable) issues remain with this technique:

- A clean way to calibration this special TDC, which is based on the jTDC implementation, is not yet solved. Since now the TDC clock and the measured channel which is the global trigger show expected correlations, the INL calibration (c.f. section 3.3) should be performed with an independent uncorrelated data sample to prevent a bias and achieve full precision.

- The phase locked loop in the FPGA sometimes loses the synchronization to the external clock. This seems to be related to electronics noise mainly on the transmitter side and has to be investigated further.

For these reasons, it is not yet in standard use and was also not used for the analyses performed in this thesis.

APPENDIX C

Beam Asymmetry Extraction

On the following pages, the azimuthal distributions of the normalized difference of reconstructed photoproduction events for the extraction of the beam asymmetry, are shown including statistical uncertainties.

- The azimuthal distributions for π^0 photoproduction, using the dataset from June / July 2015, are presented in appendix C.1.
- The azimuthal distributions for ω photoproduction, using the dataset from June / July 2015, are presented in appendix C.2.
- The azimuthal distributions for ω photoproduction, using the dataset from October / November 2015, are presented in appendix C.3.

For the distributions shown for ω photoproduction, neither the displayed uncertainties nor the values themselves should be regarded as reliable, as discussed in more detail in section 6.6.

C.1 Distributions for π^0 Photoproduction, June / July 2015 Data

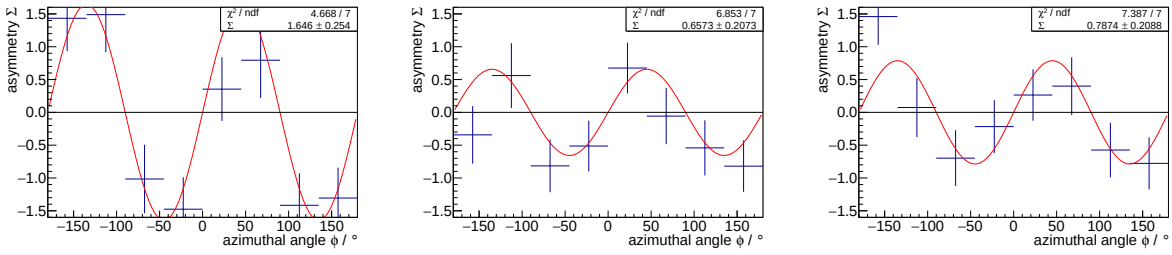

(a) $\Theta_{\mathrm{CM}}^{\mathrm{meson}} = 50°$ to $60°$ (b) $\Theta_{\mathrm{CM}}^{\mathrm{meson}} = 60°$ to $70°$ (c) $\Theta_{\mathrm{CM}}^{\mathrm{meson}} = 70°$ to $80°$

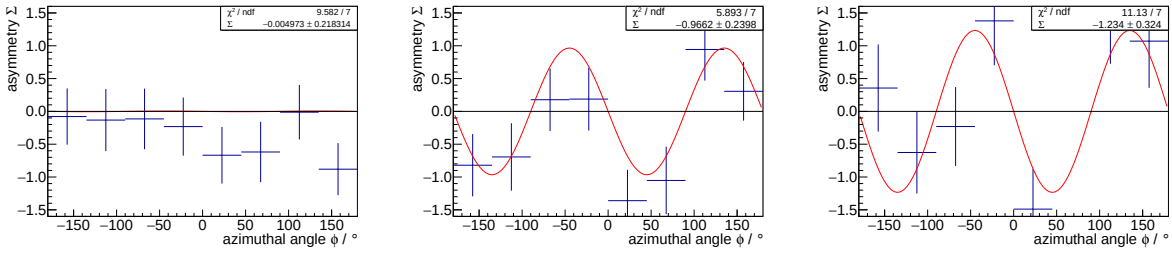

(d) $\Theta_{\mathrm{CM}}^{\mathrm{meson}} = 80°$ to $90°$ (e) $\Theta_{\mathrm{CM}}^{\mathrm{meson}} = 90°$ to $100°$ (f) $\Theta_{\mathrm{CM}}^{\mathrm{meson}} = 100°$ to $110°$

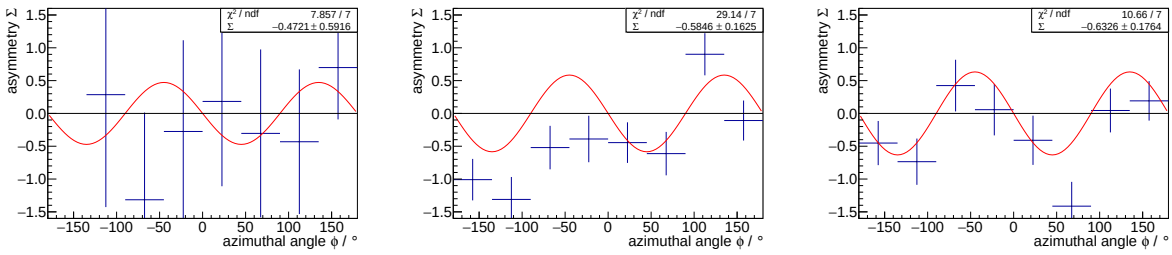

(g) $\Theta_{\mathrm{CM}}^{\mathrm{meson}} = 110°$ to $120°$ (h) $\Theta_{\mathrm{CM}}^{\mathrm{meson}} = 120°$ to $130°$ (i) $\Theta_{\mathrm{CM}}^{\mathrm{meson}} = 130°$ to $140°$

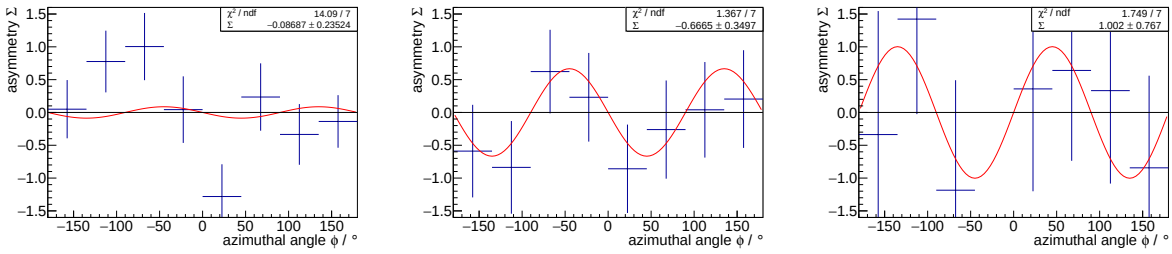

(j) $\Theta_{\mathrm{CM}}^{\mathrm{meson}} = 140°$ to $150°$ (k) $\Theta_{\mathrm{CM}}^{\mathrm{meson}} = 150°$ to $160°$ (l) $\Theta_{\mathrm{CM}}^{\mathrm{meson}} = 160°$ to $170°$

Figure C.1: Azimuthal distribution of the normalized difference of π^0 photoproduction events for the extraction of the beam asymmetry, including statistical uncertainties. The data shown is for incoming photon energies E_γ between 1100 MeV and 1150 MeV in different bins of $\Theta_{\mathrm{CM}}^{\mathrm{meson}}$.

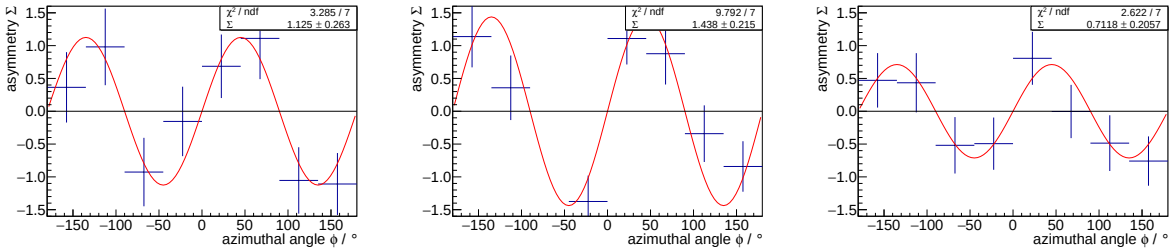

(a) $\Theta_{\mathrm{CM}}^{\mathrm{meson}} = 50°$ to $60°$ (b) $\Theta_{\mathrm{CM}}^{\mathrm{meson}} = 60°$ to $70°$ (c) $\Theta_{\mathrm{CM}}^{\mathrm{meson}} = 70°$ to $80°$

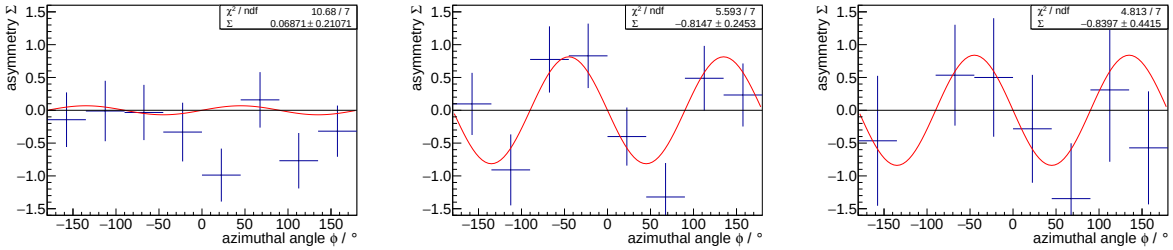

(d) $\Theta_{\mathrm{CM}}^{\mathrm{meson}} = 80°$ to $90°$ (e) $\Theta_{\mathrm{CM}}^{\mathrm{meson}} = 90°$ to $100°$ (f) $\Theta_{\mathrm{CM}}^{\mathrm{meson}} = 100°$ to $110°$

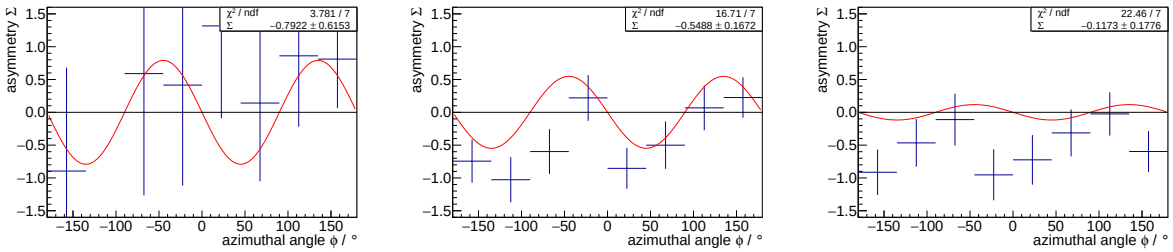

(g) $\Theta_{\mathrm{CM}}^{\mathrm{meson}} = 110°$ to $120°$ (h) $\Theta_{\mathrm{CM}}^{\mathrm{meson}} = 120°$ to $130°$ (i) $\Theta_{\mathrm{CM}}^{\mathrm{meson}} = 130°$ to $140°$

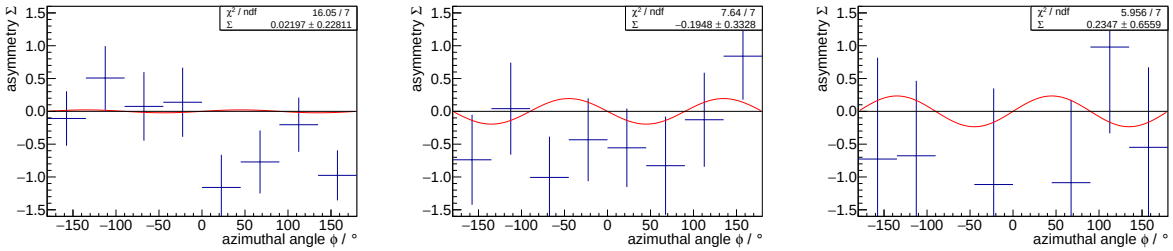

(j) $\Theta_{\mathrm{CM}}^{\mathrm{meson}} = 140°$ to $150°$ (k) $\Theta_{\mathrm{CM}}^{\mathrm{meson}} = 150°$ to $160°$ (l) $\Theta_{\mathrm{CM}}^{\mathrm{meson}} = 160°$ to $170°$

Figure C.2: Azimuthal distribution of the normalized difference of π^0 photoproduction events for the extraction of the beam asymmetry, including statistical uncertainties. The data shown is for incoming photon energies E_γ between 1150 MeV and 1200 MeV in different bins of $\Theta_{\mathrm{CM}}^{\mathrm{meson}}$.

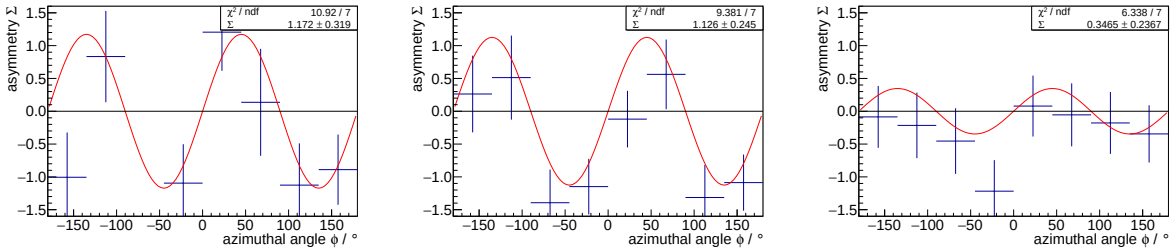

(a) $\Theta_{\mathrm{CM}}^{\mathrm{meson}} = 50°$ to $60°$ (b) $\Theta_{\mathrm{CM}}^{\mathrm{meson}} = 60°$ to $70°$ (c) $\Theta_{\mathrm{CM}}^{\mathrm{meson}} = 70°$ to $80°$

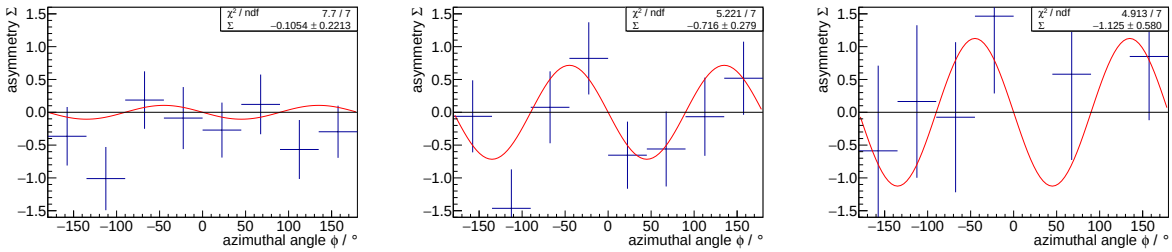

(d) $\Theta_{\mathrm{CM}}^{\mathrm{meson}} = 80°$ to $90°$ (e) $\Theta_{\mathrm{CM}}^{\mathrm{meson}} = 90°$ to $100°$ (f) $\Theta_{\mathrm{CM}}^{\mathrm{meson}} = 100°$ to $110°$

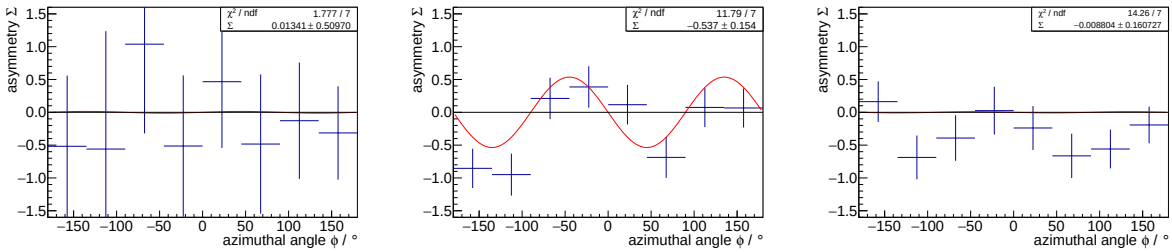

(g) $\Theta_{\mathrm{CM}}^{\mathrm{meson}} = 110°$ to $120°$ (h) $\Theta_{\mathrm{CM}}^{\mathrm{meson}} = 120°$ to $130°$ (i) $\Theta_{\mathrm{CM}}^{\mathrm{meson}} = 130°$ to $140°$

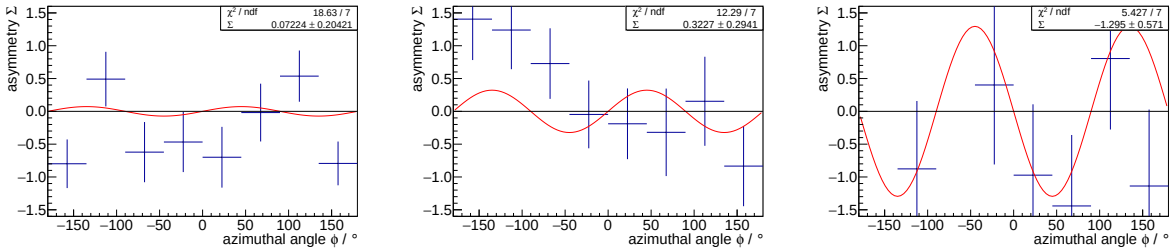

(j) $\Theta_{\mathrm{CM}}^{\mathrm{meson}} = 140°$ to $150°$ (k) $\Theta_{\mathrm{CM}}^{\mathrm{meson}} = 150°$ to $160°$ (l) $\Theta_{\mathrm{CM}}^{\mathrm{meson}} = 160°$ to $170°$

Figure C.3: Azimuthal distribution of the normalized difference of π^0 photoproduction events for the extraction of the beam asymmetry, including statistical uncertainties. The data shown is for incoming photon energies E_γ between 1200 MeV and 1250 MeV in different bins of $\Theta_{\mathrm{CM}}^{\mathrm{meson}}$.

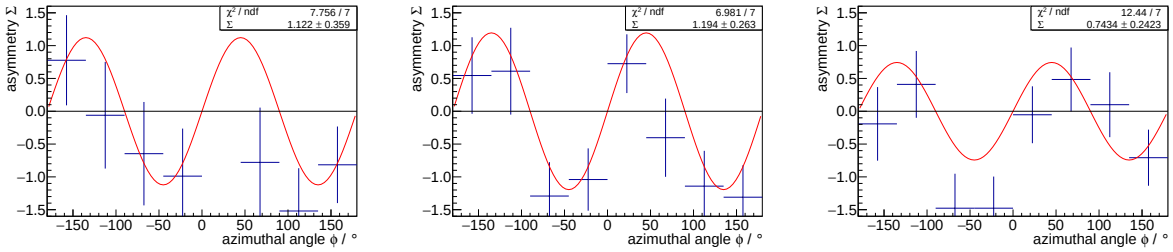

(a) $\Theta_{\mathrm{CM}}^{\mathrm{meson}} = 50°$ to $60°$ (b) $\Theta_{\mathrm{CM}}^{\mathrm{meson}} = 60°$ to $70°$ (c) $\Theta_{\mathrm{CM}}^{\mathrm{meson}} = 70°$ to $80°$

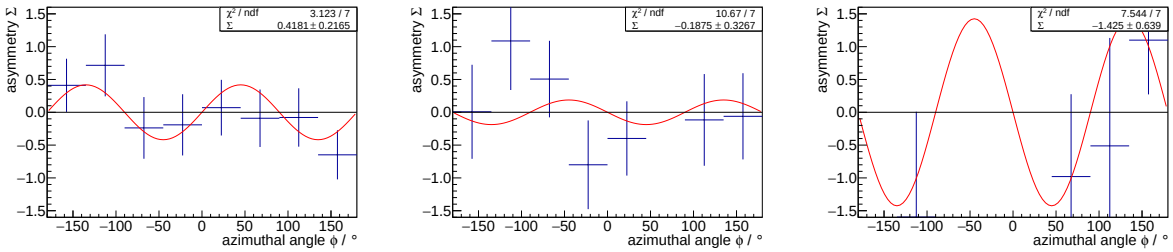

(d) $\Theta_{\mathrm{CM}}^{\mathrm{meson}} = 80°$ to $90°$ (e) $\Theta_{\mathrm{CM}}^{\mathrm{meson}} = 90°$ to $100°$ (f) $\Theta_{\mathrm{CM}}^{\mathrm{meson}} = 100°$ to $110°$

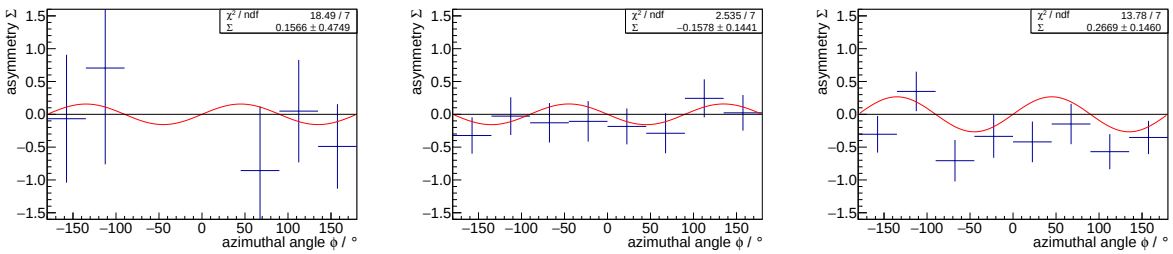

(g) $\Theta_{\mathrm{CM}}^{\mathrm{meson}} = 110°$ to $120°$ (h) $\Theta_{\mathrm{CM}}^{\mathrm{meson}} = 120°$ to $130°$ (i) $\Theta_{\mathrm{CM}}^{\mathrm{meson}} = 130°$ to $140°$

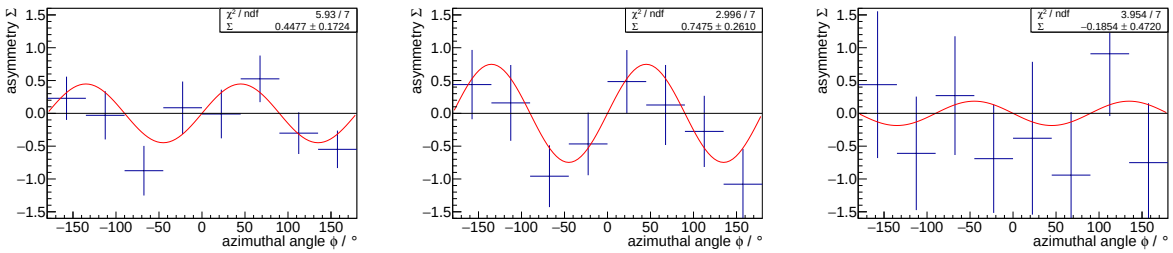

(j) $\Theta_{\mathrm{CM}}^{\mathrm{meson}} = 140°$ to $150°$ (k) $\Theta_{\mathrm{CM}}^{\mathrm{meson}} = 150°$ to $160°$ (l) $\Theta_{\mathrm{CM}}^{\mathrm{meson}} = 160°$ to $170°$

Figure C.4: Azimuthal distribution of the normalized difference of π^0 photoproduction events for the extraction of the beam asymmetry, including statistical uncertainties. The data shown is for incoming photon energies E_γ between 1250 MeV and 1300 MeV in different bins of $\Theta_{\mathrm{CM}}^{\mathrm{meson}}$.

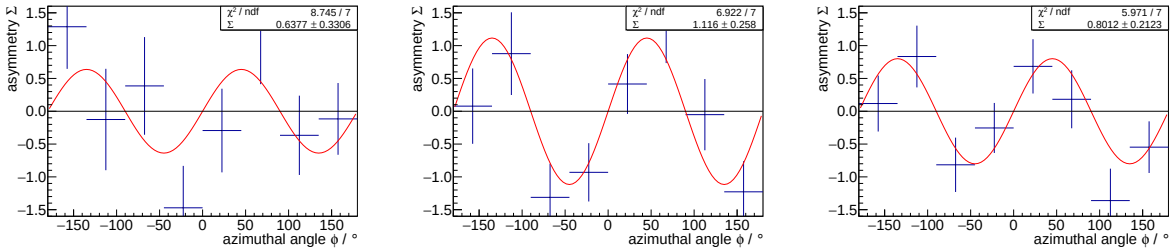

(a) $\Theta_{\mathrm{CM}}^{\mathrm{meson}} = 50°$ to $60°$ (b) $\Theta_{\mathrm{CM}}^{\mathrm{meson}} = 60°$ to $70°$ (c) $\Theta_{\mathrm{CM}}^{\mathrm{meson}} = 70°$ to $80°$

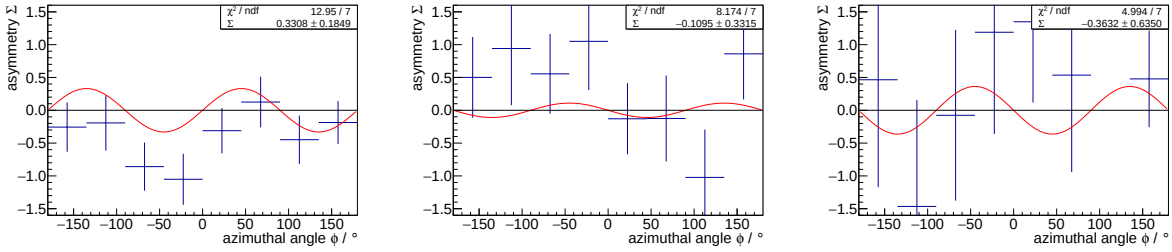

(d) $\Theta_{\mathrm{CM}}^{\mathrm{meson}} = 80°$ to $90°$ (e) $\Theta_{\mathrm{CM}}^{\mathrm{meson}} = 90°$ to $100°$ (f) $\Theta_{\mathrm{CM}}^{\mathrm{meson}} = 100°$ to $110°$

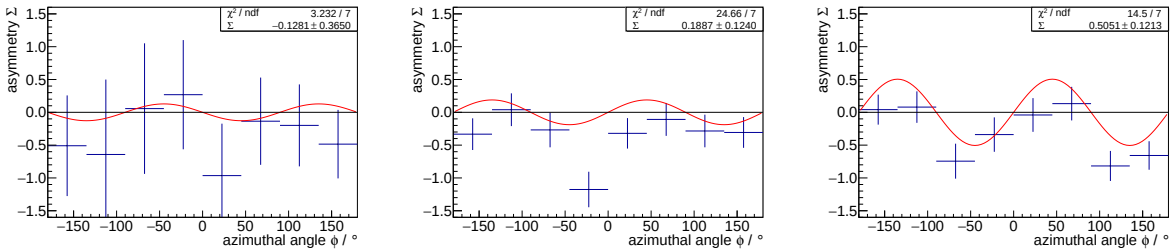

(g) $\Theta_{\mathrm{CM}}^{\mathrm{meson}} = 110°$ to $120°$ (h) $\Theta_{\mathrm{CM}}^{\mathrm{meson}} = 120°$ to $130°$ (i) $\Theta_{\mathrm{CM}}^{\mathrm{meson}} = 130°$ to $140°$

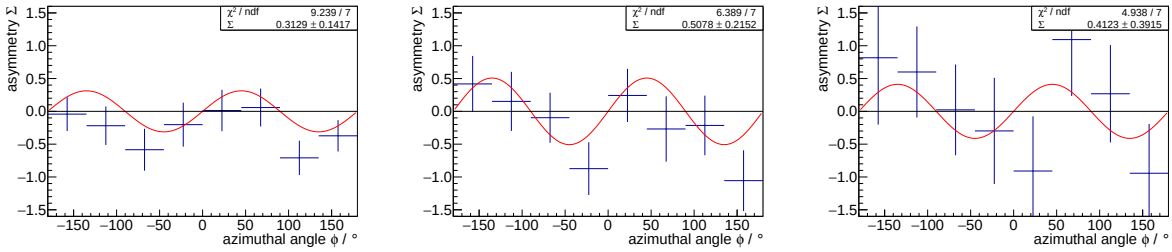

(j) $\Theta_{\mathrm{CM}}^{\mathrm{meson}} = 140°$ to $150°$ (k) $\Theta_{\mathrm{CM}}^{\mathrm{meson}} = 150°$ to $160°$ (l) $\Theta_{\mathrm{CM}}^{\mathrm{meson}} = 160°$ to $170°$

Figure C.5: Azimuthal distribution of the normalized difference of π^0 photoproduction events for the extraction of the beam asymmetry, including statistical uncertainties. The data shown is for incoming photon energies E_γ between 1300 MeV and 1350 MeV in different bins of $\Theta_{\mathrm{CM}}^{\mathrm{meson}}$.

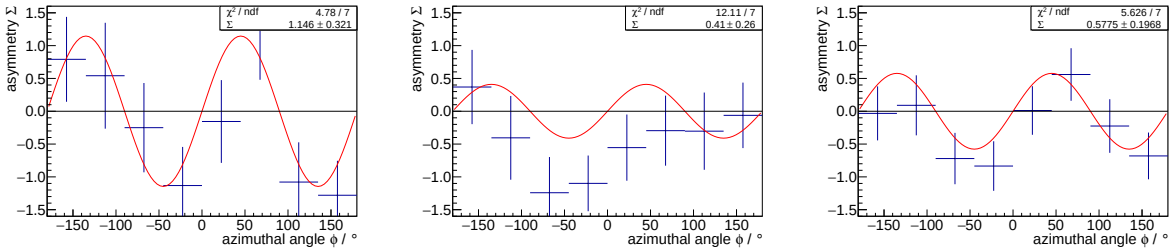

(a) $\Theta_{\mathrm{CM}}^{\mathrm{meson}} = 50°$ to $60°$ (b) $\Theta_{\mathrm{CM}}^{\mathrm{meson}} = 60°$ to $70°$ (c) $\Theta_{\mathrm{CM}}^{\mathrm{meson}} = 70°$ to $80°$

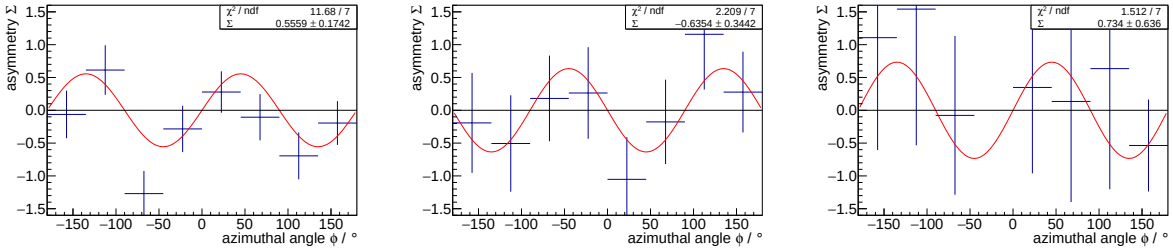

(d) $\Theta_{\mathrm{CM}}^{\mathrm{meson}} = 80°$ to $90°$ (e) $\Theta_{\mathrm{CM}}^{\mathrm{meson}} = 90°$ to $100°$ (f) $\Theta_{\mathrm{CM}}^{\mathrm{meson}} = 100°$ to $110°$

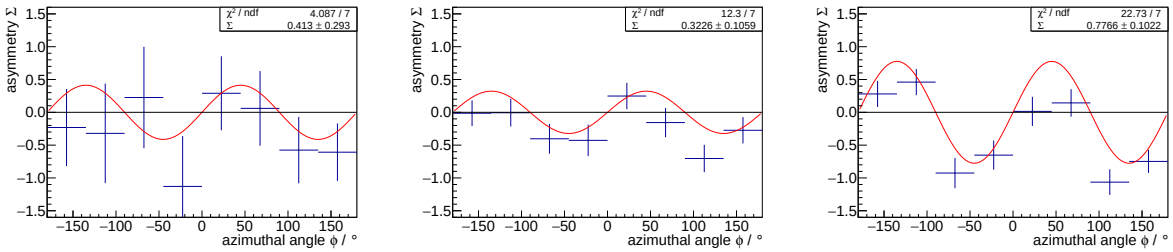

(g) $\Theta_{\mathrm{CM}}^{\mathrm{meson}} = 110°$ to $120°$ (h) $\Theta_{\mathrm{CM}}^{\mathrm{meson}} = 120°$ to $130°$ (i) $\Theta_{\mathrm{CM}}^{\mathrm{meson}} = 130°$ to $140°$

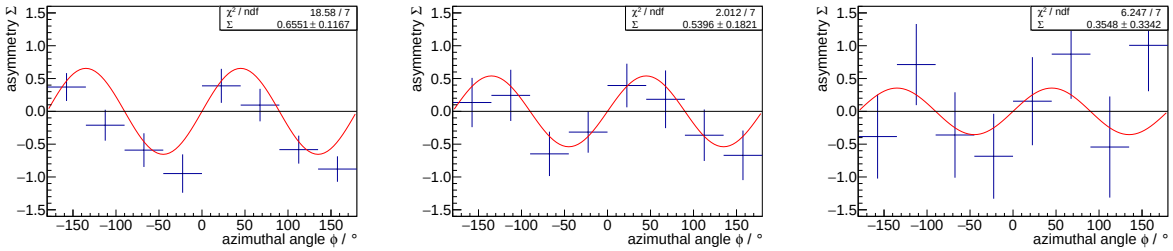

(j) $\Theta_{\mathrm{CM}}^{\mathrm{meson}} = 140°$ to $150°$ (k) $\Theta_{\mathrm{CM}}^{\mathrm{meson}} = 150°$ to $160°$ (l) $\Theta_{\mathrm{CM}}^{\mathrm{meson}} = 160°$ to $170°$

Figure C.6: Azimuthal distribution of the normalized difference of π^0 photoproduction events for the extraction of the beam asymmetry, including statistical uncertainties. The data shown is for incoming photon energies E_γ between 1350 MeV and 1400 MeV in different bins of $\Theta_{\mathrm{CM}}^{\mathrm{meson}}$.

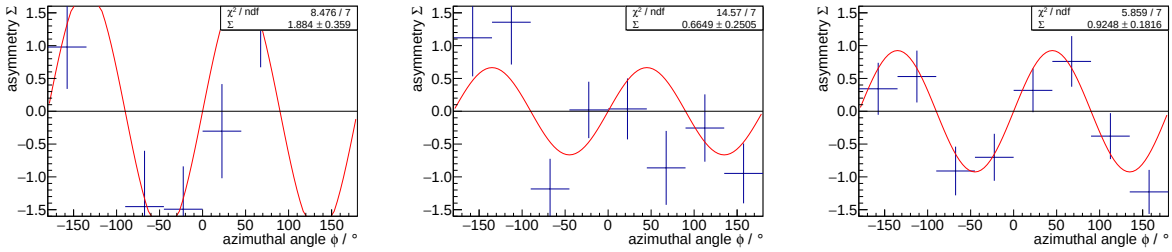

(a) $\Theta_{\mathrm{CM}}^{\mathrm{meson}} = 50°$ to $60°$ (b) $\Theta_{\mathrm{CM}}^{\mathrm{meson}} = 60°$ to $70°$ (c) $\Theta_{\mathrm{CM}}^{\mathrm{meson}} = 70°$ to $80°$

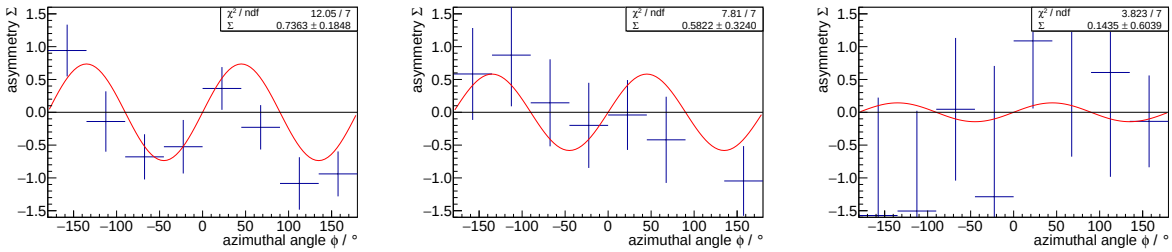

(d) $\Theta_{\mathrm{CM}}^{\mathrm{meson}} = 80°$ to $90°$ (e) $\Theta_{\mathrm{CM}}^{\mathrm{meson}} = 90°$ to $100°$ (f) $\Theta_{\mathrm{CM}}^{\mathrm{meson}} = 100°$ to $110°$

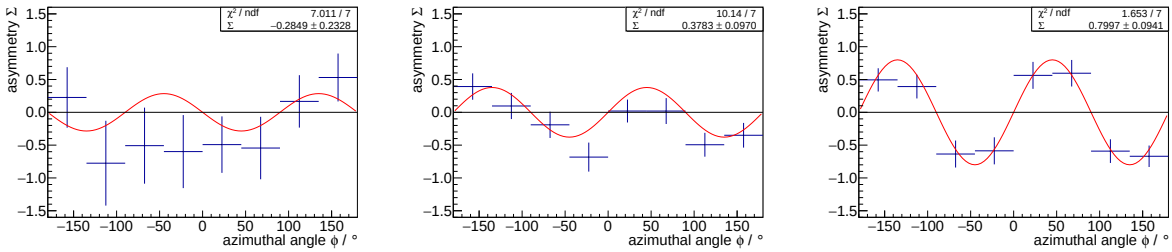

(g) $\Theta_{\mathrm{CM}}^{\mathrm{meson}} = 110°$ to $120°$ (h) $\Theta_{\mathrm{CM}}^{\mathrm{meson}} = 120°$ to $130°$ (i) $\Theta_{\mathrm{CM}}^{\mathrm{meson}} = 130°$ to $140°$

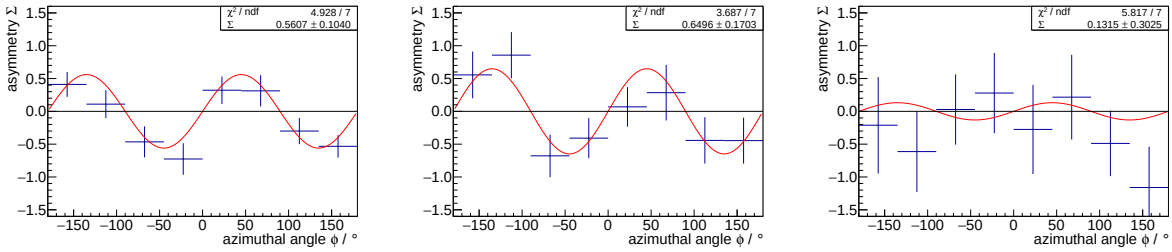

(j) $\Theta_{\mathrm{CM}}^{\mathrm{meson}} = 140°$ to $150°$ (k) $\Theta_{\mathrm{CM}}^{\mathrm{meson}} = 150°$ to $160°$ (l) $\Theta_{\mathrm{CM}}^{\mathrm{meson}} = 160°$ to $170°$

Figure C.7: Azimuthal distribution of the normalized difference of π^0 photoproduction events for the extraction of the beam asymmetry, including statistical uncertainties. The data shown is for incoming photon energies E_γ between 1400 MeV and 1450 MeV in different bins of $\Theta_{\mathrm{CM}}^{\mathrm{meson}}$.

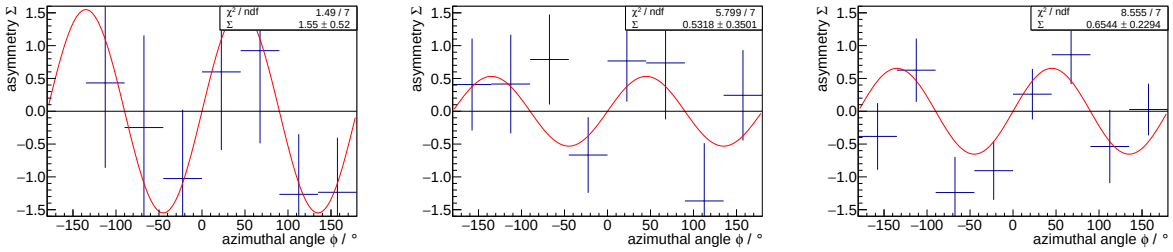

(a) $\Theta_{\mathrm{CM}}^{\mathrm{meson}} = 50°$ to $60°$ (b) $\Theta_{\mathrm{CM}}^{\mathrm{meson}} = 60°$ to $70°$ (c) $\Theta_{\mathrm{CM}}^{\mathrm{meson}} = 70°$ to $80°$

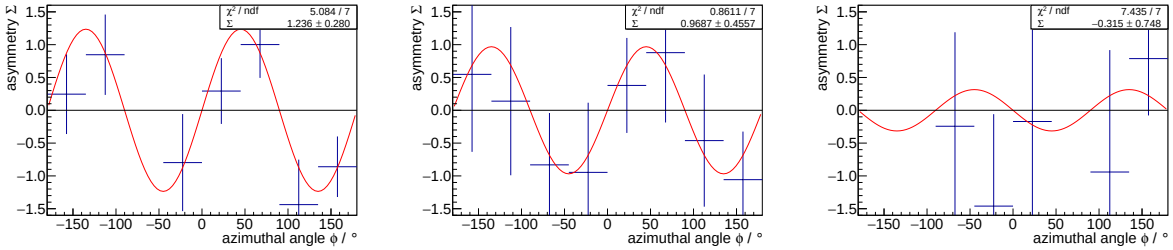

(d) $\Theta_{\mathrm{CM}}^{\mathrm{meson}} = 80°$ to $90°$ (e) $\Theta_{\mathrm{CM}}^{\mathrm{meson}} = 90°$ to $100°$ (f) $\Theta_{\mathrm{CM}}^{\mathrm{meson}} = 100°$ to $110°$

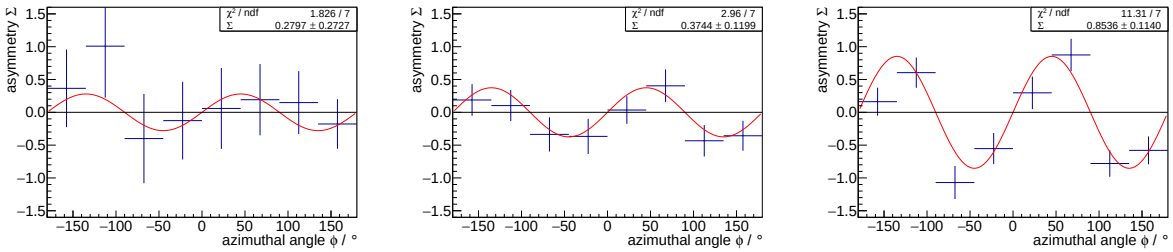

(g) $\Theta_{\mathrm{CM}}^{\mathrm{meson}} = 110°$ to $120°$ (h) $\Theta_{\mathrm{CM}}^{\mathrm{meson}} = 120°$ to $130°$ (i) $\Theta_{\mathrm{CM}}^{\mathrm{meson}} = 130°$ to $140°$

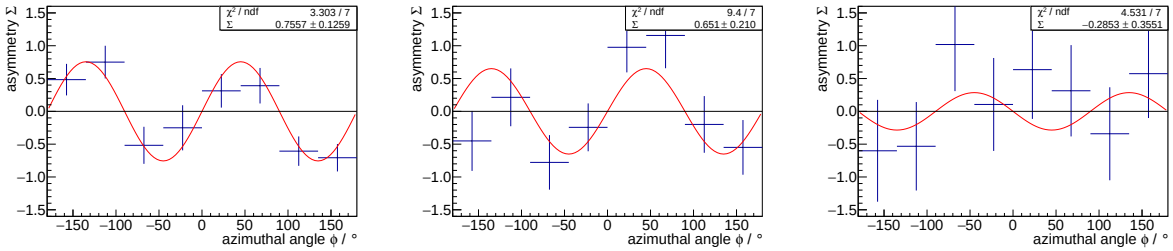

(j) $\Theta_{\mathrm{CM}}^{\mathrm{meson}} = 140°$ to $150°$ (k) $\Theta_{\mathrm{CM}}^{\mathrm{meson}} = 150°$ to $160°$ (l) $\Theta_{\mathrm{CM}}^{\mathrm{meson}} = 160°$ to $170°$

Figure C.8: Azimuthal distribution of the normalized difference of π^0 photoproduction events for the extraction of the beam asymmetry, including statistical uncertainties. The data shown is for incoming photon energies E_γ between 1450 MeV and 1500 MeV in different bins of $\Theta_{\mathrm{CM}}^{\mathrm{meson}}$.

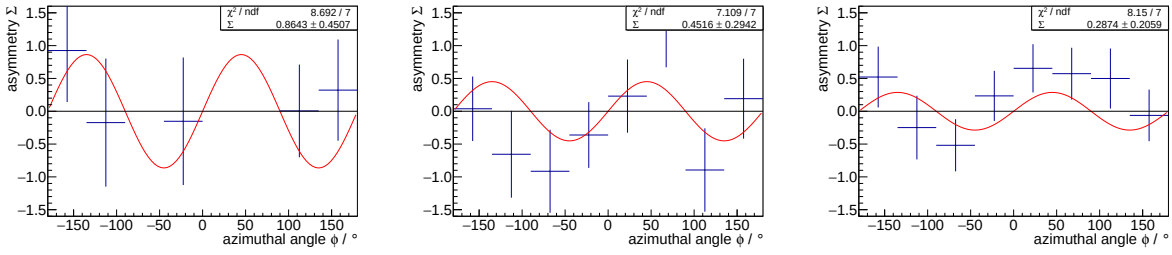

(a) $\Theta_{\mathrm{CM}}^{\mathrm{meson}} = 50°$ to $60°$ (b) $\Theta_{\mathrm{CM}}^{\mathrm{meson}} = 60°$ to $70°$ (c) $\Theta_{\mathrm{CM}}^{\mathrm{meson}} = 70°$ to $80°$

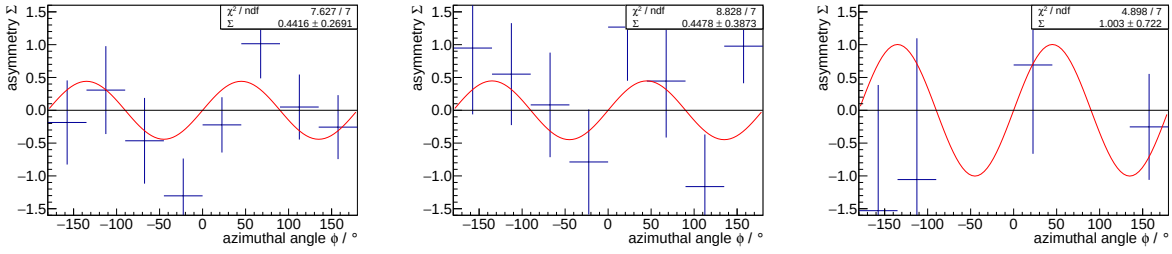

(d) $\Theta_{\mathrm{CM}}^{\mathrm{meson}} = 80°$ to $90°$ (e) $\Theta_{\mathrm{CM}}^{\mathrm{meson}} = 90°$ to $100°$ (f) $\Theta_{\mathrm{CM}}^{\mathrm{meson}} = 100°$ to $110°$

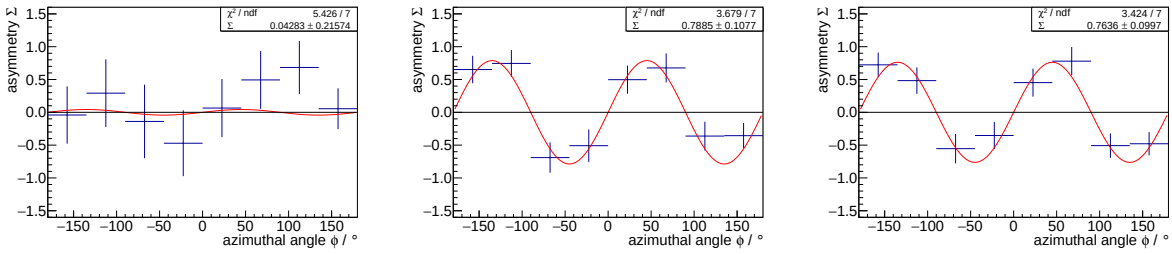

(g) $\Theta_{\mathrm{CM}}^{\mathrm{meson}} = 110°$ to $120°$ (h) $\Theta_{\mathrm{CM}}^{\mathrm{meson}} = 120°$ to $130°$ (i) $\Theta_{\mathrm{CM}}^{\mathrm{meson}} = 130°$ to $140°$

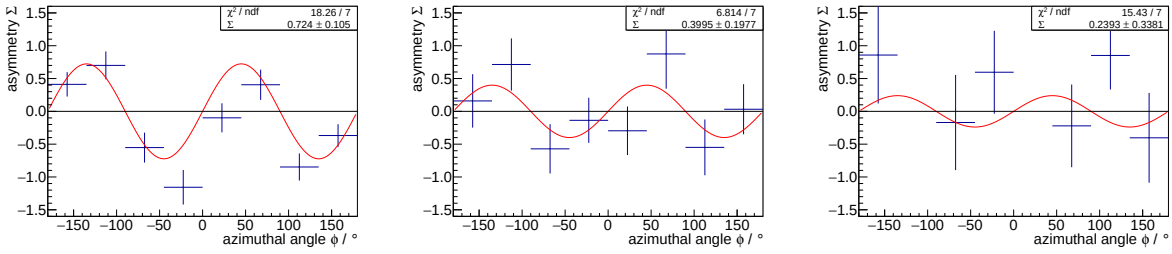

(j) $\Theta_{\mathrm{CM}}^{\mathrm{meson}} = 140°$ to $150°$ (k) $\Theta_{\mathrm{CM}}^{\mathrm{meson}} = 150°$ to $160°$ (l) $\Theta_{\mathrm{CM}}^{\mathrm{meson}} = 160°$ to $170°$

Figure C.9: Azimuthal distribution of the normalized difference of π^0 photoproduction events for the extraction of the beam asymmetry, including statistical uncertainties. The data shown is for incoming photon energies E_γ between 1500 MeV and 1550 MeV in different bins of $\Theta_{\mathrm{CM}}^{\mathrm{meson}}$.

C.2 Distributions for ω Photoproduction, June / July 2015 Data

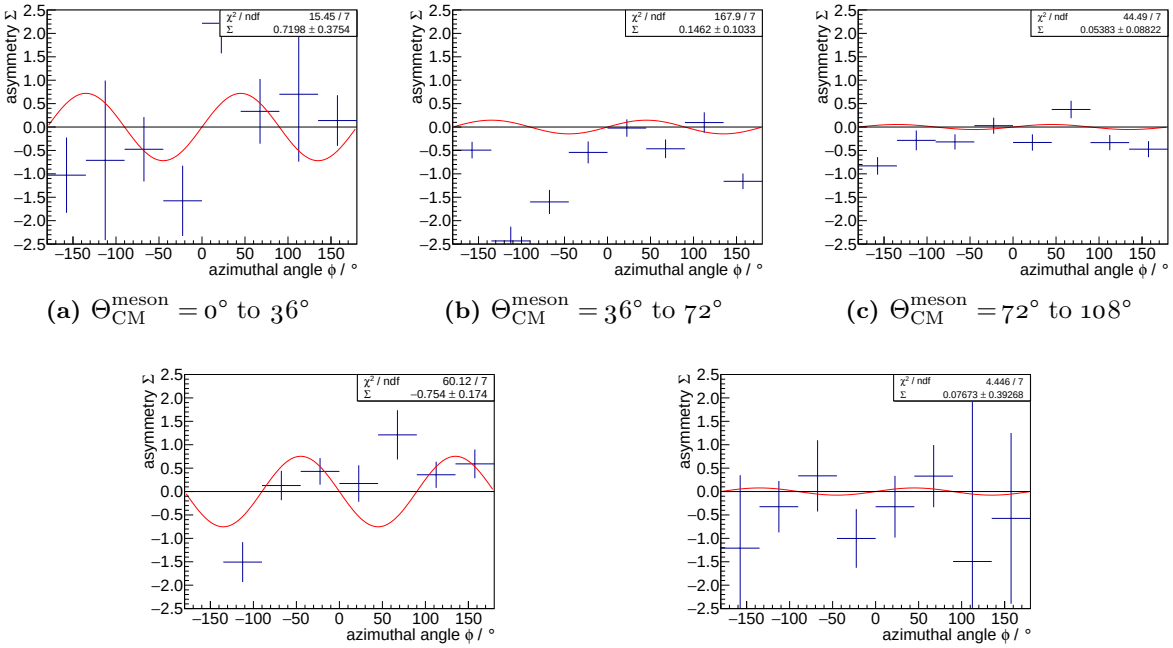

(a) $\Theta_{\mathrm{CM}}^{\mathrm{meson}} = 0°$ to $36°$ (b) $\Theta_{\mathrm{CM}}^{\mathrm{meson}} = 36°$ to $72°$ (c) $\Theta_{\mathrm{CM}}^{\mathrm{meson}} = 72°$ to $108°$

(d) $\Theta_{\mathrm{CM}}^{\mathrm{meson}} = 108°$ to $144°$ (e) $\Theta_{\mathrm{CM}}^{\mathrm{meson}} = 144°$ to $180°$

Figure C.10: Azimuthal distribution of the normalized difference of ω photoproduction events for the extraction of the beam asymmetry, including statistical uncertainties. The results shown have been extracted from the June / July 2015 data set for incoming photon energies E_γ between 1150 MeV and 1250 MeV in different bins of $\Theta_{\mathrm{CM}}^{\mathrm{meson}}$.

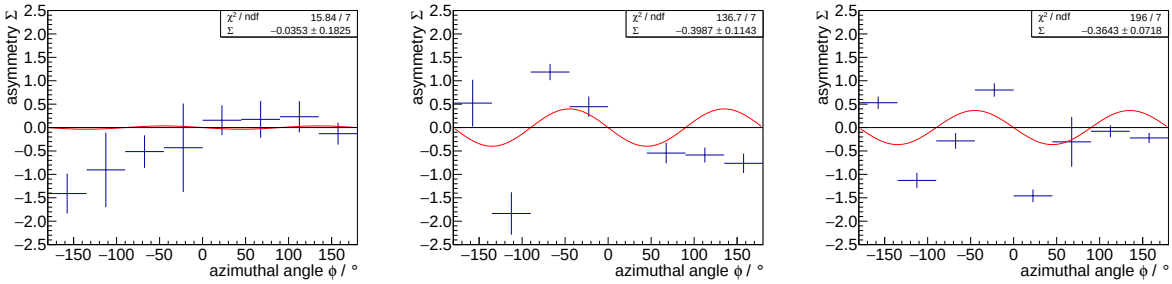

(a) $\Theta_{\mathrm{CM}}^{\mathrm{meson}} = 0°$ to $36°$ **(b)** $\Theta_{\mathrm{CM}}^{\mathrm{meson}} = 36°$ to $72°$ **(c)** $\Theta_{\mathrm{CM}}^{\mathrm{meson}} = 72°$ to $108°$

(d) $\Theta_{\mathrm{CM}}^{\mathrm{meson}} = 108°$ to $144°$ **(e)** $\Theta_{\mathrm{CM}}^{\mathrm{meson}} = 144°$ to $180°$

Figure C.11: Azimuthal distribution of the normalized difference of ω photoproduction events for the extraction of the beam asymmetry, including statistical uncertainties. The results shown have been extracted from the June / July 2015 data set for incoming photon energies E_γ between 1250 MeV and 1350 MeV in different bins of $\Theta_{\mathrm{CM}}^{\mathrm{meson}}$.

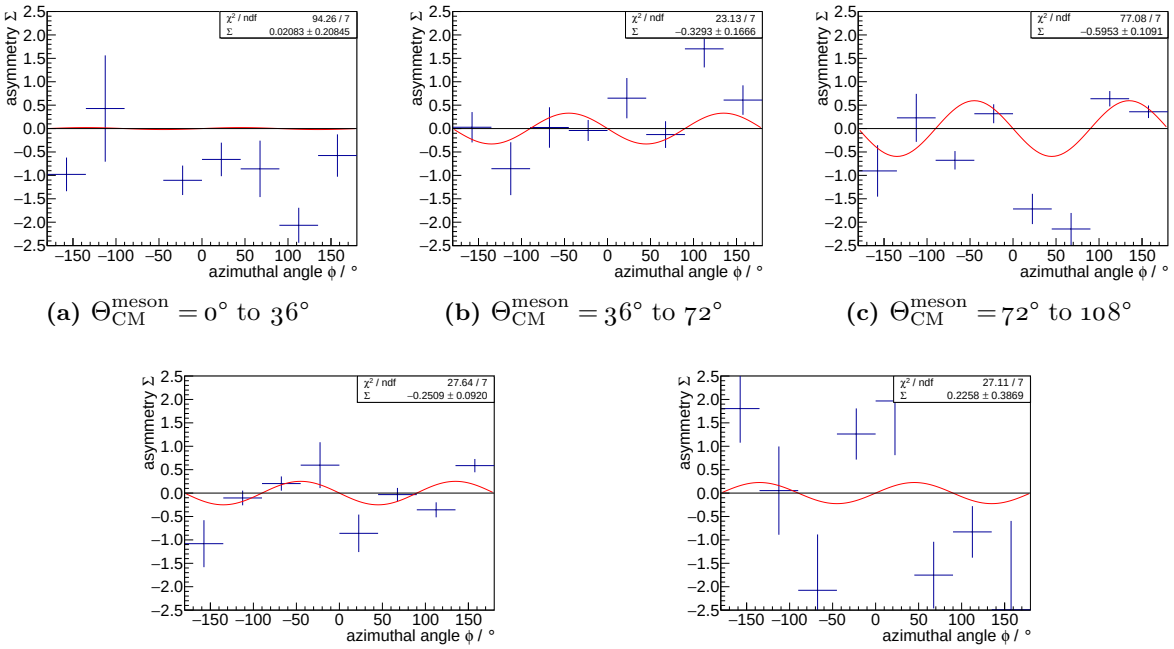

(a) $\Theta_{\mathrm{CM}}^{\mathrm{meson}} = 0°$ to $36°$ **(b)** $\Theta_{\mathrm{CM}}^{\mathrm{meson}} = 36°$ to $72°$ **(c)** $\Theta_{\mathrm{CM}}^{\mathrm{meson}} = 72°$ to $108°$

(d) $\Theta_{\mathrm{CM}}^{\mathrm{meson}} = 108°$ to $144°$ **(e)** $\Theta_{\mathrm{CM}}^{\mathrm{meson}} = 144°$ to $180°$

Figure C.12: Azimuthal distribution of the normalized difference of ω photoproduction events for the extraction of the beam asymmetry, including statistical uncertainties. The results shown have been extracted from the June / July 2015 data set for incoming photon energies E_γ between 1350 MeV and 1450 MeV in different bins of $\Theta_{\mathrm{CM}}^{\mathrm{meson}}$.

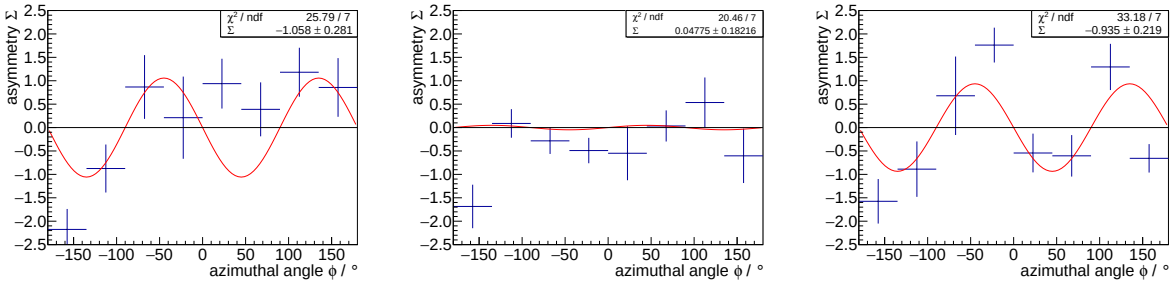

(a) $\Theta_{\mathrm{CM}}^{\mathrm{meson}} = 0°$ to $36°$ **(b)** $\Theta_{\mathrm{CM}}^{\mathrm{meson}} = 36°$ to $72°$ **(c)** $\Theta_{\mathrm{CM}}^{\mathrm{meson}} = 72°$ to $108°$

(d) $\Theta_{\mathrm{CM}}^{\mathrm{meson}} = 108°$ to $144°$ **(e)** $\Theta_{\mathrm{CM}}^{\mathrm{meson}} = 144°$ to $180°$

Figure C.13: Azimuthal distribution of the normalized difference of ω photoproduction events for the extraction of the beam asymmetry, including statistical uncertainties. The results shown have been extracted from the June / July 2015 data set for incoming photon energies E_γ between 1450 MeV and 1550 MeV in different bins of $\Theta_{\mathrm{CM}}^{\mathrm{meson}}$.

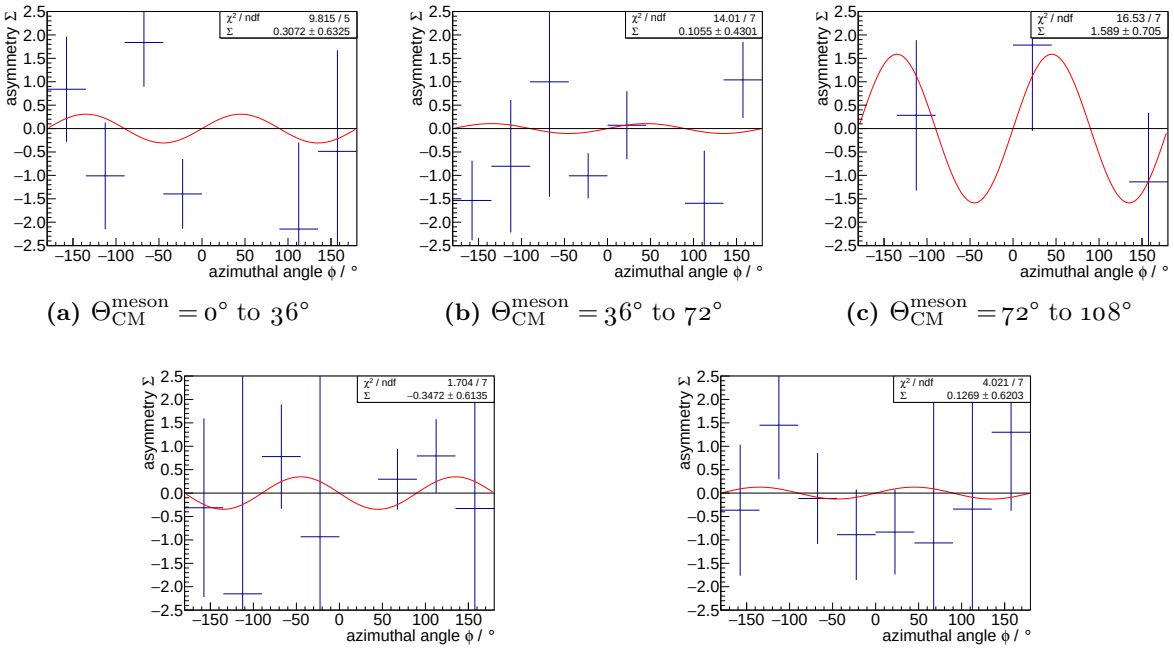

(a) $\Theta_{\mathrm{CM}}^{\mathrm{meson}} = 0°$ to $36°$ **(b)** $\Theta_{\mathrm{CM}}^{\mathrm{meson}} = 36°$ to $72°$ **(c)** $\Theta_{\mathrm{CM}}^{\mathrm{meson}} = 72°$ to $108°$

(d) $\Theta_{\mathrm{CM}}^{\mathrm{meson}} = 108°$ to $144°$ **(e)** $\Theta_{\mathrm{CM}}^{\mathrm{meson}} = 144°$ to $180°$

Figure C.14: Azimuthal distribution of the normalized difference of ω photoproduction events for the extraction of the beam asymmetry, including statistical uncertainties. The results shown have been extracted from the June / July 2015 data set for incoming photon energies E_γ between 1550 MeV and 1650 MeV in different bins of $\Theta_{\mathrm{CM}}^{\mathrm{meson}}$.

C.3 Distributions for ω Photoproduction, Oct. / Nov. 2015 Data

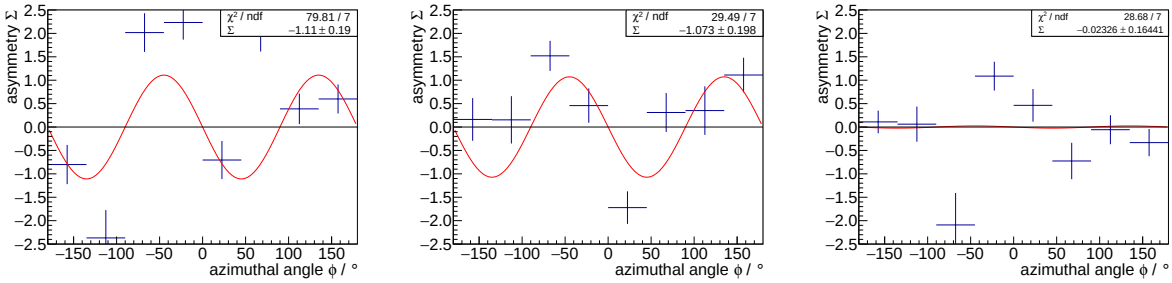

(a) $\Theta_{\mathrm{CM}}^{\mathrm{meson}} = 0°$ to $36°$ (b) $\Theta_{\mathrm{CM}}^{\mathrm{meson}} = 36°$ to $72°$ (c) $\Theta_{\mathrm{CM}}^{\mathrm{meson}} = 72°$ to $108°$

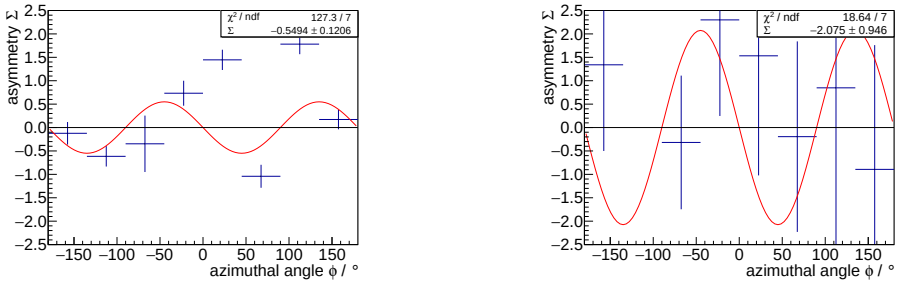

(d) $\Theta_{\mathrm{CM}}^{\mathrm{meson}} = 108°$ to $144°$ (e) $\Theta_{\mathrm{CM}}^{\mathrm{meson}} = 144°$ to $180°$

Figure C.15: Azimuthal distribution of the normalized difference of ω photoproduction events for the extraction of the beam asymmetry, including statistical uncertainties. The results shown have been extracted from the October / November 2015 data set for incoming photon energies E_γ between 1350 MeV and 1450 MeV in different bins of $\Theta_{\mathrm{CM}}^{\mathrm{meson}}$.

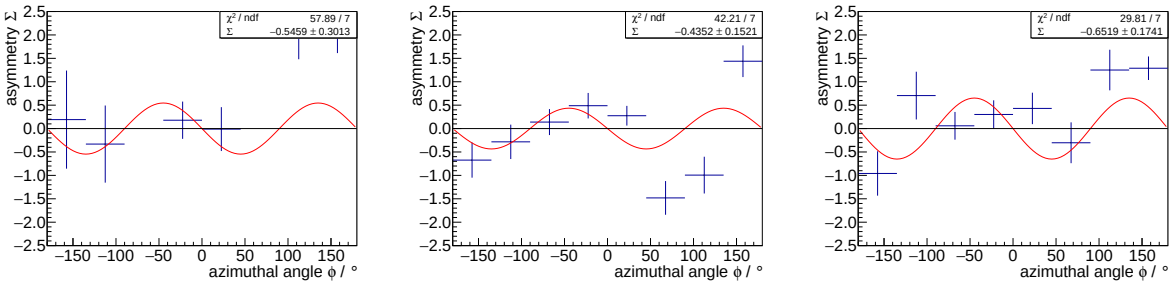

(a) $\Theta_{\mathrm{CM}}^{\mathrm{meson}} = 0°$ to $36°$ **(b)** $\Theta_{\mathrm{CM}}^{\mathrm{meson}} = 36°$ to $72°$ **(c)** $\Theta_{\mathrm{CM}}^{\mathrm{meson}} = 72°$ to $108°$

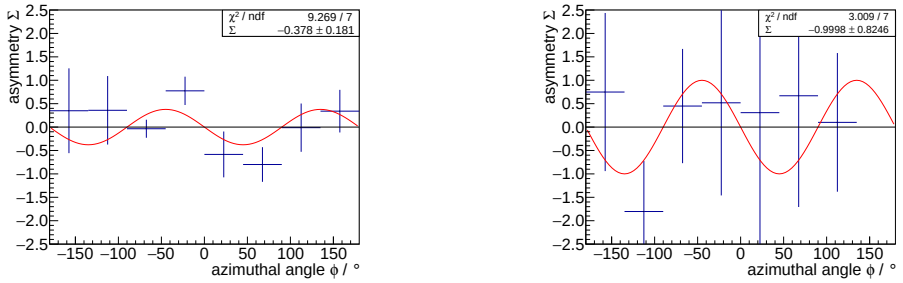

(d) $\Theta_{\mathrm{CM}}^{\mathrm{meson}} = 108°$ to $144°$ **(e)** $\Theta_{\mathrm{CM}}^{\mathrm{meson}} = 144°$ to $180°$

Figure C.16: Azimuthal distribution of the normalized difference of ω photoproduction events for the extraction of the beam asymmetry, including statistical uncertainties. The results shown have been extracted from the October / November 2015 data set for incoming photon energies E_γ between 1450 MeV and 1550 MeV in different bins of $\Theta_{\mathrm{CM}}^{\mathrm{meson}}$.

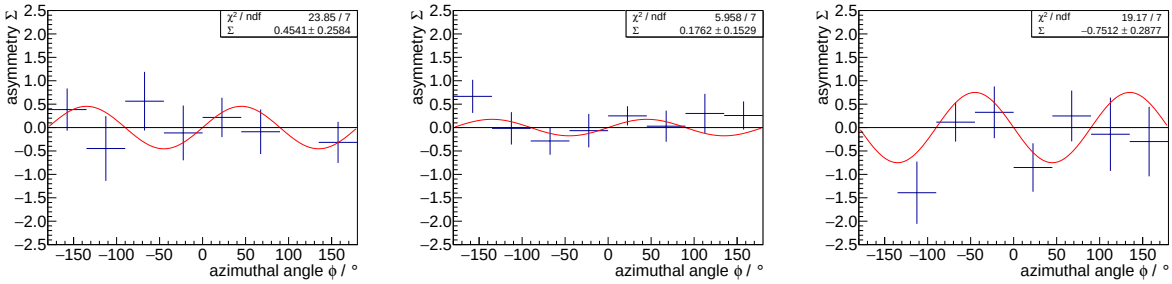

(a) $\Theta_{\mathrm{CM}}^{\mathrm{meson}} = 0°$ to $36°$ **(b)** $\Theta_{\mathrm{CM}}^{\mathrm{meson}} = 36°$ to $72°$ **(c)** $\Theta_{\mathrm{CM}}^{\mathrm{meson}} = 72°$ to $108°$

(d) $\Theta_{\mathrm{CM}}^{\mathrm{meson}} = 108°$ to $144°$ **(e)** $\Theta_{\mathrm{CM}}^{\mathrm{meson}} = 144°$ to $180°$

Figure C.17: Azimuthal distribution of the normalized difference of ω photoproduction events for the extraction of the beam asymmetry, including statistical uncertainties. The results shown have been extracted from the October / November 2015 data set for incoming photon energies E_γ between 1550 MeV and 1650 MeV in different bins of $\Theta_{\mathrm{CM}}^{\mathrm{meson}}$.

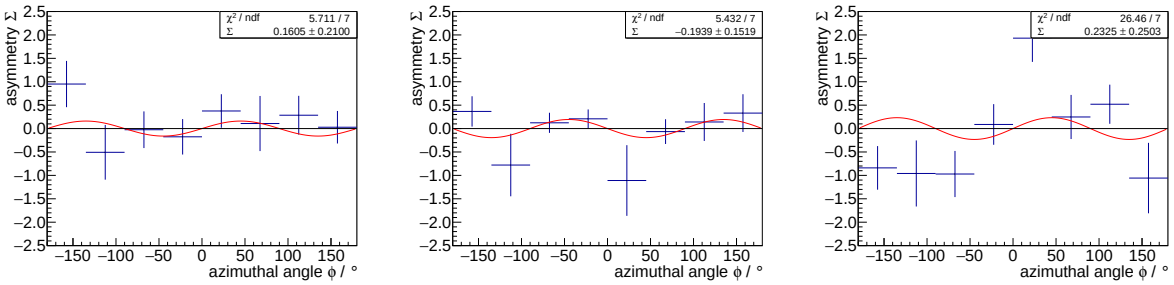

(a) $\Theta_{\mathrm{CM}}^{\mathrm{meson}} = 0°$ to $36°$ **(b)** $\Theta_{\mathrm{CM}}^{\mathrm{meson}} = 36°$ to $72°$ **(c)** $\Theta_{\mathrm{CM}}^{\mathrm{meson}} = 72°$ to $108°$

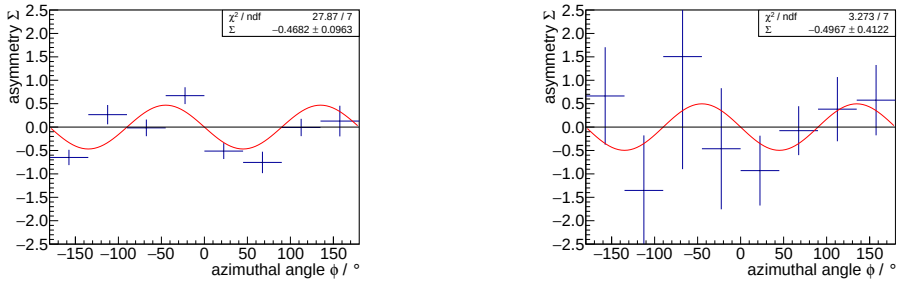

(d) $\Theta_{\mathrm{CM}}^{\mathrm{meson}} = 108°$ to $144°$ **(e)** $\Theta_{\mathrm{CM}}^{\mathrm{meson}} = 144°$ to $180°$

Figure C.18: Azimuthal distribution of the normalized difference of ω photoproduction events for the extraction of the beam asymmetry, including statistical uncertainties. The results shown have been extracted from the October / November 2015 data set for incoming photon energies E_γ between 1650 MeV and 1750 MeV in different bins of $\Theta_{\mathrm{CM}}^{\mathrm{meson}}$.

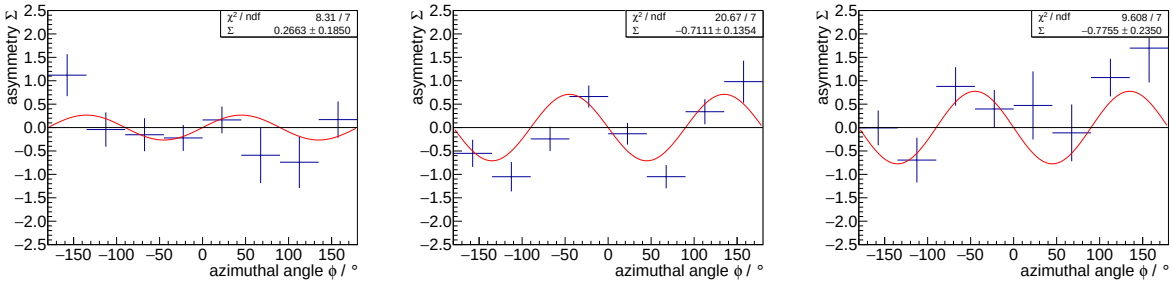

(a) $\Theta_{\mathrm{CM}}^{\mathrm{meson}} = 0°$ to $36°$ **(b)** $\Theta_{\mathrm{CM}}^{\mathrm{meson}} = 36°$ to $72°$ **(c)** $\Theta_{\mathrm{CM}}^{\mathrm{meson}} = 72°$ to $108°$

(d) $\Theta_{\mathrm{CM}}^{\mathrm{meson}} = 108°$ to $144°$ **(e)** $\Theta_{\mathrm{CM}}^{\mathrm{meson}} = 144°$ to $180°$

Figure C.19: Azimuthal distribution of the normalized difference of ω photoproduction events for the extraction of the beam asymmetry, including statistical uncertainties. The results shown have been extracted from the October / November 2015 data set for incoming photon energies E_γ between 1750 MeV and 1850 MeV in different bins of $\Theta_{\mathrm{CM}}^{\mathrm{meson}}$.

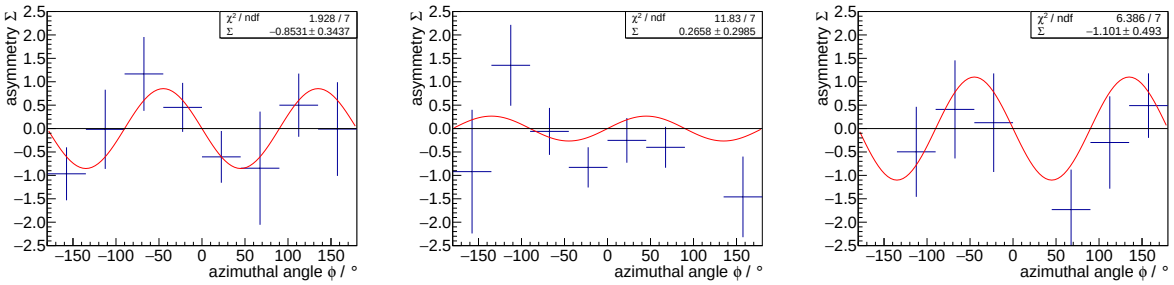

(a) $\Theta_{\mathrm{CM}}^{\mathrm{meson}} = 0°$ to $36°$ (b) $\Theta_{\mathrm{CM}}^{\mathrm{meson}} = 36°$ to $72°$ (c) $\Theta_{\mathrm{CM}}^{\mathrm{meson}} = 72°$ to $108°$

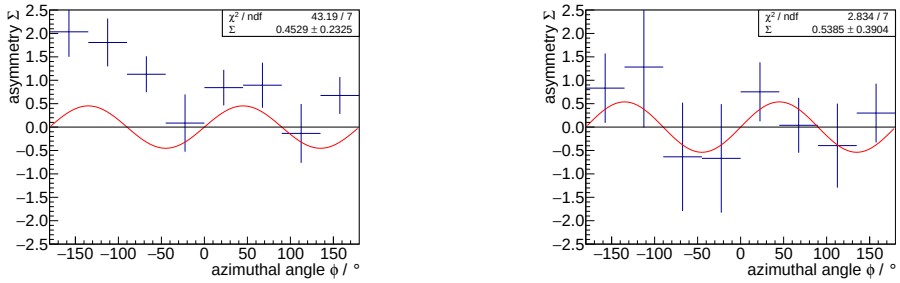

(d) $\Theta_{\mathrm{CM}}^{\mathrm{meson}} = 108°$ to $144°$ (e) $\Theta_{\mathrm{CM}}^{\mathrm{meson}} = 144°$ to $180°$

Figure C.20: Azimuthal distribution of the normalized difference of ω photoproduction events for the extraction of the beam asymmetry, including statistical uncertainties. The results shown have been extracted from the October / November 2015 data set for incoming photon energies E_γ between 1850 MeV and 1950 MeV in different bins of $\Theta_{\mathrm{CM}}^{\mathrm{meson}}$.

List of Figures

List of Tables

Glossary

ADC

An **A**nalogue to **D**igital **C**onverter is a device for digitization of analogue information. Commonly, this is a voltage or an integrated energy information such as a charge. A charge sensitive ADC is commonly called 'QDC'.

CLAS

CEBAF **L**arge **A**cceptance **S**pectrometer, at the **C**ontinuous **E**lectron **B**eam **A**ccelerator **F**acility.

CLB

'**C**onfigurable **L**ogic **B**lock'. A group of slices of different type is grouped to a CLB. It forms a repeating structure on the FPGA.

dead time

The 'dead time' is the time during which a system does not accept new information, for example, a data acquisition system may discard trigger signals, and hence all related event information, if the read out is already in progress and all event buffers are filled.

DESY

Deutsches **E**lektronen-**Sy**nchrotron, a national research centre located in Hamburg, Germany.

DLL

'**D**elay–**l**ocked **l**oop', a chain of controllable delays which are adjusted by a control-loop to create a defined overall delay, thus allowing for clock-signal generation. In many cases, logical inverters are used and their number and operating voltage are varied.

DSP

Digital **S**ignal **P**rocessing.

ELAN

'**EL**ektronstreuung **A**n **N**ukleonen' (german), i.e. electron scattering on nucleons.

ESRF

European **S**ynchrotron **R**adiation **F**acility, located in Grenoble.

ExPIORA

'**Ex**tended **P**luggable **O**bjectoriented **R**OOT*ified* **A**nalysis'. A data analysis framework used at the CB-ELSA/TAPS and BGO-OD experiments in Bonn. It is described in more detail in chapter 5.

FPGA

'**F**ield **P**rogrammable **G**ate **A**rray', an integrated circuit consisting of CLBs. The configuration is done by using a bitfile which enables / disables certain paths and sets the initial state of all elements (e.g. memory registers, lookup tables). Using this method, dynamic programming or reprogramming of hardware logic is possible.

FSM

A **F**inite **S**tate **M**achine can be described as a very simple processor with a fixed program and instruction set. It consists of a register keeping the current state (like a program counter), and a logical description of the operations to be executed in this state. This normally includes a conditional or unconditional change of the state register.

gate

A logic signal which is used to block or unblock a device or another signal. This is for example used in a DAQ-busy state to prevent retriggering while readout is still in progress, or to define the integration time of an ADC. In this way, a introduces a wanted or unwanted dead time or live time into a system.

GRAAL

GRenoble **A**nneau **A**ccelerateur **L**aser.

INL

An '**I**ntegral **N**on-**L**inearity' correction is required to overcome non-linearities induced by analogue electronics such as delay elements or capacitors. Due to inevitable manufacturing spread of the electrical properties of these elements, the system inherits this spread, for example in form of different widths of the sample bins in time or energy. An INL correction corrects for this varying bin size by proper measurement and mapping of the effective bin widths. It is commonly performed by using signals distributed uniformly in the measured variable as input, integrating over all sample bins and scaling the result by the dynamic range. It is described in more detail in section 3.3.

jDisc

Combination of a discriminator mezzanine with the jTDC firmware, allowing to measure the time-over-threshold in addition to the leading edge time. More details are provided in section 4.4.6 and a detailed study of the measured information is performed in section 4.6.

jTDC

TDC implemented as firmware for commercial FPGA boards by J. Bieling (c.f. [Bie]). It is based on a carry-chain sampling technique. More details are provided in section 4.4.5 and appendix A.1.

LEPS2

The second **L**aser **E**lectron **P**hoton Experiment at **S**Pring8.

LEVB

The terminology LEVB is used for the '**l**ocal **ev**ent **b**uilders' of the BGO-OD experiment. These read out data from several modules and create a data stream which is then sent to the event saver.

live time

The 'live time' is the time during which a system is free to accept new information, for example, new trigger signals which may start the read out of electronics modules. It must be noted that 'live time' does not mean that the data is actually recorded.

LUT

'**L**ook **U**p **T**able', a memory element which can be loaded with an init value and is used to map combinations of logical inputs (used like addresses) to a logical output value.

MAMI

MAinz **MI**crotron.

mezzanine

The term mezzanine is used to describe a piggyback daughter board, more details in section 4.4.6.

NIM

'**N**uclear **I**nstrumentation **M**odule', an IO standard defining the logic levels for '1' and '0' using negative currents (or alternatively, negative voltages at 50 Ω resistance).

PAC

Physics **A**dvisory **C**ommittee.

PAW

'**P**hysics **A**nalysis **W**orkstation', a software tool for data analysis and visualization in high energy physics developed starting in 1986 (c.f. [Bru+89]).

pipelining

Pipelining is a method used to reduce the complexity of routing and placing and at the same time allow for more complex logic if e.g. combined with a FSM. To achieve this, the digital values are stored in flip-flops and copied to other flip-flops in the next clock cycle in the sense of a shift register. This delays the digital data only without "halting" the FPGA, thus not creating any dead time. It allows the placer and router to position the flip-flops further apart, so the time-critical paths with several levels of logic start with a "refreshed" signal with less initial path length, allowing for more levels of logic without timing violations (but introducing a time-offset).

PLL

'**P**hase–**l**ocked **l**oop', an oscillator stabilized using a control-loop. In many cases, a ring of delays is used (often made up by logical inverters, controlled by changing their number and operating voltage). A PLL is used to generate a derived clock signal by using coincidences with a reference clock.

PNPI

Petersburg **N**uclear **P**hysics **I**nstitute.

ROOT

An object-oriented analysis framework implemented in C++, including a full-featured C++-interpreter (c.f. [BR97]. It is developed at CERN and is widely used in particle physics experiments.

SADC

A **S**ampling **A**nalogue to **D**igital **C**onverter is an ADC which samples the signal amplitude in several time intervals. The module then either provides the raw samples for software analysis, or extracted features from detected pulses, such as start time, maximum amplitude and integral.

SAPHIR

Spectrometer **A**rrangement for **PH**oton **I**nduced **R**eactions.

scaler

'Scalers' are hardware counters which count up if an input signal is high. Usually, they check the signal with a fixed frequency which also defines their maximum counting rate. In

addition, a scaler module commonly features a counter which is increased each clock cycle to determine the total measurement time in terms of clock cycles. Combining these two pieces of information, the rate of a clock-synchronous signal can be measured. Commonly, an additional gate input allows to enable or disable the counting functionality of all channels, for example to only measure during the live time of an experiment. More details are for example provided in appendix A.2 along the description of a jTDC-based trigger.

shift register

A serial data storage. Data is shifted into the register each clock cycle and can be taken out at the end of the shift register, thus effectively creating a digital delay and / or storage.

slice

The smallest repeating block structure of logic gates on an FPGA. Depending on the model and type of FPGA used, different types of slices can exist forming one CLB. They are in many cases differentiated by the type of LUTs and logic functions available, the memory connectivity or the availability of carry-chain elements.

spill

one extraction period of the cycle of the ELSA accelerator.

SPring8

Super **P**hoton **ring**-8 GeV.

TDC

A **T**ime to **D**igital **C**onverter is a device detecting events in a signal train recording the time at which they occured. In particle physics they are generally used to record leading and / or trailing edges of digital pulses, nowadays with resolutions in the order of picoseconds, usually combined with a trigger signal to select a subset of the recorded events and to provide a reference time in the data.

time walk

'Time walk' describes a dependence of a recorded signal time on the signal height, which is the case for example if the digitization is performed by using a leading edge discriminator. A detailed description and illustration of this effect is provided in section 4.8.

ToT

The **T**ime **o**ver **T**hreshold is the time for which a signal exceeds a given threshold value. A detailed explanation is provided in section 4.6.

VME

VMEbus (VME-**bus**). An asynchronous bus system which was originally using a 16 bit wide databus and a 24 bit wide addressbus. Nowadays, VME32 is widely common using

32 bits for both addressbus and databus. VME64 and several different extensions are also available. The asynchronous bus allows for extensibility with customized boards and the bus is designed to be compatible with many computing architectures, which makes it an ideal choice for data acquisition.

XML

'e**X**tensible **M**arkup **L**anguage' is a structured markup language used commonly to encapsulate information which needs to be both machine and human readable. Its use in the analysis framework of this thesis is described in more detail in section 5.1.3.

Acknowledgements

I hereby acknowledge all the supporters who have helped directly and indirectly towards achieving the successful conclusion of this thesis.

First of all, I wish to thank Prof. Dr. Friedrich Klein who did not only provide the topic covering a hardware and an analysis part, but also supported me in finding the ideal way to take my personal focus on the more technical aspects into account. This extends to the full working group, especially to Dr. Valentina Vegna who gave me strong support in terms of the physics background, shared her analysis experience and was open to follow me through my differing analysis approach at BGO-OD and through the several hardware and software projects along the way. Additionally, she did support me in an incredible way in the final phases of writing, by providing a large and detailed feedback with suggestions for improvements covering all technical details laid out in this thesis.

Further thanks go to Dr. Daniel Elsner, especially for his strong support during the ToF project and during the development of many presentations, abstracts and posters along the way. I would also like to thank John Bieling, who has developed the jTDC, trigger logic and FPGA-based scalers which now provide the technical foundation of most detector readouts throughout the BGO-OD experiment. This especially relates to the trigger system, the time alignment procedures and the time of flight readout which have been covered extensively within this thesis. This work would not have been possible without the support by John Bieling and Georg Scheluchin who adapted the FPGA firmwares accordingly.

A huge thanks goes to Dr. Jürgen Hannappel, who has shared the office space with me for several years even before I started to work on my PhD thesis. This includes many technical discussions and development of ideas covering a very diverse range across the field. Working together, we managed to establish a very successful collaboration especially in the development and improvement of the common analysis software. I have collected most of my technical experience and knowledge of the experiment from him. In his time as technical coordinator of the experiment, he did for example develop the ‘ToF tracking’ approach and proposed the development of the jDisc mezzanine which is now used widely throughout the experimental setup. I wish him the best of luck for this future career.

My next thanks go to Dr. Daniel Hammann, who has not only developed and supported the DAQ of the BGO-OD experiment, but joined in on many technical discussions also in the development of the analysis software. He laid the foundation for the combinatorics algorithm to

construct the reaction final states, which is used in all analyses presented in this thesis. This also holds for Georg Scheluchin, who contributed by also implementing software tools in a generic way usable by the full collaboration, such as the kinematic fit which has been used for the analyses performed in this thesis.

Finally, I would like to thank all members of the working group HSAG, who have made my time as a graduate student a great experience altogether and let the years pass by way too fast: Dr. Thomas Zimmermann and Dr. Andreas Bella, who graduated before me, Dr. Tom Jude, and also the many diploma, bachelor and master students who have helped to develop the experiment in the setup phase and during shifting. Notably, I'd like to mention Peter Meiß who designed the holding structure for the ToF1 and ToF2 walls, and Patrick Bauer who performed a characterization of all scintillator bars in a testing setup and supported the installation of the new ToF setup in the experimental area. I would also like to thank all the external members of the BGO-OD collaboration, without whom a project of this scale would just have been impossible.

The strong support by the ELSA group should not go without mentioning in these acknowledgements. Without the investment of many hours during day and night time, the stable beam conditions which were the basis for the datasets recorded in this thesis would not have been achieved.

Last, but for sure not least, I would like to thank my family for the full support throughout all the years: for the daily 'shuttle service' to university and back, adapting to my often anomalous time-schedule, and for backing up all the decisions I have taken along the way — and just for being who they are, available whenever I needed support.

This strong support by my parents, my grandmother and her life partner for sure is not to be regarded as self-evident and has opened up the necessary freedom to completely delve into my thesis work, producing the many pages you are now holding in hand.